

AN ABSTRACT OF THE DISSERTATION OF

Brendan T. Flynn for the degree of Doctor of Philosophy in Chemical Engineering presented on May 2, 2014.

Title: Functional Materials for Advanced Energy and Electronic Devices.

Abstract approved:

Gregory S. Herman

Advances in energy technologies and electronics have typically occurred through either heightened performance or cost reduction. This dissertation explores both routes through a series of fundamental material studies that may contribute to the enabling of next generation devices. Solution based syntheses and deposition of chemical products offer a low cost alternative to conventional vacuum based methods, and is examined through the wet synthesis of CuZnSnS_4 light absorbing nanoparticles. The nanoparticles were synthesized by both microwave-assisted and continuous flow techniques, and at relatively modest temperatures with inexpensive solvents. Varying the initial concentration of precursors allowed a facile method to modify the nanoparticle composition. For the continuous flow system, consideration of fluid flow dynamics provided a means to control the generation of gas within the reactor to allow for improved mixing. Processing of as-deposited solution based films to form more functional variants was studied in further detail by way of the $\text{Hf}(\text{OH})_{4-2x-2y}(\text{O}_2)_x(\text{SO}_4)_y \cdot q\text{H}_2\text{O}$ (HfSOx)

material system. Surface analytical techniques revealed that control of the catalytically active acid sites may be possible with optimization of water exposure and post-exposure annealing temperature of dehydrated films. Thermal and electron stimulated desorption of peroxide containing HfSO_x films revealed complex surface dynamics. The total desorption cross sections of O_2 for 500-2000 eV incident electrons was $\sim 10^{-16} \text{ cm}^2$. Interfacial formation and chemistry was investigated by evaporating platinum onto amorphous indium gallium zinc oxide, an increasingly common interface type found in memristors and other novel electronics. Metallic indium formed upon platinum deposition, and the interface had an unexpectedly low Schottky barrier height of 0.25 eV, likely as a result of the reactive interface. Finally, the surface properties of highly oriented LaFeO_3 films were characterized and modified through reductive annealing. Iron was found to exist in three oxidation states depending on the annealing temperature and location within the film. In addition, the concentration and types of oxygen species were also found to vary based on proximity to the surface and the thermal treatment. Together, the aforementioned studies are related by the potential manufacturing steps of inexpensive, innovative energy and electronic devices. These steps include solution synthesis and deposition, processing to form a functional film, interface formation, and adapting the film's surface properties to suit its intended application.

©Copyright by Brendan T. Flynn
May 2, 2014
All Rights Reserved

Functional Materials for Advanced Energy and Electronic Devices

by

Brendan T. Flynn

A DISSERTATION

submitted to

Oregon State University

in partial fulfillment of
the requirements for the
degree of

Doctor of Philosophy

Presented May 2, 2014
Commencement June 2014

Doctor of Philosophy dissertation of Brendan T. Flynn presented on May 2, 2014.

APPROVED:

Major Professor, representing Chemical Engineering

Head of the School of Chemical, Biological, & Environmental Engineering

Dean of the Graduate School

I understand that my dissertation will become part of the permanent collection of Oregon State University libraries. My signature below authorizes release of my dissertation to any reader upon request.

Brendan T. Flynn, Author

ACKNOWLEDGEMENTS

My adviser Gregory S. Herman has mentored me and guided my work for the past five years. Thank you for your time, patience, and sound advice. I look forward to using the skills and knowledge I have gained under your tutelage for the rest of my career.

During my year at the Pacific Northwest National Laboratory I learned an incredible amount from the scientists and my fellow Ph.D. interns. In particular, I would like to thank Michael Henderson, Mark Engelhard, and Suntharampillai Thevuthasan. Mike, Mark, and Theva, your contributions to this work and my growth as a scientist and engineer have been invaluable.

At Oregon State University, Chris Tasker has been supportive of my work in the cleanroom and has gone well beyond that expected in assisting me in other areas. In addition, the Herman group students and post-doctoral researchers have all heavily influenced this work and I owe them my gratitude. I would especially like to thank Richard Oleksak. I am a much better student and researcher due to his influence.

Finally, I would like to thank Professor Judy Wornat of Louisiana State University. Professor Wornat enthusiastically gave over an hour of her unscheduled time, late in the day, to an unremarkable student in her Thermodynamics class who was unsure about graduate school. This act of kindness changed my life and ultimately gave the world another Ph.D. in

Chemical Engineering. Thank you Professor Wornat for showing me what it means to be a great scientist and human being.

CONTRIBUTION OF AUTHORS

A large number of people have contributed to the work in this dissertation, and I will clarify their roles in this section. Beginning with the microwave-assisted synthesis of CuZnSnS_4 described in Chapter 3, Wei Wang completed the solar cell fabrication and performed the current-voltage testing, while Chih-hung Chang provided equipment use and data interpretation.

The continuous flow synthesis of CuZnSnS_4 described in Chapter 4 began as an undergraduate senior design project with undergraduates Ian L. Braly and Philip A. Glover completing the initial work. Richard P. Oleksak assisted in interpreting the transmission electron microscopy data, and Chris Durgan performed and filmed reactions.

Chapter 5 concerns the HfSO_x studies, with which a large portion was completed at the Pacific Northwest National Laboratory. Alan Telecky, Benjamin L. Clark, and Douglas A. Keszler were the HfSO_x experts and deposited films and helped interpret data. Daeho Kim and Janos Szanyi provided use of their equipment and ran the experiments at PNNL. Líney Árnadóttir has expertise in surface analytical techniques and assisted data comprehension.

Amorphous indium gallium zinc oxide forms the focus of Chapter 7. Richard P. Oleksak performed the transmission electron microscopy experiments and clarified their results. My manager at PNNL, Theva Thevuthasan, aided with data analysis throughout the experimental process.

Chapter 8 involves the growth and modification of LaFeO_3 , and all of the coauthors listed in the chapter were substantially involved with analyzing the resulting complex data. Experimentally, Kelvin H.L. Zhang grew the LaFeO_3 films, Sandeep Manandhar performed the Rutherford backscattering spectrometry experiment, Tamas Varga collected the x-ray diffraction data, and Robert L. Colby analyzed the films with transmission electron microscopy.

Professor Greg Herman contributed to all aspects of this work.

TABLE OF CONTENTS

	<u>Page</u>
CHAPTER 1: INTRODUCTION	1
Solution Synthesis of CZTS Nanoparticle Inks	3
HafSO _x Film Functionalization	5
Pt/a-IGZO Memristor Interfaces	7
Surface Modification of LaFeO ₃ Catalysts	8
References	10
Figures	13
CHAPTER 2: ANALYTICAL TECHNIQUES	17
Inductively Coupled Plasma – Atomic Emission Spectroscopy	18
X-ray Diffraction	18
Raman Spectroscopy	20
Scanning Electron Microscopy	21
Energy Dispersive Spectroscopy	22
Transmission Electron Microscopy	23

TABLE OF CONTENTS (Continued)

	<u>Page</u>
Ultraviolet-Visible Spectroscopy	23
Thermogravimetric Analysis	24
Solar Cell Performance Characterization	25
Temperature Programmed Desorption.....	26
Electron Stimulated Desorption	27
X-ray Photoelectron Spectroscopy	28
Rutherford Backscattering Spectrometry	30
Reflection High-Energy Electron Diffraction	31
References	31
Figures.....	35
 CHAPTER 3: MICROWAVE ASSISTED SYNTHESIS OF $\text{Cu}_2\text{ZnSnS}_4$ COLLOIDAL NANOPARTICLE INKS	 41
 Abstract	 42
 Introduction.....	 43

TABLE OF CONTENTS (Continued)

	<u>Page</u>
Experimental Methods.....	46
Results and Discussion	49
Conclusion	58
Acknowledgements	59
References.....	59
Figures	68
 CHAPTER 4: CONTINUOUS FLOW MESOFLUIDIC SYNTHESIS OF Cu ₂ ZnSnS ₄ NANOPARTICLE INKS	 77
Abstract	78
Introduction.....	79
Experimental Methods	80
Results and Discussion	81
Conclusion.....	87
Acknowledgements	88
References	86

TABLE OF CONTENTS (Continued)

	<u>Page</u>
Figures.....	92
 CHAPTER 5: <i>IN SITU</i> CHARACTERIZATION OF AQUEOUS-BASED HAFNIUM OXIDE HYDROXIDE SULFATE THIN FILMS	 98
Abstract	99
Introduction.....	100
Experimental Methods	101
Results and Discussion	103
Conclusion.....	113
Acknowledgements	113
References	114
Figures.....	120
 CHAPTER 6: THERMAL AND ELECTRON BEAM MODIFICATION OF HafSO _x INORGANIC RESISTS	 124
Abstract	125
Introduction.....	126

TABLE OF CONTENTS (Continued)

	<u>Page</u>
Experimental Methods.....	127
Results and Discussion	129
Conclusion.....	138
References	139
Figures.....	144
 CHAPTER 7: Pt/a-IGZO JUNCTION CHARACTERIZED BY <i>IN SITU</i> PHOTOEMISSION	 149
 Abstract	 150
Introduction.....	151
Experimental Methods.....	152
Results and Discussion	154
Conclusion.....	159
References	160
Figures.....	163

TABLE OF CONTENTS (Continued)

	<u>Page</u>
CHAPTER 8: GROWTH AND SURFACE MODIFICATION OF LaFeO_3 THIN FILMS INDUCED BY REDUCTIVE ANNEALING.....	168
Abstract	169
Introduction.....	170
Experimental Methods.....	171
Results and Discussion	175
Conclusion.....	181
References	182
Figures.....	187
 CHAPTER 9: CONCLUSION AND FUTURE DIRECTIONS	194
 BIBLIOGRAPHY	200

LIST OF FIGURES

<u>Figure</u>	<u>Page</u>
1.1 Earth abundance and price of elements in thin film PV absorbers	13
1.2 Heat, ultraviolet light, and accelerated electrons can all break the peroxide bond in HfSO_x and cause polymerization of the Hf-O framework..	14
1.3 Simplified memristor device structure	15
1.4 Emissions from a spark-ignited gasoline engine as a function of the intake air-fuel ratio, A/F (g-air/g-fuel)	16
2.1 Diffracted x-rays are reinforced if the angle θ satisfies Bragg's law.....	35
2.2 Raman spectra are produced by the scattering of incident radiation $h\nu_{\text{in}}$, molecular excitation to virtual level j , and subsequent relaxation with photon emission	36
2.3 Generation of characteristic x-rays during EDS analysis	37
2.4 Principle of TEM image and diffraction pattern generation	38
2.5 Schematic demonstrating electronic coupling between the sample and spectrometer during an XPS experiment.....	39
2.6 Grazing emission XPS studies substantially reduce the amount of signal from the bulk	40
3.1 XRD spectra of as synthesized nanoparticles and nanoparticles annealed to 400 °C for 20 minutes	69
3.2 Raman spectra of annealed (upper) and unannealed (lower) nanoparticles showing main vibrational mode at 333 cm^{-1}	70

LIST OF FIGURES (Continued)

<u>Figure</u>	<u>Page</u>
3.3 Low (5,000x) and high (200,000x) magnification SEM images of the as synthesized nanoparticles (a,b) and annealed nanoparticles (c,d)	71
3.4 TEM images illustrating particle size (a), interplanar spacing of the (112) plane (b), and SAED (c) of unannealed CZTS nanoparticles	72
3.5 UV-Vis spectra of the as synthesized CZTS nanoparticles.....	73
3.6 Thermal gravimetric analysis of CZTS nanoparticles	74
3.7 SEM image of a cross section of CZTS solar cell.....	75
3.8 Current-voltage characteristics for CZTS solar cell	76
4.1 Diagram of continuous flow reactor used for CZTS synthesis	93
4.2 Relationship between axial position and residence time	94
4.3 (a) XRD and (b) Raman spectra for CZTS nanoparticles synthesized for different residence times	95
4.4 TEM analysis shows that the CZTS nanoparticles were both (a,c) multicrystalline and (b,d)single crystalline with an (e)average size of 5.4 nm.	96
4.5 (a) XRD and (b) Raman spectra of CZTS nanoparticles, $\text{Cu}_{1.9}\text{Zn}_{1.0}\text{Sn}_{1.2}\text{S}_{3.9}$, after annealing in N_2 , N_2+S , and N_2+Se	97
5.1 Temperature programmed desorption spectra from spin-coated HafSO_x films after a 353 K anneal	120

LIST OF FIGURES (Continued)

<u>Figure</u>	<u>Page</u>
5.2 High-resolution XPS from HafSO _x films annealed to the indicated temperatures	121
5.3 Relative intensity ratios of the three fitted O 1s peak components versus annealing temperature from Fig. 5.2(c)	122
5.4 (a) Schematic of different types of Brønsted acid sites on HafSO _x and their transformation to Lewis acid sites upon desorption of water, adapted from reference [14]	123
6.1 XPS spectra of HafSO _x film after a 353 K soft bake	144
6.2 ESD spectra of HafSO _x with peroxide, without peroxide, and a clean Si substrate (for reference)	145
6.3 (a) Normalized O ₂ desorption from 500-2000 eV and the (b) corresponding total desorption cross sections	146
6.4 TPD spectra before and after 1000 eV ESD	147
6.5 Variation in SO ₂ desorption temperature as a function of time	148
7.1 Platinum deposition on a-IGZO	163
7.2 Vacuum annealing Pt/a-IGZO film	164
7.3 Cross sectional STEM image (left) and associated EDS line scan (right) of the Pt/a-IGZO film annealed to 300 °C	165
7.4 Valence band spectra of Pt/a-IGZO during Pt deposition	166

LIST OF FIGURES (Continued)

<u>Figure</u>	<u>Page</u>
7.5 Schematic of Pt/a-IGZO energy band diagram and changes in Schottky barrier with deposition time and annealing temperature	167
8.1 XRD spectrum of LFO(001) grown on YSZ(001) at 700 °C	187
8.2 Post-growth RHEED pattern of LFO(001) grown on YSZ(001) at 700 °C.	188
8.3 (a) Channeling and random RBS spectra along with the SIMNRA calculated result for the as-grown LFO film on YSZ... ..	189
8.4 HAADF-STEM images at different locations of the LFO/YSZ film	190
8.5 10° (top) and 45° (bottom) emission spectra from LFO/YSZ film oxidized and annealed in vacuum	191
8.6 Atomic concentrations from 10° (left) and 45° (right) emission spectra of LFO/YSZ film	192
8.7 Peak fits of O 1s spectra.....	193

LIST OF TABLES

<u>Table</u>	<u>Page</u>
3.1 Composition of precursor solutions and CZTS nanoparticles.....	68
4.1 Effect of residence time on composition and crystallite size.....	92

FUNCTIONAL MATERIALS FOR ADVANCED ENERGY AND ELECTRONIC DEVICES

CHAPTER 1

INTRODUCTION

In any commercial technology or research endeavor, two matters regularly pervade the minds of the scientists and engineers: cost reduction and process enhancement. Progress in these areas is not mutually exclusive, and it is through both monetary savings and improved or added functionality that science and technology evolve. If cost reduction could be achieved by switching to less energy intensive production methods or reducing the required energy budget, this would have the added benefit of lessening the contribution to anthropogenic climate forcing. Future political climates may require decreased energy use during manufacturing, or consumer preferences could drive reductions in this area, for example by buyers purchasing solar panels with a shorter energy payback period (how long it takes for the solar panel to produce the amount of energy that was needed to make it). Concurrent with cost reduction, process and device enhancement is critical for enabling innovative end products. More efficient solar cells, faster computer processors, artificial neural networks, and “intelligent” car exhaust catalysts form a short list of current research efforts, and the materials potentially used in these applications are explored in more detail in this dissertation.

A diverse set of materials were examined to gain a basic understanding of their material properties, which may enable modifying these properties to suit novel energy and electronic applications and manufacturing methods. From a broad perspective, a number of steps could be involved in

new low cost, high performance manufacturing processes. These include solution-based synthesis and deposition methods to produce the desired chemical product and film, processing to form a functional film, interface formation with other parts of the device, and finally tailoring of the surface properties to suit the device's function. The first step mentioned above was examined through the solution-based synthesis of CuZnSnS_4 (CZTS) nanoparticles for solar cell applications, and it forms the basis of Chapters 2 and 3.

To appreciate the motivation for research on CZTS, it is helpful to understand how it fits into the larger picture of photovoltaic technology. Currently, about 85-90% of the photovoltaic (PV) market is held by crystalline silicon PV modules [1]. The raw material for crystalline silicon PV modules is typically quartz, and it is relatively energy intensive to produce solar grade polysilicon from this feedstock. The direct chlorination Siemens process is widely used for this purpose, and to produce one kilogram of polysilicon, it takes 120-200 kWh[2]. To put that in perspective, it is approximately the same amount of energy as on the monthly electric bill of the two story house that I rent. Producing monocrystalline wafers from polysilicon via the Czochralski process would require even more energy. Thin film PV technologies, of which CZTS is included, can be produced with significantly less energy than their silicon counterparts. One measure to determine the relative merits of these technologies energy-wise is to compare the total

amount of energy a solar panel will produce over its lifetime versus how much energy was required to produce it. The current leading thin film PV technology, CdTe, will be used as a basis for comparison. For panels installed in the American Southwest, a CdTe panel will produce 50 times as much as energy as was used to produce it over its lifetime, compared to 25 times as much for crystalline silicon solar panels (mono- or multi-crystalline)[3].

With the advantage of reduced energy consumption and lower manufacturing costs, thin film PV could command more market share provided its efficiency increased to the level of crystalline silicon. A potential issue with increased production output for two of the leading thin film PV technologies, CdTe and CuInGaSe₂ (CIGS), is material scarcity and price. It has been forecasted that more than 30 TW of new power generation needs to be installed worldwide by 2050[4], and hopefully renewables such as solar will make up a significant fraction of the new installed capacity. As shown in Figure 1.1, the abundance of the constituent elements in CdTe and CIGS are appreciably lower than those in CZTS, and they correspondingly have a higher price[5]. Given current annual production levels of the raw materials, CdTe (9 GW/yr) and CIGS (28 GW/yr) are limited to manufacturing levels that fall well short of meeting future power demand[6].

Non-vacuum synthesis and deposition techniques are well suited to meet the challenges of such large production volumes. In relation to

conventional vacuum-based techniques, solution synthesis and deposition offers higher throughput, broad spatial compositional homogeneity, manufacturing equipment with much lower capital costs, and reduced material waste[7]. Through this lens, research interest into solution-based CZTS can be understood, and is discussed in greater detail in Chapters 3 and 4. As a final aside, it is worth mentioning that CZTS is nearly lattice-matched with Si[8], with a lattice mismatch of about 1%, and so possibilities exist for a high efficiency multi-junction tandem solar cell combining the two materials.

The next step in the manufacturing process mentioned above after wet synthesis and deposition is film functionalization. This was investigated using the material system $\text{Hf}(\text{OH})_{4-2x-2y}(\text{O}_2)_x(\text{SO}_4)_y \cdot q\text{H}_2\text{O}$, or HfSO_x . The HfSO_x films were spin coated from aqueous precursors, and very smooth films have been demonstrated using this process[9]. These films have applications as solid superacid catalysts and patternable lithography resists, naming only two. In terms of catalysis, gasoline additives such as ethanol are used to increase gasoline's octane rating and thus reduce the damaging effects of engine knock. There are substantial amounts of n-alkanes in petroleum, and so transformation of these linear alkanes into their branched isomers could boost the octane rating while reducing the amount of additives needed[10]. Sulfated zirconia, an isoelectronic analog of sulfated hafnia, has demonstrated high catalytic activity for isomerization[11]. The catalytic activity is thought to derive from the strong electron withdrawing ability of the

sulfate groups bound to metal sites, which generates electron accepting Lewis acid sites. Exposure to water can then generate proton donating Brønsted-Lowry acid sites, which has implications for HfSO_x 's ability to isomerize n-alkanes and creates opportunities to functionalize the film for catalytic purposes.

Besides its superacid capabilities, a major thrust of research at Oregon State University concerns the utility of HfSO_x as a model resist for the patterning of next generation integrated circuits. Advances in circuit performance such as processing speed and memory density are related to the number of transistors per chip. As the feature size of transistors continues to shrink, it will be more difficult to fit more components on a single chip, and thus new resists with the ability to pattern periodic nanometer-sized features on chips are needed[12]. Patterning of small features has already been demonstrated with this resist in a near-production environment[13], and it is known that the addition of peroxide controls condensation and thus its patternability (see Figure 1.2). The peroxide bonds in a μ_2 manner and decomposes upon exposure to heat or sufficiently energized light or electrons. Crosslinking and densification accompanies peroxide decomposition in the film. Insights into this decomposition mechanism could lead to greater patterning sensitivity in the material and yield a basic understanding that could be used to alter the sensitivity by metal dopants and

other means, and ultimately will help determine whether or not this material system is suitable for advanced lithography and circuit design.

After film functionalization, typically another material is deposited to form an interface, such as the n-type material to form the critical p-n junction in a solar cell or the metal electrodes deposited on an oxide in an amorphous metal oxide transistor. The chemistry and material properties at interfaces can be quite distinct and independent of the bulk properties of the two parent materials, such as the conductivity exhibited at the $\text{LaAlO}_3/\text{SrTiO}_3$ (001) interface despite both materials being bulk insulators[14]. For this reason, the interfaces used in next generation devices warrant thorough examination, and in this dissertation the platinum/amorphous indium gallium zinc oxide (Pt/a-IGZO) interface currently being used in memristors and other novel electronics is studied.

The memristor, first proposed in 1971[15], is a device that is capable of switching between a low resistance state (LRS) and a high resistance state (HRS) depending on the history of applied voltage, and so in a sense the device acts as a resistor that “remembers” its past usage. The device structure typically includes the switching or channel material sandwiched in between two metal electrodes, which all rests upon a passivated substrate as shown in Figure 1.3. During operation, one electrode is connected to ground while either a positive or negative voltage is applied to the other electrode,

inducing chemical and structural changes at the metal/channel interface which gives rise to the memristive behavior[16].

One interesting application of these Pt/a-IGZO memristors is for artificial neural networks due to their operational similarity to the brain's synapses during a learning event or memory recall. The strength of certain synaptic connections in the brain changes during a learning event, and these altered connections can be reactivated by remembering the event[17]. Essentially, the neural activity and response of the affected synapses increases, or is potentiated, and endures for a long time, hence the phenomenon is called long-term potentiation[18]. This effect can be experimentally produced by short bouts of high-frequency stimulation to a synaptic pathway in the hippocampus, which causes an immediate and sustained increase in the efficiency of synaptic transmission[19]. This behavior is similar to the memristor, where before the learning event the synaptic connections can be thought of as in a HRS, but after learning stimulation the connections abruptly switch to a LRS, and can remain in this state indefinitely. As mentioned above, the defects and chemistry at the Pt/a-IGZO interface governs the performance of the memristive device, and is the subject of Chapter 7.

Along with interfaces, the surface of a material can have remarkably different properties than the bulk material. The surface properties may be tailored to suit the device's intended function as one of the final steps in

device manufacturing. The surface properties of a catalyst are particularly important since the conversion of one molecular species to another takes place at the surface of the catalyst. Lanthanum iron oxide (LFO) is a simple perovskite that may be doped with other elements to catalyze the conversion of undesired exhaust gases to more benign products in an automobile's catalytic converter[20].

A catalytic converter is designed to reduce the level of carbon monoxide, unburned hydrocarbons, and nitrogen oxides emitted by automobiles. Carbon monoxide is poisonous, while effluent hydrocarbons and nitrogen oxides can react to generate smog and ozone in the atmosphere. The converter must oxidize carbon monoxide and hydrocarbons to carbon dioxide and water, while also reducing nitrogen oxides to molecular nitrogen. Catalysts used for this purpose generally consist of palladium particles dispersed on an oxide support[21]. Some of these catalyst formulations exhibit resilience to palladium aggregation, which hinders catalytic performance. This resilience is attributed to palladium's ability to reversibly move into and out of the oxide support depending on whether the atmosphere is oxidative or reductive[20], and so these catalysts are said to be "intelligent". Engine emissions can vary substantially depending on the engine temperature and the air to fuel ratio, as shown in Figure 1.4, and so the catalyst is subjected to both oxidizing and reducing conditions. Several research groups have completed surface studies on these types of catalysts

under oxidizing conditions because of the relevance to both catalytic converter and solid oxide fuel cell operation. A surface sensitive characterization of a model perovskite oxide under reducing conditions was warranted, and the results are presented in Chapter 8.

References:

- [1] IEA-ETSAP and IRENA Technology Brief E11 – January 2013. [Online]. Available: <http://www.irena.org/DocumentDownloads/Publications/IRENA-ETSAP%20Tech%20Brief%20E11%20Solar%20PV.pdf>
- [2] A. Goodrich, P. Hacke, Q. Wang, B. Sopori, R. Margolis, T. L. James, and M. Woodhouse, “A wafer-based monocrystalline silicon photovoltaics road map: Utilizing known technology improvement opportunities for further reductions in manufacturing costs,” *Sol. Energy Mater. Sol. Cells*, vol. 114, pp. 110-135, 2013.
- [3] V. Fthenakis, “How Long Does it Take for Photovoltaics To Produce the Energy Used?” *PE Magazine*, January-February 2012. [Online]. Available: http://www.clca.columbia.edu/236_PE_Magazine_Fthenakis_2_10_12.pdf
- [4] C. Wadia, A. P. Alivisatos, D. M. Kammen, “Materials Availability Expands the Opportunity for Large-Scale Photovoltaics Deployment,” *Environ. Sci. Technol.*, vol. 43, pp. 2072-2077, 2009.
- [5] U.S. Geological Survey, Mineral commodity summaries 2014, pp.1-196.
- [6] M. Woodhouse, A. Goodrich, R. Margolis, T.L. James, M. Lokanc, and R. Eggert, “Supply-Chain Dynamics of Tellurium, Indium, and Gallium Within the Context of PV Manufacturing Costs,” *IEEE Journal of Photovoltaics*, vol. 3, pp. 833-837, 2013.

- [7] T. Todorov and D. B. Mitzi, "Direct Liquid Coating of Chalcopyrite Light-Absorbing Layers for Photovoltaic Devices," *Eur. J. Inorg. Chem*, vol. 2010, pp. 17-28, 2010.
- [8] M. A. Green, "Silicon Wafer-Based Tandem Cells: The Ultimate Photovoltaic Solution?" *Proc. of SPIE*, vol. 8981, pp. 89810L-1 – 89810L-6, 2014.
- [9] R. P. Oleksak, R. E. Ruther, F. Luo, K. C. Fairley, S. R. Decker, W. F. Stickle, D. W. Johnson, E. L. Garfunkel, G. S. Herman, and D. A. Keszler, "Chemical and Structural Investigation of High-Resolution Patterning with HfSO_x ," *ACS Appl. Mater. Interfaces*, vol. 6, pp. 2917-2921, 2014.
- [10] V. M. Akhmedov and S. H. Al-Khowaiter, "Recent Advances and Future Aspects in the Selective Isomerization of High n-Alkanes," *Catal. Rev.*, vol. 49, pp. 33-139, 2007.
- [11] M. Hino, S. Kobayashi, and K. Arata, "Reactions of Butane and Isobutane Catalyzed by Zirconium Oxide Treated with Sulfate Ion. Solid Superacid Catalyst," *J. Am. Chem. Soc.*, vol. 101, pp. 6439-6441, 1979.
- [12] A. J. Telecky, "Photoresist and Ion-Exchange Chemistry of HfSO_x ," Ph.D. Dissertation, Oregon State University, 2012.
- [13] X. Thrun, K. -H. Choi, M. Freitag, A. Grenville, M. Gutsch, C. Hohle, J. K. Stowers, J. W. Bartha, "Evaluation of direct patternable inorganic spin-on hard mask materials using electron beam lithography," *Microelectron. Eng.*, vol. 98, pp. 226-229, 2012.
- [14] S. A. Chambers, "Epitaxial Growth and Properties of Doped Transition Metal and Complex Oxide Films," *Adv. Mater.*, vol. 22, pp. 219-248, 2010.
- [15] L. O. Chua, "Memristor – The Missing Circuit Element," *IEEE Trans. Circuit Theory*, vol. CT-18, pp. 507-519, 1971.

- [16] J. S. Rajachidambaram, "Evaluation of Amorphous Oxide Semiconductors for Thin Film Transistors (TFTs) and Resistive Random Access Memory (RRAM) Applications," Masters Thesis, Oregon State University, 2011.
- [17] S. J. Martin and R. G. M. Morris, "New Life in an Old Idea: The Synaptic Plasticity and Memory Hypothesis Revisited," *Hippocampus*, vol. 12, pp. 609-636, 2002.
- [18] A. M. White and H. S. Swartzwelder, "Age-Related Effects of Alcohol on Memory and Memory-Related Brain Function in Adolescents and Adults," *Recent Dev. Alcohol*, vol. 17, pp. 161-176, 2005.
- [19] T. V. P. Bliss and G. L. Collingridge, "A synaptic model of memory: long-term potentiation in the hippocampus," *Nature*, vol. 361, pp. 31-39, 1993.
- [20] Nishihata, J. Mizuki, T. Akao, H. Tanaka, M. Uenishi, M. Kimura, T. Okamoto, and N. Hamada, "Self-regeneration of a Pd-perovskite catalyst for automotive emissions control," *Nature*, vol. 418, pp. 164-167, 2002.
- [21] R. M. Heck, R. J. Farrauto, and S. T. Gulati, *Catalytic Air Pollution Control: Commercial Technology*. New York, NY, USA: John Wiley & Sons, 2002.Y.
- [22] J. T. Kummer, "Catalysts for Automobile Emission Control," *Prog. Energy Combust. Sci.*, vol. 6, pp. 177-199, 1980.

Figures

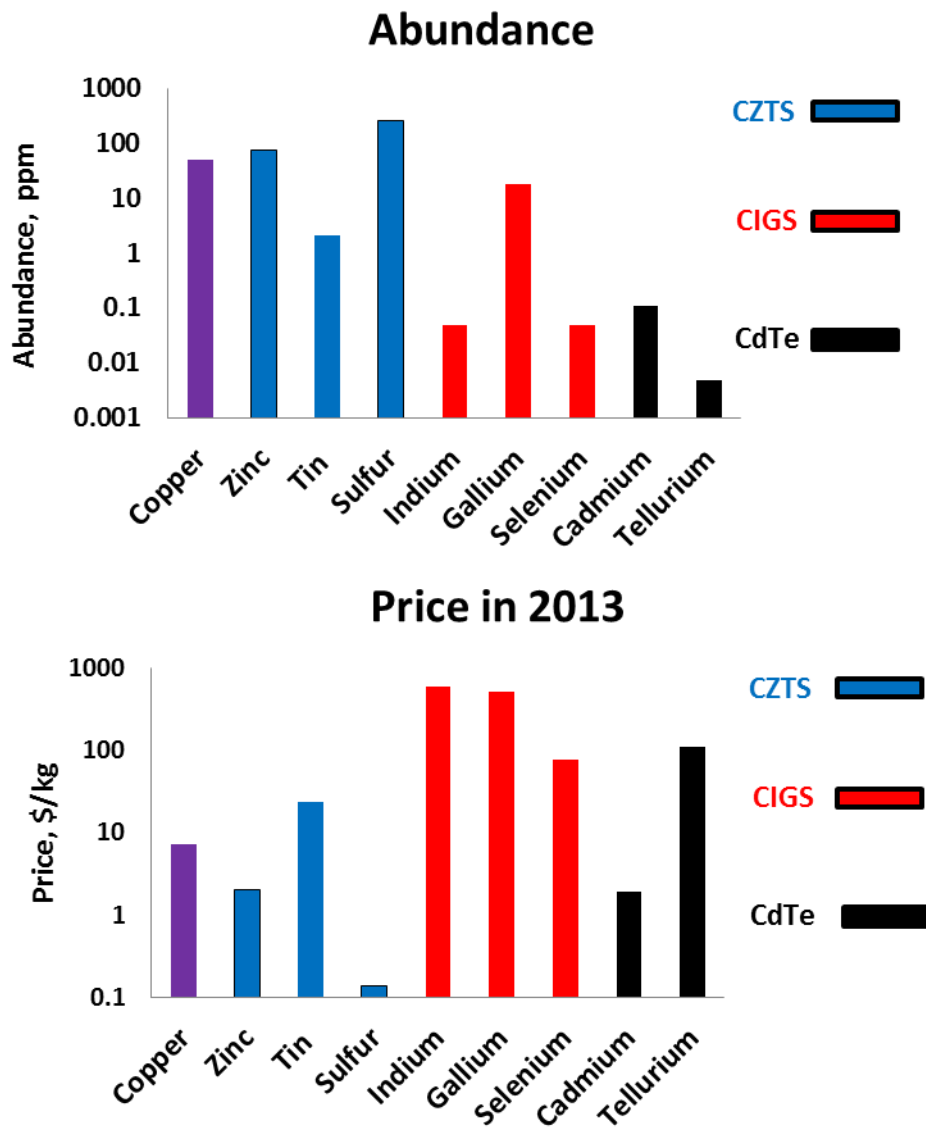


Figure 1.1 – Earth abundance and price of elements in thin film PV absorbers. Prices taken from reference [5].

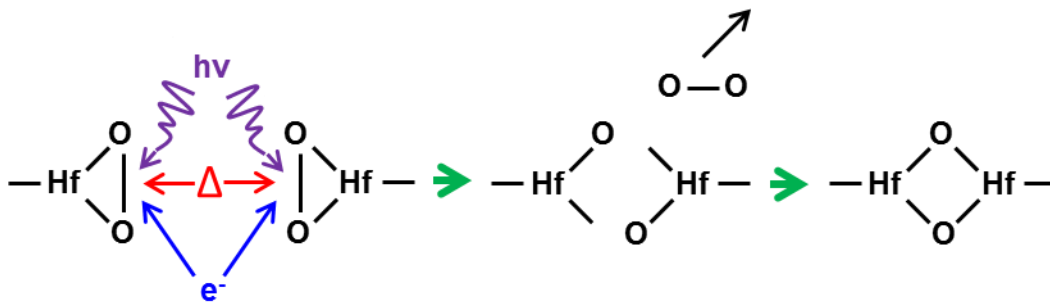


Figure 1.2 – Heat, ultraviolet light, and accelerated electrons can all break the peroxide bond in HafSO_x and cause polymerization of the Hf-O framework.

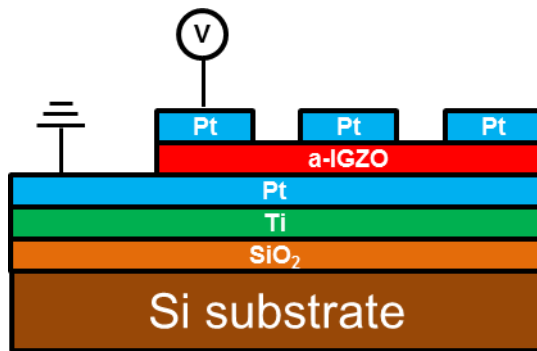


Figure 1.3 – Simplified memristor device structure. A positive or negative voltage applied to the top Pt electrode can alter the resistance in the a-IGZO layer.

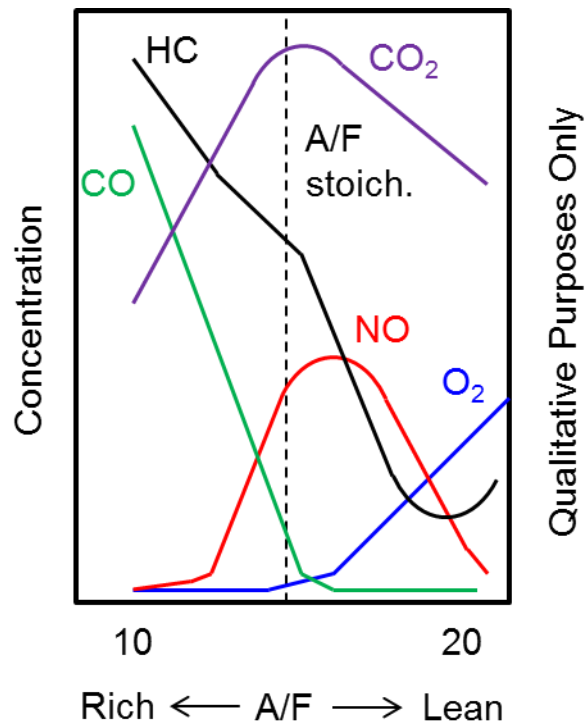


Figure 1.4 – Emissions from a spark-ignited gasoline engine as a function of the intake air-fuel ratio, A/F (g-air/g-fuel). Adapted from reference [22].

CHAPTER 2

ANALYTICAL TECHNIQUES

A variety of analytical techniques were used in this work, and a basic understanding of them will assist the reader in understanding the interpretation of data in Chapters 3-8. The experimental methods of Chapter 2, the microwave assisted synthesis of CZTS nanoparticles, will be reviewed first.

Inductively coupled plasma – atomic emission spectroscopy (ICP-AES) is a technique used to quantify the atomic concentration of a sample, typically a liquid or gas. The sample is pumped to a nebulizer where it mixes with Ar gas and is carried towards the plasma source. An Ar plasma (gaseous mixture of electrons and ions) is generated by high powered radio-frequency induction coils, which heats the plasma to temperatures well exceeding 6000 K and is sufficient to atomize the constituents in the carrier gas. As the ionized atoms relax to lower energy level by releasing photons, light is emitted with energy characteristic of the parent atom. This process of ionization and relaxation repeatedly cycles in the hot plasma, emitting a sufficient quantity of light for analysis. The intensity of light emitted at a given energy can then be correlated to the concentration of the element in the sample using a spectrometer[1].

X-ray diffraction (XRD) gives information on the structural properties and crystallite size of a solid sample, and in many labs it is used as a qualitative measure of the sample purity. In a common XRD experiment, the sample is bombarded with Cu K α x-rays (0.1542 nm wavelength), some of

which are scattered and interfere constructively at characteristic diffraction angles depending on the spacing of atomic planes in the material. The condition for interference effects is famously given by Bragg's law:

$$2d \sin \theta = n\lambda$$

For this equation, d is the interplanar spacing of atoms, θ is the diffraction angle, n is the order of diffraction, and λ is the incident x-ray wavelength. A schematic of a constructively interfering x-ray beam is shown in Fig. 2.1[2]. The interpretation of Bragg's law is that few x-rays should be expected from the sample unless they are at an angle θ which satisfies the above equation. For a particular crystallographic plane, diffraction occurs for $n = 1, 2, 3, \dots$, but the first order of diffraction is typically the only one considered. For higher orders of diffraction, multiples of the Miller indices of the plane are used. For example, when dealing with the second order diffraction ($n = 2$) of a (112) plane, planes present at half the spacing are imagined and termed the $n = 1$ diffraction from a (224) plane. A detailed discussion of the structure factor for a given plane is beyond the scope of this introduction, but it should be noted that the structure factor can be used to show that reflections from certain planes are forbidden[3].

To calculate the crystallite size, Scherrer's equation is commonly used:

$$\rho = \frac{K\lambda}{B \cos \theta}$$

The crystallite size is given by ρ , K is a morphology dependent shape factor, λ is the x-ray wavelength, the peak full width at half maximum is given by B , and θ is the Bragg angle. $K = 1$ may be generally used for a morphology independent estimate of the crystallite size[4], although tabular values of K may be found for a particular morphology and set of Miller indices[5]. The limitations of the Scherrer equation as an estimate of the true particle size result from the fact that peak width is not solely dependent on particle size. Other factors contributing to peak width include lattice strain and faults, crystallite size distribution, and instrumental broadening (e.g. imperfect focusing, slit width, etc.).

Another useful technique for characterizing nanoparticles is Raman spectroscopy. In Chapters 3 and 4, Raman analysis was used to discriminate between different possible compounds to confirm synthesis of CZTS. Raman spectra are acquired by irradiating a sample with monochromatic visible light or light close to this energy range. Molecules can absorb a photon and reemit a photon at the same energy (Rayleigh scattering), or either a higher (anti-Stokes scattering) or lower (Stokes scattering) energy than the incident light. The shift in energy or frequency of the emitted photon corresponds to the vibrational frequency of the molecule, and thus Raman spectroscopy can be used for molecular identification.

The excitation of the molecule upon absorption of incident light with energy $h\nu_{in}$ is shown in Fig. 2.2. Excitation to a virtual state j is said to occur

since the energy of the incident light normally is insufficient to excite the molecule to the lowest excited electronic states[6], and thus the depicted process is not quantized. When the molecule is initially in the ground state ($\nu = 0$), it absorbs energy equal to $h\nu_{in}$, which excites it to state j before the molecule relaxes to excited state $\nu = 1$. During the relaxation process it emits a photon with lower frequency than the incident light, $h(\nu_{in} - \nu_{vib})$, where ν_{vib} is the vibrational frequency of the molecule. As mentioned above, this is termed Stokes scattering. During anti-Stokes scattering, the molecule is initially in the $\nu = 1$ excited state, and after promotion to state j and relaxation to the ground state a photon is emitted with energy $h(\nu_{in} + \nu_{vib})$. At room temperature the relative number of molecules in the $\nu = 1$ state is small, and Stokes emission is heavily favored and generally used for Raman analysis[7].

Scanning electron microscopy (SEM) was used in this work to analyze the morphology of synthesized nanoparticles and films as well as to determine their chemical composition by energy dispersive x-ray spectroscopy (EDS). For sample imaging, a sample is irradiated with electrons ranging from 1-30 kV which lose energy as they penetrate and interact with the sample. This energy dissipation causes secondary electron emission from the sample. The secondary electrons are collected by a phosphor-photomultiplier device, or Everhart-Thornley detector. The spatial location of the primary electron beam and intensity of the detected secondary electrons are then converted into an image[3].

The EDS process begins with the ejection of an atom's inner-shell electron by the incident beam. An outer-shell electron fills the newly created core-hole, emitting an x-ray characteristic of the difference in energy between the levels, and of the atom itself. This is schematically shown in Fig. 2.3[8]. A silicon energy-dispersive x-ray detector is used to discriminate between x-rays originating from different atoms in the sample. Incident photons generate a current in the detector which is proportional to the photon energy and number of photons. The current that flows from an x-ray lasts for a short time and is recorded as a pulse. The detector system amplifies the pulse and transmits the signal to a multichannel analyzer, which determines the channel (x-ray energy) to which the pulse belongs. The counts per second recorded for a given pulse is then related to the amount of constituent material (chemical composition). Several important limitations for this technique should be considered. X-rays of a higher energy from one atom may generate x-rays of a lower energy from a different atom in a sample. For example, in a sample containing both zinc and copper, zinc $K\alpha$ (8.64 eV) x-rays can excite extra copper $K\alpha$ (8.05 eV) x-rays, which can lead to overestimating the amount of copper in the sample, and underestimating the amount of zinc in the sample. In addition, if two identical photons may enter the detector simultaneously, the detector will register this as a single photon with double the energy, termed the sum peak effect. A third source of error

results from x-ray generation from the Si atoms in the detector, or the silicon escape peak[3].

Transmission electron microscopy (TEM) provided insight into the nanoparticle size, crystal orientation, atomic planar spacing, and material composition in this dissertation. Rather than the thick samples appropriate for SEM, TEM samples are typically less than 100 nm, and images are produced by the primary electrons transmitting through the sample and impinging on a phosphor screen, with an image ultimately produced by a charge-coupled device which converts the emitted photons from the phosphor into an image. As shown in Fig. 2.4[9], diffraction patterns can also be used from TEM analysis to provide information on phase purity and crystallinity, much in the same way as XRD. Whereas diffraction in XRD is a bulk technique, electron diffraction in TEM allows the researcher to collect diffraction patterns from individual nanoparticles to determine phase purity and planar spacing. Fourier transforms of high-resolution TEM images provide information similar to a diffraction pattern. A transform of an image converts data from the spatial domain to the frequency domain, where periodic structures in the initial image appear as bright points in the resulting transform. Each point is representative of a particular frequency (e.g. from lattice planes) within the original spatial domain image.

The band gap and absorption properties of CZTS nanoparticles are a critical factor in determining its utility for solar cells, and these were analyzed

with ultraviolet-visible (UV-Vis) spectroscopy. For UV-Vis experiments in this work, a nanoparticle film was spun on a glass substrate, and a UV-Vis spectrophotometer measured the intensity of light transmitted through the sample compared to the incident light intensity. Light transmittance can be simply converted to absorbance for band gap determinations. For a semiconductor, the following relationship may be used to determine the band gap[10]:

$$(h\nu\alpha)^{1/n} = C(h\nu - E_g)$$

Here, $h\nu$ is the photon energy, α the absorption coefficient, C a constant, and E_g the band gap. The exponent n is equal to $\frac{1}{2}$ for a direct band gap semiconductor such as CZTS. The absorption coefficient is directly proportional to absorbance, A , so that plotting $(Ah\nu)^2$ vs. $h\nu$ yields a Tauc plot. Extrapolating the linear portion of the curve (absorption onset) to the abscissa gives the band gap. To determine the absorption coefficient, the Beer-Lambert Law was used:

$$\frac{\ln T}{-t} = \alpha$$

The natural logarithm of the transmittance T is divided by the negative of the film thickness to yield the absorption coefficient, which is a function of the photon energy.

Thermogravimetric analysis (TGA) is a relatively simple technique that measures a sample's mass as a function of temperature in a controlled

atmosphere. The change in mass can give information on the amount of residual capping ligands on the nanoparticles, as well as a measure of sample purity since different compounds will decompose and volatilize at different temperatures. In a typical experimental setup, the sample powder is placed into a small metal sample pan, which is then loaded into the furnace for heating. The thermocouple is placed close to the sample container for temperature measurement.

Finally, a discussion of the solar cell parameters mentioned in Chapter 3 is appropriate. Electrically, an ideal solar cell may be thought of as a current generator in parallel with a diode[11]. When the contacts of the circuit are isolated, the open circuit voltage V_{oc} will reach a maximum. If there is no potential difference across the contacts, the circuit is shorted and the current density J_{sc} through the contacts will attain its maximum value. The fill factor FF is a measure of how closely the operational maximum voltage and current density (actual maximum power) of the solar cell approach the open and short circuit values, defined as[11]:

$$FF = \frac{J_m V_m}{J_{sc} V_{oc}}$$

The efficiency η of the cell is equal to the power output divided by the incident light power input, P_{in} , or:

$$\eta = \frac{J_{sc} V_{oc} FF}{P_{in}}$$

The techniques used in Chapters 5 and 6 differed substantially from the ones used in Chapters 3 and 4, and include temperature programmed desorption (TPD), electron stimulated desorption (ESD) and x-ray photoelectron spectroscopy (XPS). TPD involves the controlled heating of a sample and monitoring the desorbed species (gas molecules or ions) with a mass spectrometer. The Polanyi-Wigner equation has been used in many cases to model the desorption rate[12]:

$$-\frac{d\theta}{dt} = v_n \theta^n \exp\left(-\frac{E_d}{RT}\right)$$

The fractional surface coverage θ changes with respect to time as a function of v_n , the preexponential factor, the desorption order n , the desorption activation energy E_d , and the temperature T , where R is the gas constant. A linear heating rate is used since desorption is temperature dependent. This prevents artifacts from being introduced into the data. The shape of peaks in desorption spectra can reflect the order of desorption, with peaks due to zeroth, first, or second order desorption generally having distinct line shapes [13]. In this work, first and second order desorption are the two most likely modes of desorption, where first order is generally attributed to non-recombinative desorption and second order is typical for molecular or atomic combination preceding desorption.

A quadrupole mass spectrometer was used to detect the desorbed species once they escaped from the film surface. This spectrometer works by

impacting neutral gas molecules with electrons and forming ions. The ions are accelerated toward four parallel cylindrical electrodes. A dc voltage is applied to pair while an RF voltage is applied to the other. By varying the voltages on the pair of rods, the spectrometer can select which ions will be detected. Only those ions with the appropriate mass-to-charge ratio will make it to the detector, while the others will not have a stable trajectory and will not be detected.

In typical ESD experiments, incident electrons can excite surface atoms into a nonbonding or antibonding state. After excitation, decay of the excited state will occur between competing mechanisms. Displacement can convert the atom's potential energy into kinetic energy, and/or other electronic decay mechanisms will relax the atom back to the ground state. If the atom is in an excited state long enough without relaxing it can translate beyond a threshold distance from the surface and desorb[14]. The Menzel-Gomer-Redhead (MGR) model of desorption is typically used to describe an excitation to a repulsive final state and is broad enough in scope to encompass more specific excitation and desorption mechanisms[15]. This model has generally been sufficient to explain the following ESD observations[16]:

- 1) More neutrals than ions desorb during ESD
- 2) Desorption cross sections for neutrals are orders of magnitude smaller than for gases, and cross sections for ions are even smaller

- 3) Different bonding modes of electronegative adsorbates have different desorption cross sections
- 4) Metallic adsorbates on metal surfaces typically do not desorb by ESD

XPS was a central part of the work performed in Chapters 5-8. XPS is a photon-in, electron-out analytical technique that can provide the elemental composition, chemical state (oxidation state, functional groups, etc.), and electronic properties (work function, ionization potential, etc.) of a sample. It is surface sensitive due to the fact that the majority of the emitted electrons originate in the first 2-3 nm of the film. This shallow sampling depth results from the limited escape distance of electrons ejected from the sample when using x-rays[17], where monochromatic Al K α is one of the most common x-ray source currently used for this technique. Experimentally, the key XPS equation is:

$$KE = h\nu - BE - \phi_{sp}$$

For this equation, the kinetic energy of the electron is given by KE , $h\nu$ is the x-ray energy, BE is the electron binding energy, and ϕ_{sp} is the work function of the spectrometer. The work function of the spectrometer is used in the above equation for the detected electron rather than the work function of the sample due to electronic coupling between the sample and analyzer, as shown in Figure 2.5[18]. Elemental and chemical state information is possible because the kinetic energy of the emitted electron is characteristic of the atom to which

it was bound and the atom's bonding environment. As a first-order explanation for a given core level electron, the more electron density surrounding the atom, the lower the binding energy of the electron. This allows XPS to distinguish between C=O and C-O bonds for example, where the C 1s electron from the carbon atom singly bonded to oxygen will have a lower binding energy.

The ejected electrons are accelerated or retarded by an electrostatic lens system to a user defined pass energy. Smaller pass energies will produce a higher resolution spectrum, but at the expense of signal intensity. Next, the electrons pass through the entrance slit of the analyzer, which in this work was a concentric hemispherical type. A potential difference is applied between the inner and outer hemispheres such that only electrons with the energy of interest will pass through the exit, while the path of other electrons will be blocked by the exit slit[19]. The spectrometer detects the kinetic energy of the photoelectron via a channel electron multiplier, and using the above equation a plot of binding energy versus counts per second is constructed. XPS analysis is usually carried out in ultra-high vacuum (UHV) conditions ($\sim 10^{-10}$ torr), primarily to avoid surface contamination. From gas kinetic theory, it's known that if every gas molecule impacting the surface sticks, then a monolayer will accumulate in about 1 second at room temperature and 10^{-6} torr, which gives the unit Langmuir [20].

XPS was used to measure the interface barrier height between platinum and amorphous indium gallium zinc oxide in Chapter 7, and the reader is referred to reference [17] for clarification on how to determine barrier heights from XPS measurements. In Chapter 8, angle-resolved XPS experiments were performed to enhance the surface signal in the spectra. The increased sensitivity to the near-surface atoms can be appreciated by inspection of Fig. 2.6, and considering the attenuation length of electrons as they travel through a solid. It is shown that the path length of electrons traveling from the bulk is significantly increased, leading to greater attenuation of the signal from these electrons at grazing emission angles.

Rutherford Backscattering Spectrometry (RBS) was used in this work for compositional depth information as well as to determine the crystalline quality of a film by channeling measurements. In typical RBS experiments like the ones discussed in Chapter 8, high energy (2 MeV) He^+ ions are accelerated toward a sample. Following the subsequent collision with the sample, the ions are backscattered toward a detector where the quantity and energy of the ions are measured. The detected signal from the ions is converted into a voltage pulse, with the magnitude of the pulse being proportional to the ion energy. The pulses are stored in a channel, and the number of pulses per channel is recorded. Atomic identification and compositional information is possible because the energy of the backscattered ions depends on the mass of the atom from which they were

scattered[8]. Film thickness information and depth profiling is possible since these are correlated with the peak width for a given species[21]. During a channeling experiment with epitaxial films, the film's major crystallographic axis is aligned to the incident beam so as to reduce the amount of random scattering as much as possible. He^+ ions impinge onto the sample, and the sample is rotated until a minimum in backscattered ion yield is obtained due to channeling through the film. The backscattering yield is recorded with respect to angle in a typical experiment to give an estimate of the quality of the film.

Lastly, reflection high energy electron diffraction (RHEED) was utilized to reveal information about the growth of the LaFeO_3 film discussed in Chapter 8. During RHEED analysis, a beam of electrons is directed towards the sample at a glancing angle to minimize the penetration below the surface. The electrons are then diffracted onto a collection grid or detector to generate a RHEED pattern. RHEED is popularly used in combination with molecular beam epitaxy to monitor the growth of the film. The diffraction pattern, shape of diffraction spots in a pattern, as well as their oscillations in intensity with growth time is used to deduce information about surface structure and the growth mode[22,23].

References:

- [1] V. A. Fassel, "Quantitative Elemental Analyses by Plasma Emission Spectroscopy," *Science*, vol. 202, pp. 183-191, 1978.
- [2] M. S. Rajachidambaram, "Investigation of Oxide Semiconductor Based Thin Films: Deposition, Characterization, Functionalization, and Electronic Applications.," Masters Thesis, Oregon State University, 2011.
- [3] P. J. Goodhew, J. Humphreys, and R. Beanland, *Electron Microscopy and Analysis*. London, UK and New York, NY, USA: Taylor & Francis, 2001.
- [4] A. Weibel, R. Bouchet, F. Boulc'h, and P. Knauth, "The Big Problem of Small Particles: A Comparison of Methods for Determination of Particle Size in Nanocrystalline Anatase Powders," *Chem. Mater.*, vol. 17, pp. 2378-2385, 2005.
- [5] J. I. Langford and A. J. C. Wilson, "Scherrer after Sixty Years: A Survey and Some New Results in the Determination of Crystallite Size," *J. Appl. Cryst.*, vol. 11, pp. 102-113, 1978.
- [6] G. L. Hornyak, J. Dutta, H. F. Tibbals, and A. K. Rao, *Introduction to Nanoscience*. Boca Raton, FL, USA: CRC Press, 2008.
- [7] D. A. Skoog, F. J. Holler, and S. R. Crouch, *Principles of Instrumental Analysis*. Independence, KY, USA: Cengage Learning, 2007.
- [8] F. Krumeich, *Properties of Electrons, their Interactions with Matter and Applications in Electron Microscopy*. [Online]. Available: <http://www.microscopy.ethz.ch/downloads/Interactions.pdf>
- [9] Y. Liu, Electron Microscopy lecture notes, Oregon State University, 2011.
- [10] J. Pankrove, *Optical Processes in Semiconductors*. New York, NY, USA: Dover, 1975.
- [11] J. Nelson, *The Physics of Solar Cells*. London, UK: Imperial College Press, 2003.

- [12] X. Guo and J. T. Yates Jr., "Dependence of effective desorption kinetic parameters on surface coverage and adsorption temperature: CO on Pd(111)," *J. Chem. Phys.*, vol. 90, pg. 6761-6766, 1989.
- [13] P. A. Redhead, "Thermal Desorption of Gases," *Vacuum*, vol. 12, pp. 203-211, 1962.
- [14] R. D. Ramsier and J. T. Yates, "Electron-stimulated desorption - principles and applications," *Surf. Sci. Rep.*, vol. 12, pp. 243-378, 1991.
- [15] T. E. Madey, D. E. Ramaker, and R. Stockbauer, "Characterization of surfaces through electron and photon stimulated desorption," *Ann. Rev. Phys. Chem.*, vol. 35, pp. 215-240, 1984.
- [16] T. E. Madey and J. T. Yates, "Electron-Stimulated Desorption As A Tool For Studies Of Chemisorption - Review," *J. Vac. Sci. Technol.*, vol. 8, pp. 525-555, 1971.
- [17] D. M. Hercules and S. H. Hercules, "Analytical Chemistry of Surfaces. Part 1. General Aspects," *J. Chem. Educ.*, vol. 61, pp. 403-409, 1984.
- [18] C. S. Fadley in *Electron Spectroscopy: Theory, Techniques, and Applications. Volume 2* (Ed. C. R. Brundle and A. D. Baker), London, UK; New York, NY, San Francisco, CA, USA: Academic Press, 1978.
- [19] J. C. Rivière in *Practical Surface Analysis*. (Ed. D. Briggs and M. P. Seah), Tiptree, UK: Anchor Brendon, 1983.
- [20] A. Klein, "Transparent Conducting Oxides: Electronic Structure-Property Relationship from Photoelectron Spectroscopy with *in situ* Sample Preparation," *J. Am. Ceram. Soc.*, vol. 96, pp. 331-345, 2013.
- [21] J. S. Rajachidambaram, "Evaluation of Amorphous Oxide Semiconductors for Thin Film Transistors (TFTs) and Resistive Random Access Memory (RRAM) Applications," Masters Thesis, Oregon State University, 2011.
- [22] W. F. Egelhoff and I. Jacob, "Reflection High-Energy Electron Diffraction (RHEED) Oscillations at 77 K," *Phys. Rev. Lett.*, vol. 62, pp. 921-924, 1989.

- [23] T. Terashima, Y. Bando, K. Iijima, K. Yamamoto, K. Hirata, K. Hayashi, K. Kamigaki, and H. Terauchi, "Reflection High-Energy Electron Diffraction Oscillations during Epitaxial Growth of High-Temperature Superconducting Oxides," *Phys. Rev. Lett.*, vol. 65, pp. 2684-2688, 1990.

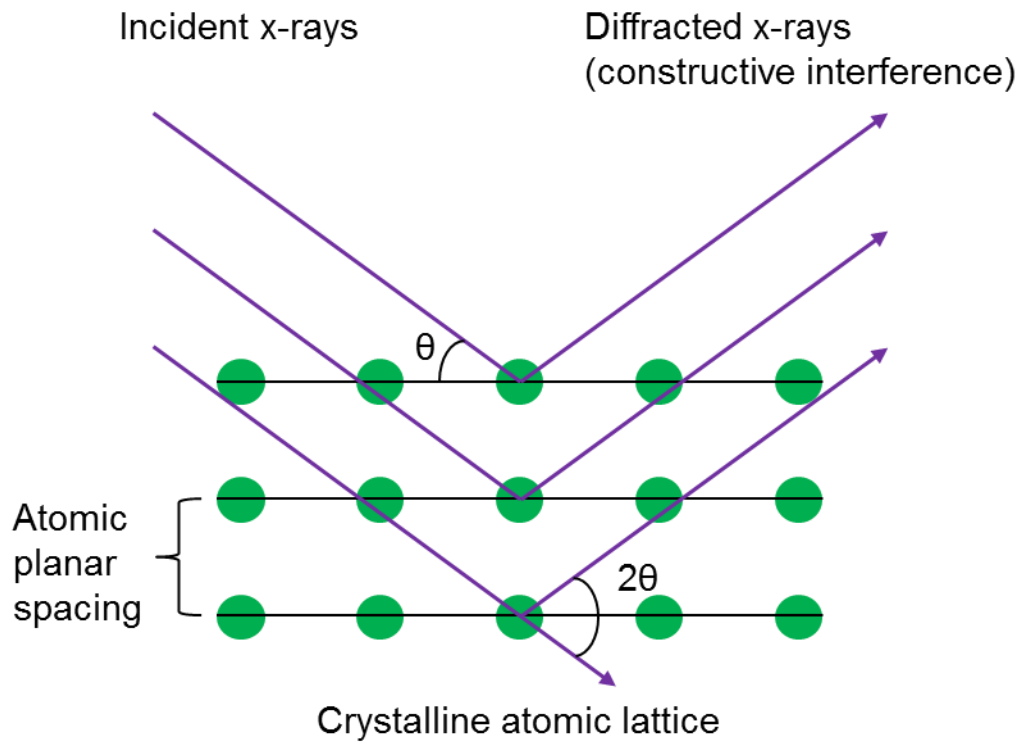
Figures

Figure 2.1 – Diffracted x-rays are reinforced if the angle θ satisfies Bragg's law. Adapted from reference [2].

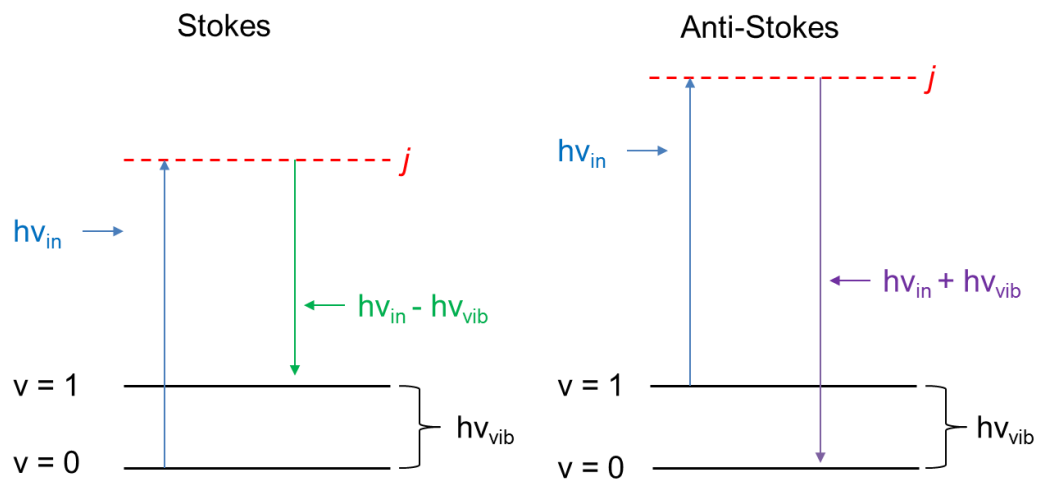


Figure 2.2 – Raman spectra are produced by the scattering of incident radiation $h\nu_{\text{in}}$, molecular excitation to virtual level j , and subsequent relaxation with photon emission. Lower frequency emission (Stokes) typically dominates higher frequency emission (Anti-Stokes) at room temperature because the ground vibrational levels are more populated. Figure adapted from reference [7].

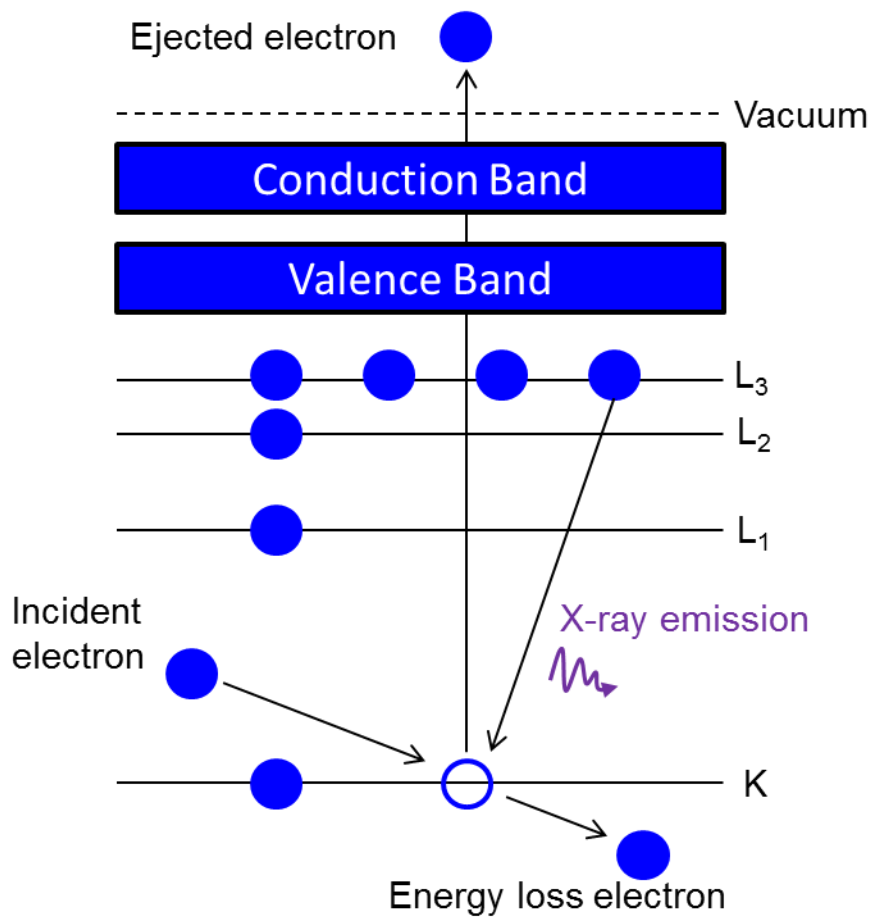


Figure 2.3 – Generation of characteristic x-rays during EDS analysis. Adapted from reference [8].

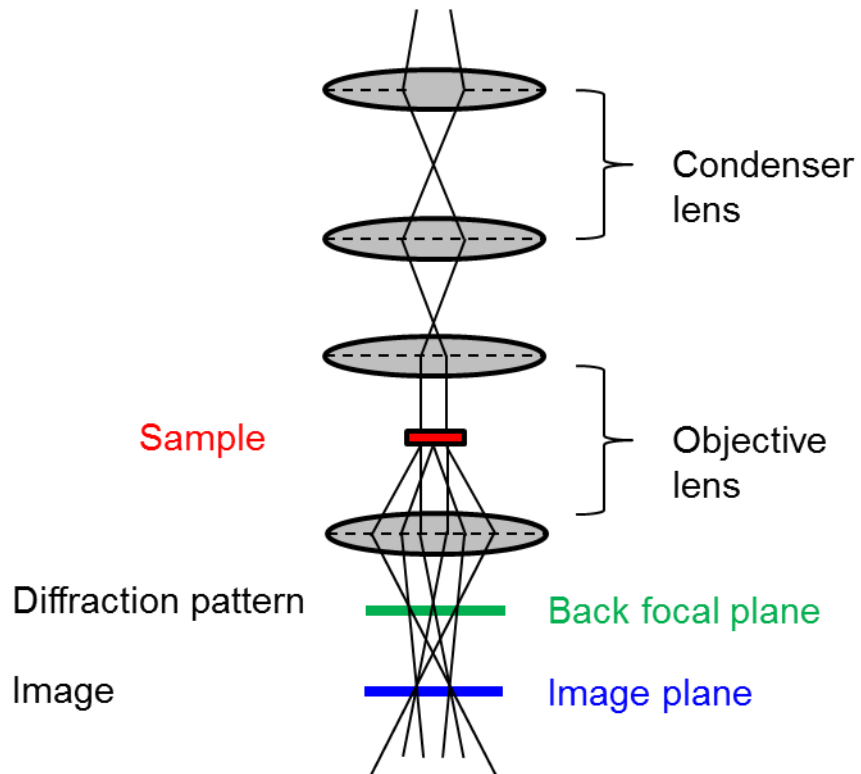


Figure 2.4 – Principle of TEM image and diffraction pattern generation. Adapted from reference [9].

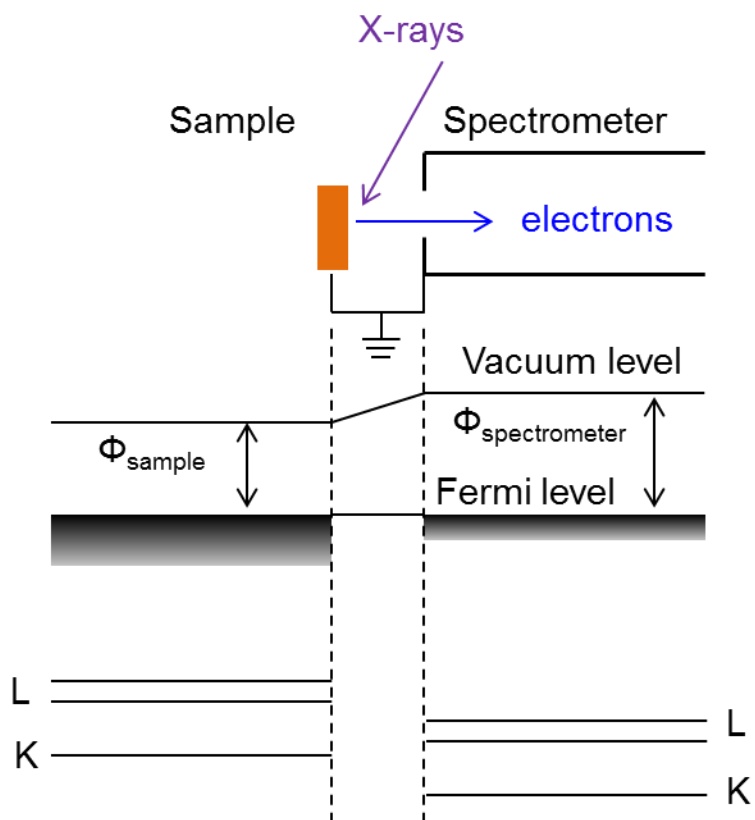


Figure 2.5 - Schematic demonstrating electronic coupling between the sample and spectrometer during an XPS experiment. Adapted from reference [15].

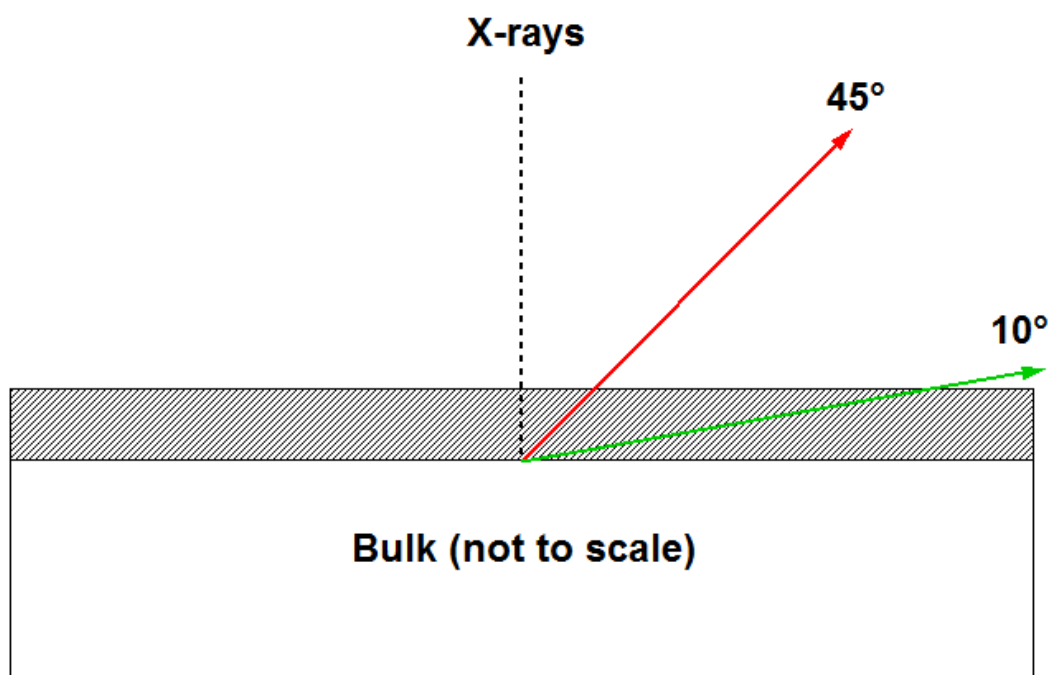


Figure 2.6 – Grazing emission XPS studies substantially reduce the amount of signal from the bulk. Note the longer path length an electron must travel to escape the surface at shallow take-off angles.

CHAPTER 3

MICROWAVE ASSISTED SYNTHESIS OF $\text{Cu}_2\text{ZnSnS}_4$
COLLOIDAL NANOPARTICLE INKS

Brendan T. Flynn,¹ Wei Wang,¹ Chih-hung Chang,¹ and Gregory S. Herman*¹

¹Oregon State University, School of Chemical, Biological and Environmental
Engineering, Corvallis, OR

*Corresponding Author

Reproduced in part from *Phys. Status Solidi A*, vol. 209, pp. 2186-2194, 2012.

Abstract

$\text{Cu}_2\text{ZnSnS}_4$ (CZTS) nanoparticle inks were synthesized for the first time by a one-pot synthesis method using microwave heating. Precursor solutions were mixed and reacted at 190 °C for 30 minutes. Varying the initial concentration of the metal chlorides in ethylene glycol was necessary to avoid formation of copper rich and zinc poor nanoparticles. Analysis of the reaction supernatant indicates that Cu^+ was fully utilized while significant amounts of Zn^{2+} remained unreacted. The CZTS nanoparticles were determined to be 7.6 ± 2.1 nm in diameter and which were agglomerated into larger clusters. A solar cell fabricated with the CZTS nanoparticles had a conversion efficiency of 0.25%.

Introduction

Thin film PV technologies offer a route to low cost and high volume solar cell manufacturing due to reductions in both material and processing costs. For example, material costs can be reduced since considerably thinner absorber layers ($\sim 1\text{-}2\ \mu\text{m}$) are required for direct band gap thin film technologies compared to indirect band gap crystalline silicon technologies ($\sim 180\ \mu\text{m}$)[1]. Likewise, processing costs can be reduced since thin film technologies can take advantage of relatively inexpensive low-temperature solution-based methods, whereas silicon technologies require several expensive high temperature and high vacuum based procedures. Increases in thin film PV cell performance has been demonstrated for both copper indium gallium diselenide (CIGS) and cadmium telluride (CdTe) which have achieved champion cell efficiencies of 20.3%[2] and 16.5%[3], respectively. While these efficiencies are impressive, these compounds suffer from high costs due to their constituent elements[4] and toxicity issues (Cd). An alternative direct band gap semiconductor that has received much recent attention is copper zinc tin sulfide (CZTS), which does not share the same price and toxicity concerns[5].

The solution-based synthesis of nanoparticle inks can provide a relatively inexpensive method for the production and integration of CZTS into thin film solar cells. Solution-based methods avoid the requirement of costly and inefficient vacuum processes and allow the possibility of roll-to-roll

printing or spray-coating processes, an attractive option for large scale and low cost manufacturing. The synthesis of CZTS nanoparticles was first reported in 2009[6-9] and recently there has been considerable interest in both CZTS and CZT(S,Se) nanoparticles[10-26]. The CZTS nanoparticles have primarily been synthesized by hot-injection and solvothermal methods, where oleylamine is often used as a solvent/surfactant by each method [13, 15]. The use of microwave heating, in the place of conventional heating, is an alternative approach to synthesizing CZTS nanoparticles that has not been previously studied.

Microwave-assisted nanoparticle synthesis has several desirable properties, including rapid heating rates that can reduce reaction times to minutes or seconds, and uniform volumetric heating which minimizes thermal gradients, allowing for higher control over nucleation and growth conditions. Microwave based methods have been used to synthesize a wide range of inorganic semiconductor nanomaterials[27], including CdTe[28-30] and more recently CIGS[31, 32]. Areas of focus for microwave-assisted synthesis of nanoparticles have included optimizing solvents and precursors for high microwave absorption and controlling the temperature profile during reaction. The polarization of dipolar molecules and ionic conduction are the two main sources of heat generation during microwave syntheses[33], so the use of a polar solvent and/or ionic species is particularly important. Ionic liquids readily absorb microwave radiation and convert it to heat, and the addition of

ionic species to the precursor solution has been shown to increase reaction rates. For example, the addition of H^+ ions reduced the formation time of ferric oxide nanoparticles from 21 to 14 minutes[34].

Solar cells utilizing solution based CZTS methods have achieved efficiencies ranging from 0.16-3.6% [7, 8, 35-44]. The most efficient CZTS cells have been fabricated by incorporating selenium into the CZTS system[14, 45]. Partial substitution of sulfur by selenium in the CZTS lattice has been shown to decrease the band gap of CZTS absorbers and increase device performance over selenium-rich devices[45]. The record efficiency for CZT(S,Se) PV cells is 10.1%, where this device was fabricated employing hydrazine via a solution-based method[46]. It is interesting to note that CZT(S,Se) is the only PV technology where solution based-methods result in higher efficiencies than cells processed by vacuum-based methods.

Microwave assisted synthesis has enabled us to produce CZTS nanoparticles from a simple one pot method at a substantially lower temperature and shorter reaction time compared to other CZTS synthesis methods. This solution-based, low energy synthesis could help lead to more cost effective and less energy intensive methods to synthesize CZTS. In these studies metal salts and thioacetamide were dissolved in ethylene glycol, a high microwave absorbing solvent, and reacted at 190 °C for 30 minutes. Optimization of precursor composition allowed the formation of

CZTS nanoparticles with controlled composition and particle size. Finally, the CZTS nanoparticles were incorporated into a PV device.

Experimental Methods

Preparation of the precursor solution was done in air under standard atmospheric conditions. Initial precursor concentrations targeted a copper poor/zinc rich nanoparticle composition. Metal chlorides were used so that all the species had the same counterion for increased chemical homogeneity in solution. Cuprous chloride (CuCl , 0.01 M), zinc chloride (ZnCl_2 , 0.026 M), and stannic chloride pentahydrate ($\text{SnCl}_4 \cdot 5\text{H}_2\text{O}$, 0.010 M) were added to 20 mL of ethylene glycol. The precursor solution was adjusted to a pH of 2 using 0.01M hydrochloric acid. In a separate beaker, thioacetamide ($\text{C}_2\text{H}_5\text{NS}$, 0.088 M) was added to 20 mL of ethylene glycol. Both mixtures were stirred separately at 50 °C for 30 minutes until the chemistries were completely dissolved. After the precursors were cooled to room temperature the solutions were mixed and 10 mL aliquots were added to four sealed glass microwave reaction vessels. The reaction was performed at low pH to accelerate decomposition of thioacetamide [47, 48] for facile incorporation of the resulting sulfur anions into the CZTS nanoparticles.

The precursor solution was reacted in a microwave reactor (MARS 5, CEM Corp., 2.450 GHz) and heated to 190 °C for 30 minutes using a 5 minute ramp and 300 W power setting. Reaction temperatures were

monitored by an optical probe that was encased in a glass well surrounded by the solution. After reaction, the vessels were allowed to cool to 100 °C before they were placed in a cold water bath. The reacted solution was then alternately centrifuged in deionized water and ethanol several times to remove unreacted species and to purify and collect the CZTS nanoparticles. Finally, the nanoparticles were suspended in ethanol and dropcast onto an appropriate substrate for analysis.

X-ray diffraction (XRD) patterns were obtained using a Bruker D8 Discover diffractometer with Cu K α radiation. Scanning electron microscope (SEM) images and compositional information using energy dispersive spectroscopy (EDS) were acquired with an FEI Quanta 3D. Particle size was determined with a Philips CM12 scanning transmission electron microscope (STEM), while high resolution TEM (HRTEM) and selected area electron diffraction (SAED) analysis was done with an FEI Titan FEG TEM. Optical absorption data was obtained using a JASCO V670 UV-Vis spectrophotometer. Composition of the nanoparticles was further analyzed with a Horiba-Jobin Yvon HR800 Raman spectrometer with 532 nm incident light. The reaction supernatant was analyzed with inductively coupled plasma atomic emission spectroscopy (ICP-AES) using a Varian Liberty 150 spectrometer. Thermogravimetric analysis (TGA) was performed using a TA Instruments TGA 2950 system.

A solar cell was fabricated with a stack consisting of borosilicate glass/Mo/CZTS/CdS/i-ZnO/Al:ZnO/Ag. CZTS nanoparticles were suspended in ethylene glycol (50 mg/mL), ultrasonicated, and spincoated onto a substrate at 300 rpm for 10 seconds followed by 1500 rpm for 30 seconds. After each coat the substrate was placed on a hot plate at 80 °C to remove volatile solvents. A total film thickness of 3.0 μm was obtained after 19 coatings. The substrate was placed in a combustion boat with 0.08 g of tin(II) sulfide and sulfur powder and annealed under flowing nitrogen at 400 °C for 20 minutes. The annealing conditions were chosen to prevent possible sulfur loss[49] and phase separation[9, 50]. The ultimate goal of this research is to fabricate solar cells with only minor thermal processing, so a moderately low annealing temperature was chosen to evaluate this feasibility. After this procedure the film thickness was about 2.4 μm . Our CZTS devices were fabricated using a similar method as reported for inkjet printed CIGS devices[51]. For this work a 50 nm n-type CdS buffer layer was deposited by chemical bath deposition on top of the annealed CZTS nanoparticle film. Both 80 nm i-ZnO and 300 nm Al:ZnO window layers were deposited by sputter deposition. Several 0.07 cm² devices were isolated by mechanical scribing. Finally, top-contacts were applied using silver paste. Solar cell performance was tested at room temperature under AM 1.5 illumination with an Oriel 96000 full spectrum solar simulator calibrated with a standard Si solar cell and PVIV-200 test station.

Results and Discussion

In this study varying the initial concentrations of precursors, as shown in Table 3.1, controlled the composition of the nanoparticles. As indicated in Table 3.1, it was necessary to significantly reduce the amount of copper precursor to attain copper poor CZTS compositions. It was estimated that the EDS compositional data had an error less than ± 1 atomic %, which was determined by averaging data from five $275 \times 350 \mu\text{m}^2$ locations chosen at random on the substrate. ASTM International has found the overall accuracy of EDS quantitative analysis with a SEM to be better than $\pm 4\%$ relative to a reference composition[52]. It should be noted that depending on the EDS detector settings, compositional data may vary significantly if the film is insufficiently thick, and for these studies care was taken to perform scans in which the signal from the silicon substrate was minimized as much as possible. It was found that the film annealed at 400°C for 20 minutes had a slightly higher atomic percentage of sulfur than the as synthesized particles, which suggests that the nanoparticles may be sulfur deficient as synthesized. The appropriate amount of sulfur required for $\text{Cu}_2\text{ZnSnS}_4$ can be assumed to be $[\text{S}] = [\text{Cu}]/2 + [\text{Zn}] + [\text{Sn}] \times 2$, based on the oxidation states of the metal cations in the binary sulfides Cu_2S , ZnS , and SnS_2 . From Table 1, the composition of sample B nanoparticles was $\text{Cu}_{1.84}\text{Zn}_{1.09}\text{Sn}_{1.05}\text{S}_{4.03}$, which corresponds to a stoichiometric amount of sulfur equal to $1.84/2 + 1.09 + 1.05 \times 2 = 4.11$, confirming the nanoparticles are likely sulfur deficient. The

higher atomic percentage of sulfur in the annealed film could then be due to a combination of changing elemental oxidation states and the accuracy of EDS quantification.

As discussed above the synthesized CZTS nanoparticles have a strong tendency toward copper rich and zinc poor compositions, which is the opposite of what is desired. It has been proposed that for optimal PV device performance, it is necessary to form CZTS films with a copper poor and zinc rich composition[53, 54]. First principles studies of CZTS have indicated that substitution of copper[55] and tin[56] at zinc sites form unfavorable deep acceptor levels, which can serve as carrier recombination centers and thus limit device performance. Furthermore, copper deficiency has been shown experimentally to enhance hole carrier concentration[57]. Thus it is important to ensure zinc rich conditions during the formation of CZTS films for optimal performance in a solar cell. This is not a simple task when synthesizing CZTS nanoparticles due to the variable reactivity among the metal cations, and thus controlling cationic reactivity has been a point of emphasis in order to produce high quality nanoparticles with the desired composition. Our method of controlling the initial metal cation concentrations is a direct approach for obtaining the desired composition of the CZTS nanoparticles, and ultimately the CTZS films. Other researchers have evaluated other methods as well. For example, one group found that increasing the reaction temperature above 220 °C led to a relative increase in Zn and Sn cation

complex reactivity than the Cu cation complex, thus enabling the formation of single phase CZTS nanoparticles[20]. Likewise, alkane thiols have been used to reduce the reaction rate of Cu^+ and control the Cu/In ratio in CuInS_2 nanoparticles[58]. The use of dodecanethiol as a capping agent has also impacted CZTS nanoparticle synthesis by enabling formation of wurtzite phase CZTS nanoparticles as opposed to the desired kesterite structure[16]. The choice of solvent also affects cation reactivity, with one group reporting success forming CZTS nanoparticles in ethylene glycol but formation of Cu_2SnS_3 when using ethanol[19].

ICP-AES analysis of the reaction supernatant was performed to estimate the extent of reaction of the chloride based chemistries. In all cases, no copper was found in the supernatant and the Zn/Sn ratio for the supernatant was much higher than the initial precursor solution. Using one sample as a typical example, the precursor metal ratios were $\text{Cu}/(\text{Zn}+\text{Sn}) = 0.56$ and $\text{Zn}/\text{Sn} = 2.3$, while the ratios in the supernatant post reaction were $\text{Cu}/(\text{Zn}+\text{Sn}) = 0.0$ and $\text{Zn}/\text{Sn} = 8.4$. These results indicate a much higher reactivity for copper and a corresponding low reactivity of zinc for the formation of CZTS. A similar finding on the low incorporation of zinc has also been noted elsewhere[59] for solution-based CZTSe nanocrystal synthesis. In this prior study, CZTSe nanoparticles were synthesized by the hot-injection method from metal chlorides and trioctylphosphine selenide, and were analyzed by EDS and X-ray photoelectron spectroscopy. It was determined

that ~3% of the initial zinc and ~30% of the initial tin was incorporated in the $\text{Cu}_2\text{Zn}_x\text{Sn}_y\text{Se}_{1+x+2y}$ stannite nanoparticles.

XRD was used to analyze the crystallinity and phase of the CZTS nanoparticles. In Figure 3.1 we show XRD spectra for both as synthesized particles dropcast onto a glass substrate and a dropcast film annealed to 400 °C. Three broad peaks attributed to the (112), (220), and (312) planes are observed (JCPDS 26-0575) for the as synthesized nanoparticles. These peaks are the most intense for CZTS and are occasionally the only planes distinguishable in the XRD spectrum for CZTS nanoparticles [9, 11, 12]. There was a slight shoulder on the peak centered at 28.5°, which has been observed in other CZTS nanoparticle work[6, 8, 60]. It has been proposed that this shoulder could be caused by a Cu_{2-x}S impurity phase[24], the wurtzite phase of ZnS (JCPDS 36-1450), or stacking faults due to cation disorder in CZTS[16, 61, 62]. The average crystallite size of the nanoparticles was calculated to be 7.3 nm using the Scherrer method. Sharper and more intense peaks in the XRD pattern of the annealed sample suggest higher crystalline order and/or larger domain size, with a calculated average crystallite size of 26.8 nm. Several additional XRD peaks attributable to CZTS also appear in the diffraction pattern. These peaks are found at 18.2°, 33.0°, 69.2°, and 76.4°, corresponding to the (101), (200), (008), and (332) planes, respectively. Since the synthesized nanoparticles are small, the broad peaks in the XRD spectrum could potentially mask other impurity

phases so other techniques were used to characterize the nanoparticles, which will be discussed below.

Raman spectroscopy was performed to further confirm the phase purity of both the nanoparticles and annealed film and results are shown in Fig. 3.2. Both spectra have significant peaks centered at 333 cm^{-1} and 287 cm^{-1} . These features have been attributed to A_1 symmetry, a result of the vibration of sulfur atoms in the lattice[63]. The peak position of the most intense peak at 333 cm^{-1} is consistent with other CZTS nanoparticle work [21, 25], however the position is slightly red shifted when compared to other reported values for large grain CZTS films [63-66]. The red shift may be due to a decrease in phonon frequency for the A_1 vibrational mode associated with particle size[67]. This Raman mode has experimentally been shown to be the most intense for CZTS as opposed to impurity phases[21, 25, 63-66]. The broad peak at about 287 cm^{-1} is characteristic of CZTS Raman spectra but not ZnS[68] or tetragonal Cu_2SnS_3 [69] spectra. In addition, we observed no peaks for Cu_{2-x}S at 475 cm^{-1} , further suggesting that high quality kesterite CZTS was synthesized.

The morphology of the CZTS nanoparticle films was investigated using both SEM and TEM. In Figure 3.3, SEM images were obtained with magnifications of 5,000x and 200,000x and the appropriate scale bars are indicated. At higher magnification it is evident that the CZTS nanoparticles agglomerate and form relatively large nanoparticle clusters. Fig. 3.3a-b are

for the coated CZTS nanoparticle films after an initial drying step at 30 °C, while Fig. 3.3c-d are for the same films after annealing to 400 °C for 20 minutes. A comparison between Figure 3.3a and c indicates the formation of a denser film with less porosity after the CZTS nanoparticles are annealed. Furthermore, a comparison between Figure 3.3b and d indicates that larger grains were formed after the annealing step. Larger grain sizes reduce the relative number of grain boundaries and the corresponding recombination centers and traps and should lead to higher PV device performance. High annealing temperatures and/or long annealing times generally lead to larger grain formation, but this must be balanced against possible phase separation, oxidation, or decomposition of the precursors.

TEM images are shown for as-synthesized CZTS nanoparticles in Fig. 3.4a-b, while SAED is shown in Fig. 3.4c. The image in Fig. 3.4a was obtained with a magnification of 125,000x and shows polydisperse spherical particles 7.6 ± 2.1 nm in diameter. In the inset in Fig. 3.4a we plot a distribution of particle sizes as extracted from the TEM image. We find that these values are in good agreement with the crystallite size calculated from the XRD data. The spacing of atomic planes in an HRTEM image and a corresponding fast Fourier transform (FFT) pattern can be used to help verify formation of CZTS with the kesterite structure. In Fig. 3.4b, a HRTEM image (620,000x) shows individual atomic planes in a CZTS nanoparticle, while a FFT pattern is shown in the inset. An interplanar spacing of 0.31 nm was

measured and attributed to (112) crystallographic planes, and the diffraction spots in the FFT pattern can be indexed to the CZTS structure, corresponding to the (112), (220) and (004) planes as viewed along the [110] zone axis. JEMS software was used to generate a simulated CZTS pattern for indexing the diffraction spots. Figure 3.4c shows an SAED image that was taken over several nanoparticles. Three prominent diffraction rings were observed corresponding to the (112), (220), and (312) planes of kesterite CZTS. These electron microscopy techniques are particularly important for phase identification of CZTS nanoparticles due to the broad nature of the diffraction peaks in XRD and scattering peaks in the Raman spectra.

The optical absorption spectrum of the as synthesized particles is shown in Fig. 3.5. For direct band gap compounds, the band gap may be calculated by plotting the product of photon energy and absorbance squared versus photon energy from the absorbance spectrum, or $(\alpha h\nu)^2$ versus $h\nu$, and finding the intercept of the abscissa. This method gives a band gap of 1.5 eV, which is near optimum for a solar cell and in good agreement with theoretical[70] and experimental values for CZTS[71-73] . The absorption coefficient of the formed CZTS films can be estimated to be $\sim 5 \times 10^4 \text{ cm}^{-1}$ which is comparable to values obtained by other studies[72, 74].

To better understand the thermal properties of the CZTS nanoparticles we performed TGA by heating the particles to 600 °C with a ramp rate of 29 °C/min under flowing nitrogen. This maximum temperature was used

since annealing temperatures usually don't exceed 600 °C for the fabrication of CZTS solar cells. Figure 3.6 shows the mass change of the nanoparticles versus temperature. Initially there is a small mass loss below 100 °C, likely due to the loss of ethanol and water that absorbed to the nanoparticle surface during the cleaning process. The mass continues to decrease from 100 – 300 °C at a low rate, and the next significant mass loss transition occurs at ~300° C. Weight loss begins to slow after 400 °C and overall there is relatively little weight change, with a total loss of ~7% over the entire temperature range. Various nanoparticle compounds were synthesized under analogous conditions to CZTS and analyzed with TGA to provide further insight into the CZTS weight loss regime from 300-400 °C, including Cu_{1-x}S , SnS_2 , ZnS , Cu_2SnS_3 , and SnO_2 . The results suggest that the weight loss is not due to the loss of residual organic content, as some compounds had virtually no weight loss from 300-400 °C. Cu_{1-x}S , Cu_2SnS_3 , and ZnS were the only compounds with significant weight loss before 400 °C, so the weight loss in the CZTS sample from 300-400 °C may partially be explained by the decomposition or volatilization of some combination of these species. It is unlikely that the weight loss is due to SnS volatilization, as this doesn't occur at a significant rate in CZTS films until 550 °C under vacuum conditions [50]. Chory et al. also used intermediate boiling point organic compounds for CZTS synthesis, and found that weight loss due to organic decomposition was virtually completed by 450 °C [12]. Shin et al. utilized aqueous precursors in

a two step microwave assisted synthesis to produce CZTS nanoparticles, and similarly had less than 10% weight loss up to 600 °C[62]. Insight into the mechanism of film formation is necessary in order to minimize non-stoichiometric material loss and control grain growth during the annealing process to produce cost effective, high performance nanoparticle PV devices.

These data suggest that high quality CZTS nanoparticles can be synthesized using a one-pot microwave-assisted process. We have fabricated PV cells to further characterize the optoelectronic properties of films formed from the CZTS nanoparticles. The CZTS PV cells were fabricated as described above and their electrical characteristics are given in Figure 3.7. The device had an open circuit voltage (V_{oc}) of 289 mV, a short circuit current of 1.79 mA/cm², a fill factor (FF) of 47.9%, and a total area power conversion efficiency (η) of 0.25%. The cell suffers from a very low photocurrent, which can be explained in part by viewing a cross section of the device, shown in Figure 3.8. The CZTS layer of the device is seen to be quite porous, consisting of small grains and thus a corresponding large number of grain boundaries to act as recombination centers for electron-hole pairs. Pure sulfide, solution based CZTS solar cells have had low efficiencies compared to those utilizing vacuum-based methods, as the highest efficiencies for pure sulfide devices have been 3.6%[40] and 8.4%[75] for solution and vacuum-based CZTS cells, respectively. There are relatively few reports in the literature concerning solar cells incorporating CZT(S,Se)

nanoparticles in which to compare our results. Steinhagen et al. reported an efficiency of 0.23% for a CZTS cell that was not annealed[8]. Typically solution-based CZT(S,Se) cells are fabricated with an annealing step in the 500-600 °C range to improve crystallinity and promote grain growth, although higher temperatures (>550 °C) have also been shown to lead to the formation of undesirable phases[50]. Guo et al. demonstrated an increase in efficiency of their CZTSSe devices by altering the CZTS nanoparticle composition (i.e., the Cu/(Zn+Sn) and Zn/Sn ratios), whereby improving the efficiency of their devices from 0.8% to 7.2%[7, 14]. However, it should be noted in these prior studies that the particles were synthesized in unreactive ambient atmospheres, which may reduce incorporation of impurities that can reduce device performance.

Conclusion

Microwave assisted synthesis of CZTS nanoparticle inks has been demonstrated using a one-pot synthesis method. The use of microwave radiation has enabled the synthesis of CZTS nanoparticles with a shorter reaction time and at a lower temperature when compared with other methods in the literature. We used ethylene glycol as the solvent due to the intermediate boiling point and the high microwave absorptivity. We found that the composition of the nanoparticles can be controlled by varying the initial precursor concentration, and that it was necessary to run the reactions with

an excess of zinc and a reduction of copper to obtain optimal values of $\text{Cu}/(\text{Zn}+\text{Sn})=0.86$ and $\text{Zn}/\text{Sn} = 1.04$. XRD, SAED, and Raman spectroscopy indicate that the synthesized CZTS nanoparticles have the desired kesterite crystal structure. Finally, the synthesized CZTS nanoparticles were incorporated into a solar cell with a maximum efficiency of 0.25%, open circuit potential of 289 mV, a short circuit current of $1.79 \text{ mA}/\text{cm}^2$, and a fill factor of 47.9%.

Acknowledgements

The authors would like to thank Teresa Sawyer and Dr. Yi Liu of Oregon State University for their help with SEM/TEM imaging as well as Dr. Sujing Xie of the University of Oregon for her TEM work. Funding was graciously provided by Sharp Laboratories of America and the Oregon Nanoscience and Microtechnologies Institute (ONAMI). A portion of this work was performed at the Oregon Process Innovation Center for Sustainable Solar Cell Manufacturing.

References:

- [1] S. Mehta, "State of the Solar Union: Present and Future," *IEEE Power and Energy Magazine*, vol. 9, pp. 96-94, 2011.
- [2] P. Jackson, D. Hariskos, E. Lotter, S. Paetel, R. Wuerz, R. Menner, W. Wischmann, and M. Powalla, "New world record efficiency $\text{Cu}(\text{In},\text{Ga})\text{Se}_2$ thin-film solar cells beyond 20%," *Prog. Photovoltaics*, vol. 19, pp. 894-897, 2011.

- [3] X. Wu, "High-efficiency polycrystalline CdTe thin-film solar cells," *Sol. Energy*, vol. 77, pp. 803-814, 2004.
- [4] U.S. Geological Survey, Mineral commodity summaries 2011, pp. 1-198.
- [5] D. B. Mitzi, O. Gunawan, T. K. Todorov, K. Wang, and S. Guha, "The path towards a high-performance solution-processed kesterite solar cell," *Sol. Energy Mater. Sol. Cells*, vol. 95, pp. 1421-1436, 2011.
- [6] S. C. Riha, B. A. Parkinson, and A. L. Prieto, "Solution-Based Synthesis and Characterization of $\text{Cu}_2\text{ZnSnS}_4$ Nanocrystals," *J. Am. Chem. Soc.*, vol. 131, pp. 12054-12055, 2009.
- [7] Q. J. Guo, H. W. Hillhouse, and R. Agrawal, "Synthesis of $\text{Cu}_2\text{ZnSnS}_4$ Nanocrystal Ink and Its Use for Solar Cells," *J. Am. Chem. Soc.*, vol. 131, pp. 11672-11673, 2009.
- [8] C. Steinhagen, M. G. Panthani, V. Akhavan, B. Goodfellow, B. Koo, and B. A. Korgel, "Synthesis of $\text{Cu}_2\text{ZnSnS}_4$ Nanocrystals for Use in Low-Cost Photovoltaics," *J. Am. Chem. Soc.*, vol. 131, pp. 12554-12555, 2009.
- [9] T. Todorov, M. Kita, J. Carda, and P. Escribano, " $\text{Cu}_2\text{ZnSnS}_4$ films deposited by a soft-chemistry method," *Thin Solid Films*, vol. 517, pp. 2541-2544, 2009.
- [10] C. Chory, F. Zutz, F. Witt, H. Borchert, and J. Parisi, "Synthesis and characterization of $\text{Cu}_2\text{ZnSnS}_4$," *Phys. Status Solidi C*, vol. 7, pp. 1486-1488, 2010.
- [11] T. Kameyama, T. Osaki, K. Okazaki, T. Shibayama, A. Kudo, S. Kuwabata, and T. Torimoto, "Preparation and photoelectrochemical properties of densely immobilized $\text{Cu}_2\text{ZnSnS}_4$ nanoparticle films," *J. Mater. Chem.*, vol. 20, pp. 5319-5324, 2010.
- [12] H. Wei, W. Guo, Y. Sun, Z. Yang, and Y. Zhang, "Hot-injection synthesis and characterization of quaternary $\text{Cu}_2\text{ZnSnSe}_4$ nanocrystals," *Mater. Lett.*, vol. 64, pp. 1424-1426, 2010.

- [13] P. Dai, X. Shen, Z. Lin, Z. Feng, H. Xu, and J. Zhan, "Band-gap tunable $(\text{Cu}_2\text{Sn})_{x/3}\text{Zn}_{1-x}\text{S}$ nanoparticles for solar cells," *Chem. Commun.*, vol. 46, pp. 5749-5751, 2010.
- [14] Q. Guo, G. M. Ford, W. C. Yang, B. C. Walker, E. A. Stach, H. W. Hillhouse, and R. Agrawal, "Fabrication of 7.2% Efficient CZTS_{Se} Solar Cells Using CZTS Nanocrystals," *J. Am. Chem. Soc.*, vol. 132, pp. 17384-17386, 2010.
- [15] S. C. Riha, S. J. Fredrick, J. B. Sambur, Y. J. Liu, A. L. Prieto, and B. A. Parkinson, "Photoelectrochemical Characterization of Nanocrystalline Thin-Film $\text{Cu}_2\text{ZnSnS}_4$ Photocathodes," *ACS Appl. Mater. Interfaces*, vol. 3, pp. 58-66, 2011.
- [16] X. Lu, Z. Zhuang, Q. Peng, and Y. Li, "Wurtzite $\text{Cu}_2\text{ZnSnS}_4$ nanocrystals: a novel quaternary semiconductor," *Chem. Commun.*, vol. 47, pp. 3141-3143, 2011.
- [17] M. Cao and Y. Shen, "A mild solvothermal route to kesterite quaternary $\text{Cu}_2\text{ZnSnS}_4$ nanoparticles," *J. Cryst. Growth*, vol. 318, pp. 1117-1120, 2011.
- [18] Y. L. Zhou, W. H. Zhou, Y. F. Du, M. Li, and S. X. Wu, "Sphere-like kesterite $\text{Cu}_2\text{ZnSnS}_4$ nanoparticles synthesized by a facile solvothermal method," *Mater. Lett.*, vol. 65, pp. 1535-1537, 2011.
- [19] O. Zaberca, A. Gillorin, B. Durand, and J. Y. Chane-Ching, "A general route to the synthesis of surfactant-free, solvent-dispersible ternary and quaternary chalcogenide nanocrystals," *J. Mater. Chem.*, vol. 21, pp. 6483-6486, 2011.
- [20] X. Wang, Z. Sun, C. Shao, D. M. Boye, and J. Zhao, "A facile and general approach to polynary semiconductor nanocrystals via a modified two-phase method," *Nanotechnology*, vol. 22, pp. 245605, 2011.
- [21] C. Zou, L. Zhang, D. Lin, Y. Yang, Q. Li, X. Xu, and S. Huang, "Facile synthesis of $\text{Cu}_2\text{ZnSnS}_4$ nanocrystals," *CrystEngComm*, vol. 13, pp. 3310-3313, 2011.
- [22] H. Wei, Z. C. Ye, M. Li, Y. J. Su, Z. Yang, and Y. F. Zhang, "Tunable band gap $\text{Cu}_2\text{ZnSnS}_{4x}\text{Se}_{4(1-x)}$ nanocrystals: experimental and first-principles calculations," *CrystEngComm*, vol. 13, pp. 2222-2226, 2011.

- [23] J. Chane-Ching, A. Gillorin, O. Zaberca, A. Balocchi, and X. Marie, "Highly-crystallized quaternary chalcopyrite nanocrystals via a high-temperature dissolution–reprecipitation route," *Chem. Commun.*, vol. 47, pp. 5229-5231, 2011.
- [24] G. M. Ford, Q. J. Guo, R. Agrawal, and H. W. Hillhouse, "Earth Abundant Element $\text{Cu}_2\text{Zn}(\text{Sn}_{1-x}\text{Ge}_x)\text{S}_4$ Nanocrystals for Tunable Band Gap Solar Cells: 6.8% Efficient Device Fabrication," *Chem. Mater.*, vol. 23, pp. 2626-2629, 2011.
- [25] Y. Wang and H. Gong, "Low Temperature Synthesized Quaternary Chalcogenide $\text{Cu}_2\text{ZnSnS}_4$ from Nano-Crystallite Binary Sulfides *J. Electrochem. Soc.*, vol. 158, pp. H800-H803, 2011.
- [26] W. Haas, T. Rath, A. Pein, J. Rattenberger, G. Trimmel, and F. Hofer, "The stoichiometry of single nanoparticles of copper zinc tin selenide," *Chem. Commun.*, vol. 47, pp. 2050-2052, 2011.
- [27] I. Bilecka and M. Niederberger, "Microwave chemistry for inorganic nanomaterials synthesis," *Nanoscale*, vol. 2, pp. 1358-1374, 2010.
- [28] R. S. Singh, V. K. Rangari, S. Sanagapalli, V. Jayaraman, S. Mahendra, and V. P. Singh, "Nano-structured CdTe, CdS and TiO_2 for thin film solar cell applications," *Sol. Energy Mater. Sol. Cells*, vol. 82, pp. 315-330, 2004.
- [29] L. Li, H. F. Qian, and J. C. Ren, "Rapid synthesis of highly luminescent CdTe nanocrystals in the aqueous phase by microwave irradiation with controllable temperature," *Chem. Commun.*, vol. 4, pp. 528-530, 2005.
- [30] Y. He, H. T. Lu, L. M. Sai, W. Y. Lai, Q. L. Fan, L. H. Wang, and W. Huang, "Microwave-Assisted Growth and Characterization of Water-Dispersed CdTe/CdS Core-Shell Nanocrystals with High Photoluminescence," *J. Phys. Chem. B*, vol. 110, pp. 13370-13374, 2006.
- [31] L. Al Juhaïman, L. Scoles, D. Kingston, B. Patarachao, D. Wang, and F. Bensebaa, "Green synthesis of tunable $\text{Cu}(\text{In}_{1-x}\text{Ga}_x)\text{Se}_2$ nanoparticles using non-organic solvents," *Green Chem.*, vol. 12, pp. 1248-1252, 2010.

- [32] C. V. Sun, J. S. Gardner, G. Long, C. Bajracharya, A. Thurber, A. Punnoose, R.G. Rodriguez, and J.J. Pak, "Controlled Stoichiometry for Quaternary $\text{CuIn}_x\text{Ga}_{1-x}\text{S}_2$ Chalcopyrite Nanoparticles from Single-Source Precursors via Microwave Irradiation," *Chem. Mater.*, vol. 22, pp. 2699-2701, 2010.
- [33] C. O. Kappe, "Controlled Microwave Heating in Modern Organic Synthesis," *Angew. Chem. Int. Edit.*, vol. 43, pp. 6250-6284, 2004.
- [34] Q. Li and Y. Wei, "Study on Preparing Monodispersed Hematite Nanoparticles by Microwave-induced Hydrolysis of Ferric Salts Solution," *Mater. Res. Bull.*, vol. 33, pp. 779-782, 1998.
- [35] J. J. Scragg, P. J. Dale, L. M. Peter, G. Zoppi, and I. Forbes, "New routes to sustainable photovoltaics: evaluation of $\text{Cu}_2\text{ZnSnS}_4$ as an alternative absorber material," *Phys. Status Solidi B*, vol. 245, pp. 1772-1778, 2008.
- [36] K. Tanaka, M. Oonuki, N. Moritake, and H. Uchiki, " $\text{Cu}_2\text{ZnSnS}_4$ thin film solar cells prepared by non-vacuum processing," *Sol. Energy Mater. Sol. Cells*, vol. 93, pp. 583-587, 2009.
- [37] J. J. Scragg, D. M. Berg, and P. J. Dale, "A 3.2% efficient Kesterite device from electrodeposited stacked elemental layers," *J. Electroanal. Chem.*, vol. 646, pp. 52-59, 2010.
- [38] A. Wangperawong, J. S. King, S. M. Herron, B. P. Tran, K. Pangan-Okimoto, and S. F. Bent, "Aqueous bath process for deposition of $\text{Cu}_2\text{ZnSnS}_4$ photovoltaic absorbers," *Thin Solid Films*, vol. 519, pp. 2488-2492, 2011.
- [39] K. Tanaka, Y. Fukui, N. Moritake, and H. Uchiki, "Chemical composition dependence of morphological and optical properties of $\text{Cu}_2\text{ZnSnS}_4$ thin films deposited by sol-gel sulfurization and $\text{Cu}_2\text{ZnSnS}_4$ thin film solar cell efficiency," *Sol. Energy Mater. Sol. Cells*, vol. 95, pp. 838-842, 2011.
- [40] A. Ennaoui, M. Lux-Steiner, A. Weber, D. Abou-Ras, I. Kotschau, H. W. Schock, R. Schurr, A. Holzing, S. Jost, R. Hock, T. Voss, J. Schulze, and A. Kirbs, " $\text{Cu}_2\text{ZnSnS}_4$ thin film solar cells from electroplated precursors: Novel low-cost perspective," *Thin Solid Films*, vol. 517, pp. 2511-2514, 2009.

- [41] N. Moritake, Y. Fukui, M. Oonuki, K. Tanaka, and H. Uchiki, "Preparation of $\text{Cu}_2\text{ZnSnS}_4$ thin film solar cells under non-vacuum condition," *Phys. Status Solidi C*, vol. 6, pp. 1233-1236, 2009.
- [42] P. Reuter, T. Rath, A. Fischereder, G. Trimmel, and P. Hadley, "Electron Beam-Induced Current (EBIC) in Solution-Processed Solar Cells," *Scanning*, vol. 33, pp. 1-6, 2011.
- [43] M. Y. Yeh and D. -S. Wu, "Preparation of $\text{Cu}_2\text{ZnSnS}_4$ treated with Post-sulfurization in a Sulfur Vapor Atmosphere," *Adv. Mat. Res.*, vol. 239-242, pp. 642-645, 2011.
- [44] W. Ki and H. W. Hillhouse, "Earth-Abundant Element Photovoltaics Directly from Soluble Precursors with High Yield Using a Non-Toxic Solvent," *Adv. Energy Mater.*, vol. 1, pp. 732-735, 2011.
- [45] T. Todorov, K. Reuter, and D. B. Mitzi, "High-Efficiency Solar Cell with Earth-Abundant Liquid-Processed Absorber," *Adv. Mater.*, vol. 22, pp. E156-E159, 2010.
- [46] D. A. R. Barkhouse, O. Gunawan, T. Gokmen, T. K. Todorov, and D. B. Mitzi, "Device Characteristics of a 10.1% hydrazine-processed $\text{Cu}_2\text{ZnSn}(\text{Se},\text{S})_4$ solar cell," *Prog. Photovoltaics*, vol. 20, pp. 6-11, 2012.
- [47] M. K. M. Berrada, F. Gruy, and M. Cournil, "Synthesis of zinc sulfide multi-scale agglomerates by homogenous precipitation-parametric study and mechanism," *J. Cryst. Growth*, vol. 311, pp. 2459-2465, 2009.
- [48] H. M. Yang, C. H. Huang, and X. H. Su, "Synthesis of homogeneous PVP-capped SnS_2 submicron particles via microwave irradiation," *Mater. Lett.*, vol. 60, pp. 3714-3417, 2006.
- [49] M. Y. Yeh, C. C. Lee, and D. S. Wu, "Influences of synthesizing temperatures on the properties of $\text{Cu}_2\text{ZnSnS}_4$ prepared by sol-gel spin-coated deposition," *J. Sol-Gel Sci. Technol.*, vol. 52, pp. 65-68 2009.
- [50] A. Weber, R. Mainz, and H. W. Schock, "On the Sn loss from thin films of the material system Cu-Zn-Sn-S in high vacuum," *J. Appl. Phys.*, vol. 107, pp. 013516, 2010.

- [51] W. Wang, Y. -W. Su, and C. -h. Chang, "Inkjet printed chalcopyrite $\text{CuIn}_x\text{Ga}_{1-x}\text{Se}_2$ thin film solar cells *Sol. Energy Mater. Sol. Cells*, vol. 95, pp. 2616-2620, 2011.
- [52] ASTM Standard E1508 - 98, "Standard Guide for Quantitative Analysis by Energy-Dispersive Spectroscopy," ASTM International, DOI: 10.1520/E1508-98R08, 2008.
- [53] H. Katagiri, " $\text{Cu}_2\text{ZnSnS}_4$ thin film solar cells," *Thin Solid Films*, vol. 480, pp. 426-432, 2005.
- [54] T. Kobayashi, K. Jimbo, K. Tsuchida, S. Shinoda, T. Oyanagi, and H. Katagiri, "Investigation of $\text{Cu}_2\text{ZnSnS}_4$ -Based Thin Film Solar Cells Using Abundant Materials," *Jpn. J. Appl. Phys.*, vol. 44, pp. 783-787, 2005.
- [55] S. Chen, X. Gong, A. Walsh, and S. Wei, "Defect physics of the kesterite thin-film solar cell absorber $\text{Cu}_2\text{ZnSnS}_4$," *Appl. Phys. Lett.*, vol. 96, pp. 021902, 2010.
- [56] K. Biswas, S. Lany, and A. Zunger, "The electronic consequences of multivalent elements in inorganic solar absorbers: Multivalency of Sn in $\text{Cu}_2\text{ZnSnS}_4$," *Appl. Phys. Lett.*, vol. 96, pp. 201902, 2010.
- [57] T. Prabhakar and N. Jampana, "Effect of sodium diffusion on the structural and electrical properties of $\text{Cu}_2\text{ZnSnS}_4$ thin films," *Sol. Energy Mater. Sol. Cells*, vol. 95, pp. 1001-1004, 2011.
- [58] R. Xie, M. Rutherford, and X. Peng, "Formation of High-Quality I-III-VI Semiconductor Nanocrystals by Tuning Relative Reactivity of Cationic Precursors," *J. Am. Chem. Soc.*, vol. 131, pp. 5691-5697, 2009.
- [59] A. Shavel, J. Arbiol, and A. Cabot, "Synthesis of Quaternary Chalcogenide Nanocrystals: Stannite $\text{Cu}_2\text{Zn}_x\text{Sn}_y\text{Se}_{1+x+2y}$," *J. Am. Chem. Soc.*, vol. 132, pp. 4514-4515, 2010.
- [60] Y. -L. Zhou, W. -H. Zhou, M. Li, Y. -F. Du, and S. -X. Wu, "Hierarchical $\text{Cu}_2\text{ZnSnS}_4$ Particles for a Low-Cost Solar Cell: Morphology Control and Growth Mechanism *J. Phys. Chem. C*, vol. 115, pp. 19632-19639, 2011.
- [61] M. D. Regulacio, C. Ye, S. H. Lim, M. Bosman, E. Ye, S. Chen, Q. -H. Xu, and M. -Y. Han, "Colloidal Nanocrystals of Wurtzite-Type

- $\text{Cu}_2\text{ZnSnS}_4$: Facile Noninjection Synthesis and Formation Mechanism,” *Chem. Eur. J.*, vol. 18, pp. 3127-3131, 2012.
- [62] S. W. Shin, J. H. Han, C. Y. Park, A. V. Moholkar, J. Y. Lee, and J. H. Kim, “Quaternary $\text{Cu}_2\text{ZnSnS}_4$ nanocrystals: Facile and low cost synthesis by microwave-assisted solution method,” *J. Alloy. Compd.*, vol. 516, pp. 96-101, 2012.
 - [63] M. Himmrich and H. Haeuseler, “Far infrared studies on stannite and wurtzstannite type compounds,” *Spectrochim. Acta A*, vol. 47, pp. 933-942 1991.
 - [64] P. A. Fernandes, P. M. P. Salome, and A. F. da Cunha, “Growth and Raman scattering characterization of $\text{Cu}_2\text{ZnSnS}_4$ thin films,” *Thin Solid Films* vol. 517, pp. 2519-2523, 2009.
 - [65] K. Wang, B. Shin, K. B. Reuter, T. Todorov, D. B. Mitzi, and S. Guha, “Structural and elemental characterization of high efficiency $\text{Cu}_2\text{ZnSnS}_4$ solar cells,” *Appl. Phys. Lett.*, vol. 98, pp. 051912, 2011.
 - [66] X. Fontané, L. Calvo-Barrio, V. Izquierdo-Roca, E. Saucedo, A. Pérez-Rodriguez, J. Morante, D. Berg, P. Dale, and S. Siebentritt, “In-depth resolved Raman scattering analysis for the identification of secondary phases: Characterization of $\text{Cu}_2\text{ZnSnS}_4$ layers for solar cell applications,” *Appl. Phys. Lett.*, vol. 98, pp. 181905, 2011.
 - [67] Y. -T. Nien, B. Zaman, J. Ouyang, I. -G. Chen, C. -S. Hwang, and K. Yu, “Raman scattering for the size of CdSe and CdS nanocrystals and comparison with other techniques,” *Mater. Lett.* vol. 62, pp. 4522-4524, 2008.
 - [68] Y. Cheng, C. Jin, F. Gao, X. Wu, W. Zhong, S. Li, and P. Chu, “Raman scattering study of zinc blende and wurtzite ZnS,” *J. Appl. Phys.*, vol. 106, pp. 123505, 2009.
 - [69] P. A. Fernandes, P. M. P. Salome, and A. F. da Cunha, “A study of ternary Cu_2SnS_3 and Cu_3SnS_4 thin films prepared by sulfurizing stacked metal precursors,” *J. Phys. D Appl. Phys.*, vol. 43, pp. 215403, 2010.
 - [70] S. Y. Chen, X. G. Gong, A. Walsh, and S. H. Wei, “Crystal and electronic band structure of $\text{Cu}_2\text{ZnSnX}_4$ (X=S and Se) photovoltaic

absorbers: First-principles insights *Appl. Phys. Lett.*, vol. 94, pp. 041903, 2009.

- [71] H. Katagiri, N. Sasaguchi, S. Hando, S. Hoshino, J. Ohashi, and T. Yokota, "Preparation and evaluation of $\text{Cu}_2\text{ZnSnS}_4$ thin films by sulfurization of E-B evaporated precursors," *Sol. Energy Mater. Sol. Cells*, vol. 49, pp. 407-414, 1997.
- [72] K. Ito and T. Nakazawa, "Electrical and Optical Properties of Stannite-Type Quaternary Semiconductor Thin Films," *Jpn. J. Appl. Phys.*, vol. 27, pp. 2094-2097, 1988.
- [73] Y. F. Liu, M. Y. Ge, Y. Yue, Y. Sun, Y. Z. Wu, X. Chen, and N. Dai, "Colloidal $\text{Cu}_2\text{ZnSnS}_4$ nanocrystals generated by a facile route using ethylxanthate molecular precursors," *Phys. Status Solidi-R.*, vol. 5, pp. 113-115, 2011.
- [74] J. -S. Seol, S. -Y. Lee, J. -C. Lee, H. -D. Nam, and K. -H. Kim, "Electrical and optical properties of $\text{Cu}_2\text{ZnSnS}_4$ thin films prepared by rf magnetron sputtering process," *Sol. Energy Mater. Sol. Cells*, vol. 75, pp. 155-162, 2003.
- [75] B. Shin, O. Gunawan, Y. Zhu, N. A. Bojarczuk, S. J. Chey, and S. Guha, "Thin film solar cell with 8.4% power conversion efficiency using an earth-abundant $\text{Cu}_2\text{ZnSnS}_4$ absorber," *Prog. Photovolt: Res. Appl.*, vol. 21, pp. 72-76, 2013.

Figures

	Cu/(Zn+Sn)	Zn/Sn	Cu(at%)	Zn (at%)	Sn (at%)	S (at%)
Sample A precursor solution	0.75	1.43				
Sample A nanoparticles (EDS)	1.53	0.27	30.0	4.13	15.5	50.4
Sample B precursor solution	0.30	2.53				
Sample B nanoparticles (EDS)	0.86	1.04	23.0	13.6	13.1	50.4
Sample B annealed (EDS)	0.89	0.93	22.1	11.9	12.8	53.2

Table 3.1 - Composition of precursor solutions and CZTS nanoparticles

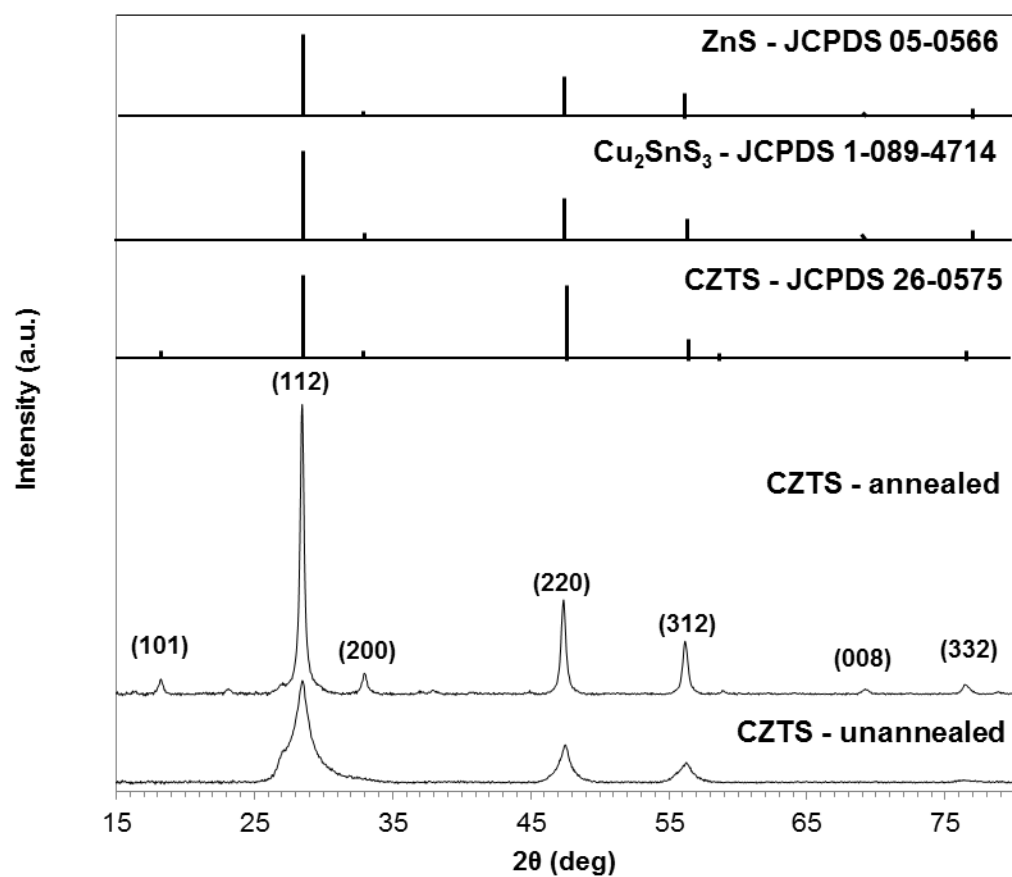


Figure 3.1 - XRD spectra of as synthesized nanoparticles and nanoparticles annealed to 400 °C for 20 minutes.

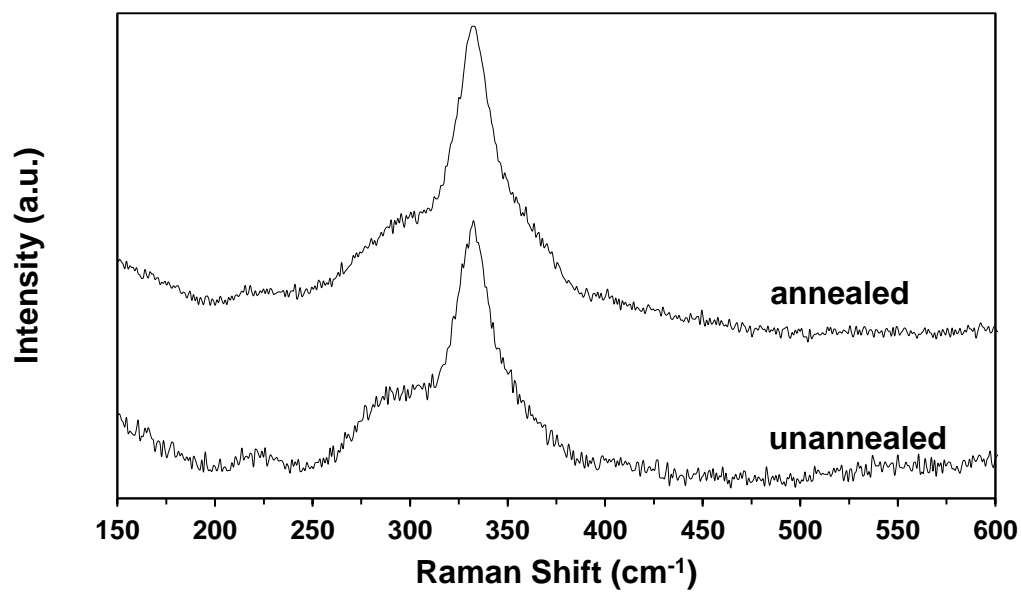


Figure 3.2 - Raman spectra of annealed (upper) and unannealed (lower) nanoparticles showing main vibrational mode at 333 cm⁻¹.

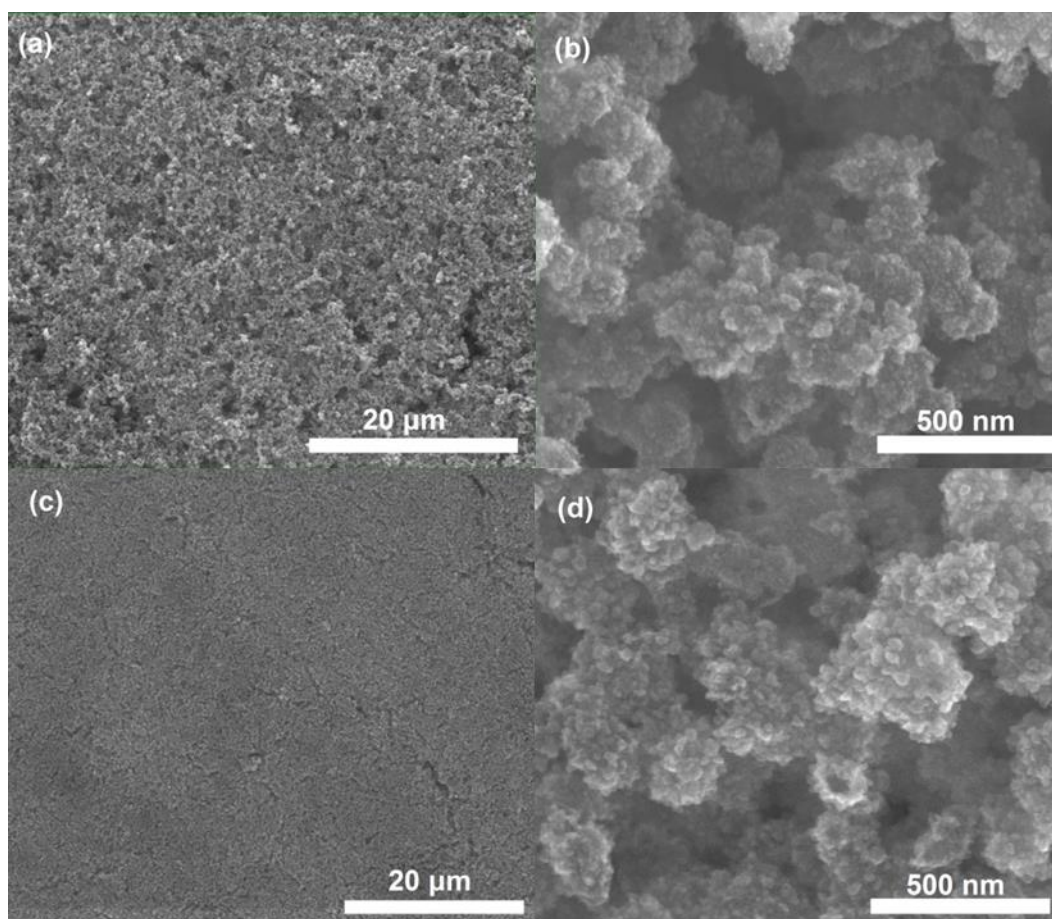


Figure 3.3 - Low (5,000x) and high (200,000x) magnification SEM images of the as synthesized nanoparticles (a,b) and annealed nanoparticles (c,d).

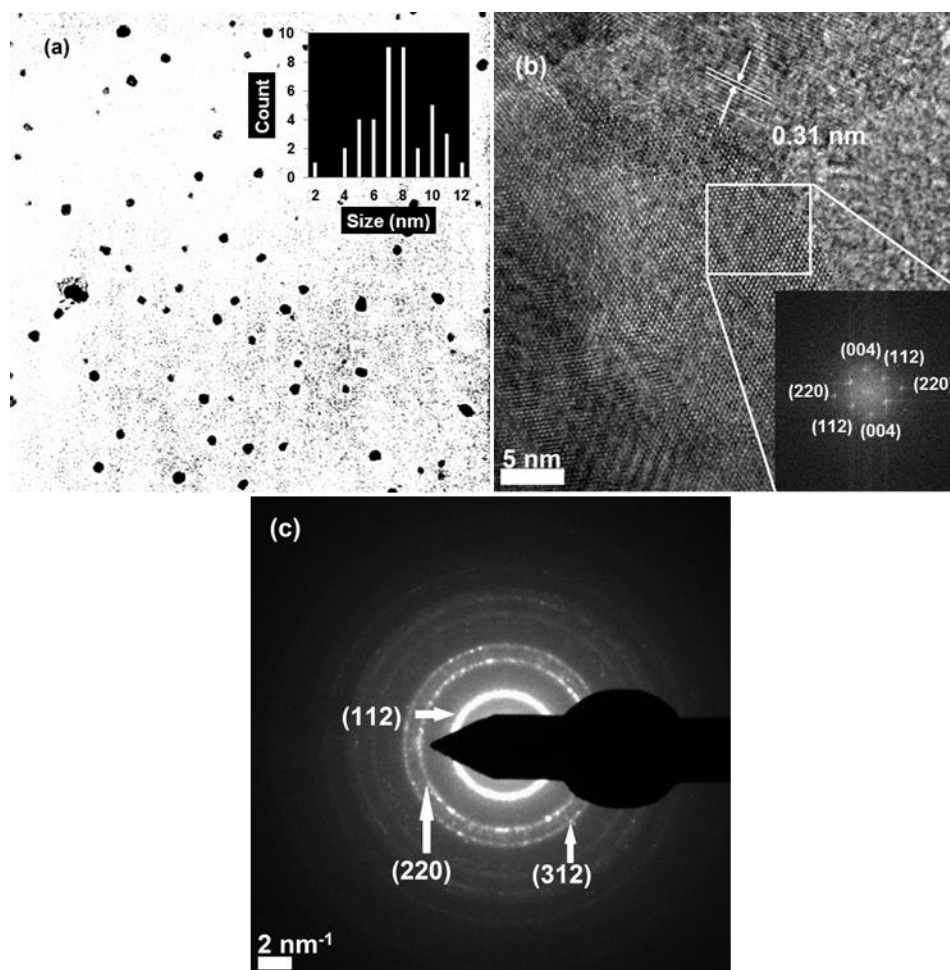


Figure 3.4 - TEM images illustrating particle size (a), interplanar spacing of the (112) plane (b), and SAED (c) of unannealed CZTS nanoparticles. Magnifications for (a) and (b) were 125,000x and 620,000x. A distribution of the particle sizes is shown in the inset in (a), while a FFT is shown in (b) of the indicated particle.

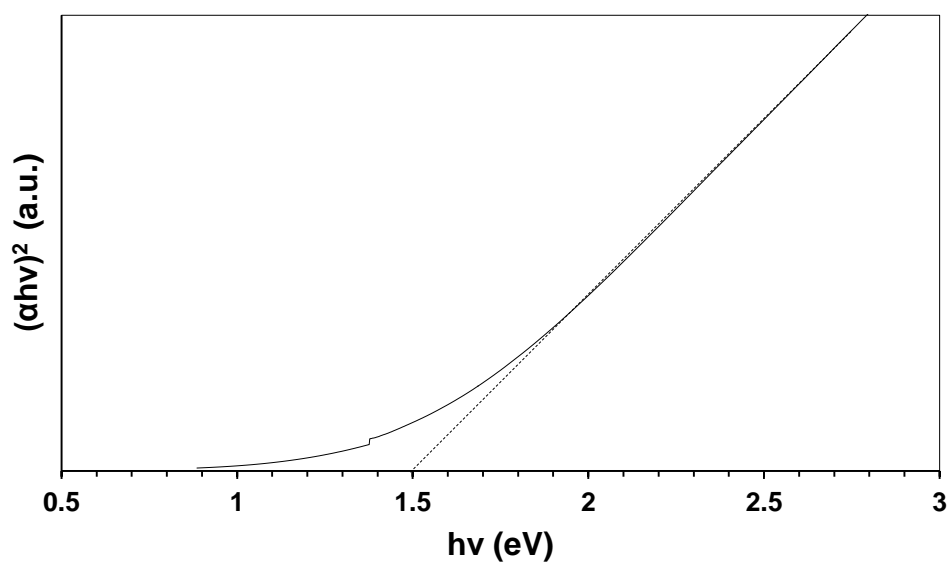


Figure 3.5 - UV-Vis spectra of the as synthesized CZTS nanoparticles.

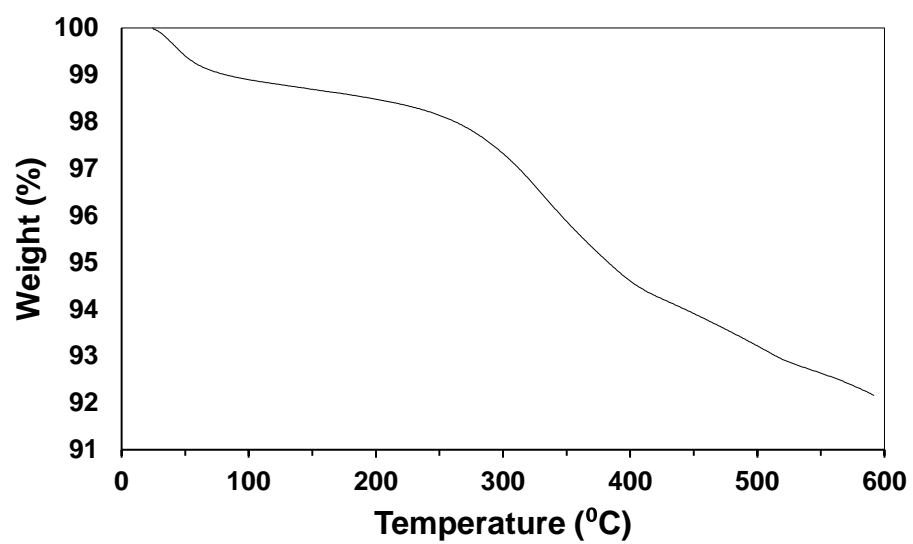


Figure 3.6 - Thermal gravimetric analysis of CZTS nanoparticles.

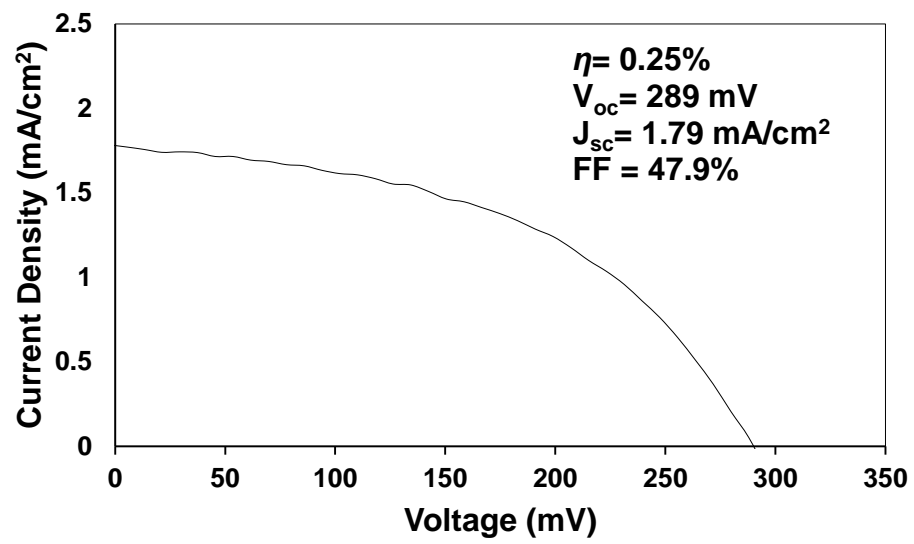


Figure 3.7 - Current-voltage characteristics for CZTS solar cell.

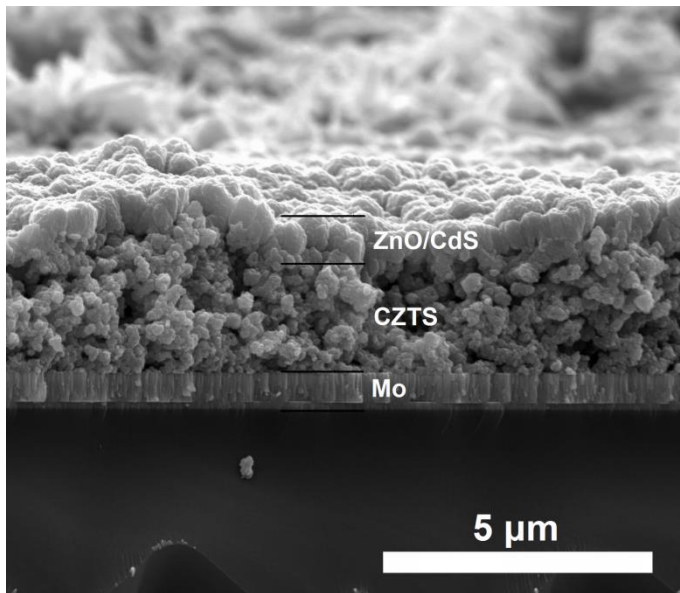


Figure 3.8 - SEM image of a cross section of CZTS solar cell.

CHAPTER 4

CONTINUOUS FLOW MESOFLUIDIC SYNTHESIS OF
 $\text{Cu}_2\text{ZnSnS}_4$ NANOPARTICLE INKS

Brendan T. Flynn,¹ Ian L. Braly,¹ Philip A. Glover,¹ Richard P. Oleksak,¹ Chris Durgan,¹ and Gregory S. Herman^{*1}

¹Oregon State University, School of Chemical, Biological and Environmental Engineering, Corvallis, OR

^{*}Corresponding Author

Reproduced in part from *Mater. Lett.*, vol. 107, pp. 214-217, 2013.

Abstract

Copper zinc tin sulfide (CZTS) nanoparticles were synthesized via a continuous flow mesofluidic reactor. Reaction temperature, residence time, and precursor concentrations were used to control nanoparticle composition. CZTS was found to form initially by the nucleation of Cu_{2-x}S with subsequent incorporation of the remaining metal species as dictated by the cation reactivity, where $\text{Cu}^+ > \text{Sn}^{+4} > \text{Zn}^{+2}$. CZTS nanoparticle films annealed in a selenium-containing atmosphere resulted in the formation of copper zinc tin selenide nanoparticles with much larger particle sizes.

Introduction

Copper zinc tin sulfide (CZTS) is a good absorber candidate for low cost thin film solar cells due to its excellent optical properties[1, 2] and relatively high abundance of its constituent elements. CZTS is isoelectronic with copper indium gallium diselenide (CIGS), which is currently used in commercial thin film solar modules[3]. In 2012, the prices of indium and gallium were roughly 275 times that of zinc and 15 times that of tin[4]. For high volume solar cell production, CZTS would likely provide significant cost advantages compared to CIGS due to the relatively lower cost of zinc and tin, provided comparable solar cell efficiencies [5].

Solution processing of CZTS offers a low cost and high throughput alternative to vacuum based methods[6]. Several different solution based approaches to synthesizing CZTS have been studied, where the focus has been on batch synthetic methods[7-10]. Hydrazine[11, 12], electroplating[13], sol-gel [14, 15], spray pyrolysis[16], solvothermal[17], and microwave-assisted[18] methods have also been used to synthesize CZTS for solar cells. Recently it has been demonstrated that continuous flow processes have potential for the large scale, solution based synthesis of CZTS nanomaterials[19]. Further studies on reaction chemistries and conditions are required to optimize CZTS synthesis.

In this study we investigated the synthesis of CZTS nanoparticles utilizing a mesofluidic continuous flow reactor using a low-cost solvent

system. The flow in the reactor was segmented in a controlled manner by gas generation within the reaction stream to assist in narrowing the nanoparticle size distribution and minimize clogging. It was found that the nanoparticle composition could be controlled by optimizing the residence time, reaction temperature, and concentration of precursors.

Experimental Methods

Triethylene glycol (TEG) was used to dissolve cuprous chloride (0.005 M), zinc chloride (0.00545 M), and stannic chloride pentahydrate (0.00286M) and in a separate beaker thioacetamide ($\text{C}_2\text{H}_5\text{NS}$, 0.0226 M). Room temperature precursor solutions were pumped through separate preheating coils using a peristaltic pump as shown in Fig. 4.1. The reactor used perfluoroalkoxy (PFA) tubing (ID = 1.59 mm). Burst nucleation of the nanoparticles occurred in a mesofluidic T-mixer (Parker GTC-2) with a minimum diameter of 2.38 mm. The liquid flow was self-segmented by gas produced within the reactor by evaporation of the solvent, release of dissolved gas, and/or decomposition of thioacetamide to hydrogen sulfide.

After nucleation, the solution flowed through PFA tubing submerged in a heated bath. At the exit of the bath, polyether ether ketone (PEEK) tubing (ID = 0.76 mm) was attached and placed in ice. This section of tubing quenched the reaction and increased the operating pressure within the

system. The increase in operating pressure prevented excessive vapor formation, which could lead to erratic flow rates.

The nanoparticle reaction products were washed several times in deionized water and ethanol prior to analysis. Annealing studies were performed at 500 °C for 20 minutes in a tube furnace under flowing nitrogen (300 mL/min at 15 kPa system pressure), with or without sulfur or selenium powders. These conditions are referenced as N₂, N₂+S, and N₂+Se, respectively.

Nanoparticle film morphology and composition was determined using a FEI Quanta 3D (30 kV beam energy) by scanning electron microscopy and energy dispersive X-ray spectroscopy (EDS), respectively. Raman spectra were obtained with a Horiba-Jobin Yvon HR800 Raman spectrometer with 532 nm radiation. X-ray diffraction (XRD) analysis was performed with a Bruker D8 Discover diffractometer with Cu K α radiation. The composition of the precursor solution and post-reaction supernatant were analyzed by inductively coupled plasma atomic emission spectroscopy (ICP-AES) using a Varian Liberty 150 spectrometer. High resolution imaging of the as synthesized particles was performed using a FEI Titan FEG transmission electron microscope (TEM).

Results and Discussion

The controlled generation and segmentation of gas was an enabling feature of the reactor design. Segmentation helps narrow the particle size distribution by ensuring a more uniform residence time for the nanoparticles when compared to a single phase laminar flow. In laminar flow, fluid velocity decreases towards the tube wall due to drag, resulting in a longer residence time for those nanoparticles closest to the wall. As a result the nanoparticles near the wall of the tube will grow larger than those in the middle of the tube. In contrast, for segmented flows the nanoparticles recirculate between two high pressure gas-liquid interfaces which results in a uniform residence time for all the nanoparticles, as depicted in Fig. 4.2.

Two equations were used to qualitatively understand which variables could be adjusted to increase the pressure drop. The Hagen-Poiseuille equation for laminar flow

$$\Delta P = 128 \left(\mu Q L / \pi D^4 \right) \quad (1)$$

reveals the dependence of the pressure drop ΔP on the fluid viscosity μ , volumetric flow rate Q , tube length L , and tube inner diameter D in the liquid phase. Bretherton[20] gave the pressure drop over a single bubble moving in a low Reynolds number liquid as

$$\Delta P = 7.16 \left(3\mu U / \sigma \right)^{2/3} (\sigma / D) \quad (2)$$

where U is the bubble speed and σ the interfacial tension. The utility of decreasing the inner diameter at the quenching section is seen by the strong dependence of the pressure drop on this variable. Triethylene glycol has a non-linear viscosity-temperature relationship[21], where the fluid viscosity increases markedly after cooling below about 60 °C, and this is also seen to have a pronounced effect on system pressure. Therefore, submerging the PEEK tubing in an ice bath served the dual purpose of quenching the reaction and elevating system pressure.

Residence time had a pronounced effect on the composition and size of the CZTS nanoparticles. Initial studies were performed with stoichiometric precursor solutions reacted at 215 °C for residence times $\tau < 1$, $\tau = 28$, and $\tau = 49$ minutes. EDS results are given in Table 4.1. As residence time increased, the relative copper content decreased while sulfur content increased. Significant zinc content was only observed for $\tau > 28$ min. The XRD spectra in Fig. 4.1(a) show four main diffraction peaks at $2\theta = 28.4^\circ$, 32.9° , 47.3° , and 56.0° , which correspond to the (112), (200)/(004), (220)/(204), and (312)/(116) planes of kesterite CZTS. These planes were indexed using JCPDS 26-0575 and by simulating the CZTS structure with JEMS software[22] and are shown as the reference pattern at the top of Fig.

4.1(a). Performing a Scherrer analysis on the (112) peak for CZTS nanoparticles reacted for $\tau < 1$, $\tau = 28$, and $\tau = 49$ min gave particle sizes of 7.6 nm, 8.6 nm, and 13.8 nm, respectively. The Raman spectra in Fig. 4.3(b) have two main peaks at ~ 289 and 332 cm^{-1} . These peaks have previously been assigned to the A_1 vibrational modes in the CZTS lattice[23]. A large increase in the relative intensity of the peak positioned at 332 cm^{-1} was found for $\tau = 49$ min, which may be related to the incorporation of zinc, the larger size of the nanoparticles, and/or greater crystalline order of the nanoparticles. In a prior study, a comparison of Raman spectra from CZTS and tetragonal Cu_2SnS_3 thin films reveal an analogous intensity increase for the 332 cm^{-1} peak in the case of CZTS[24]. In addition, the tetragonal Cu_2SnS_3 Raman spectrum is nearly identical in shape and relative peak intensity compared to the Raman spectra obtained for $\tau < 1$ min and $\tau = 28$ min reactions in this study, suggesting the formation of Cu_2SnS_3 at shorter residence times. The position of the Raman peak at $331\text{-}332 \text{ cm}^{-1}$ has been reported for both CZTS thin films[25] and nanoparticles[26], but was red shifted compared to typical values of $\sim 336\text{-}339 \text{ cm}^{-1}$ [23, 24]. The small nanoparticle size combined with cation disorder may contribute to the broad red shifted 332 cm^{-1} peak observed in this study[27, 28].

The relative metal cation reaction rates were estimated by comparing the composition of the metal precursor solution and the post-reaction supernatant using ICP-AES. For precursor solutions with stoichiometric metal

cation concentrations only 0.23% of the initial copper, 9% of the initial tin, and 20% of the initial zinc remained in the post-reaction supernatant for the $\tau < 1$ min reaction. Relative reaction rates for the metal cations were estimated to be $\text{Cu}^+ > \text{Sn}^{4+} > \text{Zn}^{2+}$. This is in agreement with a prior continuous flow CZTS study where increasing residence time resulted in a decrease in the copper content and an increase in the zinc content for CZTS nanoparticles[19].

To obtain the desired CZTS nanoparticle stoichiometry we have optimized the reaction temperature, residence time, and initial concentration of precursors. Optimal reaction conditions were obtained at 230 °C with $\tau = 75$ min and metal precursor solution composition ratios of $\text{Cu}/(\text{Zn}+\text{Sn}) = 0.60$ and $\text{Zn}/\text{Sn} = 1.9$. The sulfur precursor was in excess by 1.65x, which is based on the following relationship $[\text{S}] = 1.65 \times ([\text{Cu}]/2 + [\text{Zn}] + [\text{Sn}] \times 2)$. For this reaction no copper remained in the post-reaction supernatant, compared to 4% of the tin and 24% of the zinc, which resulted in CZTS nanoparticles with the following composition $\text{Cu}_{1.9}\text{Zn}_{1.0}\text{Sn}_{1.2}\text{S}_{3.9}$. Both single and multicrystalline CZTS nanoparticles were synthesized using the optimized reaction conditions as shown by the high-resolution TEM results in Fig. 4.4(a) and (b). Fast Fourier transforms (FFT) of the TEM images are shown in Fig. 4.4(c) and (d), and both types of nanoparticles can be indexed to the CZTS kesterite structure, where the diffraction spots correspond to the (220)/(204) and (332)/(316) planes as viewed along the [112] zone axis. The bright field TEM image in Fig. 4.4(e) shows individual CZTS nanoparticles, which have an

average size of 5.4 nm with a standard deviation of 2.0 nm, as determined by measuring 50 nanoparticles. In Fig. 4.5 the lowermost XRD spectrum is for the as synthesized CZTS nanoparticles and has four broad diffraction peaks similar to the XRD patterns shown in Fig. 4.3(a). The nanoparticle crystallite size was estimated to be 13.6 nm using the Scherrer analysis of the (112) diffraction peak. Agglomeration may prevent the observation of a representative distribution of nanoparticles, which may explain the discrepancy between particle sizing using TEM and XRD analysis[29]. The Raman spectrum is shown in Fig. 4.5(b) for the as synthesized CZTS nanoparticles where the A_1 vibrational modes of CZTS at 333 cm^{-1} and 288 cm^{-1} were observed, in close agreement with Raman data from other CZTS nanoparticle work[19]. For these reaction conditions there was no Cu_{2-x}S formed as indicated by the absence of a Raman peak at 475 cm^{-1} .

The optimized CZTS nanoparticles were annealed at $500\text{ }^\circ\text{C}$ for 20 min in nitrogen (N_2), sulfur (N_2+S), and selenium (N_2+Se). As shown in Fig. 4.5(a) the XRD peaks become narrower and more intense after each annealing treatment. CZTS crystallite sizes were calculated using the Scherrer method after annealing in N_2 , N_2+S and N_2+Se ambient and were determined to be 25.3, 27.6, and 43.4 nm, respectively. After the N_2+Se anneal the main peaks at $2\theta = 28.4^\circ$, 47.3° , and 56.0° all shift to smaller angles due to lattice expansion, as can be seen more clearly by the inset in Fig. 4.5. This N_2+Se annealing process leads to the formation of CZTSe from the CZTS starting

material based on the magnitude of the peak shifts, and the absence of the peak at $2\theta = 32.9^\circ$, which were consistent with the CZTSe reference pattern (JCPDS 52-0868) shown in the upper portion of the figure. The Raman spectra shown in Fig. 4.5(b) confirms that sulfur was replaced by selenium in the nanoparticles after the N_2+Se anneal. For the as synthesized nanoparticles, and those annealed in N_2 , and N_2+S , the main CZTS A_1 vibrational modes were observed. After the N_2+Se anneal these peaks were red-shifted, and the Raman spectrum is in good agreement with prior CZTSe studies[30, 31], with peaks located at 173 cm^{-1} , 193 cm^{-1} , and 232 cm^{-1} . This is consistent with the change in relative mass between S and Se, and that the A_1 vibrational modes in CZTS result from the motion of sulfur ions, and in CZTSe result from the motion of selenium ions.

Conclusion

Continuous flow methods show promise for the synthesis of CZTS. In this study CZTS nanoparticles were synthesized in a mesofluidic continuous flow reactor at modest temperatures using low cost solvents. Segmented flow was achieved within the reactor by the controlled generation of gas, which improved mixing of the nanoparticles and reduced particle size distributions. The CZTS nanoparticles were formed by a multistep reaction where $Cu_{2-x}S$ initially formed, followed by the incorporation of Sn, and then finally Zn. The CZTS stoichiometry was controlled by adjusting the initial

precursor concentration, the reaction time, and the reaction temperature.

This approach allowed us to use metal precursors with equivalent counterions and avoid complex organic additives. Finally, the CZTS nanoparticles were converted to CZTSe after a N_2+Se anneal as indicated by EDS, XRD, and Raman data.

Acknowledgements

The authors would like to thank Hsiao-Wen Huang for assistance with the ICP-AES measurements. The authors gratefully acknowledge support from Sharp Laboratories of America and the National Science Foundation through CCI phase II grant number CHE-1102637 for the Center for Sustainable Materials Chemistry.

References:

- [1] J. -S. Seol, S. -Y. Lee, J. -C. Lee, H. -D. Nam, and K. -H. Kim, "Electrical and optical properties of Cu_2ZnSnS_4 thin films prepared by rf magnetron sputtering process," *Sol. Energy Mater Sol Cells*, vol. 75, pp. 155-162, 2003.
- [2] H. Katagiri, "Cu₂ZnSnS₄ thin film solar cells," *Thin Solid Films*, vol. 480, pp. 426-432, 2005.
- [3] S. Niki, M. Contreras, I. Repins, M. Powalla, K. Kushiya, S. Ishizuka, and K. Matsubara, "CIGS absorbers and processes," *Prog. Photovoltaics Res. Appl.*, vol. 18, pp. 453-466, 2010.
- [4] U.S. Geological Survey, Mineral commodity summaries 2013, pp. 1-201.

- [5] I. Repins, N. Vora, C. Beall, S. H. Wei, Y. Yan, M. Romero, G. Teeter, H. Du, B. To, M. Young, and R. Noufi, "Kesterites and Chalcopyrites: A Comparison of Close Cousins," *Mater. Res. Soc. Symp. P.*, vol. 1324, pp. mrss11-1324, 2011.
- [6] T. Todorov and D.B. Mitzi, "Direct Liquid Coating of Chalcopyrite Light-Absorbing Layers for Photovoltaic Devices," *Eur. J. Inorg. Chem.*, vol. 1, pp. 17-28, 2010.
- [7] A. Shavel, J. Arbiol, and A. Cabot, "Synthesis of Quaternary Chalcogenide Nanocrystals: Stannite $\text{Cu}_2\text{Zn}_x\text{Sn}_y\text{Se}_{1+x+2y}$," *J. Am. Chem. Soc.*, vol. 132, pp. 4514-4515, 2010.
- [8] S. C. Riha, B. A. Parkinson, and A. L. Prieto, "Compositionally Tunable $\text{Cu}_2\text{ZnSn}(\text{S}_{1-x}\text{Se}_x)_4$ Nanocrystals: Probing the Effect of Se-Inclusion in Mixed Chalcogenide Thin Films," *J. Am. Chem. Soc.*, vol. 133, pp. 15272-15275, 2011.
- [9] Q. J. Guo, H. W. Hillhouse, and R. Agrawal, "Synthesis of $\text{Cu}_2\text{ZnSnS}_4$ Nanocrystal Ink and Its Use for Solar Cells," *J. Am. Chem. Soc.*, vol.131, pp. 11672-11673, 2009.
- [10] C. Jiang, J. S. Lee, and D. V. Talapin, "Soluble Precursors for CuInSe_2 , $\text{CuIn}_{1-x}\text{Ga}_x\text{Se}_2$, and $\text{Cu}_2\text{ZnSn}(\text{S},\text{Se})_4$ Based on Colloidal Nanocrystals and Molecular Metal Chalcogenide Surface Ligands," *J. Am. Chem. Soc.*, vol. 134, pp. 5010-5013, 2012.
- [11] S. Bag, O. Gunawan, T. Gokmen, Y. Zhu, T. K. Todorov, and D. B. Mitzi, "Low band gap liquid-processed CZTSe solar cell with 10.1% efficiency," *Energy & Environ. Sci.*, 5 (2012) 7060-7065.
- [12] T. K. Todorov, J. Tang, S. Bag, O. Gunawan, T. Gokmen, Y. Zhu, and D. B. Mitzi, "Beyond 11% Efficiency: Characteristics of State-of-the-Art $\text{Cu}_2\text{ZnSn}(\text{S},\text{Se})_4$ Solar Cells," *Adv Energy Mater.*, vol. 3, pp. 34-38, 2013.
- [13] S. Ahmed, K. B. Reuter, O. Gunawan, L. Guo, L. T. Romankiw, and H. Deligianni, "A High Efficiency Electrodeposited $\text{Cu}_2\text{ZnSnS}_4$ Solar Cell," *Adv. Energy Mater.*, vol. 2, pp. 253-259, 2012.
- [14] A. Fischereder, T. Rath, W. Haas, H. Amenitsch, J. Albering, D. Meischler, S. Larissegger, M. Edler, R. Saf, F. Hofer, and G. Trimmel,

- "Investigation of $\text{Cu}_2\text{ZnSnS}_4$ Formation from Metal Salts and Thioacetamide," *Chem. Mater.*, vol. 22, pp. 3399-3406, 2010.
- [15] W. Ki and H. W. Hillhouse, "Earth-Abundant Element Photovoltaics Directly from Soluble Precursors with High Yield Using a Non-Toxic Solvent," *Adv. Energy Mater.*, vol. 1, pp. 732-735, 2011.
- [16] Y. B. K. Kumar, G. S. Babu, P. U. Bhaskar, and V. S. Raja, "Preparation and characterization of spray-deposited $\text{Cu}_2\text{ZnSnS}_4$ thin films," *Sol. Energy Mater. Sol. C*, vol. 93, pp. 1230-1237, 2009.
- [17] Y. -L. Zhou, W. -H. Zhou, M. Li, Y. -F. Du, and S. -X. Wu, "Hierarchical $\text{Cu}_2\text{ZnSnS}_4$ Particles for a Low-Cost Solar Cell: Morphology Control and Growth Mechanism *J. Phys. Chem. C*, vol. 115, pp. 19632-19639, 2011.
- [18] B. T. Flynn, W. Wang, C. -h. Chang, and G. S. Herman, "Microwave Assisted Synthesis of $\text{Cu}_2\text{ZnSnS}_4$ Colloidal Nanoparticle Inks," *Phys. Status Solidi A*, vol. 209, pp. 2186-2194, 2012.
- [19] A. Shavel, D. Cadavid, M. Ibáñez, A. Carrete, and A. Cabot, "Continuous Production of $\text{Cu}_2\text{ZnSnS}_4$ Nanocrystals in a Flow Reactor," *J. Am. Chem. Soc.*, vol. 134, pp. 1438-1441, 2012.
- [20] F. P. Bretherton, "The motion of long bubbles in tubes," *J. Fluid Mech.*, vol. 10, pp. 166-188, 1961.
- [21] E. Obermeier, S. Fischer, and D. Bohne, "Thermal Conductivity, Density, Viscosity, and Prandtl-Numbers of Di- and Triethylene Glycol-Water Mixtures," *Ber. Bunsenges. Phys. Chem.*, vol. 89, pp. 805-809, 1985.
- [22] S. Hall, J. Szymanski, and J. Stewart, "Kesterite, $\text{Cu}_2(\text{Zn,Fe})\text{SnS}_4$ and Stannite, $\text{Cu}_2(\text{Fe,Zn})\text{SnS}_4$, Structurally Similar but Distinct Minerals," *Can. Mineral.*, vol. 16, pp. 131-137, 1978.
- [23] M. Himmrich and H. Haeuseler, "Far infrared studies on stannite and wurtzstannite type compounds," *Spectrochim. Acta A*, vol. 47, pp. 933-942 1991.
- [24] P. A. Fernandes, P. M. P. Salomé, and A. F. da Cunha, "Study of polycrystalline $\text{Cu}_2\text{ZnSnS}_4$ films by Raman scattering," *J. Alloy Compd*, vol. 509, pp. 7600-7606, 2011.

- [25] P. M. P. Salome, J. Malaquias, P. A. Fernandes, M. S. Ferreira, A. F. da Cunha, J. P. Leitao, J. C. Gonzalez, and F. M. Martinaga, "Growth and characterization of $\text{Cu}_2\text{ZnSn}(\text{S},\text{Se})_4$ thin films for solar cells," *Sol. Energy Mater. Sol. C.*, vol. 101, pp. 147-153, 2012.
- [26] C. Zou, L. Zhang, D. Lin, Y. Yang, Q. Li, X. Xu, and S. Huang, "Facile synthesis of $\text{Cu}_2\text{ZnSnS}_4$ nanocrystals," *CrystEngComm*, vol. 13, pp. 3310-3313, 2011.
- [27] G. Gouadec and P. Colomban, "Raman Spectroscopy of nanomaterials: How spectra relate to disorder, particle size and mechanical properties," *Prog. Cryst. Growth Ch.*, vol. 53, pp. 1-56, 2007.
- [28] I. H. Campbell and P. M. Fauchet, "The Effects of Microcrystal Size and Shape on the One Phonon Raman-spectra of Crystalline Semiconductors," *Solid State Commun.*, vol. 58, pp. 739-741, 1986.
- [29] A. Weibel, R. Bouchet, F. Boulc'h, and P. Knauth, "The Big Problem of Small Particles: A Comparison of Methods for Determination of Particle Size in Nanocrystalline Anatase Powders," *Chem. Mater.*, vol. 17, pp. 2378-2385, 2005.
- [30] M. Altosaar, J. Raudoja, K. Timmo, M. Danilson, M. Grossberg, J. Krustok, E. Mellikov, " $\text{Cu}_2\text{Zn}_{1-x}\text{Cd}_x\text{Sn}(\text{Se}_{1-y}\text{S}_y)_4$ solid solutions as absorber materials for solar cells," *Phys. Status Solidi A*, vol. 205, pp. 167-170, 2008.
- [31] M. Ganchev, J. Iljina, L. Kaupmees, T. Raadik, O. Volobujeva, A. Mere, M. Altosaar, J. Raudoja, E. Mellikov, "Phase composition of selenized $\text{Cu}_2\text{ZnSnSe}_4$ thin films determined by X-ray diffraction and Raman spectroscopy," *Thin Solid Films*, vol 519, pp. 7394-7398, 2011.

Figures

Residence time, min	Composition, atomic %				Crystallite size, nm
	Cu	Zn	Sn	S	
< 1	44.15	1.36	15.37	39.13	7.6
28	33.19	0.88	14.52	51.44	8.6
49	33.77	6.27	12.12	47.85	13.8

Table 4.1 - Effect of residence time on composition and crystallite size.

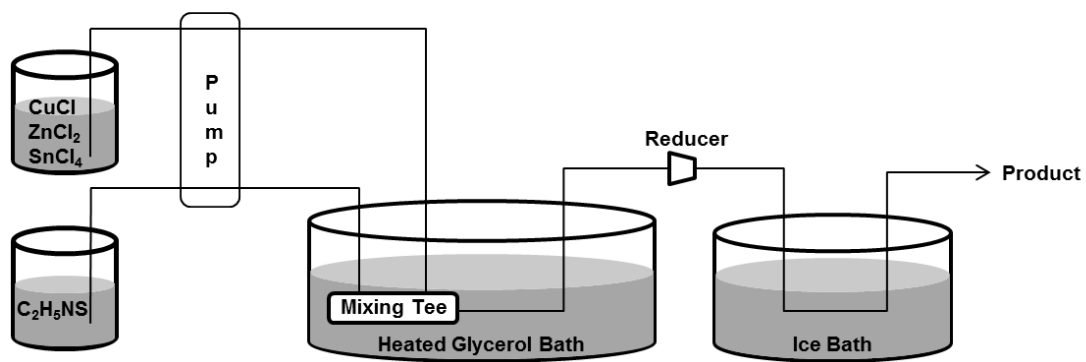


Figure 4.1 - Diagram of continuous flow reactor used for CZTS synthesis.

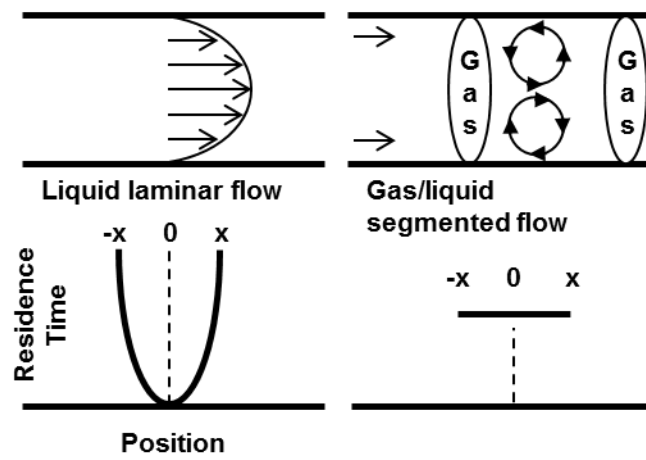


Figure 4.2 – Relationship between axial position and residence time.

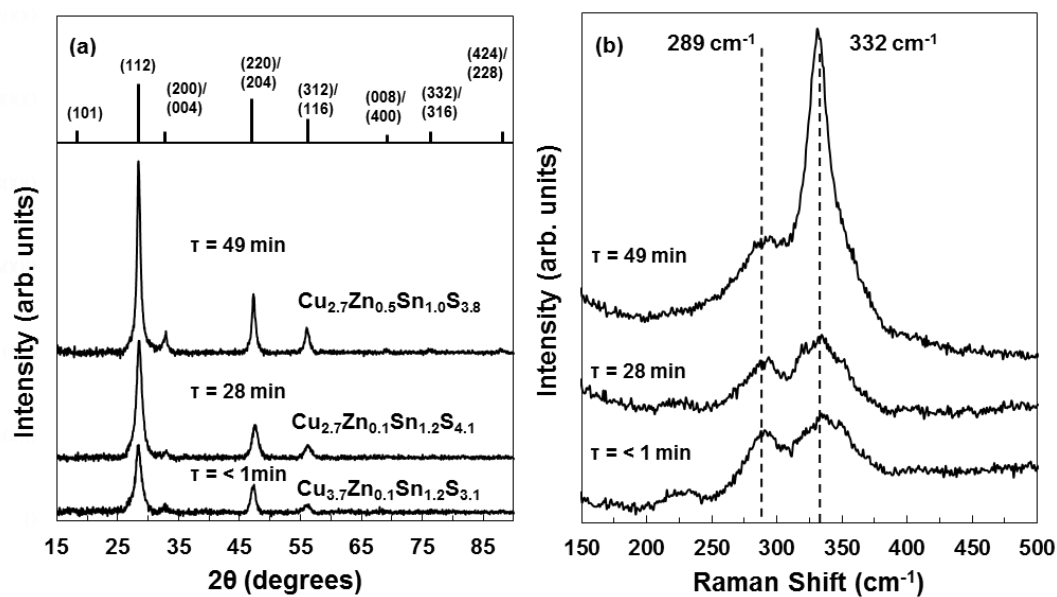


Figure 4.3 - (a) XRD and (b) Raman spectra for CZTS nanoparticles synthesized for different residence times. The composition, as determined by EDS, is also shown.

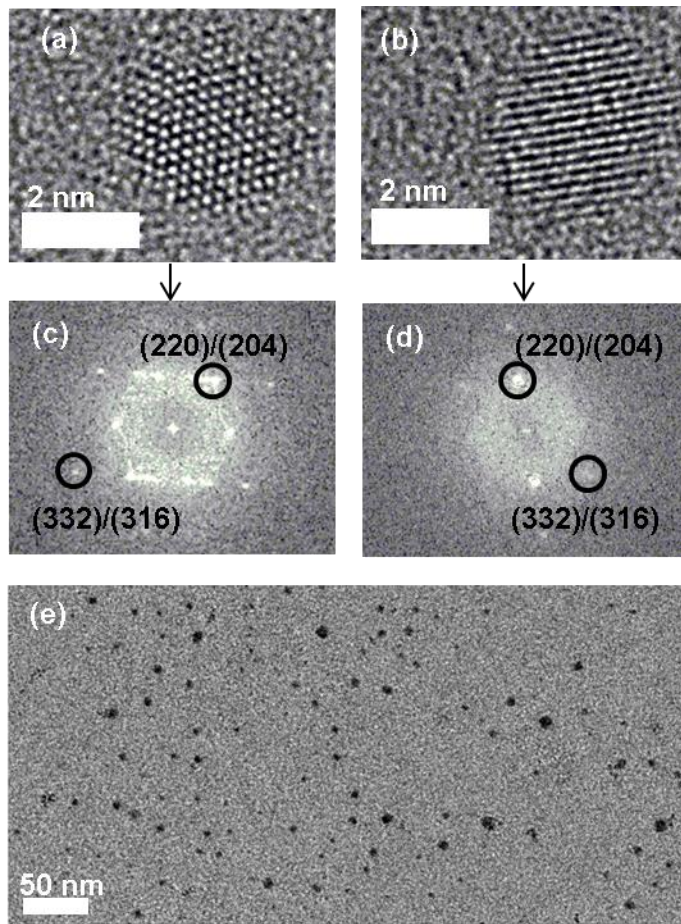


Figure 4.4 - TEM analysis shows that the CZTS nanoparticles were both (a,c) multicrystalline and (b,d) single crystalline with an (e) average size of 5.4 nm.

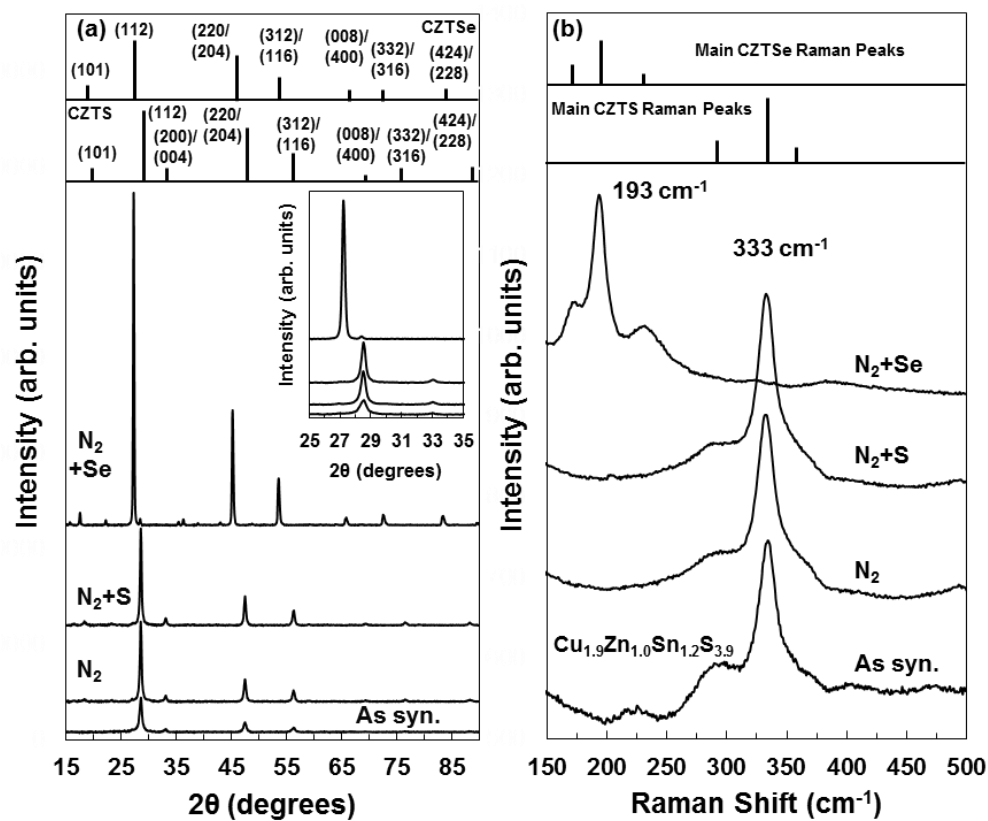


Figure 4.5 - (a) XRD and (b) Raman spectra of CZTS nanoparticles, $Cu_{1.9}Zn_{1.0}Sn_{1.2}S_{3.9}$, after annealing in N_2 , N_2+S , and N_2+Se .

CHAPTER 5

IN SITU CHARACTERIZATION OF AQUEOUS-BASED HAFNIUM
OXIDE HYDROXIDE SULFATE THIN FILMS

Brendan T. Flynn,¹ Daeho Kim,² Benjamin L. Clark,³ Alan Telecky,⁴ Líney
Árnadóttir,¹ Janos Szanyi,² Douglas A. Keszler⁴ and Gregory S. Herman^{1*}

¹Oregon State University, School of Chemical, Biological and Environmental
Engineering, 102 Gleeson Hall, Corvallis, OR 97331–2702, USA.

²Pacific Northwest National Laboratory, Chemical and Materials Sciences
Division, Richland, WA, USA

³Inpria Corporation, 2001 NW Monroe Ave, Corvallis, OR 97330, USA

⁴Oregon State University, Department of Chemistry, 153 Gilbert Hall,
Corvallis, OR 97331-4003, USA

*Corresponding Author

Reproduced in part from *Surf. Interface Anal.*, vol. 46, pp. 210-214, 2013.

Abstract

The dehydration of hafnium oxide hydroxide sulfate thin films was studied using temperature programmed desorption (TPD) and X-ray photoelectron spectroscopy. Films were found to desorb water up to 750 K with a maximum desorption rate at ~480 K. Carbon dioxide desorption was also observed in TPD measurements, which was related to contamination of precursor solutions and/or films by CO₂ from the atmosphere. The O 1s spectra obtained for in-situ annealed samples were fit with three components corresponding to Hf-O, hydroxyl groups, and sulfate groups. Water TPD measurements from the dehydrated surface indicate the presence of two desorption states corresponding to molecularly and dissociatively adsorbed water.

Introduction

Hafnium oxide hydroxide sulfate, $(\text{HfO})_{1-x-z/2}(\text{OH})_z(\text{SO}_4)_x$ (HafSOx), has recently been shown to be a high-performance dielectric in thin-film transistors[1–3] and to function as a high-sensitivity, high-resolution inorganic resist[4,5] under both electron and photon irradiation. HafSOx films can be deposited using aqueous based chemistries without the use of bulky organic ligands. This approach allows rapid, facile condensation with minimal volume change, leading to the formation of films exhibiting densities exceeding those realized via conventional metal-organic sol–gel methods[1,2]. Instead of organic additives, HafSOx precursor solutions are stabilized by inorganic species, e.g. halide and sulfato ligands, which limit crystallization and inhibit condensation. Dehydration, condensation, and densification of the films are initiated at quite modest temperatures of ~ 353 K[1]. Homogeneous, nonporous, and atomically smooth Hf-containing films (< 10 nm thick) have been formed by spin-coating the precursors and annealing across the temperature range of $353 - 1273$ K[1].

HafSOx also belongs to a group of sulfated early transition metal acidic oxides that are well known for their high catalytic activity[6–11]. Sulfated zirconia, an isoelectronic analog of HafSOx, exhibits exceptional activity in the isomerization of n-alkanes[6,12]. The roles of surface acidity, metal oxide composition, and method of preparation in controlling the acid-catalyzed reaction mechanisms of the isomerization processes are still under

investigation[13,14]. It has been proposed that the application of surface-science techniques to investigate the adsorption-desorption properties from model thin-film systems will provide additional insights on catalytic mechanisms and material properties for these complex systems[15,16].

The diverse applications and promising potential of HfSO_x thin films warrant further investigation into both the dehydration processes of the films and the corresponding surface chemistry. In this study we have characterized HfSO_x thin films with temperature programmed desorption (TPD) and in-situ X-ray photoelectron spectroscopy (XPS). The TPD measurements were performed to monitor dehydration and to probe the desorption properties of D_2O from dehydrated HfSO_x films, while XPS was used to monitor changes in the surface chemistry associated with dehydration and chemical desorption.

Experimental Methods

An aqueous HfSO_x solution was prepared by forming two dilute precursor solutions that were mixed just prior to spin-coating, as described previously[1]. In brief, the first precursor solution was formed by dissolving HfOCl_2 in deionized water while the second precursor solution was formed by diluting H_2SO_4 with deionized water. These two solutions were combined so that the aqueous HfSO_x solution had a metal-cation concentration of ~ 0.15 M with $\sim 70\%$ sulfate relative to the metal concentration. This solution was

spin-coated on an oxidized silicon coupon at 2000 rpm for 45 s, followed by heating on a hotplate at 353 K for three min. Only one spin-coating cycle was used, yielding a film thickness of ~25 nm as determined by spectroscopic ellipsometry.

TPD and XPS were performed in an ultrahigh vacuum (UHV) system described in detail elsewhere[17]. The samples were mounted to a molybdenum backing plate, which was directly connected to a liquid nitrogen reservoir using high purity tantalum leads. For the TPD experiments, the tantalum leads and backing plate were resistively heated leading to an increase in sample temperature, which was monitored using a type-C thermocouple that was attached to the front surface of the sample using a ceramic adhesive. A linear heating rate of ~10 K/s was used to heat the sample to ~750 K and up to ten mass charge ratios (m/e) were monitored using a quadrupole mass spectrometer. After heating to 750 K, the dehydrated samples were then cooled with liquid nitrogen and exposed to D₂O for a given length of time with an uncalibrated directional doser. Typical exposures used in this study resulted in multilayer desorption of D₂O at ~160 K, suggesting saturation of the surface with water[17]. For the XPS studies, nonmonochromatized Al K α radiation was used and all spectra were obtained with a 45° electron emission angle. An analyzer pass energy of 25 eV was used for the high-resolution XPS data. For *in-situ* annealing the HafSO_x films were heated in UHV by resistive heating and then cooled to room

temperature (RT) prior to XPS acquisition. Since the HafSOx films are insulating, charge compensation was accomplished by referencing all the spectra to the Hf 4f_{7/2} peak at 17.1 eV[18]. It should be noted that a wide range of Hf 4f_{7/2} binding energies have been reported for HfO₂ likely due to complications related to sample charging, and we will discuss these challenges in more detail below[19-22]. XPSPEAK4.1[23] software was used for peak fitting, and the procedure used for this analysis was kept consistent for all of the sample conditions. In brief, a Shirley background was used and the relative area, full width at half maximum (FWHM), %Lorentzian – Gaussian (%L-G) ratios, and peak positions were allowed to vary. The number of peaks for fitting was manually varied and the fewest number of peaks that gave a reasonable fit were used for the analysis.

Results and Discussion

TPD data for HafSOx films that were heated to 353 K prior to introduction into the UHV system are illustrated in Fig. 5.1. As expected, there is a significant water desorption signal during the sample temperature ramp during the TPD scan. The water desorption feature (m/e = 18) exhibits a rapid onset at 370 K, reaches a maximum desorption rate at ~480 K, and then returns to the initial water partial pressure at ~680 K. A broad desorption feature is not entirely unexpected, since there is likely to be a broad range of energies associated with aqua and hydroxo ligand binding, and the broad

range of depths from which the water needs to diffuse through the film to the surface prior to desorption[24]. TGA analysis of HfSO_x powders has indicated that there is significant weight loss in three domains corresponding to desorption of loosely bound water ($< 473 \text{ K}$), desorption of water through the reaction of hydroxyl species (473 to 973 K), and the decomposition of sulfate ($>973 \text{ K}$)[1]. This TGA analysis corresponds well with the broad desorption peak observed in the TPD. The only other main desorption species observed for temperatures below 750 K was for CO_2 ($m/e = 44$), cf. Fig. 5.1. The assignment of the $m/e = 44$ desorption features to CO_2 versus N_2O was confirmed by comparison with the C ($m/e = 12$) and N ($m/e = 14$) data, where the C ($m/e = 12$) data matched the CO_2 desorption features while N ($m/e = 14$) data did not. As noted above, no carbon-containing species were intentionally introduced into the precursors during preparation. We suspect that the precursor solutions or the thin films prior to the TPD experiments are adsorbing $\text{CO}_2(\text{g})$ from the ambient atmosphere. For example, it has been shown that CO_2 from the atmosphere readily reacts with hafnium oxide films resulting in the formation of carbonate species[25]. The CO_2 TPD spectra have two main desorption features, a low temperature feature at 430 K and a high temperature feature at 600 K . These two different desorption states are likely related to weakly bound carbonic acid species and a more strongly bound metal-carbonate species, respectively. This assignment is based on the observation that the low temperature CO_2

desorption begins at the same temperature as the water desorption, while the high temperature CO₂ desorption occurs in the same temperature regime as nanostructured oxide surfaces[26] and solution deposited oxide films[27]. Finally, no evidence for the desorption of sulfate or chlorine was observed from the films for TPD measurements up to 750 K.

High-resolution XPS Hf 4f, S 2p, and O 1s data from the HafSO_x films for several different in-situ annealing temperatures are summarized in Fig. 5.2 (a-c). In these measurements, the HafSO_x films were annealed in UHV at temperatures between 298 and 1000 K. For clarity, only a limited set of data is shown in Fig. 5.2 (a-c). In all cases, survey scans from the HafSO_x films indicated that carbon was the main impurity. The solid lines in Fig. 5.2 correspond to the experimental data, while the dashed lines correspond to peak fitting of the different core level spectra. The spectra have been offset in intensity for clarity. The sharpest and most intense Hf 4f and O 1s core levels from the HafSO_x films were obtained for films annealed to 1000 K (as shown in the upper portion of the figures). These high-temperature data were used to define the initial fitting parameters for the core levels. After the 1000 K anneal, sulfur was no longer present on the surface and therefore the 750 K annealed data were used to define the initial fitting parameters for the S 2p spectra.

The Hf 4f spectra were fit with a spin-orbit-split doublet (1.65 eV)[19]. To obtain a good fit for the Hf 4f spectra, it was necessary to increase the

FWHM from 1.47 eV for the 1000 K spectra to 1.65 eV for the RT spectra, and to 1.85 eV for the intermediate temperature spectra. The need for the increased FWHM can be seen in Fig. 5.2(a), where the splitting between the spin-orbit-split doublets was less well defined for intermediate temperatures. Using a second spin-orbit-split doublet shifted from the first to account for potentially different oxidation states of hafnium did not provide an adequate fit to the Hf 4f spectra given the relative large shifts to lower binding energies for the sub-oxide (2.75 eV) and metallic (3.94 eV) components[19]. An early study on the oxidation of hafnium metal indicated that there was a 0.2 eV shift to higher binding energy for the Hf 4f spectra when samples were oxidized at elevated temperatures compared to RT[20], while a later study found that hafnium oxide films deposited with different HfO_x stoichiometries gave a 0.6 eV shift to lower binding energy for the Hf 4f spectra when samples had stoichiometric ($x = 2.09$) versus hyperstoichiometric ($x = 2.24$) compositions[22]. Although it was possible to fit the Hf 4f spectra with two doublets shifted by 0.6-0.9 eV from one another, this procedure did not result in a unique fit of the experimental data. Based on our fitting of the O 1s data, to be discussed below, it may actually be necessary to fit the Hf 4f spectra with three doublets due to the different electronegativities of the species bound to hafnium. Unique fits to the experimental data will be even more difficult in this case. We have therefore accounted for inhomogeneity of the Hf species by increasing the FWHM of the Hf 4f doublet, as the film was

dehydrated. The S 2p spectra were fit with a spin-orbit-split doublet (1.2 eV)[28,29] and a constant FWHM (1.85 eV) for all annealing conditions. The main change in the S 2p spectra was a shift to slightly higher binding energy from 168.4 eV at RT to 168.9 eV at 750 K. In all cases, these values are consistent with sulfate species and not a conversion to sulfite or other sulfur oxidation state upon annealing[8,16,30,31].

The O 1s spectra are the most complex from these samples and several different methods were examined to fit the data. Initially, we focused on fitting the O 1s spectra for the 1000 K data since it was dominated by a single peak with no contribution from the sulfate groups, which desorb from the film below this temperature. We found that there was a main component located at 530.5 eV, which we assign to oxygen bound to hafnium (Hf-O), and a higher binding energy shoulder located at 531.9 eV, which we assign to oxygen from surface hydroxyl groups. These assignments are consistent with O 1s spectra obtained from HfO₂ films deposited by atomic layer deposition[32], electron beam evaporation[33], and sol-gel chemistries[24]. Studies on other metal oxides have also suggested that this higher energy peak can be assigned to defective oxide sites in the crystalline lattice. In this study we are not able to distinguish between hydroxyl groups or defective oxide sites for the higher energy shoulder. However, the relatively high increase in water partial pressures during the annealing process, due to the aqueous-based chemistries used for this study, makes our assignment to a

hydroxyl species adsorbed to the surface reasonable. As seen in Fig. 2(c), the O 1s spectra for samples annealed at 500 and 700 K appear to consist of both a low and a high binding-energy component. For these spectra, however, we have tried fitting the data by allowing a large degree of freedom in the relative binding energies, intensities, and FWHM for both components, but we were not able to obtain consistent fits to the entire series of data at different annealing temperatures. We found that it was necessary to include a third O 1s component and to increase the FWHM to 1.79 eV, compared to 1.69 eV that was determined for the 1000 K spectra, to obtain reasonable fits. To minimize the number of fitting parameters, we kept the FWHM and the binding-energy difference between the low and medium energy peaks fixed. This approach allowed us to consistently fit ten O 1s spectra for HfSO_x samples annealed to temperatures between RT to 750 K. Based on our analysis, we assign the low binding energy O 1s peak to Hf-O, the middle binding energy O 1s peak shifted by 1.5 eV to hydroxyl groups, and the high binding energy O1s peak shifted by 2.3 – 2.8 eV to sulfate groups. The peak separation between the Hf-O and Hf-OH peaks is consistent with binding energy differences in the 1 to 1.5 eV range for hydroxyl groups and oxygen bound to metal cations which have been observed previously for a variety of metal oxides[17,35,36]. The binding-energy difference between the sulfate and Hf-O peak decreased from 2.8 eV at RT to 2.3 eV at 750 K. There has been a fairly wide range of values reported in the literature for the sulfate O

1s binding energy, and with the binding-energy difference between the sulfate and metal-O peak[8,15,37]. Compared to prior studies we find good agreement for the relative binding energies for our metal-O, hydroxyl, and sulfate components when more than two components are fit to the O 1s spectra for sulfated metal oxides[37,38]. Other studies have reported a single high energy shoulder that is shifted ~ 1.5 to 1.8 eV higher binding energy than the metal-O peak, and assign this component to sulfate and hydroxyl groups[8,15]. The O 1s spectra have also been fit to three components where the sulfate component and the water component are shifted to 1.6 and 2.8 eV higher energy, respectively, compared to the metal-O peak[31]. We did not assign an O 1s component to molecular water since the binding energy difference between water and the metal-O peak is typically on the order of 3.2 - 3.5 eV, which is much larger than the values obtained from our analysis[17,35,38]. We find that our O 1s peak assignments are consistent with the TPD measurements, where the O 1s peak assigned to hydroxyls decreased as the sample was heated due to recombination of hydroxyls that desorb as water, while both the Hf-O and sulfate components increased in intensity during over the same temperature regime. The change in relative intensity of the three distinct components in the O 1s spectra versus temperature may also be correlated with the broadening observed in the Hf 4f spectra. For these studies the low- and high-temperature O 1s spectra are dominated by a single component, and it is these temperatures that we

observe the sharpest Hf 4f spectra. For intermediate temperatures, the O 1s spectra have three components, and it is at these temperatures that we observe broadening of the Hf 4f spectra. This broadening could be due to the different electronegativities of the species bound to hafnium in the intermediate temperature range. Finally, a further complication in the analysis of the O 1s spectra is that the Hf 4s has a binding energy that is very close to the O 1s (Hf-O) binding energy[39,40]. In our analysis we did not include the Hf 4s component when fitting the O 1s spectra since it has been estimated that the Hf 4s signal will only contribute ~8% of the total combined Hf 4s and O 1s signals for HfO₂[41].

The relative intensity ratios for the three fitted O 1s peak components versus annealing temperature are shown in Fig. 5.3. We find major changes in the trends of the fitted O 1s data versus temperature, where both the relative Hf-O and sulfate signals increased with increasing annealing temperature, while the relative hydroxyl signal decreased with increasing annealing temperature. Based on the TPD results shown in Fig. 5.1, we would expect that the hydroxyl signal would be reduced for this annealing temperature range due to their recombination and desorption as water. A similar reduction in the hydroxyl signal relative to the Hf-O signal was observed during annealing of HfO₂ films formed by sol-gel based chemistries[24]. We also find minor changes in the trends of the fitted O 1s data versus annealing temperature, where the rate of increase for the Hf-O

and the sulfate signals are slightly different. For example, the Hf-O relative intensity is initially larger than the sulfate relative intensity; however, after annealing, the sulfate relative intensity is higher than the Hf-O signal. If this high binding-energy feature were primarily associated with water, then it would be expected that the relative intensity would decrease as opposed to increase in this temperature range. It is also unlikely that surface segregation of sulfate causes this relative increase in the sulfate component of the O 1s spectra since we find that the S 2p/Hf 4f intensity ratio is unchanged over the same temperature range. Based on these observations, we, therefore, conclude that the high binding-energy feature in the O 1s spectra is primarily associated with sulfate groups, and the minor changes in relative intensities shown in Fig. 5.3 may be related to the challenges in uniquely fitting the broad O 1s spectra.

The surface acid properties of sulfated metal oxides are known to drive a wide range of catalytic reactions[6-12]. In this study, we have characterized the surface chemistry of dehydrated HfSO_x surface by performing D_2O TPD experiments. Fig. 5.4(a) shows a schematic of a HfSO_x surface where the Brønsted acid sites are transformed to Lewis acid sites upon desorption of water. Three different Brønsted acid sites are shown, representing water bound to metal-cation sites at the surface, protons bound to the sulfate groups, and terminal hydroxyls bound to metal cations. The direct desorption of water from Brønsted acid sites (I) or the desorption of water through the

recombination of a proton at Brønsted acid sites (II) and terminal hydroxyl at Brønsted acid sites (III) both lead to the formation of Lewis acid sites on the HafSO_x surface. It has been proposed that the presence of both Brønsted acid and Lewis acid sites are a necessary condition for the acid-catalyzed isomerization of butane[42]. To investigate these different adsorption sites, we exposed the dehydrated HafSO_x surface to D_2O for several different time intervals with the sample held below ~ 200 K. TPD spectra for two different D_2O ($m/e = 20$) exposures from the dehydrated HafSO_x surface are shown in Fig. 5.4(b). Two main desorption peaks are observed – a well-defined sharp peak at 285 K and a second much broader peak at 500 K. The desorption temperature for the low-temperature feature is consistent with previous studies of molecular water adsorbed to metal-cation sites on oxide surfaces[43-45]. The water desorption features at temperatures above RT can often be related to dissociated water on zirconia surfaces[46,47] or defective sites at oxide surfaces[43,44], while the broad desorption features may also be related to the inhomogeneous nature of the surface where a broad distribution of adsorption states likely exist[43,44,48]. The two desorption peaks in TPD spectra, therefore, suggest both molecular and dissociative adsorption of water on the dehydrated surface at low temperature. These results indicate that direct control over both Brønsted acid and Lewis acid sites are possible through optimization of both water exposures to the dehydrated films and post-exposure annealing

temperatures. Controlling the relative ratio of these acid sites may allow opportunities to better understand their role for acid catalyzed reactions on sulfated metal oxide surfaces.

Conclusion

By using TPD and XPS methods, we have found that solution deposited HafSO_x films undergo complex dehydration chemistries. TPD measurements reveal a broad water desorption peak indicative of a variety of adsorption states. The films were also found to be contaminated with carbonate, where desorption of CO₂(g) occurs at two different temperatures which can be related to differences in chemical coordination in the HafSO_x films. XPS analysis indicates that there are three features associated with the O 1s spectra, which were correlated with Hf-O, hydroxyl groups, and sulfate groups present in the HafSO_x films. Finally, results of D₂O TPD experiments from dehydrated films are consistent with both molecular and dissociative adsorption of water at low temperatures. The underlying mechanism can be related to the transition from Brønsted acid sites (when water is adsorbed) to Lewis acid sites (when water desorbs).

Acknowledgements

This material is based upon work supported by the National Science Foundation under Grant No. CHE-1102637. Support has also been provided

by Oregon State University and the Oregon Nanoscience and Microtechnologies Institute. A portion of the research was performed using Environmental Molecular Sciences Laboratory, a national scientific user facility sponsored by the Department of Energy's Office of Biological and Environmental Research and located at Pacific Northwest National Laboratory. BLC and DAK have a financial interest in Inpria Corp.

References:

- [1] J. T. Anderson, C. L. Munsee, C. M. Hung, T. M. Phung, G. S. Herman, D. C. Johnson, J. F. Wager, and D. A. Keszler, "Solution-Processed HafSO_x and ZircSO_x Inorganic Thin-Film Dielectrics and Nanolaminates," *Adv. Funct. Mater.*, vol. 17, pp. 2117-2124, 2007.
- [2] D. A. Keszler, J. T. Anderson, and S. T. Meyers, in *Solution Processing of Inorganic Materials* (Ed: D. B. Mitzi), Hoboken, NJ, USA: John Wiley & Sons, 2009.
- [3] M. Alemayehu, J. E. Davis, M. Jackson, B. Lessig, L. Smith, J. D. Sumega, C. Knutson, M. Beekman, D. C. Johnson, and D. A. Keszler, "Tunable dielectric thin films by aqueous, inorganic solution-based processing," *Solid State Sci.*, vol. 13, pp. 2037-2040, 2011.
- [4] J. Stowers and D. A. Keszler, "High resolution, high sensitivity inorganic resists," *Microelectron Eng.*, vol. 86, pp. 730-733, 2009.
- [5] A. Telecky, P. Xie, J. Stowers, A. Grenville, B. Smith, and D. A. Keszler, "Photopatternable inorganic hardmask," *J. Vac. Sci. Technol. B*, vol. 28, pp. C6S19-C6S22, 2010.
- [6] M. Hino, S. Kobayashi, and K. Arata, "Reactions of Butane and Isobutane Catalyzed by Zirconium Oxide Treated with Sulfate Ion. Solid Superacid Catalyst," *J. Am. Chem. Soc.*, vol. 101, pp. 6439-6441, 1979.

- [7] M. Hino and K. Arata, "Synthesis of solid superacid catalyst with acid strength of $H_0 \leq -16.04$," *J. Chem. Soc., Chem. Commun.*, vol. 18, pp. 851-852, 1980.
- [8] M. Hino, M. Kurashige, H. Matsushashi, and K. Arata, "The surface structure of sulfated zirconia: Studies of XPS and thermal analysis," *Thermochim. Acta*, vol. 441, pp. 35-41, 2006.
- [9] Y. Wang, K.-Y. Lee, S. Choi, J. Liu, L.-Q. Wang, and C. H. F. Peden, "Grafting sulfated zirconia on mesoporous silica," *Green Chem.*, vol. 9, pp. 540-544, 2007.
- [10] D. H. Kim, J. Szanyi, J. H. Kwak, X. Q. Wang, J. C. Hansen, M. Engelhard, and C. H. F. Peden, "Effects of Sulfation Level on the Desulfation Behavior of Presulfated Pt-BaO/Al₂O₃ Lean NO_x Trap Catalysts: A Combined H₂ Temperature-Programmed Reaction, in Situ Sulfur K-Edge X-ray Absorption Near-Edge Spectroscopy, X-ray Photoelectron Spectroscopy, and Time-Resolved X-ray Diffraction Study," *J. Phys. Chem. C*, vol. 113, pp. 7336-7341, 2009.
- [11] E. J. Eterigho, J. G. M. Lee, and A. P. Harvey, "Triglyceride cracking for biofuel production using a directly synthesised sulphated zirconia catalyst," *Bioresource Technol.*, vol. 102, pp. 6313-6316, 2011.
- [12] C. Breitkopf, "An Integrated Catalytic and Transient Study of Sulfated Zirconias: Investigation of the Reaction Mechanism and the Role of Acidic Sites in n-Butane Isomerization," *ChemCatChem*, vol. 1, pp. 259-269, 2009.
- [13] L. K. Noda, N. S. Gonçalves, S. M. de Borba, and J. A. Silveira, "Raman spectroscopy and thermal analysis of sulfated ZrO₂ prepared by two synthesis routes," *Vib. Spectrosc.*, vol. 44, pp. 101-107, 2007.
- [14] B. Azambre, L. Zenboury, J. V. Weber, and P. Burg, "Surface characterization of acidic ceria-zirconia prepared by direct sulfation," *Appl. Surf. Sci.*, vol. 256, pp. 4570-4581, 2010.
- [15] C. Breitkopf, H. Papp, X. Li, R. Olindo, J. A. Lercher, R. Lloyd, S. Wrabec, F. C. Jentoft, K. Meinel, S. Förster, K.-M. Schindler, H. Neddermeyer, W. Widdra, A. Hofmann, and J. Sauer, "Activation and isomerization of n-butane on sulfated zirconia model systems—an integrated study across the materials and pressure gaps," *Phys. Chem. Chem. Phys.*, vol. 9, pp. 3600-3618, 2007.

- [16] R. Lloyd, T. W. Hansen, W. Ranke, F. C. Jentoft, and R. Schlögl, "Adsorption-desorption equilibrium investigations of n-butane on nanocrystalline sulfated zirconia thin films *Appl. Catal. A-Gen.*, vol. 391, pp. 215-224, 2011.
- [17] G. S. Herman, Y. J. Kim, S. A. Chambers, and C. H. F. Peden, "Interaction of D₂O with CeO₂(001) Investigated by Temperature-Programmed Desorption and X-ray Photoelectron Spectroscopy," *Langmuir*, vol. 15, pp. 3993-3997, 1999.
- [18] M. Engelhard, J. Herman, R. Wallace, and D. Baer, "As-Received, Ozone cleaned, and Ar⁺ Sputtered Surfaces of Hafnium Oxide Grown by Atomic Layer Deposition and Studied by XPS," *Surf. Sci. Spectra*, vol. 18, pp. 46-57 2011.
- [19] S. Suzer, S. Sayan, M. M. Banaszak Holl, E. Garfunkel, Z. Hussain, and N. M. Hamdan, "Soft x-ray photoemission studies of Hf oxidation," *J. Vac. Sci. Technol. A*, vol. 21, pp. 106-109, 2003.
- [20] C. Morant, L. Galán, and J. M. Sanz, "An XPS Study of the Initial Stages of Oxidation of Hafnium," *Surf. Interface Anal.*, vol. 16, pp. 304-308, 1990.
- [21] R. L. Miller, S. H. McKinney, and A. R. Chourasia, "Core Level XPS of Elemental Hafnium and Hafnium Dioxide," *Surf. Sci. Spectra*, vol. 15, pp. 59-69, 2008.
- [22] J. P. Lehan, Y. Mao, B. G. Bovard, and H. A. Macleod, "Optical and Microstructural Properties of Hafnium Dioxide Thin Films," *Thin Solid Films*, vol. 250, pp. 227-250, 1991.
- [23] Freeware available at <http://www.phy.cuhk.edu.hk/~surface>
- [24] H. Shimizu, T. Sato, S. Konagali, M. Ikeda, T. Takahashi, and T. Nishide, "Temperature-Programmed Desorption Analyses of Sol-Gel Deposited and Crystallized HfO₂ Films," *Jpn. J. Appl. Phys.*, vol. 46, pp. 4209-4214, 2007.
- [25] T. Gougousi, D. Niu, R. W. Ashcraft, and G. N. Parsons, "Carbonate formation during post-deposition ambient exposure of high-k dielectrics," *Appl. Phys. Lett.* vol. 83, 3543-3545, 2003.

- [26] J. D. Baniecki, M. Ishii, K. Kurihara, K. Yamanaka, T. Yano, K. Shinozaki, T. Imada, Y. Kobayashi, "Chemisorption of water and carbon dioxide on nanostructured BaTiO₃–SrTiO₃(001) surfaces," *J. Appl. Phys.*, vol. 106, pp. 054109, 2009.
- [27] S. Aukkaravittayapun, C. Thanachayanont, T. Theapsiri, W. Veerasai, Y. Sawada, T. Kondo, S. Tokiwa, T. Nishide, "Temperature Programmed Desorption of F-Doped SnO₂ Films Deposited by Inverted Pyrosol Technique," *J. Therm. Anal. Calorim.*, vol. 85, pp. 811-815, 2006.
- [28] D. G. Castner, K. Hinds, and D. W. Grainger, "X-ray Photoelectron Spectroscopy Sulfur 2p Study of Organic Thiol and Disulfide Binding Interactions with Gold Surfaces," *Langmuir*, vol. 12, pp. 5083-5086, 1996.
- [29] T. M. Willey, A. L. Vance, T. van Buuren, C. Bostedt, L. J. Terminello, and C. S. Fadley, "Rapid Degradation of Alkanethiol-Based Self-Assembled Monolayers on Gold in Ambient Laboratory Conditions," *Surf. Sci.* vol. 576, pp. 188-196, 2005.
- [30] A. F. Lee, K. Wilson, A. Goldoni, R. Larciprete, and S. Lizzit, "A fast XPS study of sulphate promoted propene decomposition over Pt{111}," *Surf. Sci.*, vol. 513, pp. 140-148, 2002.
- [31] K. Ebitani, H. Konno, T. Tanka, and H. Hattori, "*In-situ* XPS Study of Zirconium Oxide Promoted by Platinum and Sulfate Ion," *J. Catal.*, vol. 135, pp. 60-67, 1992.
- [32] D. Barreca, A. Milanov, R. A. Fischer, A. Devi, and E. Tondello, "Hafnium oxide thin film grown by ALD: An XPS study," *Surf. Sci. Spectra* , vol. 14, pp. 34-40, 2007.
- [33] M. F. Al-Kuhaili, S. M. A. Durrani, and E. E. Khawaja, "Characterization of hafnium oxide thin films prepared by electron beam evaporation," *J. Phys. D. Appl. Phys.*, vol. 37, pp. 1254-1261, 2004.
- [34] J. C. C. Fan and J. B. Goodenough, "X-ray photoemission spectroscopy studies of Sn-doped indium-oxide films," *J. Appl. Phys.*, vol. 48, pp. 3524-3531, 1977.
- [35] S. Yamamoto, T. Kendelewicz, J. T. Newberg, G. Ketteler, D. E. Starr, E. R. Mysak, K. J. Andersson, H. Ogasawara, H. Bluhm, M. Salmeron,

- G. E. Brown, and A. Nilsson, "Water Adsorption on $\alpha\text{-Fe}_2\text{O}_3(0001)$ at near Ambient Conditions," *J. Phys. Chem. C*, vol. 114, pp. 2256-2266, 2010.
- [36] L. E. Walle, A. Borg, E. M. J. Johansson, S. Plogmaker, H. Rensmo, P. Uvdal, and A. Sandell, "Mixed Dissociative and Molecular Water Adsorption on Anatase $\text{TiO}_2(101)$," *J. Phys. Chem. C*, vol. 115, pp. 9545-9550, 2011.
- [37] S. Ardizzone, C. L. Bianchi, M. Signoretto, "Zr(IV) surface chemical state and acid features of sulphated-zirconia samples," *Appl. Surf. Sci.*, vol. 136, pp. 213-220, 1998.
- [38] Y. Liang, P. M. A. Sherwood, D. K. Paul, "Valence and Core Photoemission of the Films formed Electrochemically on Nickel in Sulfuric Acid," *J. Chem. Soc. Faraday Trans.*, vol. 90, pp. 1271-1278, 1994.
- [39] R. Nyholm, A. Berndtsson, and N. Mårtensson, "Core level binding energies for the elements Hf to Bi ($Z = 72-83$)," *J. Phys. C. Solid St. Phys.*, vol. 13, pp. L1091-L1096, 1980.
- [40] C. L. Perkins, R. Singh, M. Trenary, T. Tanaka, and Y. Paderno, "Surface properties of Hafnium diboride(0001) as determined by X-ray photoelectron spectroscopy and scanning tunneling microscopy," *Surf. Sci.*, vol. 470, pp. 215-225, 2001.
- [41] Z. J. Yan, R. Xu, Y. Y. Wang, S. Chen, Y. L. Fan, and Z. M. Jiang, "Thin HfO_2 films grown on Si(100) by atomic oxygen assisted molecular beam epitaxy," *Appl. Phys. Lett.*, vol. 85, pp. 85-87, 2004.
- [42] D. Spielbauer, G. A. H. Mekhemer, M. I. Zaki, and K. Knözinger, "Acidity of sulfated zirconia as studied by FTIR spectroscopy of adsorbed CO and NH_3 as probe molecules," *Catal. Lett.*, vol. 40, pp. 71-79, 1996.
- [43] M. A. Henderson, "Structural sensitivity in the dissociation of water on TiO_2 single-crystal surfaces," *Langmuir*, vol. 12, pp. 5093-5098, 1996.
- [44] M. A. Henderson, "The interaction of water with solid surfaces: fundamental aspects revisited," *Surf. Sci. Rep.*, vol. 46, pp. 1-308, 2002.

- [45] G. S. Herman, Z. Dohnálek, N. Ruzycki, and U. Diebold, "Experimental Investigation of the Interaction of Water and Methanol with Anatase- TiO_2 (101)," *J. Phys. Chem. B*, vol. 107, pp. 2788-2795, 2003.
- [46] A. Hofmann and J. Sauer, "Surface Structure of Hydroxylated and Sulfated Zirconia. A Periodic Density-Functional Study," *J. Phys. Chem. B*, vol. 108, pp. 14652-14662, 2004.
- [47] A. Gorski, V. Yurkiv, D. Starukhin, and H. -R. Volpp, " H_2O chemisorption and H_2 oxidation on yttria-stabilized zirconia: Density functional theory and temperature-programmed desorption studies," *J. Power Sources*, vol. 196, pp. 7188-7194, 2011.
- [48] C. -W. Yi and J. Szanyi, " D_2O Adsorption on an Ultrathin Alumina Film on $\text{NiAl}(110)$," *J. Phys. Chem. C*, vol. 111, pp. 17597-17602, 2007.

Figures

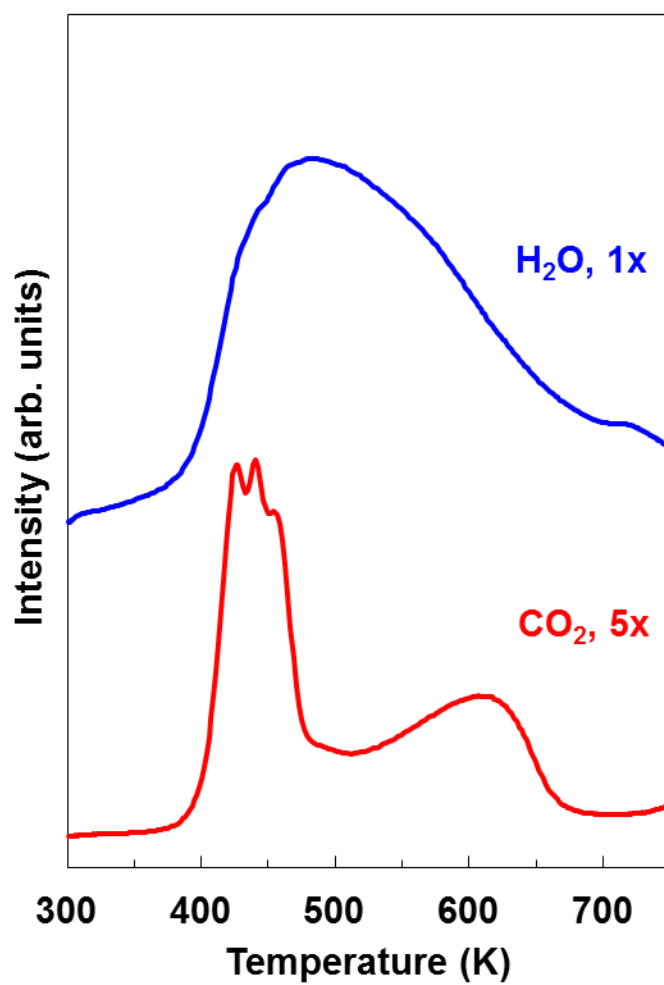


Figure 5.1 – Temperature programmed desorption spectra from spin-coated HafSOx films after a 353 K anneal.

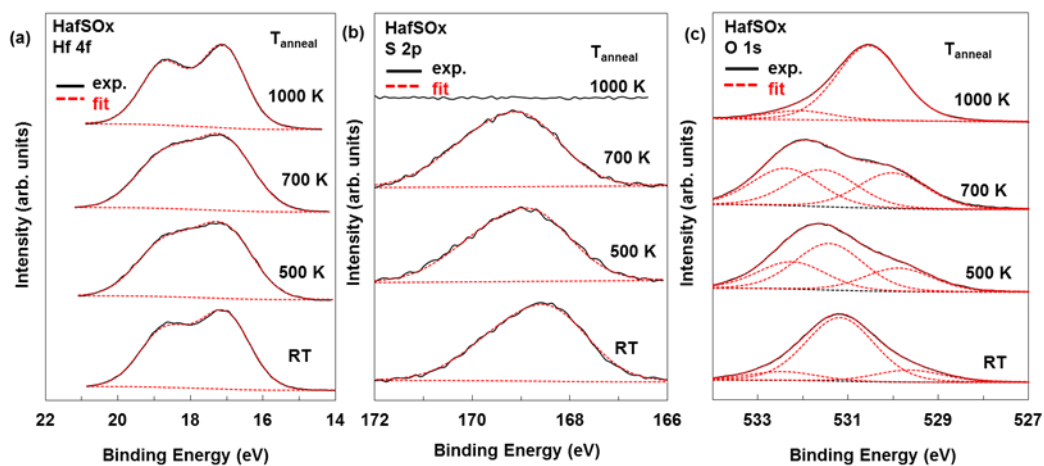


Figure 5.2 - High-resolution XPS from HafSOx films annealed to the indicated temperatures. (a) Hf 4f; (b) S 2p; and (c) O 1s. The raw data are shown as solid lines while the fits to the data are shown as dashed lines.

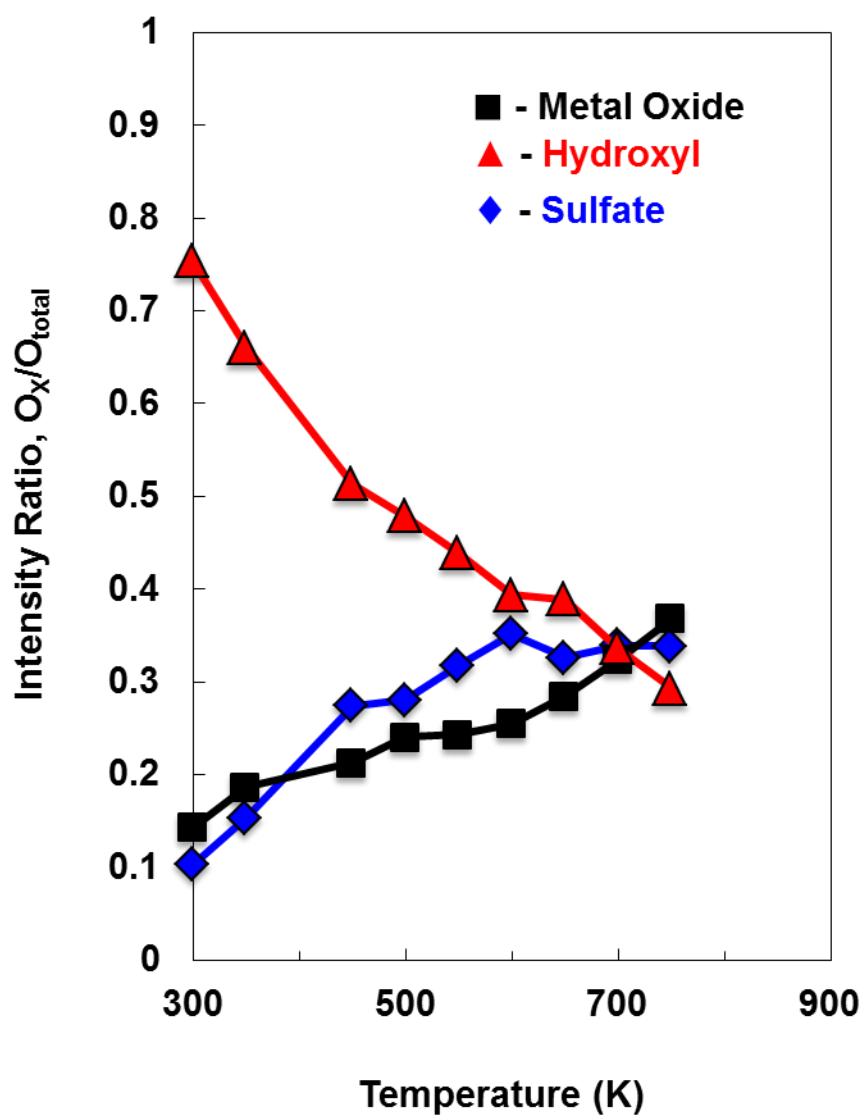


Figure 5.3 - Relative intensity ratios of the three fitted O 1s peak components versus annealing temperature from Fig. 5.2(c). The square markers(■) correspond to the Hf-O component, the triangle markers(▲) correspond to hydroxyls, and the diamond markers(◆) correspond to sulfate.

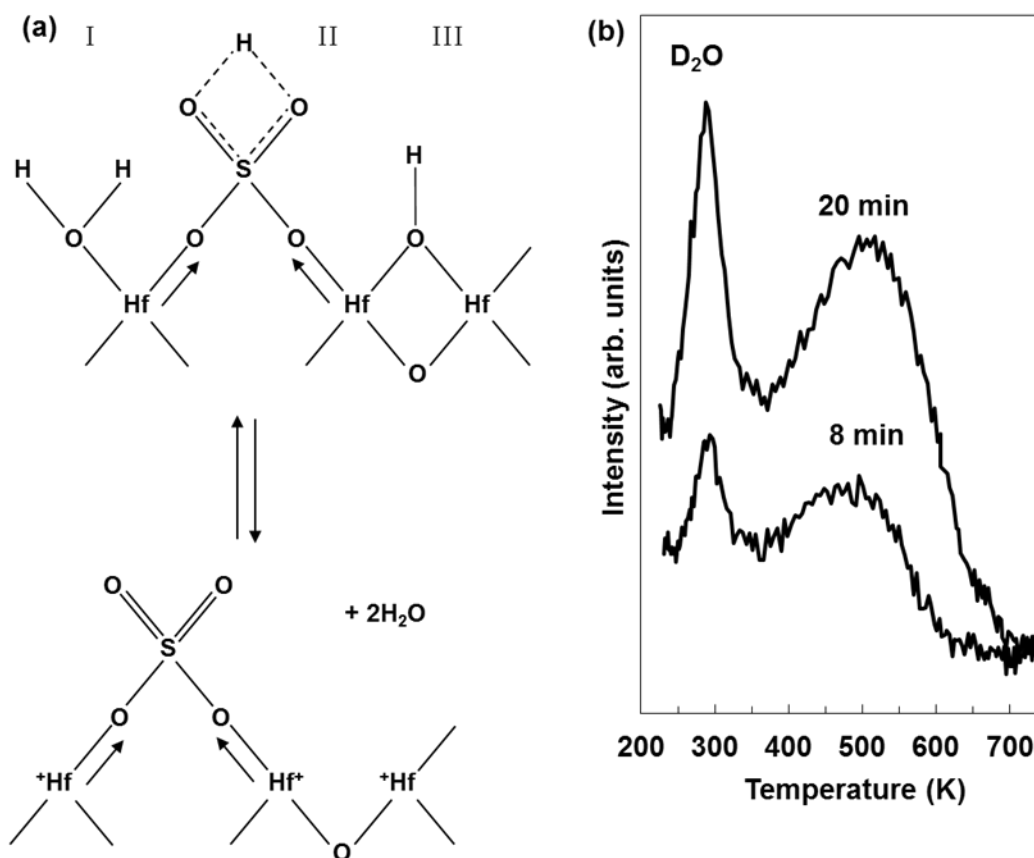


Figure 5.4 – (a) Schematic of different types of Brønsted acid sites on HafSO_x and their transformation to Lewis acid sites upon desorption of water, adapted from reference [14]. (b) TPD data for dehydrated HafSO_x films and two different D_2O exposures.

CHAPTER 6

THERMAL AND ELECTRON BEAM MODIFICATION OF HfSO_x
INORGANIC RESISTSBrendan T. Flynn¹ and Gregory S. Herman^{1*}¹Oregon State University, School of Chemical, Biological and Environmental
Engineering, Corvallis, OR USA

*Corresponding Author

Abstract

The inorganic resist $\text{Hf}(\text{OH})_{4-2x-2y}(\text{O}_2)_x(\text{SO}_4)_y \cdot q\text{H}_2\text{O}$ (HafSOx) was characterized by x-ray photoelectron spectroscopy (XPS), temperature programmed desorption (TPD), and electron-stimulated desorption (ESD) to provide insight into the chemical nature of the material and the mechanisms related to its use in nanoscale lithography. XPS composition analysis of the surface of the films revealed they were sulfate rich. The thermal desorption energy of O_2 was determined to be 1.3 eV. This is 1.5 eV lower than expected by calculations and experiments from similar systems. O_2 desorbed from HafSOx films containing peroxide using TPD and ESD but not from those without peroxide. These data support the hypothesis that peroxide ligands control the patternability of the material. The primary electron energy O_2 desorption dependence was studied and total desorption cross sections were calculated for O_2 from 500-2000 eV, ranging from 10^{-15} – 10^{-16} cm^2 .

Introduction

Sustained advances in the performance of electronics have been driven in part by the miniaturization of transistors on integrated circuits. Integrated circuits with transistors smaller than 20 nm are now commercially viable[1] and research into novel resists capable of helping exceed this benchmark continues. Nanoscale patterning based on extreme ultraviolet (EUV) sources or electron-beam lithography (EBL) may ultimately rely on inorganic resists as opposed to organic chemically amplified resists (CARs) due to the inherent drawbacks of CARs. Acid blur[2] and shot noise[3] limit the resolution of organic CAR resists and could restrict their use in next generation patterning technologies[4]. In contrast, the inorganic resist hydrogen silsesquioxane (HSQ) has been used to pattern 10 nm lines at 10 nm half pitch[5] and 5 nm half pitch dot arrays[6]. Despite this superior ability to pattern highly resolved dense features, HSQ suffers from relatively poor sensitivities[7, 8]. Alternative metal oxide based inorganic resists[9, 10] may offer a pathway to satisfy industry requirements for sensitivity, resolution, and line-edge roughness (LER).

One such metal oxide resist is $\text{Hf}(\text{OH})_{4-2x-2y}(\text{O}_2)_x(\text{SO}_4)_y \cdot q\text{H}_2\text{O}$, (HafSOx)[11]. Peroxide-free HafSOx has been characterized in the context of high- κ dielectrics[11], nanolaminates[11, 12], and catalytic[13] applications, but more numerous studies exist concerning the peroxide-containing version and its use as a lithographic resist[8, 10, 14-20]. Addition of peroxide

prevents condensation in the as-deposited films and limits formation of Hf-O-Hf bonds. Upon exposure to sufficiently energetic radiation, electrons, and/or heat, the peroxo groups in HafSO_x decompose and initiate the film condensation process, resulting in a solubility switch (soluble to insoluble) that permits removal of the unexposed soluble regions in basic developers [10, 18].

This patterning mechanism has enabled 8 nm half pitch lines written with an exposure dose of ~200 mJ/cm²[8] using EUV lithography. The relatively low sensitivity of the resist at high resolution necessitates continued research into the resist's exposure mechanisms to reduce the exposure dose and increase patterning speed required for nanodimensional patterning. Further insight into the radiation induced chemistries of HafSO_x may prove beneficial for increasing sensitivity and enabling its use as a next generation resist. This study focuses on the characterization of peroxide-containing HafSO_x with temperature programmed desorption (TPD) and electron stimulated desorption (ESD). These techniques have allowed us to probe the bonding interactions of molecular and atomic species and electron induced chemistries in the films.

Experimental Methods

Native oxide silicon substrates were rinsed in acetone, methanol, and DI water, blow dried with nitrogen, and treated in a UV-ozone cleaner for 15

minutes prior to spin coating the HfSO_x precursor solution. 1.0 M aqueous solutions of $\text{HfOCl}_2 \cdot 8\text{H}_2\text{O}$ (98+%, Alfa Aesar) and H_2SO_4 (Mallinckrodt) were prepared with 18.2 M Ω water. The HfSO_x precursor solution was prepared by adding chilled 30 wt% $\text{H}_2\text{O}_2(\text{aq})$ (Macron) to the $\text{HfOCl}_2(\text{aq})$ solution followed by dilution with 18.2 M Ω water and finally addition of the $\text{H}_2\text{SO}_4(\text{aq})$ solution. The final solution contained a hafnium concentration of 0.15 M with molar ratios equaling 1 : 0.7 : 3 for hafnium : sulfate : peroxide. The solution was manually deposited through a syringe, using a 0.45 μm filter, at the center of the stationary silicon substrate, followed by spin coating at 3000 rpm for 30 s. The spin coated HfSO_x films were then soft baked at 353 K for 180 s.

X-ray photoelectron measurements (XPS) were taken with a PHI 5000 VersaProbe system equipped with a hemispherical analyzer. Monochromated Al K α x-rays (1486.6 eV) were used with a spot size of 100 μm and an analyzer pass energy of 23.5 eV. The sample to analyzer take-off angle was fixed at 45°. XPS spectra were obtained with 0.1 eV steps and 100 ms per step. To minimize x-ray induced film condensation the electron and ion gun neutralizers were not used and the number of scans was reduced until no changes were observed in the O 1s spectra compared to the initial spectrum. TPD and ESD experiments were performed at a base pressure of $\sim 3 \times 10^{-9}$ Torr in a chamber equipped with a Hiden Analytical IDP quadrupole mass spectrometer. The spectrometer has a secondary electron multiplier

detector and electron impact ionizer. For these experiments the spectrometer ionizer was turned on with a 67 V potential with respect to the ionization cage so that neutrals and ions were both detected. The temperature was measured by a type-K thermocouple in contact with the back surface of the ceramic heating stage, with the sample mounted on the other side. Samples were held in place on the heating stage by spring-loaded ceramic pins during the TPD experiments. A linear heating rate of 10 K/min was used. For all ESD experiments the current was 0.838 μA as measured by a Faraday cup at the tip of the electron gun. The beam spot size (~ 1.0 cm diameter) was measured visually with a phosphor screen, which together with the measured current gives a current density of 1.07 $\mu\text{A}/\text{cm}^2$.

Results and Discussion

XPS analysis of the soft baked HfSO_x films was performed to assess the atomic composition and chemical states prior to thermal or electron beam treatments. The Hf 4f, S 2p, and O 1s spectra are shown in Fig. 6.1, where the spectra were charge calibrated to adventitious carbon = 284.8 eV[21]. The Hf 4f can be resolved into a spin orbit split doublet with a Hf 4f_{7/2} BE position of 17.6 eV. This BE is consistent with Hf^{4+} [21]. The binding energy (BE) position of the S 2p_{3/2} at 169.0 eV is characteristic of sulfate[22, 23]. The O 1s spectrum can be fit to three components and is dominated by a middle BE component that constitutes 86% of the total peak intensity. A high

BE and low BE peak were required to adequately fit the spectrum and they comprise 10% and 4% of the total O 1s peak area, respectively. A full-width at half-maximum (FWHM) of 1.67 eV was used for the three peaks with Gaussian-Lorentzian lineshapes consisting of 90% Gaussian character.

In our prior work with this material system we have used three peaks to fit the O 1s spectrum[13], but it has also been fit with two peaks by other researchers[16]. We have found that fitting with two peaks was only possible using a large FWHM (1.9 eV), large BE separation between the two peaks (2.6 eV), and excessive error between the peak envelope and experimental data at the high BE side of the spectrum. For this reason, and the prior variable temperature studies[13], we have used three components where the low, middle, and high BE components were attributed to Hf-O-Hf bonds, hydroxo/peroxo bonds[24, 25], and sulfate groups, respectively. The high BE feature is suspected to be primarily associated with sulfate and not water due to its sustained intensity when heating up to 700 K[13].

The S/Hf ratio determined by XPS in these films was 0.8. From prior studies involving titration of dissolved films to determine the O₂ content[18] and the precursor S/Hf ratio, the HfSO_x film composition has been estimated as $\text{Hf}(\text{OH})_{1.6}(\text{O}_2)_{0.5}(\text{SO}_4)_{0.7} \cdot q\text{H}_2\text{O}$, which gives a S/Hf ratio of 0.7. The S/Hf ratio in the precursor solution should be the same as that in the film because no Hf or S is expected to leave the film during spin coating and after the 353 K soft bake process. The XPS results indicate a slightly sulfate rich surface,

with a surface composition $\text{Hf}(\text{OH})_{1.4}(\text{O}_2)_{0.5}(\text{SO}_4)_{0.8} \cdot q\text{H}_2\text{O}$. This is supported by transmission electron microscopy chemical analysis of HfSOx cross sections which show segregation of sulfur toward the surface[17]. The sulfur segregation could play an important role in patterning as the greater sulfate density at the surface could alter the film's interaction with incident electrons or photons and the basic developer.

The primary ESD desorption species are plotted versus exposure time in Fig. 6.2. The primary electron beam energy was 1000 eV and the film was exposed for a sufficient length of time to achieve a $1000 \mu\text{C}/\text{cm}^2$ dose, which is the approximate dosage previously used when patterning HfSOx [15]. In Fig. 6.2, the electron beam was unblanked after two minutes to begin electron exposure and the primary desorbed species from HfSOx were measured, and correspond to mass-to-charge ratios (m/z) 2, 16, 17, 18, 28, 32, and 44. These m/z values are interpreted as molecular hydrogen, atomic oxygen, hydroxyl groups, water, carbon monoxide, molecular oxygen, and carbon dioxide, respectively. No desorption products were observed for sulfur oxides ($m/z = 64, 80, \text{ or } 96$), so sulfur can be excluded from contributing to the $m/z = 32$ signal. Desorption of carbon monoxide ($m/z = 28$) and dioxide ($m/z = 44$) presumably resulted from atmospheric carbon contamination of the precursor solution or film. With the exception of H_2 and O_2 , desorption signals were observed to rapidly increase before tapering off and reaching a steady state plateau. The initial spike is due to electronic desorption mechanisms while

thermal energy likely contributes[26] to the sustained signal intensity at long exposure times. Experimental and theoretical work have demonstrated that localized beam heating due to incident electrons can increase the local temperature of resists and substrates by tens of degrees[27, 28], with the temperature increase dependent on the dosage and electron energy. HafSOx is expected to have a relatively low thermal conductivity[29, 30] on the order of $\sim 1 \text{ W}/(\text{m}\cdot\text{K})$, and so thermal desorption could affect the ESD spectra for longer exposure times.

Focusing on desorption signals $m/z = 16$ and 32, the absence of any desorption signal from $m/z = 16$ with the ionizer off indicates that the $m/z = 16$ spectrum shown in Fig. 6.2 results from fragmentation of parent species and not O^+ . This is supported by the fact that the shape of the $m/z = 16$ desorption spectrum is virtually the same as the water, carbon monoxide, and carbon dioxide spectra, and that $m/z = 16$ desorption occurs in films with and without peroxide. By similar logic the $m/z = 17$ spectra is likely due to cracking of desorbed water molecules. O_2 desorption in the peroxide containing HafSOx film increases at a much higher rate than the other species when exposed to the electron beam and gradually decays. The near absence of ionic desorption species and correspondingly the dominance of neutrals suggests that the basic Menzel-Gomer-Redhead (MGR) model[31, 32] of desorption can adequately describe the oxygen desorption behavior, where atomic excitation (typically interpreted as a valence level excitation,

although the original MGR model did not specify the initial excitation level[33]) promotes an electron into a nonbonding or antibonding state. The surface species then finds itself in a repulsive final state and desorbs. A mechanism such as the Knotek-Feibelman (KF) model of desorption by Auger decay[34, 35] may be more appropriate. Since no O^+ was detected in these studies double Auger decay processes are unlikely and/or neutralization of O^+ occurs before desorption.

ESD spectra for a $HafSO_x$ film without peroxide and a clean silicon substrate are included in Fig. 6.2 for comparison with the peroxide containing film. The biggest difference between the peroxide and peroxide-free spectra is that no O_2 desorbs from the peroxide-free film. This provides additional evidence that the metal-peroxo bond is radiation sensitive, and that the desorption of O_2 in these experiments originates from the decomposition of the metal-peroxo species. Examination of the clean silicon spectra indicates significant differences compared to the $HafSO_x$ films. In fact, virtually all of the water desorption signal and corresponding molecular fragments at $m/z = 16$ and 17 comes from the $HafSO_x$ film and not the background, while background CO and CO_2 contribute to signals observed from the films.

The incident electron beam energy dependence of O_2 desorption was investigated and the results are presented in Fig. 6.3. In Fig. 6.3(a) the desorption spectra have been normalized so that all spectra have the same maximum and minimum peak heights, and in general the rate of decay after

reaching maximum desorption decreases as the electron energy increases. This trend has been observed in Na^+ desorption from glass from 500-4000 eV[36], and while the desorption of neutral O_2 from HafSO_x and Na^+ desorption from glass are seemingly two very disparate processes, it is interesting to note the similarities in the desorption spectra shown in Fig. 6.3(a) and in reference [36]. Desorption of Na^+ in the 500-4000 eV energy range was modeled reasonably well by considering a combined desorption and diffusion process, and thus a similar mechanism may be applicable in this work. The authors modeled the Na^+ desorption signal by

$$QMS(t) \cong \beta \frac{J\sigma}{\varepsilon} C_{Na}(t)$$

In this equation $QMS(t)$ is the Na^+ desorption signal, β is a proportionality constant, J is the current density, σ is the ionic desorption cross section, ε is the elementary charge, and $C_{Na}(t)$ is the concentration of surface Na^+ . $C_{Na}(t)$ is represented by an integro-differential diffusion equation, and so appropriate choices of boundary conditions and constants (e.g. diffusivity or ion mobility) may be made to analyze the role of diffusion in the desorption process.

The total desorption cross sections for O_2 were calculated and shown in Fig. 6.3(b). The initial decay of the O_2 signals were approximately first order as shown by plotting the natural logarithm of the signals versus exposure time. For first order desorption, the desorption rate may be given as[37]

$$\frac{QMS}{QMS_{init}} = \exp\{-(JQ/\varepsilon)t\}$$

Here QMS is the mass spectrometer signal and QMS_{init} the initial signal, J is the current density (A/cm^2), Q is the total cross section for the process (cm^2), ε is the elementary charge (1.602×10^{-19} A.s), and t is the exposure time. A plot of the natural logarithm versus exposure time can then be used to determine Q from the slope of the decay spectrum. In these studies the cross section for desorption at 500 eV gave the highest value at 1×10^{-15} cm^2 while the smallest cross section of 1×10^{-16} cm^2 was found for desorption at 1800 eV. These cross sections are relatively high and of the same magnitude as molecular oxygen adsorbed on metals[38, 39]. One possible explanation for these high cross sections is that $HfSO_x$ is a wide band gap material, which may limit rapid relaxation of excited atoms by electrons from the substrate[40], and thus the excited O_2 species are sufficiently long lived to desorb with high probability from the surface.

The 2000 eV O_2 desorption spectrum exhibited anomalous behavior and did not follow the trend of decreasing desorption cross section with higher electron energy. Nonlinear behavior has also been observed for oxygen desorption from SrO , MgO , and BaO in the energy range 100-1000 eV[41], where the maximum O_2^+ desorption from these oxides plateaus and begins to decrease for higher electron beam energies. Numerous factors may contribute to this behavior at higher electron energies. At larger energies

(>~1000 eV), direct momentum transfer between an incident electron and surface atom is adequately energetic to break chemical bonds in addition to electronic energy transfer[42]. The attenuation length of electrons approximately triples with increasing energy from 500 to 2000 eV, which may cause radiation chemistries to occur much deeper in the films resulting in a higher diffusional component to the peak shape. Another complicating factor is that at higher electron energies Hf $M\alpha$ x-rays (1644 eV) are generated which may induce further structural changes in the film, although the 1800 eV spectrum follows the trend of decreasing desorption cross section with higher energy. While not conclusive, some combination of these effects may contribute to the anomalous peak shape of the 2000 eV O₂ desorption spectrum.

Heating HafSOx films post-exposure can help improve contrast[20], so TPD was used to characterize the differences in peroxide containing HafSOx films before and after 1000 eV ESD. The film was exposed to air after exposure, as would be the case in practice before development. Desorption spectra are shown with and without normalization in Fig. 6.4. The main desorption species were the same as for ESD with the inclusion of sulfur dioxide ($m/z = 64$), which was due to decomposition of sulfate groups. There is a low temperature desorption peak in the carbon monoxide and carbon dioxide post-exposure spectra that is absent in the unexposed film. In general, ESD seemed to narrow the desorption peaks in the exposed film.

Variation in peak shapes and maximum desorption temperatures prevents a more in-depth analysis of these results. Spectra are displayed in Fig. 6.5 which highlight the instability of the SO₂ desorption spectra over time. This instability was attributed to inconsistent thermocouple contact with the heating stage, which altered output heating power.

The maximum desorption temperatures for O₂ mirrors that of H₂O. If it is assumed that O₂ desorption is independent of coverage (first-order reaction) and that the activation energy of desorption is constant with temperature, the maximum desorption temperature can be used to find the activation energy by the Redhead equation[43]:

$$\frac{E}{RT_p} = \ln\left(\frac{\nu T_p}{\beta}\right) - 3.64$$

In this equation E is the activation energy, R is the gas constant, T_p is the maximum desorption temperature (K), ν is the pre-exponential factor (s⁻¹), and β is the linear heating rate (K/s). With an assumed $\nu = 10^{15} \text{ s}^{-1}$ (multilayer O₂ desorption[44]) and $\beta = 0.167 \text{ K/s}$, the activation energy for O₂ desorption was found to be ~1.3 eV. For reference, given the aforementioned temperature instability, a +/- 50 K shift in the O₂ desorption temperature will change the activation energy by +/- 0.2 eV. DFT calculations predict the bond dissociation energy of peroxide HfO₂²⁺ to be 2.8 eV[45], and experimental studies have shown the decomposition by photon stimulated desorption of surface peroxide on rutile TiO₂ (110) occurs at 2.8 eV[46]. The lower energy

observed in HafSOx could be a result of molecular interactions with the peroxide, such as water solvation and presence of the sulfate species.

Conclusion

TPD, ESD, and XPS were used to characterize thermal and electron beam induced dynamics of HafSOx. The surface chemistry was found to be sulfate rich with composition $\text{Hf}(\text{OH})_{1.4}(\text{O}_2)_{0.5}(\text{SO}_4)_{0.8} \cdot q\text{H}_2\text{O}$ based on XPS analysis. The thermal desorption energy of O_2 was estimated as 1.3 eV based on the maximum desorption temperature during TPD experiments. ESD spectra indicate that both electron-stimulated and thermally driven processes contribute to desorption. Future experiments performing ESD at a lower substrate temperature or with reduced current density could minimize thermal effects. In addition, Raman spectroscopy on exposed films could reveal the degree of peroxide decomposition, while XPS on the same samples would provide complementary information. Total desorption cross sections were established for O_2 from 500-2000 eV, with a maximum value of $1 \times 10^{-15} \text{ cm}^2$ determined at an electron energy of 500 eV. These desorption cross sections will provide a reference for future experiments where the sensitivity of HafSOx is tuned for a given type of radiation by the addition of other metal ions. The experiments in this work help progress understanding of the modification of HafSOx inorganic resists for next generation lithography.

References

- [1] J. Bort (2013), "This Looks Like An Ordinary PC But It's Powered By Some Impossibly Small Technology," [Online]. Available: <http://www.businessinsider.com/intel-shows-pc-using-broadwell-14nm-chips-2013-9>
- [2] P. Kruit and S. Steenbrink, "Local critical dimension variation from shot-noise related line edge roughness," *J. Vac. Sci. Technol. B*, vol. 23, pp. 3033-3036, 2005.
- [3] J. W. Thackeray, "Materials challenges for sub-20-nm lithography," *J. Micro/Nanolith. MEMS MOEMS*, vol. 10, pp. 033009, 2011.
- [4] P. P. Naulleau, C. N. Anderson, L.-M. Baclea-an, P. Denham, S. George, K. A. Goldberg, G. Jones, B. McClinton, R. Miyakawa, S. Rekawa, and N. Smith, "Critical challenges for EUV resist materials," *Proc. SPIE*, vol. 7972, pp. 797202, 2011.
- [5] A. E. Grigorescu, M. C. van der Krogt, C. W. Hagen, and P. Kruit, "10 nm lines and spaces written in HSQ, using electron beam lithography," *Microelectron. Eng.*, vol. 84, pp. 822-824, 2007.
- [6] V. R. Manfrinato, L. H. Zhang, D. Su, H. G. Duan, R. G. Hobbs, E. A. Stach, and K. K. Berggren, "Resolution Limits of Electron-Beam Lithography toward the Atomic Scale," *Nano Lett.*, vol. 13, pp. 1555-1558, 2013.
- [7] A. E. Grigorescu and C. W. Hagen, "Resists for sub-20-nm electron beam lithography with a focus on HSQ: state of the art," *Nanotechnology*, vol. 20, pp. 292001, 2009.
- [8] Y. Ekinici, M. Vockenhuber, M. Hojeij, L. Wang, and N. M. Mojarad, "Evaluation of EUV resist performance with interference lithography towards 11 nm half-pitch and beyond," *Proc. SPIE*, vol. 8679, pp. 867910, 2013.
- [9] M. E. Krysak, J. M. Blackwell, S. E. Putna, M. J. Leeson, T. R. Younkin, S. Harlson, K. Frasure, and F. Gstrein, "Investigation of novel inorganic resist materials for EUV lithography," *Proc. SPIE*, vol. 9408, pp. 904805, 2014.

- [10] J. K. Stowers, A. Telecky, M. Kocsis, B. L. Clark, D. A. Keszler, A. Grenville, C. N. Anderson, and P. P. Naulleau, "Directly patterned inorganic hardmask for EUV lithography," *Proc. SPIE*, vol. 7969, pp. 796915, 2011.
- [11] J. T. Anderson, C. L. Munsee, C. M. Hung, T. M. Phung, G. S. Herman, D. C. Johnson, J. F. Wager, and D. A. Keszler, "Solution-Processed HafSO_x and ZircSO_x Inorganic Thin-Film Dielectrics and Nanolaminates," *Adv. Funct. Mater.*, vol. 17, pp. 2117-2124, 2007.
- [12] M. Alemayehu, J. E. Davis, M. Jackson, B. Lessig, L. Smith, J. D. Sumega, C. Knutson, M. Beekman, D. C. Johnson, and D. A. Keszler, "Tunable dielectric thin films by aqueous, inorganic solution-based processing," *Solid State Sci.*, vol. 13, pp. 2037-2040, 2011.
- [13] B. T. Flynn, D. Kim, B. L. Clark, A. Telecky, L. Arnadottir, J. Szanyi, D. A. Keszler, and G. S. Herman "In-situ characterization of aqueous-based hafnium oxide hydroxide sulfate thin films," *Surf. Interface Anal.*, vol. 46, pp. 210-215, 2014.
- [14] X. Thrun, K. H. Choi, M. Freitag, A. Grenville, M. Gutsch, C. Hohle, J. K. Stowers, and J. W. Bartha, "Evaluation of direct patternable inorganic spin-on hard mask materials using electron beam lithography," *Microelectron. Eng.*, vol. 98, pp. 226-229, 2012.
- [15] J. K. Stowers and D. A. Keszler, "High resolution, high sensitivity inorganic resists," *Microelectron. Eng.*, vol. 86, pp. 730-733, 2009.
- [16] R. P. Oleksak, R. E. Ruther, F. Luo, K. C. Fairley, S. R. Decker, W. F. Stickle, D. W. Johnson, E. L. Garfunkel, G. S. Herman, and D. A. Keszler, "Chemical and structural investigation of high-resolution patterning with HafSO_x," *ACS Appl. Mater. Interfaces*, vol. 6, pp. 2917-2921, 2014.
- [17] R. P. Oleksak and G. S. Herman, "Characterization of high-resolution HafSO_x inorganic resists," *Proc. SPIE*, vol. 9048, pp. 90483H, 2014.
- [18] J. M. Amador, S. R. Decker, S. E. Lucchini, R. E. Ruther, and D. A. Keszler, "Patterning chemistry of HafSO_x resist," *Proc. SPIE*, vol. 9051, pp. 90511A, 2014.

- [19] R. E. Ruther, B. M. Baker, J. H. Son, W. H. Casey, and M. Nyman, "Hafnium Sulfate Prenucleation Clusters and the Hf-18 Polyoxometalate Red Herring," *Inorg. Chem.*, vol. 53, pp. 4234-4242, 2014.
- [20] J. K. Stowers, A. J. Telecky, D. A. Keszler, and A. Grenville, "Patterned Inorganic Layers, Radiation Based Patterning Compositions and Corresponding Methods," U.S. Patent 8,415,000 B2, 2013.
- [21] M. Engelhard, J. Herman, R. Wallace, and D. Baer, "As-Received, Ozone Cleaned and Ar+ Sputtered Surfaces of Hafnium Oxide Grown by Atomic Layer Deposition and Studied by XPS," *Surf. Sci. Spectra*, vol. 18, pp. 46-57, 2012.
- [22] M. Hino, M. Kurashige, H. Matsushashi, and K. Arata, "The surface structure of sulfated zirconia: Studies of XPS and thermal analysis," *Thermochim. Acta*, vol. 441, pp. 35-41, 2006.
- [23] K. Ebitani, H. Konno, T. Tanaka, and H. Hattori, "In-Situ XPS Study of Zirconium Oxide Promoted by Platinum and Sulfate Ion," *J. Catal.*, vol. 135, pp. 60-67, 1992.
- [24] J. C. Dupin, D. Gonbeau, P. Vinatier, and A. Levasseur, "Systematic XPS studies of metal oxides, hydroxides and peroxides," *Phys. Chem. Chem. Phys.*, vol. 2, pp. 1319-1324, 2000.
- [25] J. H. Park, Y. B. Yoo, K. H. Lee, W. S. Jang, J. Y. Oh, S. S. Chae, and H. K. Baik, "Low-Temperature, High-Performance Solution-Processed Thin-Film Transistors with Peroxo-Zirconium Oxide Dielectric," *ACS Appl. Mater. Interfaces*, vol. 5, pp. 410-417, 2013.
- [26] Z. Cui, "A new analytical model for simulating resist heating in electron beam lithography," *J. Phys. D Appl. Phys.*, vol. 25, pp. 919-923, 1992.
- [27] D. C. Chu, W. K. Wong, K. E. Goodson, and R. F. W. Pease, "Transient temperature measurements of resist heating using nanothermocouples," *J. Vac. Sci. Technol. B*, vol. 21, pp. 2985-2989, 2003.
- [28] T. R. Groves, "Theory of beam-induced substrate heating," *J. Vac. Sci. Technol. B*, vol. 14, pp. 3839-3844, 1996.

- [29] R. A. Wiedle, M. Warner, J. Tate, P. N. Plassmeyer, and C. J. Page, "Thermal conductivity of amorphous thin-film Al-P-O on silicon," *Thin Solid Films*, vol. 548, pp. 225-229, 2013.
- [30] M. A. Panzer, M. Shandalov, J. A. Rowlette, Y. Oshima, Y. W. Chen, P. C. McIntyre, and K. E. Goodson, "Thermal Properties of Ultrathin Hafnium Oxide Gate Dielectric Films," *IEEE Electr. Device L.*, vol. 30, pp. 1269-1271, 2009.
- [31] D. Menzel and R. Gomer, "Desorption from metal surfaces by low-energy electrons," *J. Chem. Phys.*, vol. 41, pp. 3311-3328, 1964.
- [32] P. Redhead, "Interaction of slow electrons with chemisorbed oxygen," *Can. J. Phys.*, vol. 42, pp. 886-905, 1964.
- [33] T. E. Madey, D. E. Ramaker, and R. Stockbauer, "Characterization of surfaces through electron and photon stimulated desorption," *Ann. Rev. Phys. Chem.*, vol. 35, pp. 215-240, 1984.
- [34] P. J. Feibelman and M. L. Knotek, "Reinterpretation of electron-stimulated desorption data from chemisorption systems," *Phys. Rev. B*, vol. 18, pp. 6531-6539, 1978.
- [35] M. L. Knotek and P. J. Feibelman, "Ion Desorption By Core-Hole Auger Decay," *Phys. Rev. Lett.*, vol. 40, pp. 964-967, 1978.
- [36] F. Ohuchi and P. H. Holloway, "General-model of sodium desorption and diffusion during electron-bombardment of glass," *J. Vac. Sci. Technol.*, vol. 20, pp. 863-867, 1982.
- [37] T. E. Madey and J. T. Yates, "Electron-Stimulated Desorption As A Tool For Studies Of Chemisorption - Review," *J. Vac. Sci. Technol.*, vol. 8, pp. 525-555, 1971.
- [38] I. I. Rzeznicka, J. Lee, and J. T. Yates, "Electron-stimulated desorption study of oxygen adsorbed on Ag(110). Observation of inclined physisorbed species," *J. Phys. Chem. C*, vol. 111, pp. 3705-3709, 2007.
- [39] T. E. Madey and J. T. Yates, "Desorption by electron impact - Oxygen adsorbed on tungsten," *Surf. Sci.*, vol. 11, pp. 327-351, 1968.

- [40] R. M. Jaeger, K. Homann, H. Kühlenbeck, and H. J. Freund, "Lifetimes of electronically excited-states of molecules on oxide versus metal-surfaces," *Chem. Phys. Lett.*, vol. 203, pp. 41-45, 1993.
- [41] P. Wargo and W. G. Shepherd, "Electron-Bombardment-Induced Dissociation of Alkaline Earth Oxides," *Phys. Rev.*, vol. 106, pp. 694-703, 1957.
- [42] R. D. Ramsier and J. T. Yates, "Electron-stimulated desorption - principles and applications," *Surf. Sci. Rep.*, vol. 12, pp. 243-378, 1991.
- [43] P. Redhead, "Thermal desorption of gases," *Vacuum*, vol. 12, pp. 203-211, 1962.
- [44] H. Schlichting and D. Menzel, "Techniques for attainment, control, and calibration of cryogenic temperatures at small single-crystal samples under ultrahigh-vacuum," *Rev. Sci. Instrum.*, vol. 64, pp. 2013-2022, 1993.
- [45] C. Lourenco, M. D. Michelini, J. Marcalo, J. K. Gibson, and M. C. Oliveira, "Gas-Phase Reaction Studies of Dipositive Hafnium and Hafnium Oxide Ions: Generation of the Peroxide HfO_2^{2+} ," *J. Phys. Chem. A*, vol. 116, pp. 12399-12405, 2012.
- [46] M. A. Henderson, M. M. Shen, Z. T. Wang, and I. Lyubinetsky, "Characterization of the Active Surface Species Responsible for UV-Induced Desorption of O_2 from the Rutile TiO_2 (110) Surface," *J. Phys. Chem. C*, vol. 117, pp. 5774-5784, 2013.

Figures

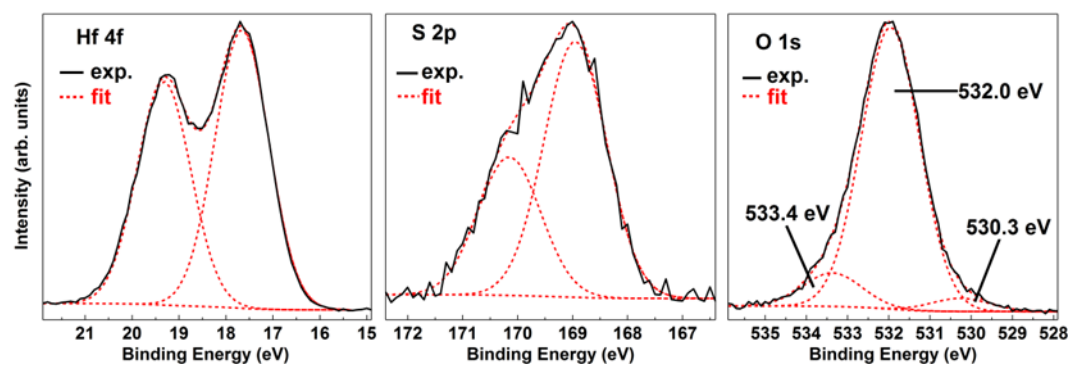


Figure 6.1 – XPS spectra of HafSOx film after a 353 K soft bake.

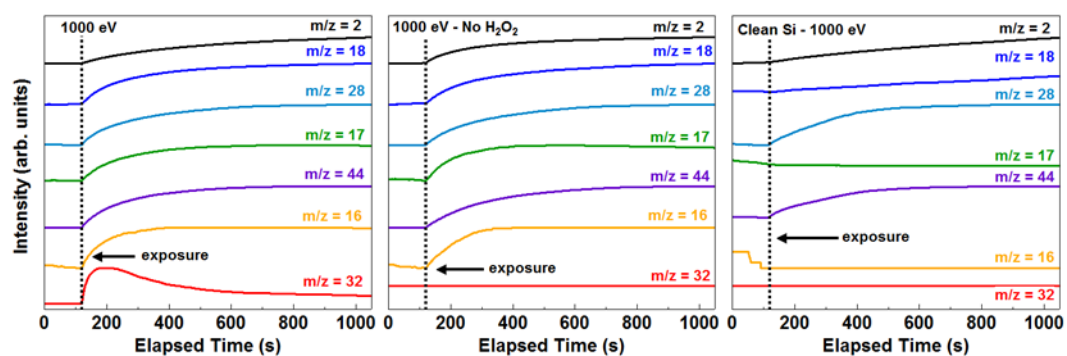


Figure 6.2 – ESD spectra of $HafSO_x$ with peroxide, without peroxide, and a clean Si substrate (for reference).

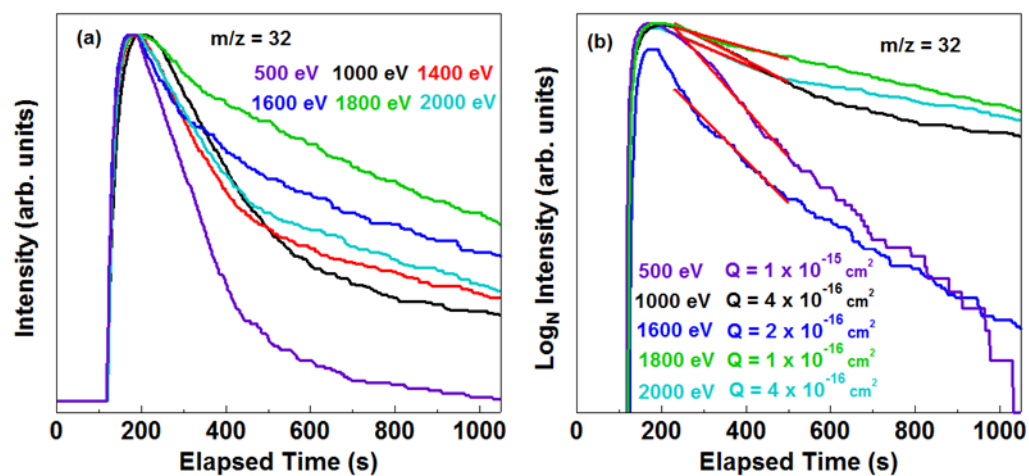


Figure 6.3 – (a) Normalized O_2 desorption from 500-2000 eV and the (b) corresponding total desorption cross sections.

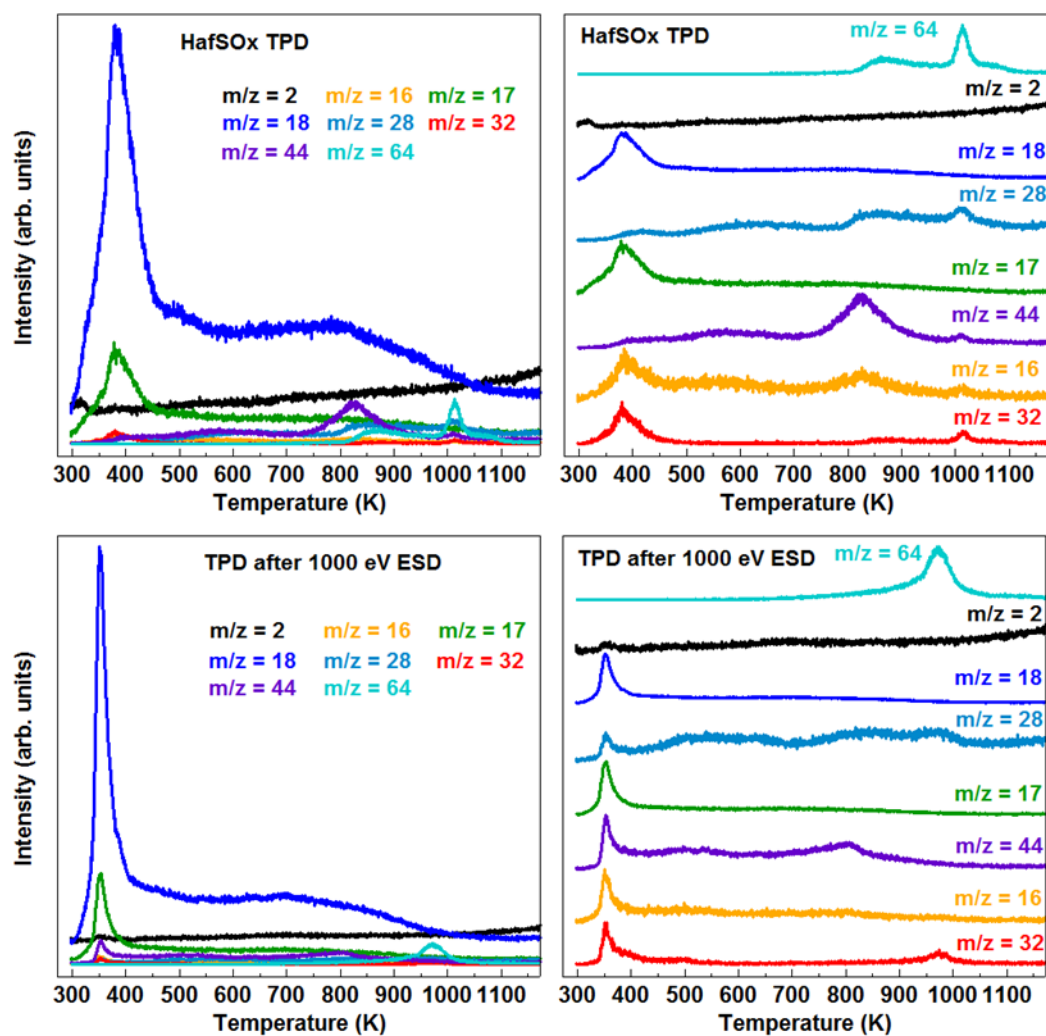


Figure 6.4 – TPD spectra before and after 1000 eV ESD

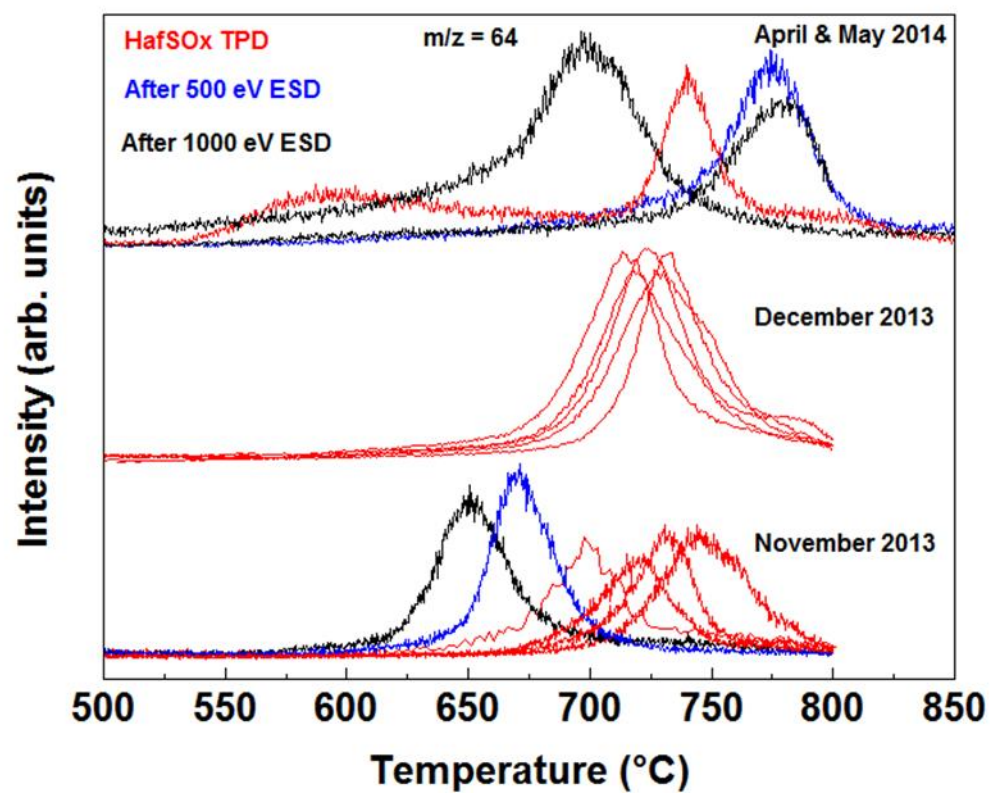


Figure 6.5 – Variation in SO_2 desorption temperature as a function of time

CHAPTER 7

Pt/a-IGZO JUNCTION CHARACTERIZED BY *IN SITU*
PHOTOEMISSION

Brendan T. Flynn¹, Richard P. Oleksak¹, Suntharampillai Thevuthasan², and
Gregory S. Herman^{1*}

¹Oregon State University, School of Chemical, Biological and Environmental
Engineering, Corvallis, OR USA

²Environmental Molecular Sciences Laboratory, Pacific Northwest National
Laboratory, Richland, WA USA

*Corresponding Author

Abstract

Memristors and other types of novel electronics increasingly use a structure that includes a platinum and amorphous indium gallium zinc oxide (a-IGZO) interface. The chemical and electronic properties of this junction can substantially impact device performance. In this study, a Pt/a-IGZO interface was formed and studied by *in situ* x-ray photoelectron spectroscopy. The a-IGZO core levels shifted by 0.4-0.6 eV to lower binding energy after Pt deposition due to band bending. Although a Schottky-type diode is expected for this interface, a barrier height of 0.25 eV was determined, and remained virtually unchanged after subsequent heating. The low barrier height may be explained by the reactive interface formed between Pt and a-IGZO, where x-ray photoelectron spectroscopy indicated the partial reduction of In^{3+} to In^0 after deposition of Pt on a-IGZO, with a significant increase in the relative intensity of the reduced In^0 compared to In^{3+} after annealing in vacuum.

Introduction

New and improved types of electronic devices are being enabled by amorphous oxide semiconductors like a-IGZO. Commonly used as a channel material for thin film transistors, a-IGZO generally has superior electron mobility relative to amorphous silicon, and a lower processing temperature combined with greater uniformity when compared to polycrystalline silicon[1]. Recently a-IGZO platinum interfaces have been used to modulate the properties of metal-semiconductor field-effect transistors[2] and memristors[3-5]. In particular, memristors may offer a path to exceed the storage capacity of Flash memory[5] and could help realize artificial neural networks by emulating the brain's synapses, complete with short/long term memory and learning functions[3].

It is known that interfacial reactions at the metal/oxide heterojunction in memristors heavily influence the current-voltage characteristics and in fact may be critical for bipolar resistive switching[6,7]. In addition to interfacial reactions, the electronic coupling between the metal and oxide as measured by the Schottky barrier height will also impact the electronic transport properties. A high barrier height of 1.1 eV is predicted for the Pt/a-IGZO interface, however near-ohmic behavior has been observed[8] and a range of barrier heights from 0.55-1.2 eV reported[2,9-11]. These studies determined the barrier height of the Pt/a-IGZO junction using electrical characterization, but the literature is lacking in the determination of the barrier height by XPS

and characterization of the resulting interfacial chemistry. The goal of this study was to characterize a Pt/a-IGZO interface via *in situ* XPS to determine the interface reactivity and estimate the barrier height to help clarify the range of properties that have been previously reported for Pt/a-IGZO interfaces.

Experimental Methods

50 nm a-IGZO films were deposited onto TiN/Ti/SiO₂/Si substrates by RF sputtering at room temperature in a 5% O₂/95% Ar gas mixture. The atomic composition of the as-deposited films was In_{2.5}Ga_{2.1}ZnO_{9.8} as determined by Rutherford backscattering spectrometry (RBS). Samples were then annealed for 1 hour at 300 °C in air and treated for 5 minutes in oxygen plasma prior to introduction into the XPS instrument (PHI VersaProbe) with attached ultra-high vacuum (UHV) chamber for sample processing and Pt deposition.

After introduction into the vacuum system and prior to depositing Pt, the a-IGZO samples were lightly sputtered for 1 minute (500 V, 1.33 μ A, 3 x 3 mm²) and then heated to 300 °C for 10 minutes in 1.0 x 10⁻⁶ Torr O₂ to completely remove carbon contamination and oxidize the films. Quantitative measurements from XPS indicate the atomic concentration was In_{2.5}Ga_{2.4}ZnO_{6.8}, suggesting an oxygen-deficient and gallium-rich surface when compared to the more bulk sensitive RBS data. Pt was sequentially deposited by e-beam evaporation at a pressure of 6.0 x 10⁻⁹ Torr and

subsequently transferred into the XPS chamber for analysis. Vacuum annealing after Pt deposition was done in an attached UHV chamber.

All XPS spectra were taken with monochromatized Al K α x-rays (1486.6 eV) at an emission angle of 45°, with a spot size of 100 μ m and pass energy of 23.5 eV. The spectra were charge calibrated with a sputter cleaned Au foil standard. Except for Pt, peak fitting of the core levels began with the spectrum from the clean and oxidized film, and for subsequent fitting of the other spectra the full width at half maximum (FWHM) was allowed to vary by \pm 0.05 eV, the percent Gaussian (%G, Gaussian/Lorentzian line shape) remained fixed, and the peak areas and positions were unconstrained. A Lorentzian asymmetric line shape convoluted with a Gaussian was used to fit the Pt 4f and In⁰ peaks.

For scanning transmission electron microscopy (STEM) analysis samples were prepared as cross sections via the lift out method using an FEI Quanta 3D Dual Beam scanning electron microscope with a gallium ion beam. STEM analysis was performed using an FEI Titan G2 80-200 transmission electron microscope with ChemiSTEM operating at 200 kV. A high angle annular dark field (HAADF) detector was used for imaging. Energy dispersive X-ray spectroscopy (EDS) line scans were collected with a step size of 0.5 nm and averaged over 1.5 nm to reduce noise. The scans were analyzed with Bruker Esprit 1.9 software using a manual background subtraction and quantification without standards.

Results and Discussion

The In $3d_{5/2}$ XPS spectra are displayed in Fig. 7.1. For the clean a-IGZO film, the In $3d_{5/2}$ spectrum could be fit with a single peak corresponding to fully oxidized In-O bonding with a binding energy of 445.2 eV, in good agreement with other a-IGZO XPS studies in the literature[12,13]. As the thickness of the Pt overlayer increased after depositing for 90 minutes, the main In $3d_{5/2}$ peak shifted to lower binding energy by 0.4 eV. Once Pt was deposited for 60 minutes, a second asymmetric peak was needed in order to adequately fit the In $3d_{5/2}$ spectra. This second peak had a binding energy of 443.9 eV, and was located about 1 eV to lower binding energy compared to the the fully oxidized In-O peak, which is consistent with the position of metallic In $3d_{5/2}$ [14,15]. The In metal peak accounts for 14% of the total In $3d_{5/2}$ signal after the deposition was complete, indicating that a substantial amount of In was reduced. The amount of In⁰ increased dramatically after annealing in vacuum to 200 °C as shown in Fig. 7.2. The binding energy separation between the In³⁺ and In⁰ peaks increases from 1 eV to 1.3 eV, and the In⁰ peak accounts for 58% of the In $3d_{5/2}$ signal after annealing to 300 °C. In the absence of prominent changes in the line shapes of the other core level spectra shown in Fig. 7.2, it appears more likely that In segregation to the top of the Pt film, rather than In bonding to another matrix element is responsible for the changes in the In $3d_{5/2}$ spectra. Deviations from an abrupt metal-

semiconductor interface and reduction of the substrate have commonly occurred when depositing a metal onto a clean semiconductor[16,17], and in the case of Pt deposited onto InP, In segregation is expected from theoretical calculations[18] and has been experimentally observed[19].

Fig. 7.1 and 7.2 show the dynamic nature of the O 1s spectra with Pt deposition and vacuum annealing. The binding energy of lattice oxygen in clean a-IGZO was found to be 530.9 eV, which is somewhat higher than that found in other reports[20-22]. This is likely due to the different film preparation method and peak fitting strategy used in this work. The clean a-IGZO was fit with two peaks, one for lattice oxygen and another small peak comprising 5% of the oxygen signal and located 1.6 eV to higher binding energy. This smaller peak was attributed to hydroxyl groups, which are commonly found 1.1-1.6 eV higher than the lattice oxygen peak for metal oxides[23-25]. For the thickest Pt film, the relative concentration of OH to the total O content increased to 13%, and decreased to 9% after annealing to 300 °C as shown in Fig. 7.2. The higher energy O 1s peak increases in relative intensity during Pt deposition, which would indicate out-diffusion from a-IGZO and bond formation with Pt if the peak were due to oxygen deficient regions. If this were the case, an increase in the FWHM of the Pt 4f_{7/2} and O 1s would be expected to accommodate the additional bonding modes, but the FWHM of both core levels actually decrease during Pt deposition. The increase in the relative OH peak area likely results from dissociative adsorption of water from

the background of the system and from outgassing of the evaporation source during deposition.

A third peak was added to fit the spectrum after depositing for 30 minutes. This peak was located 2.3-2.7 eV higher than lattice oxygen depending on the Pt thickness, and was likely the result of C-O impurities such as carbonate[26,27] present in the UHV system that became incorporated over time. Annealing to 200 °C eliminated this higher energy impurity peak. Compared to the room temperature spectrum in Fig. 7.2, the lattice oxygen peak shifts 0.2 eV higher after annealing to 300 °C.

The line shapes of the Ga $2p_{3/2}$ and Zn $2p_{3/2}$ core levels changed little with deposition or annealing. After cleaning and oxidizing, the binding energy of Ga $2p_{3/2}$ was 1118.3 eV and Zn $2p_{3/2}$ was 1022.3 eV, similar to other studies [12]. Both peaks shifted to lower binding energy by 0.6 eV during Pt deposition, while annealing to 300 °C resulted in a positive shift of 0.3 eV and 0.4 eV for Ga $2p_{3/2}$ and Zn $2p_{3/2}$, respectively. All of the spectra for the two core levels were fit with a single peak.

In contrast to the Ga 2p and Zn 2p core levels, the line shape of Pt $4f_{7/2}$ changed significantly during deposition and annealing. The position of the peak, 71.5 eV after the first Pt deposition, shifted 0.3 eV to lower binding energy with increasing Pt thickness, which occurred in parallel with a decrease in the FWHM from 1.2 eV to 1.0 eV. Annealing to 300 °C resulted

in a further decrease in binding energy and FWHM to 71.0 eV and 0.8 eV, respectively. Interestingly, the peak intensity of the Pt 4f_{7/2} peak decreased by 21% after annealing to 300 °C. Conversely, the core level intensities for a-IGZO increased substantially once heated to 200 °C and 300 °C. Ultimately, with respect to the unannealed Pt/a-IGZO film, the In 3d_{5/2}, Ga 2p_{3/2}, Zn 2p_{3/2}, and O 1s peak intensities increased by 11%, 166%, 149%, and 49%, respectively. This suggests that Pt islands formed when the sample was heated in vacuum, which was verified by TEM analysis shown in Fig. 7.3.

A STEM image of the Pt/a-IGZO cross section and an associated EDS line scan showing trends in concentration of In, Ga, Zn, O, and Pt across the film are shown in Fig. 7.3. From bottom to top the stack consists of the substrate TiN layer, a-IGZO film, Pt surface layer, and amorphous carbon protective layer. The Pt surface layer appears much brighter than the rest of the stack due to its high molecular weight and is thus distinguishable in the STEM image by virtue of this contrast. The Pt layer appears non-uniform across the film supporting the hypothesis that island growth has occurred during annealing of the Pt/a-IGZO stack. The EDS line scan further points to this thickness non-uniformity as evidenced by the shoulders in the Pt peak.

The Schottky barrier height was estimated using the In 4d shallow core level and valence band maximum (VBM) shown in the spectra in Fig. 7.4. The VBM was determined by extrapolating the leading edge of the valence

band emission for the clean a-IGZO film without Pt deposited. The equation used to calculate the barrier height was $\Phi_B = E_G - E_{VBM} + (E_{Zn3d} - E_{Zn3d, int})$, where Φ_B is the Schottky barrier height, E_G is the band gap of a-IGZO, E_{VBM} is the binding energy of the VBM for the clean a-IGZO sample, E_{Zn3d} is the binding energy of Zn 3d_{5/2} for the clean a-IGZO sample, and $E_{Zn3d, int}$ is the binding energy of Zn 3d_{5/2} after Pt deposition. The band gap of a-IGZO films was experimentally determined to be 3.20 eV by spectroscopic ellipsometry. The barrier height was then calculated as $3.20 - 3.17 + (10.78 - 10.55) = 0.25$ eV. This value is smaller than the barrier height determined through electronic means, which ranges from 0.55-1.2 eV[9,10]. The barrier height determined through electrical studies can vary due to multiple interfaces and the interdependence of parameters[28], but the more probable reason for the low barrier height found in this work is the reactive interface formed between Pt and a-IGZO. In addition to In segregation, the surface defect concentration may contribute to the reduced Schottky barrier[29].

The reactive interface may also help explain why the experimentally determined barrier is less than the ideal Schottky barrier, given by $\Phi_B = \Phi_M - \chi_s$ for an n-type semiconductor. Φ_M is the metal work function, equal to 5.4 eV for Pt[9], and χ_s is the semiconductor electron affinity, which is 4.3 eV for a-IGZO[30], thus giving a barrier height of 1.1 eV. This is shown schematically in Fig. 7.5.

Fig. 7.5 also includes the changes in barrier height with respect to Pt thickness and annealing temperature. The barrier height changes little during Pt deposition and annealing. There is a slight decrease in the barrier height after 60 min of Pt deposition and when annealing beyond 100 °C, which corresponds to significant formation of In^0 . The fact that the barrier height remains nearly unchanged with Pt deposition and subsequent annealing indicates strong Fermi level pinning[31].

Conclusion

In summary, a barrier height of 0.25 eV was found between Pt and a-IGZO. The low barrier results from a complex interface formation between the metal and semiconductor, with XPS revealing that In^{3+} is reduced to In^0 during Pt deposition. Judging from the line shapes of the core levels it seems more likely that In segregation rather than In bonding to another element is responsible for the In^0 formation. Annealing the interface in vacuum to 200 °C induced further In metal segregation while Pt islands formed. Consideration of the interfacial reaction between Pt and a-IGZO and barrier height will help lead to enhanced memristor and transistor device performance.

References:

- [1] T. Kamiya, K. Nomura, and H. Hosono, "Present status of amorphous In–Ga–Zn–O thin-film transistors," *Sci. Technol. Adv. Mat.*, vol. 11, pp. 044305, 2010.
- [2] D. H. Lee, K. Nomura, T. Kamiya, and H. Hosono, "Metal-Semiconductor Field-Effect Transistor Made Using Amorphous In-Ga-Zn-O Channel and Bottom Pt Schottky Contact Structure at 200 °C," *ECS Solid State Lett.*, vol. 1, pp. Q8-Q10, 2012.
- [3] Z. Q. Wang, H. Y. Xu, X. H. Li, H. Yu, Y. C. Liu, and X. J. Zhu, "Synaptic Learning and Memory Functions Achieved Using Oxygen Ion Migration/Diffusion in an Amorphous InGaZnO Memristor," *Adv. Funct. Mater.*, vol. 22, pp. 2759-2765 2012.
- [4] S. C. Wu, H. T. Feng, M. J. Yu, I. T. Wang, and T. H. Hou, "Flexible Three-Bit-Per-Cell Resistive Switching Memory Using a-IGZO TFTs," *IEEE Electr. Device L.*, vol. 34, pp. 1265-1267, 2013.
- [5] Y. S. Fan, P. T. Liu, and C. H. Hsu, "Investigation on amorphous InGaZnO based resistive switching memory with low-power, high-speed, high reliability," *Thin Solid Films*, vol. 549, pp. 54-58, 2013.
- [6] H. Y. Jeong, J. Y. Lee, and S. Y. Choi, "Direct observation of microscopic change induced by oxygen vacancy drift in amorphous TiO₂ thin films," *Appl. Phys. Lett.*, vol. 97, pp. 042109, 2010.
- [7] J. S. Rajachidambaram, S. Murali, J. F. Conley, S. L. Golledge, and G. S. Herman, "Bipolar resistive switching in an amorphous zinc tin oxide memristive device," *J. Vac. Sci. Technol. B*, vol. 31, pp. 01A104, 2013.
- [8] Y. Shimura, K. Nomura, H. Yanagi, T. Kamiya, M. Hirano, and H. Hosono, "Specific contact resistances between amorphous oxide semiconductor In–Ga–Zn–O and metallic electrodes," *Thin Solid Films*, vol. 516, pp. 5899-5902, 2008.
- [9] D. H. Lee, K. Nomura, T. Kamiya, and H. Hosono, "Diffusion-Limited a-IGZO/Pt Schottky Junction Fabricated at 200 °C on a Flexible Substrate," *IEEE Electr. Device L.*, vol. 32, pp. 1695-1697, 2011.
- [10] H. Kim, S. Kim, K. K. Kim, S. N. Lee, and K. S. Ahn, "Electrical Characteristics of Pt Schottky Contacts Fabricated on Amorphous Gallium Indium Zinc Oxides," *Jpn. J. Appl. Phys.*, vol. 50, pp. 105702, 2011.

- [11] S. H. Rha, U. K. Kim, J. Jung, H. K. Kim, Y. S. Jung, E. S. Hwang, Y. J. Chung, M. Lee, J. H. Choi, and C. S. Hwang, "The Electrical Properties of Asymmetric Schottky Contact Thin-Film Transistors with Amorphous-In₂Ga₂ZnO₇," *IEEE T. Electron Dev.*, vol. 60, pp. 1128-1135, 2013.
- [12] H. Cho, E. A. Douglas, A. Scheurmann, B. P. Gila, V. Craciun, E. S. Lambers, S. J. Pearton, and F. Ren, "Al₂O₃/InGaZnO₄ Heterojunction Band Offsets by X-Ray Photoelectron Spectroscopy," *ECS Solid State Lett.*, vol. 14, pp. H431-H433, 2011.
- [13] S. Iwamatsu, K. Takechi, T. Yahagi, Y. Watanabe, H. Tanabe, and S. Kobayashi, "Depth-Profiling Study on Amorphous Indium–Gallium–Zinc Oxide Thin-Film Transistors by X-ray Photoelectron Spectroscopy," *Jpn. J. Appl. Phys.*, vol. 52, pp. 03BB03, 2013.
- [14] A. W. C. Lin, N. R. Armstrong, and T. Kuwana, "X-ray Photoelectron/Auger Electron Spectroscopic Studies of Tin and Indium Metal Foils and Oxides," *Anal. Chem.*, vol. 49, pp. 1228-1235, 1977.
- [15] M. Pessa, A. Vuoristo, M. Vulli, S. Aksela, J. Vayrynen, T. Rantala, and H. Aksela, "Solid-state effects in M_{4,5}N_{4,5}N_{4,5} Auger spectra of elements from ⁴⁹In to ⁵²Te," *Phys. Rev. B*, vol. 20, pp. 3115-3123, 1979.
- [16] C. Korber, S. P. Harvey, T. O. Mason, and A. Klein, "Barrier heights at the SnO₂/Pt interface: In situ photoemission and electrical properties," *Surf. Sci.*, vol. 602, pp. 3246-3252, 2008.
- [17] F. Chen, R. Schafranek, W. B. Wu, and A. Klein, "Reduction-induced Fermi level pinning at the interfaces between Pb(Zr,Ti)O₃ and Pt, Cu and Ag metal electrodes," *J. Phys. D Appl. Phys.*, vol. 44, pp. 255301, 2011.
- [18] Z. D. Lin, F. Xu, and J. H. Weaver, "Surface segregation at metal – III-V-compound-semiconductor interfaces," *Phys. Rev. B*, vol. 36, pp. 5777-5783, 1987.
- [19] P. Claverie, B. Carriere, R. Pinchaux, and G. Rossi, "Experimental determination of local-bonding configuration at the early stages of growth of the heterogeneous Pt/InP(110) interface by synchrotron-radiation spectroscopy," *Phys. Rev. B*, vol. 38, pp. 1659-1666, 1988.
- [20] C. H. Jung, H. I. Kang, and D. H. Yoon, "The electrical, optical, and structural properties of amorphous indium gallium zinc oxide films and channel thin-film transistors," *Solid State Electron.*, vol. 79, pp. 125-129, 2013.

- [21] J. H. Choi, S. M. Hwang, C. M. Lee, J. C. Kim, G. C. Park, J. Joo, and J. H. Lim, "Effect of Ga content and sintering time on electrical properties of InGaZnO thin film transistors fabricated by sol-gel process," *J. Cryst. Growth*, vol. 326, pp. 175-178, 2011.
- [22] J. H. Kang, E. N. Cho, C. E. Kim, M. J. Lee, S. J. Lee, J. M. Myoung, and I. Yun, "Mobility enhancement in amorphous InGaZnO thin-film transistors by Ar plasma treatment," *Appl. Phys. Lett.*, vol. 102, pp. 222103, 2013.
- [23] G. W. Simmons and B. C. Beard, "Characterization of Acid-Base Properties of the Hydrated Oxides on Iron and Titanium Metal Surfaces," *J. Phys. Chem-US*, vol. 91, pp. 1143-1148, 1987.
- [24] E. McCafferty and J. P. Wightman, "Determination of the Concentration of Surface Hydroxyl Groups on Metal Oxide Films by a Quantitative XPS Method," *Surf. Interface Anal.*, vol. 26, pp. 549-564, 1998.
- [25] D. Barreca, A. Milanov, R. A. Fischer, A. Devi, and E. Tondello, "Hafnium oxide thin film grown by ALD: An XPS study," *Surf. Sci. Spectra*, vol. 14, pp. 34-40, 2007.
- [26] A. R. Gonzalez-Elipé, J. P. Espinos, A. Fernandez, and G. Munuera, "XPS study of the surface carbonation/hydroxylation state of metal oxides," *Appl. Surf. Sci.*, vol. 45, pp. 103-108, 1990.
- [27] F. Voigts, F. Bebensee, S. Dahle, K. Volgmann, and W. Maus-Friedrichs, "The adsorption of CO₂ and CO on Ca and CaO films studied with MIES, UPS and XPS," *Surf. Sci.*, vol. 603, pp. 40-49, 2009.
- [28] R. Schafrank, S. Payan, M. Maglione, and A. Klein, "Barrier height at (Ba,Sr)TiO₃/Pt interfaces studied by photoemission," *Phys. Rev. B*, vol. 77, pp. 195310, 2008.
- [29] A. Klein, F. Sauberlich, B. Spath, T. Schulmeyer, and D. Kraft, "Non-stoichiometry and electronic properties of interfaces," *J. Mater. Sci.*, vol. 42, pp. 1890-1900, 2007.
- [30] K. Lee, K. Nomura, H. Yanagi, T. Kamiya, E. Ikenaga, T. Sugiyama, K. Kobayashi, and H. Hosono, "Band alignment of InGaZnO₄/Si interface by hard x-ray photoelectron spectroscopy," *J. Appl. Phys.*, vol. 112, pp. 033713, 2012.
- [31] W. Monch, "Metal-semiconductor contacts: electronic properties," *Surf. Sci.*, vol. 299/300, pp. 928-944, 1994.

Figures

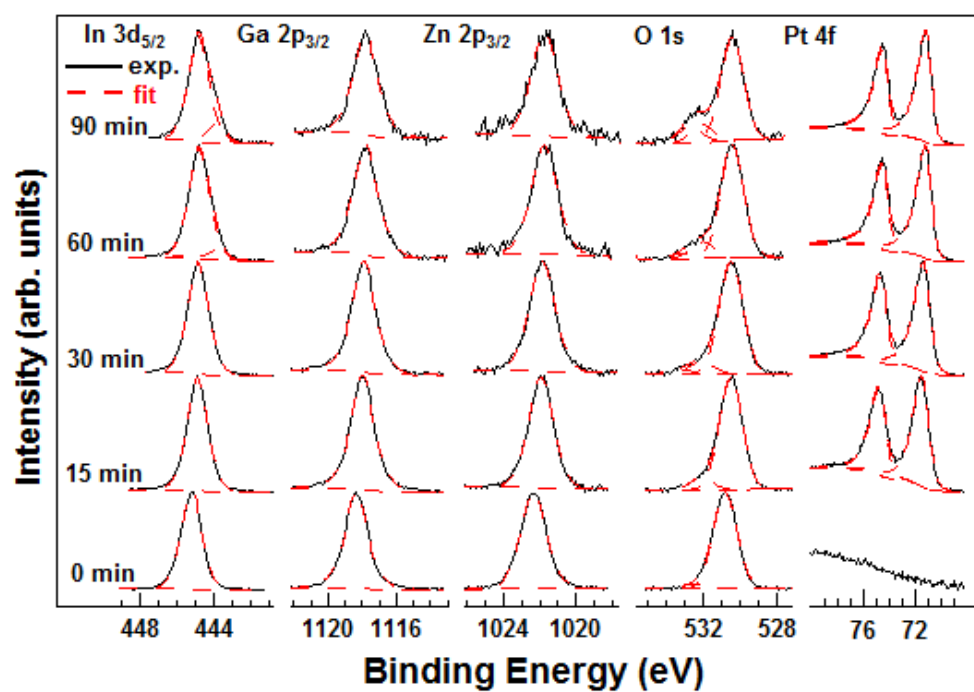


Figure 7.1 - Platinum deposition on a-IGZO. Annealing after 90 minute deposition resulted in ~8 nm thick Pt island formation.

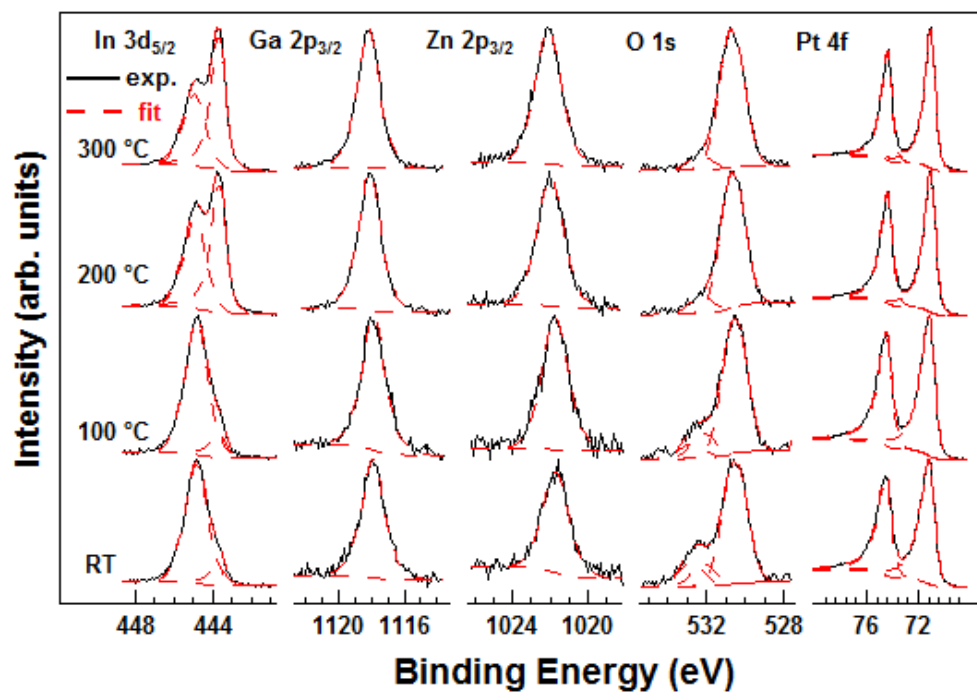


Figure 7.2 - Vacuum annealing Pt/a-IGZO film. Substantial indium reduction occurred after heating to 200 °C.

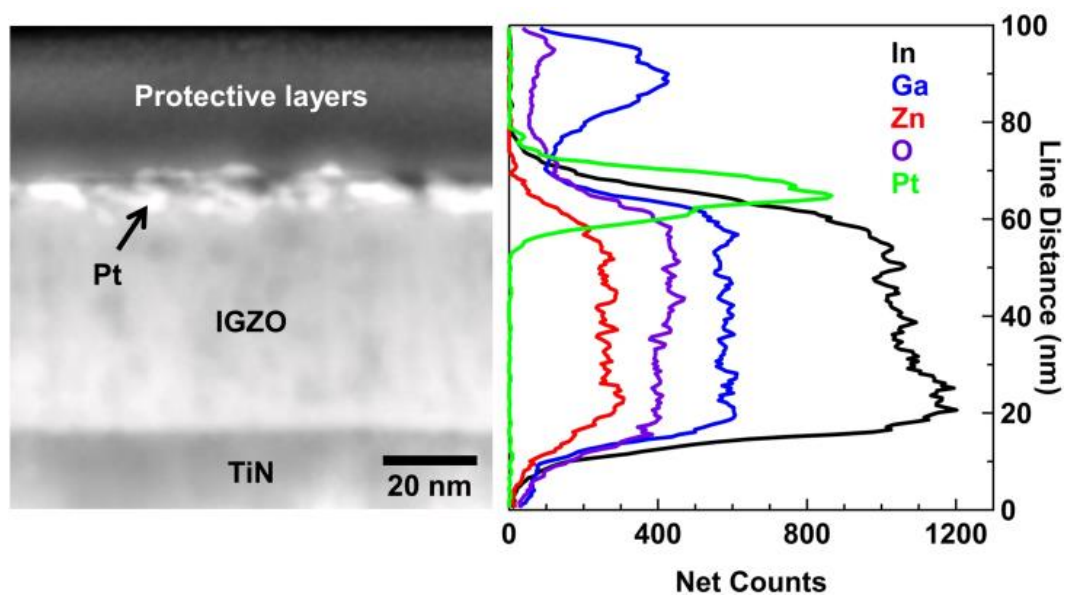


Figure 7.3 - Cross sectional STEM image (left) and associated EDS line scan (right) of the Pt/a-IGZO film annealed to 300 °C.

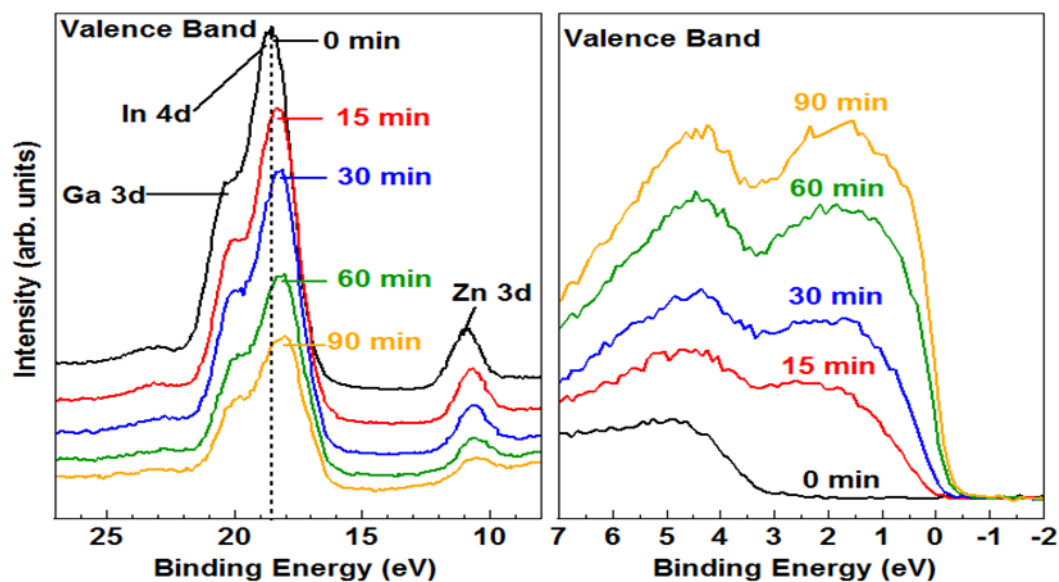


Figure 7.4 - Valence band spectra of Pt/a-IGZO during Pt deposition. A shift to lower binding energies with deposition (left) was accompanied by an increase in the valence band density of states (right).

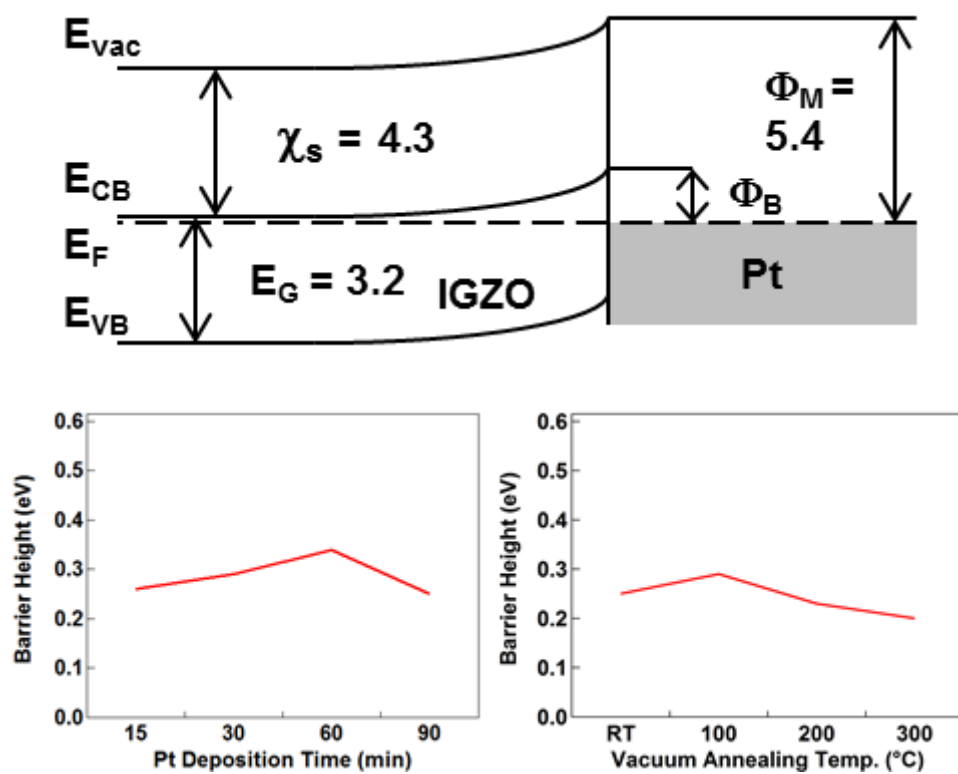


Figure 7.5 - Schematic of Pt/a-IGZO energy band diagram and changes in Schottky barrier with deposition time and annealing temperature. The barrier height Φ_B changes little with increasing Pt thickness and during annealing.

CHAPTER 8

GROWTH AND SURFACE MODIFICATION OF LaFeO_3 THIN FILMS INDUCED BY REDUCTIVE ANNEALING

Brendan T. Flynn,^{††} Kelvin H.L. Zhang,[‡] Vaithiyalingam Shutthanandan,[‡]
Tamas Varga,[‡] Robert J. Colby,[‡] Sandeep Manandhar,[‡] Richard P.
Oleksak,^{††} Mark H. Engelhard,[‡] Scott A. Chambers,[‡] Gregory S. Herman,^{††}
Michael A. Henderson,[‡] and Suntharampillai Thevuthasan^{‡*}

^{††}Oregon State University, School of Chemical, Biological, and Environmental
Engineering, Corvallis, OR USA

[‡]Environmental Molecular Sciences Laboratory, Pacific Northwest National
Laboratory, Richland, WA, USA

[‡]Fundamental and Computational Sciences Directorate, Pacific Northwest
National Laboratory, Richland, WA, USA

*Corresponding Author

Abstract

The electronic and ionic conductivity of perovskite oxides has enabled their use in diverse materials such as automotive exhaust catalysts, solid oxide fuel cell cathodes, and visible light photocatalysts. The redox chemistry at the surface of these oxides is largely dependent on the oxidation state of the transition metal as well as the oxide surface stoichiometry. In this study, the growth of LaFeO_3 (LFO) thin films on yttria-stabilized zirconia (YSZ) was characterized using both bulk and surface sensitive techniques. A combination of *in situ* reflection high energy electron diffraction (RHEED), x-ray diffraction (XRD), transmission electron microscopy (TEM) and Rutherford backscattering spectrometry (RBS) demonstrated that the film is highly oriented and stoichiometric. The film was annealed to various temperatures in an ultra-high vacuum chamber to simulate reducing conditions and studied by angle-resolved x-ray photoelectron spectroscopy (XPS). Iron was found to exist as Fe(0), Fe(II), and Fe(III) depending on the annealing temperature and spatial location within the film. A decrease in the concentration of a surface oxygen species was correlated with iron reduction. These results should help guide and enhance the design of perovskite materials for catalysts.

Introduction

LaFeO_3 (LFO) and $\text{LaFe}_{1-x}\text{M}_x\text{O}_3$ (where M = metal dopant) perovskite oxides can function as self-regenerating automotive exhaust catalysts[1], methane reformers to produce syngas[2], visible light photocatalysts[3], gas sensors[4,5], and as cathodes in solid oxide fuel cells (SOFCs)[6,7]. Iron-based perovskites are typically oxygen deficient[8,9], which in part explains the high oxide mobility within the material[10] and its suitability for certain catalytic applications such as oxygen reduction and ion transport in SOFCs. For these applications, the surface stoichiometry and transitional metal valence state can have a substantial impact on the redox chemistry. Calculations have shown that oxygen reduction occurs preferentially on FeO_2 -terminated LFO (010) surface rather than the LaO-type termination[11]. In addition, simulations suggest the termination on LFO (001) can significantly affect Pd migration into the perovskite lattice, an important result for automotive exhaust “intelligent catalysts”[12]. Aside from the surface termination, atomic vacancies are also predicted to have practical consequences for LFO catalysts. The impact of oxygen vacancies at the LFO (010) surface on CO adsorption was studied by first-principles calculations, with the adsorbate predicted to donate charge on a stoichiometric surface and accept charge when adsorbed on an oxygen deficient surface[13]. Given the range of environments in which these materials operate, it is important to

understand their surface properties after both oxidizing and reducing treatments.

The goal of this study was to probe the chemical stability of the reduced surface of a high quality model perovskite oxide with angle-resolved x-ray photoelectron spectroscopy (XPS). The ionic conductor yttria-stabilized zirconia (YSZ) was chosen as a substrate due to its lattice match with LFO as well as the potential suitability of LFO/YSZ type materials for SOFC applications[14]. A LFO thin film was processed and analyzed *in situ* to avoid contamination and to assist in unambiguous interpretation of the XPS spectra. Angle-resolved XPS studies highlight the substantial differences between the surface and bulk of the film and have implications for LFO's catalytic activity.

Experimental Methods

The LFO thin film with thickness of ~ 60 nm was grown by molecular beam epitaxy (MBE) on (001)-oriented Y-ZrO₂ (YSZ) substrates. The substrate was loaded into an ultrahigh vacuum chamber and heated at 750 °C for 20 minutes in an oxygen partial pressure of 6.0×10^{-6} Torr prior to growth. La and Fe were evaporated from high-temperature effusion cells. Flux rates were calibrated using a quartz crystal microbalance (QCM) positioned at the substrate position and *ex situ* Rutherford backscattering

spectrometry (RBS) measurements[15]. The substrate temperature was set to 700 °C and O₂ partial pressure was kept at $\sim 3.5 \times 10^{-6}$ Torr during growth.

Orientation and film quality were investigated using high-resolution x-ray diffraction (HRXRD) with a Philips X'Pert Materials Research Diffractometer (MRD) equipped with a fixed Cu anode operating at 45 kV and 40 mA. A hybrid monochromator, consisting of four-bounce double crystal Ge (220) and a Cu x-ray mirror, was placed in the incident beam path to generate monochromatic Cu K α x-rays ($\lambda = 1.54056$ Å) with a beam divergence of 12 arc seconds.

RBS measurements were carried out using 2 MeV helium ions at normal incidence (full details of the accelerator setup can be found elsewhere[16]). The backscattering spectra were collected using a silicon surface barrier detector which was positioned at a scattering angle of 150°. The SIMNRA simulation program was used to model the experimental RBS spectrum collected in a random incident direction[17]. In these simulations, the sample is divided into several thin layers of variable thickness and composition. Experimental parameters such as incident ion energy, atomic number of the incident ion, scattering angles, solid angle of detection, and the total charge deposited by the incident beam were used to simulate the experimental spectrum. The composition profiles and film areal density (in units of atoms/cm²) were then varied until the best fit to the experimental data was obtained.

The LFO/YSZ samples were exposed to ambient air after synthesis and transferred into the XPS system, which is attached to an auxiliary processing chamber. The sample was fixed to a sample holder using molybdenum clips on top of a molybdenum heating plate. During heating, the plate was biased and heated by electron beam irradiation of the molybdenum plate. Flowing liquid nitrogen cooled the sample by means of conduction via the sample holder. A type-K thermocouple contacted the sample surface and was held in place by molybdenum clips.

In the auxiliary chamber the sample was initially heated to 600 °C in 1.0×10^{-6} Torr O₂ for 10 minutes to remove adventitious carbon and oxidize the sample. For vacuum annealing, the sample was heated in 100 °C increments with a base pressure between $1.0\text{-}2.0 \times 10^{-9}$ Torr, and a 10 minute holding time at each temperature. After cooling to room temperature the sample was transferred into the XPS chamber for analysis, and the vacuum annealing process was repeated up to 700 °C. The heating rate was 1-2 °C/sec, and the cooling rate was 2-4 °C/sec.

Monochromatized Al K α x-rays were used in this study along with an analyzer pass energy of 23.5 eV. All spectra were calibrated to the binding energy (BE) of the O 1s lattice oxygen peak at 530.0 eV[18]. PHI MultiPak software was used for atomic concentration quantification using the O 1s, Fe 3p, and La 4d core levels, while CasaXPS was used for peak fitting. The O

1s spectra were fit with a Shirley background and Gaussian-Lorentzian line shapes, with the peaks' Gaussian character assumed to be 90%.

The mean escape depth (MED) of electrons at take off angles (θ) of 10° versus 45° are estimated to give a sense of the relative surface sensitivity. The inelastic mean free path (IMFP) of LaFeO_3 was estimated to be 2.4 nm using the NIST Standard Reference Database 71[19] and TPP-2M equation[20], with values for the band gap and density of the compound taken from other experimental studies[21,22]. Ignoring the effects of elastic-electron scattering, the MED is equal to the IMFP multiplied by the sine of the take-off angle. For 10° and 45° , the MED is 0.4 and 1.7 nm respectively. However, because elastic-electron scattering is typically not negligible, MEDs may be as much as twice as large at near-grazing angles as values calculated using the formula above[23].

Transmission electron microscopy (TEM) was performed using an FEI Titan 80-300 operated at 300 kV. High angle annular dark field scanning TEM (HAADF-STEM) images were collected with an inner angle >50 mrad. Cross-sections were extracted for TEM using an FEI Helios Dual beam focused ion beam and scanning electron microscope (FIB/SEM) equipped with an Omniprobe micromanipulator, following a typical liftout approach with a final cleaning at 2 kV.²⁴

Results and Discussion

The crystalline structure of the as-grown LFO film was characterized by θ -2 θ XRD, as shown in Fig. 8.1. Two strong reflections attributed to the (002) and (004) planes of YSZ are located at 34.89° and 73.63° respectively. Two additional peaks centered at 32.31° and 67.55° are associated with reflections of LFO (002) and (004) planes. The absence of peaks related to other planes in the XRD spectrum in combination with in-plane XRD measurements (not shown) and TEM data (discussed below) suggests that the film is highly oriented along the $\langle 001 \rangle$ direction. Out-of-plane lattice parameters determined by XRD are 5.540 \AA for LFO and 5.140 \AA for YSZ, resulting in a lattice mismatch of 7.8%.

This mismatch helps explain the spotty patterns observed during and after film growth by reflection high-energy electron diffraction (RHEED). The post-growth RHEED pattern is shown in Fig.8.2. The pattern suggests the growth proceeded in island mode, where three dimensional clusters coalesce to form a two dimensional layer.

Additional characterization of the film quality was performed by high-energy ion channeling. RBS spectra collected in channeling and random directions from the as grown sample are shown in Fig. 8.3(a). The leading edge of the Y/Zr plateau is shifted to lower energy due to ion energy lost when passing through the LFO film. SIMNRA was used to calculate the random spectrum shown in Fig. 8.3(a) and the spectrum is also shown (solid

line) in the figure. The stoichiometry of the film was consistent with La:Fe:O = 1:1:3 by comparison of the RBS spectra to calculated spectra for a 52 nm thick film.

The surface and/or interface peaks are not clearly visible in the channeling spectrum. The absence of these peaks indicates that the film is slightly misoriented with respect to the substrate. A small energy window at the center of the La channeling spectrum was used to calculate the minimum yield (χ_{\min}) of La. Another small energy window near the substrate Zr edge was used to calculate the minimum yield for Zr in the substrate. The minimum yield is the ratio of the yield in the channeling direction to that for a random direction. For the film, χ_{\min} for La is calculated to be 24%. This minimum yield is relatively high compared to the minimum yield measured from highly epitaxial films (usually lower than 4%). This increase is likely due to disorder in the film as evident from the TEM images shown in Fig. 8.4. Similarly, the minimum yield for the YSZ substrate (χ_{\min} for Zr = 21%) was also high compared to a bare YSZ substrate ($\chi_{\min} = 4.9\%$)[25]. High dechanneling in the film and disorder at the interface could have caused this increase in the minimum yield.

Normalized angular yield curves for La in the film and Zr in the substrate are shown in Fig. 8.3(b). The energy regions that were used to calculate the minimum yields were also used to extract the angular yield

curves. The solid line through the points is provided to guide the eye.

Aligned (channeling RBS) spectra were collected at the beginning and at the end of the each angular yield scan to check for any possible sample damage. No significant damage was observed during these measurements. In general both angular yield curves show very narrow angular widths. Since the variation of yield as a function of polar angle is similar for both La and Zr, most of the atomic rows of La in the film are parallel to the atomic rows of Zr in the substrate.

These results are consistent with observations from STEM imaging of the vacuum annealed LFO/YSZ film, where much of the LFO film appeared highly oriented but defective regions were also observed. A high resolution image of one region is seen in Fig. 8.4(a). Here the LFO is observed along the [010] zone axis and periodic edge dislocations are seen at the YSZ-LFO interface every 12 YSZ atomic planes, which gives an estimate of the lattice mismatch equal to ~8%. The high resolution image in Fig. 8.4(b) shows a second region of the film with a different LFO orientation. Although most of the LFO film grew in a single orientation from the substrate to film surface resulting in a single grain boundary, the defects and multiple orientations shown in Fig. 8.4 help explain the high channeling yield observed in the RBS data.

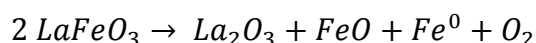
Fe 2p and valence band XPS spectra are shown in Fig. 8.5 for take-off angles of 10° and 45° and three different sample heating treatments. These

include after the film was oxidized at 600 °C, and after heating in vacuum to 400 °C and 700 °C. With regard to the La 3d and O 1s core level spectra, no major changes were observed for La with respect to take-off angle or heating, with the main La 3d_{5/2} peak remaining virtually unchanged at 834.6 eV. The O 1s spectra will be discussed in more detail below.

Little change occurs in the Fe 2p spectra with reduction for $\theta = 45^\circ$, with the exception of a very slight broadening of the main Fe 2p_{3/2} peak on the low BE side. Initially, the BE of the Fe 2p_{3/2} peak was at 710.9 eV after oxidation indicating that iron was present in the Fe³⁺ oxidation state[26]. After annealing in UHV, some of the Fe³⁺ was reduced to Fe²⁺, which has a characteristic Fe 2p_{3/2} BE position near 709.0 eV[26]. More substantial changes are seen in the $\theta = 10^\circ$ spectra. At this glancing emission angle, the broadening in the Fe 2p_{3/2} is more pronounced, with Fe reduction clearly evident at 400 °C. Heating to 700 °C induced further Fe reduction to Fe⁰. The increased peak intensity at 706.9 eV and 720.0 eV are indicative of iron metal[27], and thus a mixture of Fe³⁺, Fe²⁺, and Fe⁰ was present after this heating treatment. This presence of iron metal is also correlated with the increased density of states near the Fermi level seen in the valence band spectra. In other studies where LaFeO₃ was reduced in hydrogen atmosphere it was observed that Fe³⁺ reduced directly to Fe⁰ without a Fe²⁺ intermediate[28,29]. The presence of Fe²⁺ in this work shows that Fe

reduction can proceed sequentially and that Fe^{2+} is stable under certain conditions, which could impact this material's use in catalytic applications[30].

Coincident with formation of Fe^0 after heating to 700 °C, the Fe concentration decreases substantially at the surface as seen in Fig. 8.6, with a resultant increase in La concentration. A surface termination change might partially explain this result. Calculations have shown that for LaFeO_3 (001) the LaO termination is thermodynamically favored versus the FeO_2 termination under UHV conditions at 1000 K[12]. XPS analysis has also shown a temperature-dependent switch in the termination of LaAlO_3 [31], which was believed to stem from oxygen deficiencies in the first atomic layer. Another possibility is that the surface decomposed into Fe metal and La_2O_3 with Fe diffusion into the bulk. A possible mechanism is given by



No substantial change in the La $3d_{5/2}$ BE is expected in this case due to the similar BEs of the core level in La_2O_3 [27,32] and LFO. The absence of an accompanying change in the La 3d spectra suggests that the reduced Fe may be nucleating in small metal particles. The loss of O_2 is consistent with the O 1s peak fitting results discussed below, where the surface oxygen peak decreases with increasing temperature. An additional complicating factor is the decrease in unit cell volume that would result from decomposition and the

attendant increase in surface roughness, which could particularly affect the XPS results at the shallow take-off angle[33].

Peak fitting results are shown in Fig. 8.7 for the O 1s spectra. Initially the oxidized, $\theta = 45^\circ$ spectrum was fit using three components, one fixed at BE = 530.0 eV which was assigned to lattice oxygen and two other peaks, with all three constrained to have the same full width at half maximum (FWHM). These peak assignments were then used to fit the remaining spectra while allowing for changes in peak areas and surface oxygen BE, with the FWHM allowed to vary by ± 0.05 eV.

For the O 1s $\theta = 45^\circ$ spectra there are virtually no changes between the three sample conditions besides a downward shift of 0.25 eV of the highest BE peak after annealing. This peak is located 1.9-2.2 eV greater than lattice oxygen and comprised $\sim 3\%$ of the total peak area, while the other high BE shoulder is located ~ 1.0 eV higher than lattice oxygen and accounted for $\sim 15\%$ of the total O 1s peak. The O 1s spectra at the smaller take-off angle are visibly broader than their larger take-off angle counterparts due to the increased peak areas of the higher BE components. The highest BE component decreases from 11% to 6% with annealing, while the intermediate O 1s feature decreases from 37% to 19%. The fact that the area of these peaks increases for the smaller take-off angle indicates that they are related to surface oxygen species. Although annealing in UHV can create surface

oxygen vacancies[34], it is unlikely that these peaks are related to oxygen vacancies as the peak areas decrease with annealing rather than increase. Given the BE difference of the highest BE peak and lattice oxygen and the peak's relatively small peak area, the high BE peak is attributed to low level adsorption of background gases. No signature for carbon was present during XPS analysis, so water and/or molecular oxygen adsorbed during sample cooling and transfer are the most likely species. The intermediate oxygen peak is then attributed to a surface oxygen species, consistent with the higher BEs seen for surface oxygen in perovskites[35,36]. The decrease in peak area upon annealing of this intermediate peak is then related to the surface dynamics discussed above, namely the altered stoichiometry and decomposition.

Conclusion

The growth of LFO on YSZ was highly oriented as judged by XRD, RBS, and TEM data, however the film was not single crystalline due to the existence of several different crystalline domains observed in HRTEM images. A relatively high channeling yield compared to epitaxial films resulted from the multicrystalline nature of the LFO film. The lattice mismatch between LFO and YSZ may prevent epitaxial, defect free growth. After film growth, significant differences were detected with angle-resolved XPS

between the surface and bulk of the film, with a surface oxygen species present at higher concentration in the grazing-emission spectra. Annealing the film in UHV resulted in the sequential reduction of Fe, from Fe^{3+} to Fe^{2+} to Fe^0 . A greater degree of reduction took place at the surface, and the formation of Fe^0 likely resulted from surface decomposition. The redox properties of the LFO surface were sensitive to the experimental annealing conditions. This sensitivity suggests that appropriate methods may be developed to control the surface properties to suit a particular gas sensing or catalytic application.

References:

- [1] Y. Nishihata, J. Mizuki, T. Akao, H. Tanaka, M. Uenishi, M. Kimura, T. Okamoto, and N. Hamada, "Self-regeneration of a Pd-perovskite catalyst for automotive emissions control," *Nature*, vol. 418, pp. 164-167, 2002.
- [2] M. R. Goldwasser, M. E. Rivas, M. L. Lugo, E. Pietri, J. Perez-Zurita, M. L. Cubeiro, A. Griboval-Constant, and G. Leclercq, "Combined methane reforming in presence of CO_2 and O_2 over $\text{LaFe}_{1-x}\text{CO}_x\text{O}_3$ mixed-oxide perovskites as catalysts precursors," *Catal. Today*, vol. 107-108, pp. 106-113, 2005.
- [3] H. J. Su, L. Q. Jing, K. Y. Shi, C. H. Yao, and H. G. Fu, "Synthesis of large surface area LaFeO_3 nanoparticles by SBA-16 template method as high active visible photocatalysts," *J. Nanopart. Res.*, vol. 12, pp. 967-974, 2010.
- [4] N. N. Toan, S. Saukko, and V. Lantto, "Gas sensing with semiconducting perovskite oxide LaFeO_3 ," *Physica B*, vol. 327, pp. 279-282, 2003.

- [5] X. F. Wang, H. W. Qin, L. H. Sun, and J. F. Hu, "CO₂ sensing properties and mechanism of nanocrystalline LaFeO₃ sensor," *Sensor. Actuat. B*, vol. 188, pp. 965-971, 2013.
- [6] S. P. Simner, J. R. Bonnett, N. L. Canfield, K. D. Meinhardt, J. P. Shelton, V. L. Sprenkle, and J. W. Stevenson, "Development of lanthanum ferrite SOFC cathodes," *J. Power Sources*, vol. 113, pp. 1-10, 2003.
- [7] S. V. Chavan, and R. N. Singh, "Preparation, properties, and reactivity of lanthanum strontium ferrite as an intermediate temperature SOFC cathode," *J. Mater. Sci.*, vol. 48, pp. 6597-6604, 2013.
- [8] N. Yamazoe, "Oxidation Catalysis of Perovskites --- Relationships to Bulk Structure and Composition (Valency, Defect, etc.)," *Catal. Today*, vol. 8, pp. 175-199, 1990.
- [9] J. L. G. Fierro, and L. G. Tejuca, "Non-stoichiometric Surface Behavior of LaMO₃ Oxides as Evidenced by XPS," *Appl. Surf. Sci.*, vol. 27, pp. 453-457, 1987.
- [10] M. A. Pena, and J. L. G. Fierro, "Chemical Structures And Performance Of Perovskite Oxides," *Chem. Rev.*, vol. 101, pp. 1981-2017, 2001.
- [11] C. W. Lee, R. K. Behera, S. Okamoto, R. Devanathan, E. D. Wachsman, S. R. Phillpot, and S. B. Sinnott, "Stabilization Mechanisms of LaFeO₃ (010) Surfaces Determined with First Principles Calculations," *J. Am. Ceram. Soc.*, vol. 94, pp. 1931-1939, 2011.
- [12] B. H. Li, M. B. Katz, Q. J. Zhang, L. Chen, G. W. Graham, and X. Q. Pan, "Surface-termination-dependent Pd bonding and aggregation of nanoparticles on LaFeO₃ (001)," *J. Chem. Phys.*, vol. 138, pp. 144705, 2013.
- [13] L. H. Sun, J. F. Hu, H. W. Qin, M. Zhao, and K. Fan, "Influences of Ca Doping and Oxygen Vacancy upon Adsorption of CO on the LaFeO₃ (010) Surface: A First-Principles Study," *J. Phys. Chem. C*, vol. 115, pp. 5593-5598, 2011.

- [14] E.N. Armstrong, K.L. Duncan, and E.D. Wachsman, "Effect of A and B-site cations on surface exchange coefficient for ABO_3 perovskite materials," *Phys. Chem. Chem. Phys.*, vol. 15, pp. 2298-2308, 2013.
- [15] L. Qiao, K. H. L. Zhang, M. E. Bowden, T. Varga, V. Shutthanandan, R. Colby, Y. Du, B. Kabius, P. V. Sushko, M. D. Biegalski, and S. A. Chambers, "The Impacts of Cation Stoichiometry and Substrate Surface Quality on Nucleation, Structure, Defect Formation, and Intermixing in Complex Oxide Heteroepitaxy- LaCrO_3 on $\text{SrTiO}_3(001)$," *Adv. Funct. Mater.*, vol. 23, pp. 2953-2963, 2013.
- [16] S. Thevuthasan, C. H. F. Peden, M. H. Engelhard, D. R. Baer, G. S. Herman, W. Jiang, Y. Liang, and W. J. Weber, "The ion beam materials analysis laboratory at the environmental molecular sciences laboratory," *Nucl. Instr. Meth. A*, vol. 420, pp. 81-89, 1999.
- [17] M. Mayer, SIMNRA User's Guide, Report IPP 9/113, Max-Planck-Institut für Plasmaphysik, Garching, Germany, 1997.
- [18] S. I. Yi, Y. Liang, S. Thevuthasan, and S. A. Chambers, "Morphological and structural investigation of the early stages of epitaxial growth of $\alpha\text{-Fe}_2\text{O}_3$ (0001) on $\alpha\text{-Al}_2\text{O}_3$ (0001) by oxygen-plasma-assisted MBE," *Surf. Sci.*, vol. 443, pp. 212-220, 1999.
- [19] C. J. Powell, and A. Jablonski, NIST Electron Inelastic-Mean-Free-Path Database, version 1.2, SRD 71; National Institute of Standards and Technology: Gaithersburg, MD, 2010.
- [20] S. Tanuma, C. J. Powell, and D. R. Penn, "Calculations Of Electron Inelastic Mean Free Paths. V. Data For 14 Organic-Compounds Over The 50-2000 eV Range," *Surf. Interface Anal.*, vol. 21, pp. 165-176, 1994.
- [21] T. Arima, Y. Tokura, and J. B. Torrance, "Variation of optical gaps in perovskite-type 3d transition-metal oxides," *Phys. Rev. B*, vol. 48, pp. 17006-17009, 1993.
- [22] Y. Matuura, S. Matsushima, M. Sakamoto, and Y. Sadaoka, " NO_2 -Sensitive LaFeO_3 Film prepared by Thermal Decomposition of the Heteronuclear Complex, $\{\text{La}[\text{Fe}(\text{CN})_6 \cdot 5\text{H}_2\text{O}]\}_x$," *J. Mater. Chem.*, vol. 3, pp. 767-769, 1993.

- [23] C. J. Powell, A. Jablonski, I. S. Tilinin, S. Tanuma, and D. R. Penn, "Surface sensitivity of Auger-electron spectroscopy and X-ray photoelectron spectroscopy," *J. Electron Spectrosc.*, vol. 98, pp. 1-15, 1999.
- [24] L. A. Gianuzzi, J. L. Drown, S. R. Brown, R. B. Irwin, and F. A. Stevie, "Applications of the FIB Lift-Out Technique for TEM Specimen Preparation," *Microsc. Res. Techniq.*, vol. 41, pp. 285-290, 1998.
- [25] V. Shutthanandan, S. Thevuthasan, Y. J. Kim, and C. H. F. Peden, "Channeling Studies of CeO_2 and $\text{Ce}_{1-x}\text{Zr}_x\text{O}_2$ Films on Yttria-Stabilized $\text{ZrO}_2(111)$," *Mat. Res. Soc. Symp. Proc.*, vol. 654, pp. AA2.6.1-AA2.6.6, 2001.
- [26] T. Yamashita, and P. Hayes, "Analysis of XPS spectra of Fe^{2+} and Fe^{3+} ions in oxide materials," *Appl. Surf. Sci.*, vol. 254, pp. 2441-2449, 2008.
- [27] J. F. Moulder, W. F. Stickle, P. E. Sobol, and K. D. Bomben, *Handbook of X-ray Photoelectron Spectroscopy*. Eden Prairie, MN, USA: Perkin-Elmer Corporation, 1992.
- [28] J. M. D. Tascon, J. L. G. Fierro, and L. G. Tejuca, "Physicochemical Properties Of LaFeO_3 - Kinetics of Reduction and of Oxygen Adsorption," *J. Chem. Soc., Faraday Trans. I*, vol. 81, pp. 2399-2407, 1985.
- [29] P. E. Marti and A. Baiker, "Influence of the A-site cation in AMnO_{3+x} and AFeO_{3+x} ($\text{A} = \text{La}, \text{Pr}, \text{Nd}$ and Gd) perovskite-type oxides on the catalytic activity for methane combustion," *Catal. Lett.*, vol. 26, pp. 71-84, 1994.
- [30] J. Suntivich, H. A. Gasteiger, N. Yabuuchi, H. Nakanishi, J. B. Goodenough, and Y. Shao-Horn, "Design principles for oxygen-reduction activity on perovskite oxide catalysts for fuel cells and metal-air batteries," *Nature Chem.*, vol. 3, pp. 546-550, 2011.
- [31] P. A. W. van der Heide and J. W. Rabalais, "Photoelectron spectroscopic study of the temperature-dependent termination of the $\text{LaAlO}_3(100)$ surface," *Chem. Phys. Lett.*, vol. 297, pp. 350-356, 1998.

- [32] D. D. Sarma and C. N. R. Rao, "XPES Studies of Oxides of Second- and Third-Row Transition Metals Including Rare Earths," *J. Electron Spectrosc.*, vol. 20, pp. 25-45, 1980.
- [33] P. L. J. Gunter, O. L. J. Gijzeman, and J. W. Niemantsverdriet, "Surface roughness effects in quantitative XPS: magic angle for determining overlayer thickness," *Appl. Surf. Sci.*, vol. 115, pp. 342-346, 1997.
- [34] M. A. Henderson, C. L. Perkins, M. H. Engelhard, S. Thevuthasan, and C. H. F. Peden, "Redox properties of water on the oxidized and reduced surfaces of $\text{CeO}_2(111)$," *Surf. Sci.*, vol. 526, pp. 1-18, 2003.
- [35] E. J. Crumlin, E. Mutoro, W. T. Hong, M. D. Biegalski, H. M. Christen, Z. Liu, H. Bluhm, and Y. Shao-Horn, "In Situ Ambient Pressure X-ray Photoelectron Spectroscopy of Cobalt Perovskite Surfaces under Cathodic Polarization at High Temperatures," *J. Phys. Chem. C*, vol. 117, pp. 16087-16094, 2013.
- [36] P. A. W. van der Heide, "Systematic x-ray photoelectron spectroscopic study of $\text{La}_{1-x}\text{Sr}_x$ -based perovskite-type oxides," *Surf. Interface Anal.*, vol. 33, pp. 414-425, 2002.

Figures

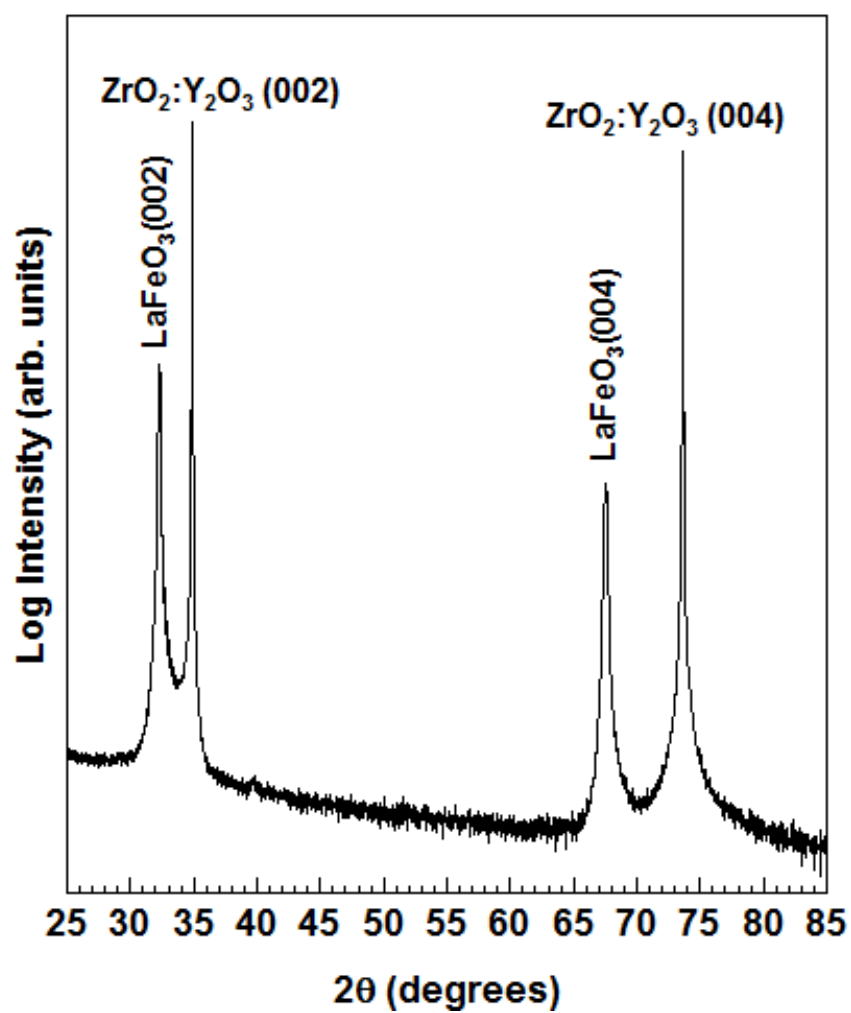


Figure 8.1 - XRD spectrum of LFO(001) grown on YSZ(001) at 700 °C.

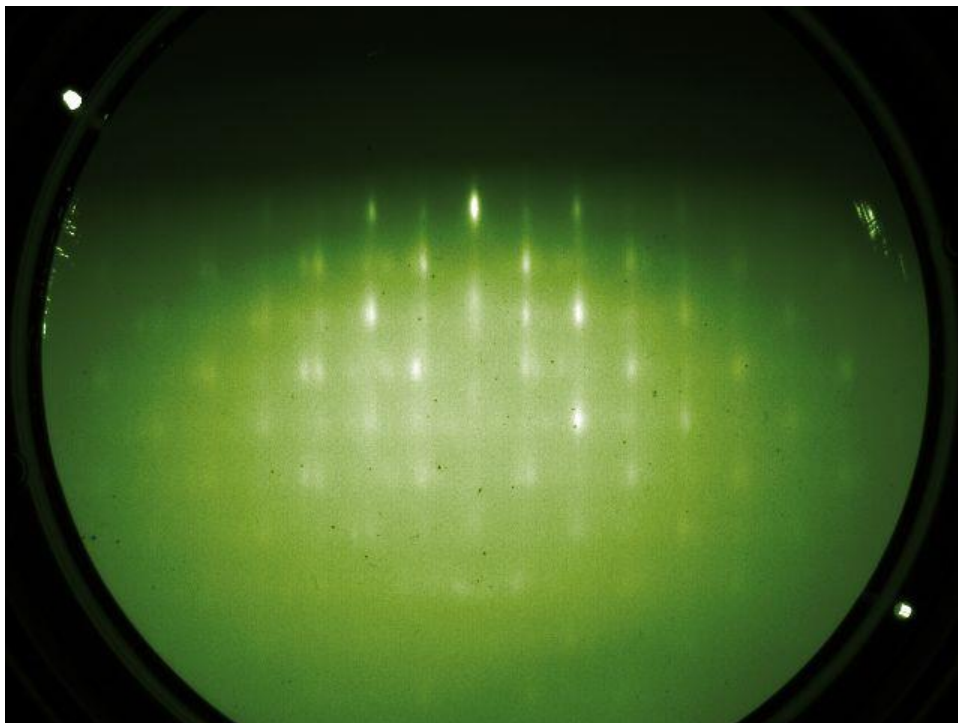


Figure 8.2 – Post-growth RHEED pattern of LFO(001) grown on YSZ(001) at 700 °C.

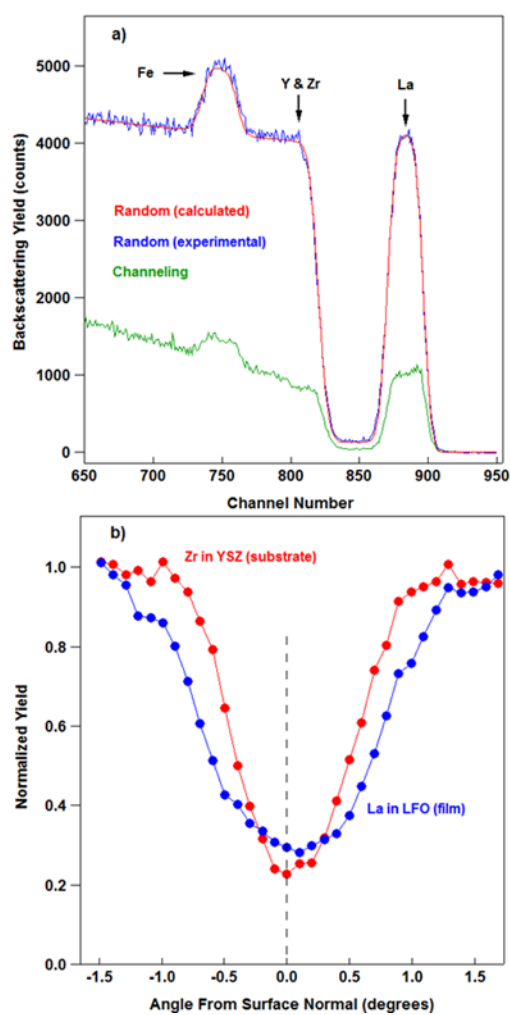


Figure 8.3 - (a) Channeling and random RBS spectra along with the SIMNRA calculated result for the as-grown LFO film on YSZ. (b) Normalized angular yield curves from La in the film and Zr in the substrate. In both cases, the incident energy of the helium beam was 2 MeV and the scattering angle was 150° .

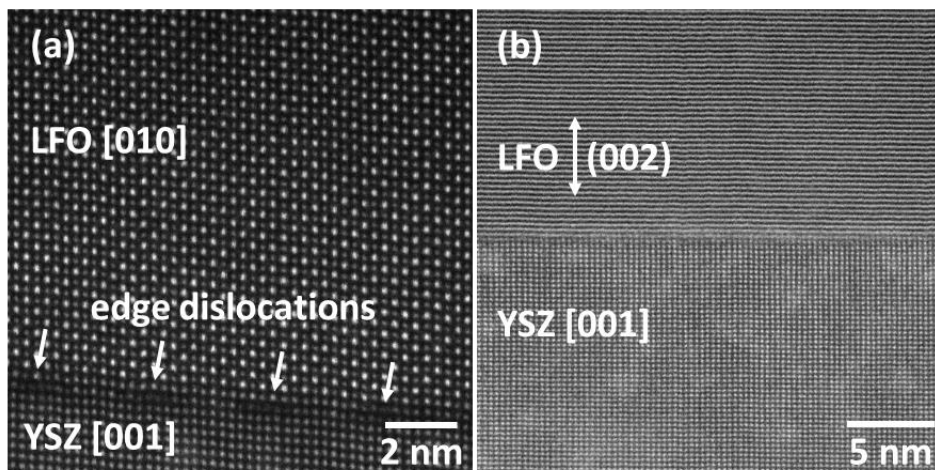


Figure 8.4 - HAADF-STEM images at different locations of the LFO/YSZ film.

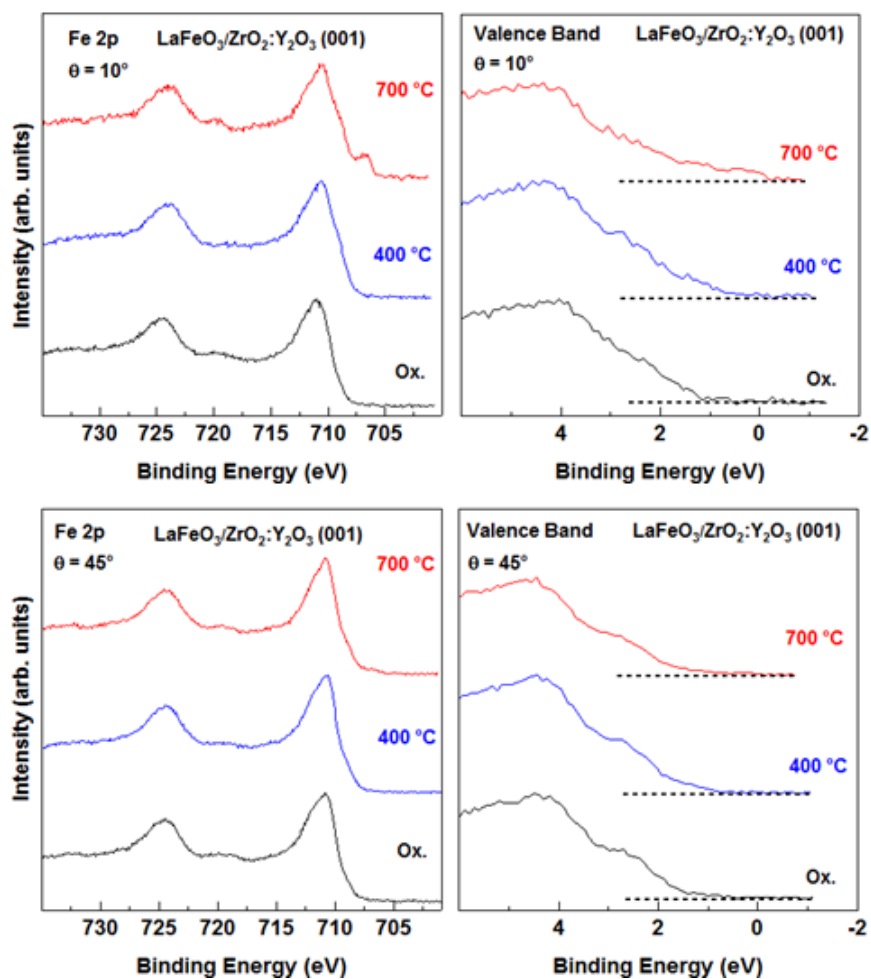


Figure 8.5 - 10° (top) and 45° (bottom) emission spectra from LFO/YSZ film oxidized and annealed in vacuum.

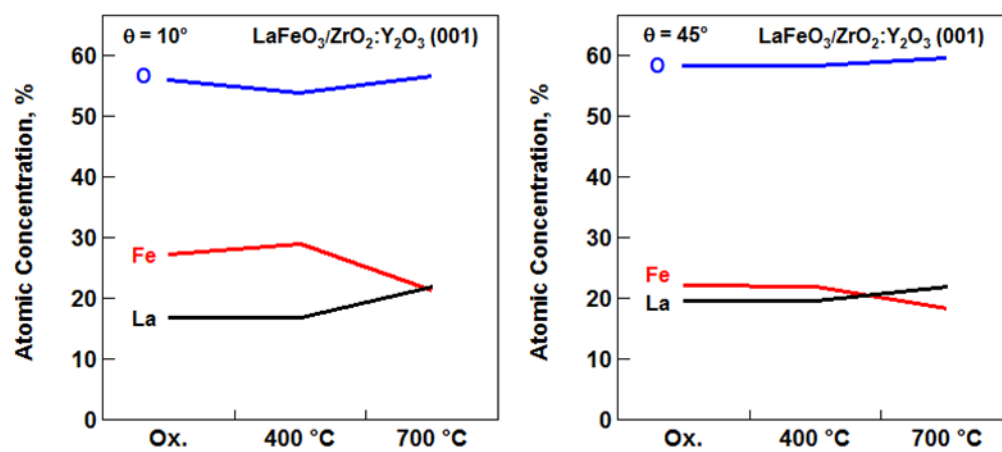


Figure 8.6 - Atomic concentrations from 10° (left) and 45° (right) emission spectra of LFO/YSZ film.

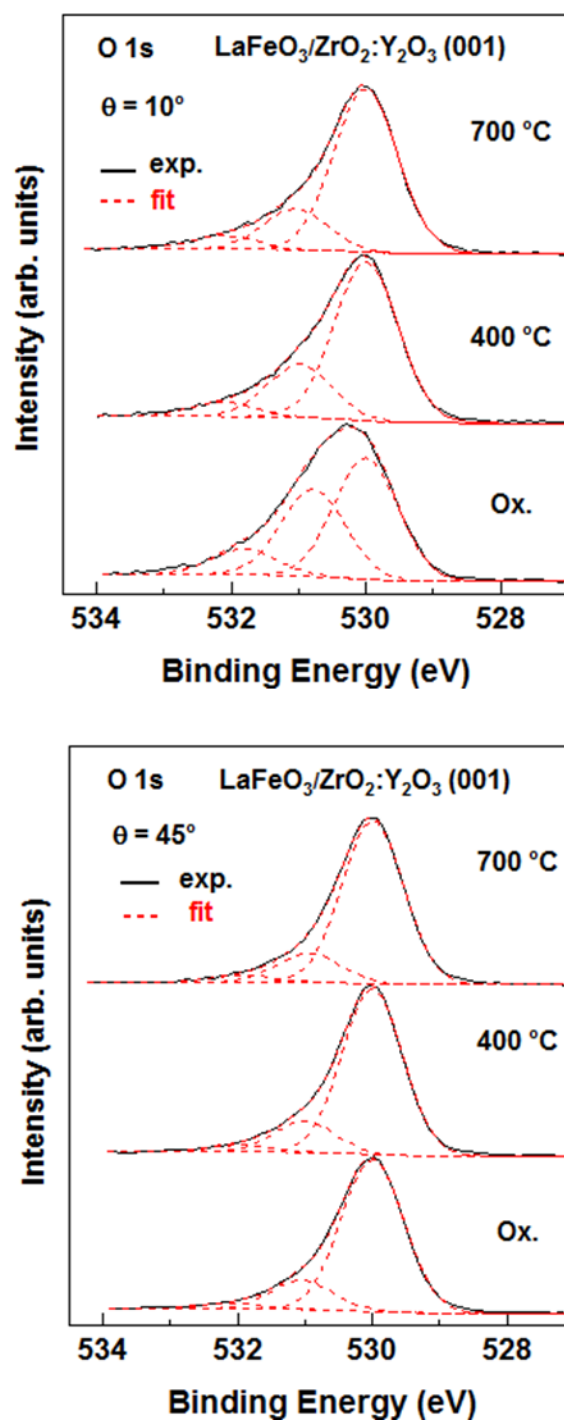


Figure 8.7 - Peak fits of O 1s spectra.

CHAPTER 9

CONCLUSION AND FUTURE DIRECTIONS

This dissertation explored ways to meet future technological and energy demands that call for greater device performance and efficiency. It was shown that usable solar absorbing inks could be made by alternative processing methods. Microwave-assisted synthesis of $\text{Cu}_2\text{ZnSnS}_4$ nanoparticles enabled a lower reaction temperature and shorter reaction time relative to most of the reports in the literature. The composition of the nanoparticles was controlled by varying the precursor concentrations, which is an important result since the highest performing CZTS solar cells to date have had off-stoichiometric compositions. As a proof-of-concept, CZTS solar cells were made with a device efficiency of 0.25%.

The microwave-assisted synthesis of CZTS was done in a batch process, but a scalable approach was demonstrated using a continuous flow reactor. A controlled, segmented flow was achieved by applying fluid mechanics principles, which led to enhanced mixing of the reactant precursors compared to laminar flow regimes. It was found that the growth of CZTS nanoparticles proceeds first by the nucleation of Cu_{2-x}S , with the subsequent incorporation of Sn^{4+} and then Zn^{2+} cations. As in the case of the microwave-assisted synthesis, no complex organic additives were used for the continuous flow process.

The dehydration and XPS study of HafSO_x showed that direct control over the film chemistry and surface acidity is possible through optimization of annealing temperatures and water exposures to dehydrated films. Sulfur was

found to exist in sulfate form independent of the degree of dehydration. The O 1s spectra were fit with three components corresponding to Hf-O, OH, and SO₄. Water exhibited a maximum desorption rate near 475 K, with desorption persisting up to 750 K. The surface acid sites of dehydrated HafSO_x were probed with D₂O adsorption/desorption, where D₂O was found to desorb by both molecular and dissociative pathways, with the TPD spectrum indicative of a broad range of adsorption sites.

Peroxide containing HafSO_x films were studied with XPS, TPD and ESD. The surface was found to be slightly sulfate rich, with composition given by $\text{Hf}(\text{OH})_{1.4}(\text{O}_2)_{0.5}(\text{SO}_4)_{0.8} \cdot q\text{H}_2\text{O}$. The thermal desorption energy of O₂ was 1.3 eV, which likely resulted from decomposition of the hafnium-peroxo species. O₂ desorbed from peroxide containing films using TPD and ESD but not from those without peroxide. This supports the hypothesis that peroxo ligands reduce the degree of Hf-O-Hf formation and enable the patternability of HafSO_x. Total desorption cross sections for O₂ were established for primary electron energies ranging from 500-2000 eV, ranging from $10^{-15} - 10^{-16} \text{ cm}^2$.

XPS analysis of the Pt/a-IGZO interface revealed that it is quite reactive, with Pt deposition inducing the reduction of a finite amount of In from In³⁺ to In⁰. Due to the absence of significant line shape changes in the Pt, Ga, and Zn core levels that would indicate alloying, the In reduction reveals that In is segregating from a-IGZO. A Schottky barrier height of 0.25 eV was

experimentally determined for the Pt/a-IGZO interface, which is lower than what is expected under ideal conditions and results from the reactive interface. Annealing the interface in UHV resulted in the formation of Pt islands.

Molecular beam epitaxial growth of LFO on YSZ resulted in a high quality, nearly single crystalline film. TEM and RBS channeling analysis provided evidence for multiple crystallographic orientations present in the film, however XRD data indicates that the film was largely single crystalline. XPS analysis revealed that the surface stoichiometry and bonding environment differed quantitatively from the bulk. It was also shown that the film's surface was sensitive to UHV annealing, with the initial Fe^{3+} being sequentially reduced to Fe^{2+} and finally Fe^0 .

Looking ahead to future studies, a logical progression in the CZTS work is to combine the benefits of microwave heating with segmented, continuous flow processing to produce high quality CZTS nanoparticles. This work has in fact begun in earnest within the Herman lab group using a custom designed microwave flow reactor. Densification of the deposited nanoparticles to form an adequately dense film for solar cell applications with minimal defects remains a challenge. Dense films can be formed by annealing the film in a confined vessel (e.g. graphite box) with selenium overpressure, but alternative annealing approaches should be considered that are more amenable to large scale manufacturing. The high selenium

vapor pressure typically used to densify CZTS nanoparticles (and form CZTSSe) forms an unfavorable MoSe_2 layer in standard device architectures, and one method to avoid confined annealing with the resultant MoSe_2 formation would be to use high-powered optical sources such as lasers to anneal the film. The efficiency of pure sulfide CZTS cells lags behind CZTSSe and CIGS cells, but pursuing the sources of the decreased efficiency is merited on one level due to the close lattice match of CZTS and Si, and thus the possibility exists to form highly efficient tandem solar cells from these materials with complementary band gaps.

A practical next step for HafSO_x characterization is measuring the catalytic activity for the isomerization of n-butane. The catalytic activity for this reaction could be measured as a function of the relative amount Brønsted-Lowry vs. Lewis acid sites, which can be controlled by the appropriate choice of annealing conditions. The patterning sensitivity of HafSO_x may be further improved by doping with other metals, where total desorption cross sections of O_2 could be measured with electron stimulated desorption as a function of the metal species and its concentration.

It would be extremely valuable to incorporate the capabilities of a semiconductor parameter analyzer inside a UHV system to enable fabrication and characterization of Pt/a-IGZO devices in a pristine environment. In practice, a two terminal connection would be needed to test memristor operation. A Pt/a-IGZO/Pt memristor could be fabricated *in situ*,

characterized by XPS, and finally tested by application of a bias to switch the memristor from a high-resistive state to a low-resistive state and back again. Additional processing such as annealing the deposited Pt layer under a partial pressure of O_2 could change the interfacial barrier height and its effect on device performance could be quantified. A three terminal connection could be used to test a-IGZO transistor operation under the influence of H_2O or O_2 , which is currently a relevant area of research.

LFO would also be a prime candidate for *in situ* catalysis testing, where the surface properties of the film could be altered by annealing and the film's conductivity measured under the influence of relevant gases such as CO_2 , H_2O , and O_2 as a measure of the film's gas sensing capabilities. Low energy electron diffraction could provide insight into the dynamic nature of the LFO film during annealing and help determine if the surface undergoes reconstruction. X-ray absorption spectroscopy of the LFO film would quantitatively reveal the degree of Fe-O hybridization as the oxidation state of Fe changes with annealing, which would be useful as the amount of hybridization or covalency of the Fe-O bond is known to affect catalytic efficacy in certain applications.

Bibliography

- [1] IEA-ETSAP and IRENA Technology Brief E11 – January 2013. [Online]. Available: <http://www.irena.org/DocumentDownloads/Publications/IRENA-ETSAP%20Tech%20Brief%20E11%20Solar%20PV.pdf>

- [2] A. Goodrich, P. Hacke, Q. Wang, B. Sopori, R. Margolis, T. L. James, and M. Woodhouse, “A wafer-based monocrystalline silicon photovoltaics road map: Utilizing known technology improvement opportunities for further reductions in manufacturing costs,” *Sol. Energy Mater. Sol. Cells*, vol. 114, pp. 110-135, 2013.

- [3] V. Fthenakis, “How Long Does it Take for Photovoltaics To Produce the Energy Used?” *PE Magazine*, January-February 2012. [Online]. Available: http://www.clca.columbia.edu/236_PE_Magazine_Fthenakis_2_10_12.pdf

- [4] C. Wadia, A. P. Alivisatos, D. M. Kammen, “Materials Availability Expands the Opportunity for Large-Scale Photovoltaics Deployment,” *Environ. Sci. Technol.*, vol. 43, pp. 2072-2077, 2009.

- [5] U.S. Geological Survey, Mineral commodity summaries 2014, pp.1-196.

- [6] M. Woodhouse, A. Goodrich, R. Margolis, T.L. James, M. Lokanc, and R. Eggert, “Supply-Chain Dynamics of Tellurium, Indium, and Gallium Within the Context of PV Manufacturing Costs,” *IEEE Journal of Photovoltaics*, vol. 3, pp. 833-837, 2013.

- [7] T. Todorov and D. B. Mitzi, “Direct Liquid Coating of Chalcopyrite Light-Absorbing Layers for Photovoltaic Devices,” *Eur. J. Inorg. Chem.*, vol. 2010, pp. 17-28, 2010.

- [8] M. A. Green, “Silicon Wafer-Based Tandem Cells: The Ultimate Photovoltaic Solution?” *Proc. of SPIE*, vol. 8981, pp. 89810L-1 – 89810L-6, 2014.

- [9] R. P. Oleksak, R. E. Ruther, F. Luo, K. C. Fairley, S. R. Decker, W. F. Stickle, D. W. Johnson, E. L. Garfunkel, G. S. Herman, and D. A. Keszler, "Chemical and Structural Investigation of High-Resolution Patterning with HfSO_x ," *ACS Appl. Mater. Interfaces*, vol. 6, pp. 2917-2921, 2014.
- [10] V. M. Akhmedov and S. H. Al-Khowaiter, "Recent Advances and Future Aspects in the Selective Isomerization of High n-Alkanes," *Catal. Rev.*, vol. 49, pp. 33-139, 2007.
- [11] M. Hino, S. Kobayashi, and K. Arata, "Reactions of Butane and Isobutane Catalyzed by Zirconium Oxide Treated with Sulfate Ion. Solid Superacid Catalyst," *J. Am. Chem. Soc.*, vol. 101, pp. 6439-6441, 1979.
- [12] A. J. Telecky, "Photoresist and Ion-Exchange Chemistry of HfSO_x ," Ph.D. Dissertation, Oregon State University, 2012.
- [13] X. Thrun, K. -H. Choi, M. Freitag, A. Grenville, M. Gutsch, C. Hohle, J. K. Stowers, J. W. Bartha, "Evaluation of direct patternable inorganic spin-on hard mask materials using electron beam lithography," *Microelectron. Eng.*, vol. 98, pp. 226-229, 2012.
- [14] S. A. Chambers, "Epitaxial Growth and Properties of Doped Transition Metal and Complex Oxide Films," *Adv. Mater.*, vol. 22, pp. 219-248, 2010.
- [15] L. O. Chua, "Memristor – The Missing Circuit Element," *IEEE Trans. Circuit Theory*, vol. CT-18, pp. 507-519, 1971.
- [16] J. S. Rajachidambaram, "Evaluation of Amorphous Oxide Semiconductors for Thin Film Transistors (TFTs) and Resistive Random Access Memory (RRAM) Applications," Masters Thesis, Oregon State University, 2011.
- [17] S. J. Martin and R. G. M. Morris, "New Life in an Old Idea: The Synaptic Plasticity and Memory Hypothesis Revisited," *Hippocampus*, vol. 12, pp. 609-636, 2002.

- [18] A. M. White and H. S. Swartzwelder, "Age-Related Effects of Alcohol on Memory and Memory-Related Brain Function in Adolescents and Adults," *Recent Dev. Alcohol*, vol. 17, pp. 161-176, 2005.
- [19] T. V. P. Bliss and G. L. Collingridge, "A synaptic model of memory: long-term potentiation in the hippocampus," *Nature*, vol. 361, pp. 31-39, 1993.
- [20] R. M. Heck, R. J. Farrauto, and S. T. Gulati, *Catalytic Air Pollution Control: Commercial Technology*. New York, NY, USA: John Wiley & Sons, 2002.
- [21] Y. Nishihata, J. Mizuki, T. Akao, H. Tanaka, M. Uenishi, M. Kimura, T. Okamoto, and N. Hamada, "Self-regeneration of a Pd-perovskite catalyst for automotive emissions control," *Nature*, vol. 418, pp. 164-167, 2002.
- [22] J. T. Kummer, "Catalysts for Automobile Emission Control," *Prog. Energy Combust. Sci.*, vol. 6, pp. 177-199, 1980.
- [23] V. A. Fassel, "Quantitative Elemental Analyses by Plasma Emission Spectroscopy," *Science*, vol. 202, pp. 183-191, 1978.
- [24] M. S. Rajachidambaram, "Investigation of Oxide Semiconductor Based Thin Films: Deposition, Characterization, Functionalization, and Electronic Applications.," Masters Thesis, Oregon State University, 2011.
- [25] P. J. Goodhew, J. Humphreys, and R. Beanland, *Electron Microscopy and Analysis*. London, UK and New York, NY, USA: Taylor & Francis, 2001.
- [26] A. Weibel, R. Bouchet, F. Boulc'h, and P. Knauth, "The Big Problem of Small Particles: A Comparison of Methods for Determination of Particle Size in Nanocrystalline Anatase Powders," *Chem. Mater.*, vol. 17, pp. 2378-2385, 2005.

- [27] J. I. Langford and A. J. C. Wilson, "Scherrer after Sixty Years: A Survey and Some New Results in the Determination of Crystallite Size," *J. Appl. Cryst.*, vol. 11, pp. 102-113, 1978.
- [28] G. L. Hornyak, J. Dutta, H. F. Tibbals, and A. K. Rao, *Introduction to Nanoscience*. Boca Raton, FL, USA: CRC Press, 2008.
- [29] D. A. Skoog, F. J. Holler, and S. R. Crouch, *Principles of Instrumental Analysis*. Independence, KY, USA: Cengage Learning, 2007.
- [30] F. Krumeich, *Properties of Electrons, their Interactions with Matter and Applications in Electron Microscopy*. [Online]. Available: <http://www.microscopy.ethz.ch/downloads/Interactions.pdf>
- [31] Y. Liu, Electron Microscopy lecture notes, Oregon State University, 2011.
- [32] J. Pankrove, *Optical Processes in Semiconductors*. New York, NY, USA: Dover, 1975.
- [33] J. Nelson, *The Physics of Solar Cells*. London, UK: Imperial College Press, 2003.
- [34] X. Guo and J. T. Yates Jr., "Dependence of effective desorption kinetic parameters on surface coverage and adsorption temperature: CO on Pd(111)," *J. Chem. Phys.*, vol. 90, pg. 6761-6766, 1989.
- [35] P. A. Redhead, "Thermal Desorption of Gases," *Vacuum*, vol. 12, pp. 203-211, 1962.
- [36] R. D. Ramsier and J. T. Yates, "Electron-stimulated desorption - principles and applications," *Surf. Sci. Rep.*, vol. 12, pp. 243-378, 1991.
- [37] T. E. Madey, D. E. Ramaker, and R. Stockbauer, "Characterization of surfaces through electron and photon stimulated desorption," *Ann. Rev. Phys. Chem.*, vol. 35, pp. 215-240, 1984.
- [38] T. E. Madey and J. T. Yates, "Electron-Stimulated Desorption As A Tool For Studies Of Chemisorption - Review," *J. Vac. Sci. Technol.*, vol. 8, pp. 525-555, 1971.

- [39] D. M. Hercules and S. H. Hercules, "Analytical Chemistry of Surfaces. Part 1. General Aspects," *J. Chem. Educ.*, vol. 61, pp. 403-409, 1984.
- [40] C. S. Fadley in *Electron Spectroscopy: Theory, Techniques, and Applications. Volume 2* (Ed. C. R. Brundle and A. D. Baker), London, UK; New York, NY, San Francisco, CA, USA: Academic Press, 1978.
- [41] J. C. Rivière in *Practical Surface Analysis*. (Ed. D. Briggs and M. P. Seah), Tiptree, UK: Anchor Brendon, 1983.
- [42] A. Klein, "Transparent Conducting Oxides: Electronic Structure-Property Relationship from Photoelectron Spectroscopy with *in situ* Sample Preparation," *J. Am. Ceram. Soc.*, vol. 96, pp. 331-345, 2013.
- [43] W. F. Egelhoff and I. Jacob, "Reflection High-Energy Electron Diffraction (RHEED) Oscillations at 77 K," *Phys. Rev. Lett.*, vol. 62, pp. 921-924, 1989.
- [44] T. Terashima, Y. Bando, K. Iijima, K. Yamamoto, K. Hirata, K. Hayashi, K. Kamigaki, and H. Terauchi, "Reflection High-Energy Electron Diffraction Oscillations during Epitaxial Growth of High-Temperature Superconducting Oxides," *Phys. Rev. Lett.*, vol. 65, pp. 2684-2688, 1990.
- [45] S. Mehta, "State of the Solar Union: Present and Future," *IEEE Power and Energy Magazine*, vol. 9, pp. 96-94, 2011.
- [46] P. Jackson, D. Hariskos, E. Lotter, S. Paetel, R. Wuerz, R. Menner, W. Wischmann, and M. Powalla, "New world record efficiency Cu(In,Ga)Se₂ thin-film solar cells beyond 20%," *Prog. Photovoltaics*, vol. 19, pp. 894-897, 2011.
- [47] X. Wu, "High-efficiency polycrystalline CdTe thin-film solar cells," *Sol. Energy*, vol. 77, pp. 803-814, 2004.
- [48] U.S. Geological Survey, Mineral commodity summaries 2011, pp. 1-198.
- [49] D. B. Mitzi, O. Gunawan, T. K. Todorov, K. Wang, and S. Guha, "The path towards a high-performance solution-processed kesterite solar cell," *Sol. Energy Mater. Sol. Cells*, vol. 95, pp. 1421-1436, 2011.

- [50] S. C. Riha, B. A. Parkinson, and A. L. Prieto, "Solution-Based Synthesis and Characterization of $\text{Cu}_2\text{ZnSnS}_4$ Nanocrystals," *J. Am. Chem. Soc.*, vol.131, 12054-12055, 2009.
- [51] Q. J. Guo, H. W. Hillhouse, and R. Agrawal, "Synthesis of $\text{Cu}_2\text{ZnSnS}_4$ Nanocrystal Ink and Its Use for Solar Cells," *J. Am. Chem. Soc.*, vol.131, pp. 11672-11673, 2009.
- [52] C. Steinhagen, M. G. Panthani, V. Akhavan, B. Goodfellow, B. Koo, and B. A. Korgel, "Synthesis of $\text{Cu}_2\text{ZnSnS}_4$ Nanocrystals for Use in Low-Cost Photovoltaics," *J. Am. Chem. Soc.*, vol. 131, pp. 12554-12555, 2009.
- [53] T. Todorov, M. Kita, J. Carda, and P. Escribano, " $\text{Cu}_2\text{ZnSnS}_4$ films deposited by a soft-chemistry method," *Thin Solid Films*, vol. 517, pp. 2541-2544, 2009.
- [54] C. Chory, F. Zutz, F. Witt, H. Borchert, and J. Parisi, "Synthesis and characterization of $\text{Cu}_2\text{ZnSnS}_4$," *Phys. Status Solidi C*, vol. 7, pp. 1486-1488, 2010.
- [55] T. Kameyama, T. Osaki, K. Okazaki, T. Shibayama, A. Kudo, S. Kuwabata, and T. Torimoto, "Preparation and photoelectrochemical properties of densely immobilized $\text{Cu}_2\text{ZnSnS}_4$ nanoparticle films," *J. Mater. Chem.*, vol. 20, pp. 5319-5324, 2010.
- [56] H. Wei, W. Guo, Y. Sun, Z. Yang, and Y. Zhang, "Hot-injection synthesis and characterization of quaternary $\text{Cu}_2\text{ZnSnSe}_4$ nanocrystals," *Mater. Lett.*, vol.64, pp. 1424-1426, 2010.
- [57] P. Dai, X. Shen, Z. Lin, Z. Feng, H. Xu, and J. Zhan, "Band-gap tunable $(\text{Cu}_2\text{Sn})_{x/3}\text{Zn}_{1-x}\text{S}$ nanoparticles for solar cells," *Chem. Commun.*, vol. 46, pp. 5749-5751, 2010.
- [58] Q. Guo, G. M. Ford, W. C. Yang, B. C. Walker, E. A. Stach, H. W. Hillhouse, and R. Agrawal, "Fabrication of 7.2% Efficient CZTS_{Se} Solar Cells Using CZTS Nanocrystals," *J. Am. Chem. Soc.*, vol. 132, pp. 17384-17386, 2010.
- [59] S. C. Riha, S. J. Fredrick, J. B. Sambur, Y. J. Liu, A. L. Prieto, and B. A. Parkinson, "Photoelectrochemical Characterization of Nanocrystalline Thin-Film $\text{Cu}_2\text{ZnSnS}_4$ Photocathodes," *ACS Appl. Mater. Interfaces*, vol. 3, pp. 58-66, 2011.

- [60] X. Lu, Z. Zhuang, Q. Peng, and Y. Li, "Wurtzite $\text{Cu}_2\text{ZnSnS}_4$ nanocrystals: a novel quaternary semiconductor," *Chem. Commun.*, vol.47, pp. 3141-3143, 2011.
- [61] M. Cao and Y. Shen, "A mild solvothermal route to kesterite quaternary $\text{Cu}_2\text{ZnSnS}_4$ nanoparticles," *J. Cryst. Growth*, vol. 318, pp. 1117-1120, 2011.
- [62] Y. L. Zhou, W. H. Zhou, Y. F. Du, M. Li, and S. X. Wu, "Sphere-like kesterite $\text{Cu}_2\text{ZnSnS}_4$ nanoparticles synthesized by a facile solvothermal method," *Mater. Lett.*, vol. 65, pp. 1535-1537, 2011.
- [63] O. Zaberca, A. Gillorin, B. Durand, and J. Y. Chane-Ching, "A general route to the synthesis of surfactant-free, solvent-dispersible ternary and quaternary chalcogenide nanocrystals," *J. Mater. Chem.*, vol. 21, pp. 6483-6486, 2011.
- [64] X. Wang, Z. Sun, C. Shao, D. M. Boye, and J. Zhao, "A facile and general approach to polynary semiconductor nanocrystals via a modified two-phase method," *Nanotechnology*, vol. 22, pp. 245605, 2011.
- [65] C. Zou, L. Zhang, D. Lin, Y. Yang, Q. Li, X. Xu, and S. Huang, "Facile synthesis of $\text{Cu}_2\text{ZnSnS}_4$ nanocrystals," *CrystEngComm*, vol. 13, pp. 3310-3313, 2011.
- [66] H. Wei, Z. C. Ye, M. Li, Y. J. Su, Z. Yang, and Y. F. Zhang, "Tunable band gap $\text{Cu}_2\text{ZnSnS}_{4x}\text{Se}_{4(1-x)}$ nanocrystals: experimental and first-principles calculations," *CrystEngComm*, vol. 13, pp. 2222-2226, 2011.
- [67] J. Chane-Ching, A. Gillorin, O. Zaberca, A. Balocchi, and X. Marie, "Highly-crystallized quaternary chalcopyrite nanocrystals via a high-temperature dissolution–reprecipitation route," *Chem. Commun.*, vol. 47, pp. 5229-5231, 2011.
- [68] G. M. Ford, Q. J. Guo, R. Agrawal, and H. W. Hillhouse, "Earth Abundant Element $\text{Cu}_2\text{Zn}(\text{Sn}_{1-x}\text{Ge}_x)\text{S}_4$ Nanocrystals for Tunable Band Gap Solar Cells: 6.8% Efficient Device Fabrication," *Chem. Mater.*, vol. 23, pp. 2626-2629, 2011.

- [69] Y. Wang and H. Gong, "Low Temperature Synthesized Quaternary Chalcogenide $\text{Cu}_2\text{ZnSnS}_4$ from Nano-Crystallite Binary Sulfides *J. Electrochem. Soc.*, vol. 158, pp. H800-H803, 2011.
- [70] W. Haas, T. Rath, A. Pein, J. Rattenberger, G. Trimmel, and F. Hofer, "The stoichiometry of single nanoparticles of copper zinc tin selenide," *Chem. Commun.*, vol. 47, pp. 2050-2052, 2011.
- [71] I. Bilecka and M. Niederberger, "Microwave chemistry for inorganic nanomaterials synthesis," *Nanoscale*, vol. 2, pp. 1358-1374, 2010.
- [72] R. S. Singh, V. K. Rangari, S. Sanagapalli, V. Jayaraman, S. Mahendra, and V. P. Singh, "Nano-structured CdTe, CdS and TiO_2 for thin film solar cell applications," *Sol. Energy Mater. Sol. Cells*, vol. 82, pp. 315-330, 2004.
- [73] L. Li, H. F. Qian, and J. C. Ren, "Rapid synthesis of highly luminescent CdTe nanocrystals in the aqueous phase by microwave irradiation with controllable temperature," *Chem. Commun.*, vol. 4, pp. 528-530, 2005.
- [74] Y. He, H. T. Lu, L. M. Sai, W. Y. Lai, Q. L. Fan, L. H. Wang, and W. Huang, "Microwave-Assisted Growth and Characterization of Water-Dispersed CdTe/CdS Core-Shell Nanocrystals with High Photoluminescence," *J. Phys. Chem. B*, vol. 110, pp. 13370-13374, 2006.
- [75] L. Al Juhaiman, L. Scoles, D. Kingston, B. Patarachao, D. Wang, and F. Bensebaa, "Green synthesis of tunable $\text{Cu}(\text{In}_{1-x}\text{Ga}_x)\text{Se}_2$ nanoparticles using non-organic solvents," *Green Chem.*, vol. 12, pp. 1248-1252, 2010.
- [76] C. V. Sun, J. S. Gardner, G. Long, C. Bajracharya, A. Thurber, A. Punnoose, R.G. Rodriguez, and J.J. Pak, "Controlled Stoichiometry for Quaternary $\text{CuIn}_x\text{Ga}_{1-x}\text{S}_2$ Chalcopyrite Nanoparticles from Single-Source Precursors via Microwave Irradiation," *Chem. Mater.*, vol. 22, pp. 2699-2701, 2010.
- [77] C. O. Kappe, "Controlled Microwave Heating in Modern Organic Synthesis," *Angew. Chem. Int. Edit.*, vol. 43, pp. 6250-6284, 2004.

- [78] Q. Li and Y. Wei, "Study on Preparing Monodispersed Hematite Nanoparticles by Microwave-induced Hydrolysis of Ferric Salts Solution," *Mater. Res. Bull.*, vol. 33, pp. 779-782, 1998.
- [79] J. J. Scragg, P. J. Dale, L. M. Peter, G. Zoppi, and I. Forbes, "New routes to sustainable photovoltaics: evaluation of $\text{Cu}_2\text{ZnSnS}_4$ as an alternative absorber material," *Phys. Status Solidi B*, vol. 245, pp. 1772-1778, 2008.
- [80] K. Tanaka, M. Oonuki, N. Moritake, and H. Uchiki, " $\text{Cu}_2\text{ZnSnS}_4$ thin film solar cells prepared by non-vacuum processing," *Sol. Energy Mater. Sol. Cells*, vol. 93, pp. 583-587, 2009.
- [81] J. J. Scragg, D. M. Berg, and P. J. Dale, "A 3.2% efficient Kesterite device from electrodeposited stacked elemental layers," *J. Electroanal. Chem.*, vol. 646, pp. 52-59, 2010.
- [82] A. Wangperawong, J. S. King, S. M. Herron, B. P. Tran, K. Pangan-Okimoto, and S. F. Bent, "Aqueous bath process for deposition of $\text{Cu}_2\text{ZnSnS}_4$ photovoltaic absorbers," *Thin Solid Films*, vol. 519, pp. 2488-2492, 2011.
- [83] K. Tanaka, Y. Fukui, N. Moritake, and H. Uchiki, "Chemical composition dependence of morphological and optical properties of $\text{Cu}_2\text{ZnSnS}_4$ thin films deposited by sol-gel sulfurization and $\text{Cu}_2\text{ZnSnS}_4$ thin film solar cell efficiency," *Sol. Energy Mater. Sol. Cells*, vol. 95, pp. 838-842, 2011.
- [84] A. Ennaoui, M. Lux-Steiner, A. Weber, D. Abou-Ras, I. Kotschau, H. W. Schock, R. Schurr, A. Holzing, S. Jost, R. Hock, T. Voss, J. Schulze, and A. Kirbs, " $\text{Cu}_2\text{ZnSnS}_4$ thin film solar cells from electroplated precursors: Novel low-cost perspective," *Thin Solid Films*, vol. 517, pp. 2511-2514, 2009.
- [85] N. Moritake, Y. Fukui, M. Oonuki, K. Tanaka, and H. Uchiki, "Preparation of $\text{Cu}_2\text{ZnSnS}_4$ thin film solar cells under non-vacuum condition," *Phys. Status Solidi C*, vol. 6, pp. 1233-1236, 2009.
- [86] P. Reuter, T. Rath, A. Fischereder, G. Trimmel, and P. Hadley, "Electron Beam-Induced Current (EBIC) in Solution-Processed Solar Cells," *Scanning*, vol. 33, pp. 1-6, 2011.

- [87] M. Y. Yeh and D. -S. Wu, "Preparation of $\text{Cu}_2\text{ZnSnS}_4$ treated with Post-sulfurization in a Sulfur Vapor Atmosphere," *Adv. Mat. Res.*, vol. 239-242, pp. 642-645, 2011.
- [88] W. Ki and H. W. Hillhouse, "Earth-Abundant Element Photovoltaics Directly from Soluble Precursors with High Yield Using a Non-Toxic Solvent," *Adv. Energy Mater.*, vol. 1, pp. 732-735, 2011.
- [89] T. Todorov, K. Reuter, and D. B. Mitzi, "High-Efficiency Solar Cell with Earth-Abundant Liquid-Processed Absorber," *Adv. Mater.*, vol. 22, pp. E156-E159, 2010.
- [90] D. A. R. Barkhouse, O. Gunawan, T. Gokmen, T. K. Todorov, and D. B. Mitzi, "Device Characteristics of a 10.1% hydrazine-processed $\text{Cu}_2\text{ZnSn}(\text{Se},\text{S})_4$ solar cell," *Prog. Photovoltaics*, vol. 20, pp. 6-11, 2012.
- [91] M. K. M. Berrada, F. Gruy, and M. Cournil, "Synthesis of zinc sulfide multi-scale agglomerates by homogenous precipitation-parametric study and mechanism," *J. Cryst. Growth*, vol. 311, pp. 2459-2465, 2009.
- [92] H. M. Yang, C. H. Huang, and X. H. Su, "Synthesis of homogeneous PVP-capped SnS_2 submicron particles via microwave irradiation," *Mater. Lett.*, vol. 60, pp. 3714-3417, 2006.
- [93] M. Y. Yeh, C. C. Lee, and D. S. Wu, "Influences of synthesizing temperatures on the properties of $\text{Cu}_2\text{ZnSnS}_4$ prepared by sol-gel spin-coated deposition," *J. Sol-Gel Sci. Technol.*, vol. 52, pp. 65-68 2009.
- [94] A. Weber, R. Mainz, and H. W. Schock, "On the Sn loss from thin films of the material system Cu-Zn-Sn-S in high vacuum," *J. Appl. Phys.*, vol. 107, pp. 013516, 2010.
- [95] W. Wang, Y. -W. Su, and C. -h. Chang, "Inkjet printed chalcopyrite $\text{CuIn}_x\text{Ga}_{1-x}\text{Se}_2$ thin film solar cells *Sol. Energy Mater. Sol. Cells*, vol. 95, pp. 2616-2620, 2011.
- [96] ASTM Standard E1508 - 98, "Standard Guide for Quantitative Analysis by Energy-Dispersive Spectroscopy," ASTM International, DOI: 10.1520/E1508-98R08, 2008.

- [97] H. Katagiri, "Cu₂ZnSnS₄ thin film solar cells," *Thin Solid Films*, vol. 480, pp. 426-432, 2005.
- [98] T. Kobayashi, K. Jimbo, K. Tsuchida, S. Shinoda, T. Oyanagi, and H. Katagiri, "Investigation of Cu₂ZnSnS₄-Based Thin Film Solar Cells Using Abundant Materials," *Jpn. J. Appl. Phys.*, vol. 44, pp. 783-787, 2005.
- [99] S. Chen, X. Gong, A. Walsh, and S. Wei, "Defect physics of the kesterite thin-film solar cell absorber Cu₂ZnSnS₄," *Appl. Phys. Lett.*, vol. 96, pp. 021902, 2010.
- [100] K. Biswas, S. Lany, and A. Zunger, "The electronic consequences of multivalent elements in inorganic solar absorbers: Multivalency of Sn in Cu₂ZnSnS₄," *Appl. Phys. Lett.*, vol. 96, pp. 201902, 2010.
- [101] T. Prabhakar and N. Jampana, "Effect of sodium diffusion on the structural and electrical properties of Cu₂ZnSnS₄ thin films," *Sol. Energy Mater. Sol. Cells*, vol. 95, pp. 1001-1004, 2011.
- [102] R. Xie, M. Rutherford, and X. Peng, "Formation of High-Quality I-III-VI Semiconductor Nanocrystals by Tuning Relative Reactivity of Cationic Precursors," *J. Am. Chem. Soc.*, vol. 131, pp. 5691-5697, 2009.
- [103] A. Shavel, J. Arbiol, and A. Cabot, "Synthesis of Quaternary Chalcogenide Nanocrystals: Stannite Cu₂Zn_xSn_ySe_{1+x+2y}," *J. Am. Chem. Soc.*, vol. 132, pp. 4514-4515, 2010.
- [104] Y. -L. Zhou, W. -H. Zhou, M. Li, Y. -F. Du, and S. -X. Wu, "Hierarchical Cu₂ZnSnS₄ Particles for a Low-Cost Solar Cell: Morphology Control and Growth Mechanism *J. Phys. Chem. C*, vol. 115, pp. 19632-19639, 2011.
- [105] M. D. Regulacio, C. Ye, S. H. Lim, M. Bosman, E. Ye, S. Chen, Q. -H. Xu, and M. -Y. Han, "Colloidal Nanocrystals of Wurtzite-Type Cu₂ZnSnS₄: Facile Noninjection Synthesis and Formation Mechanism," *Chem. Eur. J.*, vol. 18, pp. 3127-3131, 2012.
- [106] S. W. Shin, J. H. Han, C. Y. Park, A. V. Moholkar, J. Y. Lee, and J. H. Kim, "Quaternary Cu₂ZnSnS₄ nanocrystals: Facile and low cost synthesis by microwave-assisted solution method," *J. Alloy. Compd.*, vol. 516, pp. 96-101, 2012.

- [107] M. Himmrich and H. Haeuseler, "Far infrared studies on stannite and wurtzstannite type compounds," *Spectrochim. Acta A*, vol. 47, pp. 933-942 1991.
- [108] P. A. Fernandes, P. M. P. Salome, and A. F. da Cunha, "Growth and Raman scattering characterization of $\text{Cu}_2\text{ZnSnS}_4$ thin films," *Thin Solid Films* vol. 517, pp. 2519-2523, 2009.
- [109] K. Wang, B. Shin, K. B. Reuter, T. Todorov, D. B. Mitzi, and S. Guha, "Structural and elemental characterization of high efficiency $\text{Cu}_2\text{ZnSnS}_4$ solar cells," *Appl. Phys. Lett.*, vol. 98, pp. 051912, 2011.
- [110] X. Fontané, L. Calvo-Barrio, V. Izquierdo-Roca, E. Saucedo, A. Pérez-Rodriguez, J. Morante, D. Berg, P. Dale, and S. Siebentritt, "In-depth resolved Raman scattering analysis for the identification of secondary phases: Characterization of $\text{Cu}_2\text{ZnSnS}_4$ layers for solar cell applications," *Appl. Phys. Lett.*, vol. 98, pp. 181905, 2011.
- [111] Y. -T. Nien, B. Zaman, J. Ouyang, I. -G. Chen, C. -S. Hwang, and K. Yu, "Raman scattering for the size of CdSe and CdS nanocrystals and comparison with other techniques," *Mater. Lett.* vol. 62, pp. 4522-4524, 2008.
- [112] Y. Cheng, C. Jin, F. Gao, X. Wu, W. Zhong, S. Li, and P. Chu, "Raman scattering study of zinc blende and wurtzite ZnS," *J. Appl. Phys.*, vol. 106, pp. 123505, 2009.
- [113] P. A. Fernandes, P. M. P. Salome, and A. F. da Cunha, "A study of ternary Cu_2SnS_3 and Cu_3SnS_4 thin films prepared by sulfurizing stacked metal precursors," *J. Phys. D Appl. Phys.*, vol. 43, pp. 215403, 2010.
- [114] S. Y. Chen, X. G. Gong, A. Walsh, and S. H. Wei, "Crystal and electronic band structure of $\text{Cu}_2\text{ZnSnX}_4$ (X=S and Se) photovoltaic absorbers: First-principles insights *Appl. Phys. Lett.*, vol. 94, pp. 041903, 2009.
- [115] H. Katagiri, N. Sasaguchi, S. Hando, S. Hoshino, J. Ohashi, and T. Yokota, "Preparation and evaluation of $\text{Cu}_2\text{ZnSnS}_4$ thin films by sulfurization of E-B evaporated precursors," *Sol. Energy Mater. Sol. Cells*, vol. 49, pp. 407-414, 1997.

- [116] K. Ito and T. Nakazawa, "Electrical and Optical Properties of Stannite-Type Quaternary Semiconductor Thin Films," *Jpn. J. Appl. Phys.*, vol. 27, pp. 2094-2097, 1988.
- [117] Y. F. Liu, M. Y. Ge, Y. Yue, Y. Sun, Y. Z. Wu, X. Chen, and N. Dai, "Colloidal $\text{Cu}_2\text{ZnSnS}_4$ nanocrystals generated by a facile route using ethylxanthate molecular precursors," *Phys. Status Solidi-R.*, vol. 5, pp. 113-115, 2011.
- [118] J. -S. Seol, S. -Y. Lee, J. -C. Lee, H. -D. Nam, and K. -H. Kim, "Electrical and optical properties of $\text{Cu}_2\text{ZnSnS}_4$ thin films prepared by rf magnetron sputtering process," *Sol. Energy Mater. Sol. Cells*, vol. 75, pp. 155-162, 2003.
- [119] H. Katagiri, " $\text{Cu}_2\text{ZnSnS}_4$ thin film solar cells," *Thin Solid Films*, vol. 480, pp. 426-432, 2005.
- [120] S. Niki, M. Contreras, I. Repins, M. Powalla, K. Kushiya, S. Ishizuka, and K. Matsubara, "CIGS absorbers and processes," *Prog. Photovoltaics Res. Appl.*, vol. 18, pp. 453-466, 2010.
- [121] U.S. Geological Survey, Mineral commodity summaries 2013, pp. 1-201.
- [122] I. Repins, N. Vora, C. Beall, S. H. Wei, Y. Yan, M. Romero, G. Teeter, H. Du, B. To, M. Young, and R. Noufi, "Kesterites and Chalcopyrites: A Comparison of Close Cousins," *Mater. Res. Soc. Symp. P.*, vol. 1324, pp. mrss11-1324, 2011.
- [123] T. Todorov and D.B. Mitzi, "Direct Liquid Coating of Chalcopyrite Light-Absorbing Layers for Photovoltaic Devices," *Eur. J. Inorg. Chem.*, vol. 1, pp. 17-28, 2010.
- [124] S. C. Riha, B. A. Parkinson, and A. L. Prieto, "Compositionally Tunable $\text{Cu}_2\text{ZnSn}(\text{S}_{1-x}\text{Se}_x)_4$ Nanocrystals: Probing the Effect of Se-Inclusion in Mixed Chalcogenide Thin Films," *J. Am. Chem. Soc.*, vol. 133, pp. 15272-15275, 2011.
- [125] C. Jiang, J. S. Lee, and D. V. Talapin, "Soluble Precursors for CuInSe_2 , $\text{CuIn}_{1-x}\text{Ga}_x\text{Se}_2$, and $\text{Cu}_2\text{ZnSn}(\text{S,Se})_4$ Based on Colloidal Nanocrystals and Molecular Metal Chalcogenide Surface Ligands," *J. Am. Chem. Soc.*, vol. 134, pp. 5010-5013, 2012.

- [126] S. Bag, O. Gunawan, T. Gokmen, Y. Zhu, T. K. Todorov, and D. B. Mitzi, "Low band gap liquid-processed CZTSe solar cell with 10.1% efficiency," *Energy & Environ. Sci.*, 5 (2012) 7060-7065.
- [127] T. K. Todorov, J. Tang, S. Bag, O. Gunawan, T. Gokmen, Y. Zhu, and D. B. Mitzi, "Beyond 11% Efficiency: Characteristics of State-of-the-Art $\text{Cu}_2\text{ZnSn}(\text{S},\text{Se})_4$ Solar Cells," *Adv Energy Mater.*, vol. 3, pp. 34-38, 2013.
- [128] S. Ahmed, K. B. Reuter, O. Gunawan, L. Guo, L. T. Romankiw, and H. Deligianni, "A High Efficiency Electrodeposited $\text{Cu}_2\text{ZnSnS}_4$ Solar Cell," *Adv. Energy Mater.*, vol. 2, pp. 253-259, 2012.
- [129] A. Fischereder, T. Rath, W. Haas, H. Amenitsch, J. Albering, D. Meischler, S. Larissegger, M. Edler, R. Saf, F. Hofer, and G. Trimmel, "Investigation of $\text{Cu}_2\text{ZnSnS}_4$ Formation from Metal Salts and Thioacetamide," *Chem. Mater.*, vol. 22, pp. 3399-3406, 2010.
- [130] Y. B. K. Kumar, G. S. Babu, P. U. Bhaskar, and V. S. Raja, "Preparation and characterization of spray-deposited $\text{Cu}_2\text{ZnSnS}_4$ thin films," *Sol. Energy Mater. Sol. C*, vol. 93, pp. 1230-1237, 2009.
- [131] B. T. Flynn, W. Wang, C. -h. Chang, and G. S. Herman, "Microwave Assisted Synthesis of $\text{Cu}_2\text{ZnSnS}_4$ Colloidal Nanoparticle Inks," *Phys. Status Solidi A*, vol. 209, pp. 2186-2194, 2012.
- [132] A. Shavel, D. Cadavid, M. Ibáñez, A. Carrete, and A. Cabot, "Continuous Production of $\text{Cu}_2\text{ZnSnS}_4$ Nanocrystals in a Flow Reactor," *J. Am. Chem. Soc.*, vol. 134, pp. 1438-1441, 2012.
- [133] F. P. Bretherton, "The motion of long bubbles in tubes," *J. Fluid Mech.*, vol. 10, pp. 166-188, 1961.
- [134] E. Obermeier, S. Fischer, and D. Bohne, "Thermal Conductivity, Density, Viscosity, and Prandtl-Numbers of Di- and Triethylene Glycol-Water Mixtures," *Ber. Bunsenges. Phys. Chem.*, vol. 89, pp. 805-809, 1985.
- [135] S. Hall, J. Szymanski, and J. Stewart, "Kesterite, $\text{Cu}_2(\text{Zn},\text{Fe})\text{SnS}_4$ and Stannite, $\text{Cu}_2(\text{Fe},\text{Zn})\text{SnS}_4$, Structurally Similar but Distinct Minerals," *Can. Mineral.*, vol. 16, pp. 131-137, 1978.

- [136] P. A. Fernandes, P. M. P. Salomé, and A. F. da Cunha, "Study of polycrystalline $\text{Cu}_2\text{ZnSnS}_4$ films by Raman scattering," *J. Alloy Compd*, vol. 509, pp. 7600-7606, 2011.
- [137] P. M. P. Salome, J. Malaquias, P. A. Fernandes, M. S. Ferreira, A. F. da Cunha, J. P. Leitaó, J. C. Gonzalez, and F. M. Matinaga, "Growth and characterization of $\text{Cu}_2\text{ZnSn}(\text{S},\text{Se})_4$ thin films for solar cells," *Sol. Energy Mater. Sol. C.*, vol. 101, pp. 147-153, 2012.
- [138] G. Gouadec and P. Colomban, "Raman Spectroscopy of nanomaterials: How spectra relate to disorder, particle size and mechanical properties," *Prog. Cryst. Growth Ch.*, vol. 53, pp. 1-56, 2007.
- [139] I. H. Campbell and P. M. Fauchet, "The Effects of Microcrystal Size and Shape on the One Phonon Raman-spectra of Crystalline Semiconductors," *Solid State Commun.*, vol. 58, pp. 739-741, 1986.
- [140] M. Altosaar, J. Raudoja, K. Timmo, M. Danilson, M. Grossberg, J. Krustok, E. Mellikov, " $\text{Cu}_2\text{Zn}_{1-x}\text{Cd}_x\text{Sn}(\text{Se}_{1-y}\text{S}_y)_4$ solid solutions as absorber materials for solar cells," *Phys. Status Solidi A*, vol. 205, pp. 167-170, 2008.
- [141] M. Ganchev, J. Iljina, L. Kaupmees, T. Raadik, O. Volobujeva, A. Mere, M. Altosaar, J. Raudoja, E. Mellikov, "Phase composition of selenized $\text{Cu}_2\text{ZnSnSe}_4$ thin films determined by X-ray diffraction and Raman spectroscopy," *Thin Solid Films*, vol 519, pp. 7394-7398, 2011.
- [142] J. T. Anderson, C. L. Munsee, C. M. Hung, T. M. Phung, G. S. Herman, D. C. Johnson, J. F. Wager, and D. A. Keszler, "Solution-Processed HfSO_x and ZrSO_x Inorganic Thin-Film Dielectrics and Nanolaminates," *Adv. Funct. Mater.*, vol. 17, pp. 2117-2124, 2007.
- [143] D. A. Keszler, J. T. Anderson, and S. T. Meyers, in *Solution Processing of Inorganic Materials* (Ed: D. B. Mitzi), Hoboken, NJ, USA: John Wiley & Sons, 2009.
- [144] M. Alemayehu, J. E. Davis, M. Jackson, B. Lessig, L. Smith, J. D. Sumega, C. Knutson, M. Beekman, D. C. Johnson, and D. A. Keszler, "Tunable dielectric thin films by aqueous, inorganic solution-based processing," *Solid State Sci.*, vol. 13, pp. 2037-2040, 2011.

- [145] J. Stowers and D. A. Keszler, "High resolution, high sensitivity inorganic resists," *Microelectron Eng.*, vol. 86, pp. 730-733, 2009.
- [146] A. Telecky, P. Xie, J. Stowers, A. Grenville, B. Smith, and D. A. Keszler, "Photopatternable inorganic hardmask," *J. Vac. Sci. Technol. B*, vol. 28, pp. C6S19-C6S22, 2010.
- [147] M. Hino, S. Kobayashi, and K. Arata, "Reactions of Butane and Isobutane Catalyzed by Zirconium Oxide Treated with Sulfate Ion. Solid Superacid Catalyst," *J. Am. Chem. Soc.*, vol. 101, pp. 6439-6441, 1979.
- [148] M. Hino and K. Arata, "Synthesis of solid superacid catalyst with acid strength of $H_0 \leq -16.04$," *J. Chem. Soc., Chem. Commun.*, vol. 18, pp. 851-852, 1980.
- [149] M. Hino, M. Kurashige, H. Matsushashi, and K. Arata, "The surface structure of sulfated zirconia: Studies of XPS and thermal analysis," *Thermochim. Acta*, vol. 441, pp. 35-41, 2006.
- [150] Y. Wang, K.-Y. Lee, S. Choi, J. Liu, L.-Q. Wang, and C. H. F. Peden, "Grafting sulfated zirconia on mesoporous silica," *Green Chem.*, vol. 9, pp. 540-544, 2007.
- [151] D. H. Kim, J. Szanyi, J. H. Kwak, X. Q. Wang, J. C. Hansen, M. Engelhard, and C. H. F. Peden, "Effects of Sulfation Level on the Desulfation Behavior of Presulfated Pt-BaO/Al₂O₃ Lean NO_x Trap Catalysts: A Combined H₂ Temperature-Programmed Reaction, in Situ Sulfur K-Edge X-ray Absorption Near-Edge Spectroscopy, X-ray Photoelectron Spectroscopy, and Time-Resolved X-ray Diffraction Study," *J. Phys. Chem. C*, vol. 113, pp. 7336-7341, 2009.
- [152] E. J. Eterigho, J. G. M. Lee, and A. P. Harvey, "Triglyceride cracking for biofuel production using a directly synthesised sulphated zirconia catalyst," *Bioresource Technol.*, vol. 102, pp. 6313-6316, 2011.
- [153] C. Breitkopf, "An Integrated Catalytic and Transient Study of Sulfated Zirconias: Investigation of the Reaction Mechanism and the Role of Acidic Sites in n-Butane Isomerization," *ChemCatChem*, vol. 1, pp. 259-269, 2009.

- [154] L. K. Noda, N. S. Gonçalves, S. M. de Borba, and J. A. Silveira, "Raman spectroscopy and thermal analysis of sulfated ZrO_2 prepared by two synthesis routes," *Vib. Spectrosc.*, vol. 44, pp. 101-107, 2007.
- [155] B. Azambre, L. Zenbourny, J. V. Weber, and P. Burg, "Surface characterization of acidic ceria–zirconia prepared by direct sulfation," *Appl. Surf. Sci.*, vol. 256, pp. 4570-4581, 2010.
- [156] C. Breitung, H. Papp, X. Li, R. Olindo, J. A. Lercher, R. Lloyd, S. Wrabetz, F. C. Jentoft, K. Meinel, S. Förster, K.-M. Schindler, H. Neddermeyer, W. Widdra, A. Hofmann, and J. Sauer, "Activation and isomerization of n-butane on sulfated zirconia model systems—an integrated study across the materials and pressure gaps," *Phys. Chem. Chem. Phys.*, vol. 9, pp. 3600-3618, 2007.
- [157] R. Lloyd, T. W. Hansen, W. Ranke, F. C. Jentoft, and R. Schlögl, "Adsorption–desorption equilibrium investigations of n-butane on nanocrystalline sulfated zirconia thin films *Appl. Catal. A-Gen.*, vol. 391, pp. 215-224, 2011.
- [158] G. S. Herman, Y. J. Kim, S. A. Chambers, and C. H. F. Peden, "Interaction of D_2O with $\text{CeO}_2(001)$ Investigated by Temperature-Programmed Desorption and X-ray Photoelectron Spectroscopy," *Langmuir*, vol. 15, pp. 3993-3997, 1999.
- [159] M. Engelhard, J. Herman, R. Wallace, and D. Baer, "As-Received, Ozone cleaned, and Ar^+ Sputtered Surfaces of Hafnium Oxide Grown by Atomic Layer Deposition and Studied by XPS," *Surf. Sci. Spectra*, vol. 18, pp. 46-57 2011.
- [160] S. Suzer, S. Sayan, M. M. Banaszak Holl, E. Garfunkel, Z. Hussain, and N. M. Hamdan, "Soft x-ray photoemission studies of Hf oxidation," *J. Vac. Sci. Technol. A*, vol. 21, pp. 106-109, 2003.
- [161] C. Morant, L. Galán, and J. M. Sanz, "An XPS Study of the Initial Stages of Oxidation of Hafnium," *Surf. Interface Anal.*, vol. 16, pp. 304-308, 1990.
- [162] R. L. Miller, S. H. McKinney, and A. R. Chourasia, "Core Level XPS of Elemental Hafnium and Hafnium Dioxide," *Surf. Sci. Spectra*, vol. 15, pp. 59-69, 2008.

- [163] J. P. Lehan, Y. Mao, B. G. Bovard, and H. A. Macleod, "Optical and Microstructural Properties of Hafnium Dioxide Thin Films," *Thin Solid Films*, vol. 250, pp. 227-250, 1991.
- [164] Freeware available at <http://www.phy.cuhk.edu.hk/~surface>
- [165] H. Shimizu, T. Sato, S. Konagali, M. Ikeda, T. Takahashi, and T. Nishide, "Temperature-Programmed Desorption Analyses of Sol-Gel Deposited and Crystallized HfO₂ Films," *Jpn. J. Appl. Phys.*, vol. 46, pp. 4209-4214, 2007.
- [166] T. Gougousi, D. Niu, R. W. Ashcraft, and G. N. Parsons, "Carbonate formation during post-deposition ambient exposure of high-k dielectrics," *Appl. Phys. Lett.* vol. 83, 3543-3545, 2003.
- [167] J. D. Baniecki, M. Ishii, K. Kurihara, K. Yamanaka, T. Yano, K. Shinozaki, T. Imada, Y. Kobayashi, "Chemisorption of water and carbon dioxide on nanostructured BaTiO₃-SrTiO₃(001) surfaces," *J. Appl. Phys.*, vol. 106, pp. 054109, 2009.
- [168] S. Aukkaravittayapun, C. Thanachayanont, T. Theapsiri, W. Veerasai, Y. Sawada, T. Kondo, S. Tokiwa, T. Nishide, "Temperature Programmed Desorption of F-Doped SnO₂ Films Deposited by Inverted Pyrosol Technique," *J. Therm. Anal. Calorim.*, vol. 85, pp. 811-815, 2006.
- [169] D. G. Castner, K. Hinds, and D. W. Grainger, "X-ray Photoelectron Spectroscopy Sulfur 2p Study of Organic Thiol and Disulfide Binding Interactions with Gold Surfaces," *Langmuir*, vol. 12, pp. 5083-5086, 1996.
- [170] T. M. Willey, A. L. Vance, T. van Buuren, C. Bostedt, L. J. Terminello, and C. S. Fadley, "Rapid Degradation of Alkanethiol-Based Self-Assembled Monolayers on Gold in Ambient Laboratory Conditions," *Surf. Sci.* vol. 576, pp. 188-196, 2005.
- [171] A. F. Lee, K. Wilson, A. Goldoni, R. Larciprete, and S. Lizzit, "A fast XPS study of sulphate promoted propene decomposition over Pt{111}," *Surf. Sci.*, vol. 513, pp. 140-148, 2002.
- [172] K. Ebitani, H. Konno, T. Tanka, and H. Hattori, "In-situ XPS Study of Zirconium Oxide Promoted by Platinum and Sulfate Ion," *J. Catal.*, vol. 135, pp. 60-67, 1992.

- [173] D. Barreca, A. Milanov, R. A. Fischer, A. Devi, and E. Tondello, "Hafnium oxide thin film grown by ALD: An XPS study," *Surf. Sci. Spectra*, vol. 14, pp. 34-40, 2007.
- [174] M. F. Al-Kuhaili, S. M. A. Durrani, and E. E. Khawaja, "Characterization of hafnium oxide thin films prepared by electron beam evaporation," *J. Phys. D. Appl. Phys.*, vol. 37, pp. 1254-1261, 2004.
- [175] J. C. C. Fan and J. B. Goodenough, "X-ray photoemission spectroscopy studies of Sn-doped indium-oxide films," *J. Appl. Phys.*, vol. 48, pp. 3524-3531, 1977.
- [176] S. Yamamoto, T. Kendelewicz, J. T. Newberg, G. Ketteler, D. E. Starr, E. R. Mysak, K. J. Andersson, H. Ogasawara, H. Bluhm, M. Salmeron, G. E. Brown, and A. Nilsson, "Water Adsorption on α -Fe₂O₃(0001) at near Ambient Conditions," *J. Phys. Chem. C*, vol. 114, pp. 2256-2266, 2010.
- [177] L. E. Walle, A. Borg, E. M. J. Johansson, S. Plogmaker, H. Rensmo, P. Uvdal, and A. Sandell, "Mixed Dissociative and Molecular Water Adsorption on Anatase TiO₂(101)," *J. Phys. Chem. C*, vol. 115, pp. 9545-9550, 2011.
- [178] S. Ardizzone, C. L. Bianchi, M. Signoretto, "Zr(IV) surface chemical state and acid features of sulphated-zirconia samples," *Appl. Surf. Sci.*, vol. 136, pp. 213-220, 1998.
- [179] Y. Liang, P. M. A. Sherwood, D. K. Paul, "Valence and Core Photoemission of the Films formed Electrochemically on Nickel in Sulfuric Acid," *J. Chem. Soc. Faraday Trans.*, vol. 90, pp. 1271-1278, 1994.
- [180] R. Nyholm, A. Berndtsson, and N. Mårtensson, "Core level binding energies for the elements Hf to Bi ($Z = 72-83$)," *J. Phys. C. Solid St. Phys.*, vol. 13, pp. L1091-L1096, 1980.
- [181] C. L. Perkins, R. Singh, M. Trenary, T. Tanaka, and Y. Paderno, "Surface properties of Hafnium diboride(0001) as determined by X-ray photoelectron spectroscopy and scanning tunneling microscopy," *Surf. Sci.*, vol. 470, pp. 215-225, 2001.

- [182] Z. J. Yan, R. Xu, Y. Y. Wang, S. Chen, Y. L. Fan, and Z. M. Jiang, "Thin HfO_2 films grown on Si(100) by atomic oxygen assisted molecular beam epitaxy," *Appl. Phys. Lett.*, vol. 85, pp. 85-87, 2004.
- [183] D. Spielbauer, G. A. H. Mekheimer, M. I. Zaki, and K. Knözinger, "Acidity of sulfated zirconia as studied by FTIR spectroscopy of adsorbed CO and NH_3 as probe molecules," *Catal. Lett.*, vol. 40, pp. 71-79, 1996.
- [184] M. A. Henderson, "Structural sensitivity in the dissociation of water on TiO_2 single-crystal surfaces," *Langmuir*, vol. 12, pp. 5093-5098, 1996.
- [185] M. A. Henderson, "The interaction of water with solid surfaces: fundamental aspects revisited," *Surf. Sci. Rep.*, vol. 46, pp. 1-308, 2002.
- [186] G. S. Herman, Z. Dohnálek, N. Ruzycki, and U. Diebold, "Experimental Investigation of the Interaction of Water and Methanol with Anatase- TiO_2 (101)," *J. Phys. Chem. B*, vol. 107, pp. 2788-2795, 2003.
- [187] A. Hofmann and J. Sauer, "Surface Structure of Hydroxylated and Sulfated Zirconia. A Periodic Density-Functional Study," *J. Phys. Chem. B*, vol. 108, pp. 14652-14662, 2004.
- [188] A. Gorski, V. Yurkiv, D. Starukhin, and H. -R. Volpp, " H_2O chemisorption and H_2 oxidation on yttria-stabilized zirconia: Density functional theory and temperature-programmed desorption studies," *J. Power Sources*, vol. 196, pp. 7188-7194, 2011.
- [189] C. -W. Yi and J. Szanyi, " D_2O Adsorption on an Ultrathin Alumina Film on $\text{NiAl}(110)$," *J. Phys. Chem. C*, vol. 111, pp. 17597-17602, 2007.
- [190] J. Bort (2013), "This Looks Like An Ordinary PC But It's Powered By Some Impossibly Small Technology," [Online]. Available: <http://www.businessinsider.com/intel-shows-pc-using-broadwell-14nm-chips-2013-9>
- [191] P. Kruit and S. Steenbrink, "Local critical dimension variation from shot-noise related line edge roughness," *J. Vac. Sci. Technol. B*, vol. 23, pp. 3033-3036, 2005.
- [192] J. W. Thackeray, "Materials challenges for sub-20-nm lithography," *J. Micro/Nanolith. MEMS MOEMS*, vol. 10, pp. 033009, 2011.

- [193] P. P. Naulleau, C. N. Anderson, L.-M. Baclea-an, P. Denham, S. George, K. A. Goldberg, G. Jones, B. McClinton, R. Miyakawa, S. Rekawa, and N. Smith, "Critical challenges for EUV resist materials," *Proc. SPIE*, vol. 7972, pp. 797202, 2011.
- [194] A. E. Grigorescu, M. C. van der Krogt, C. W. Hagen, and P. Kruit, "10 nm lines and spaces written in HSQ, using electron beam lithography," *Microelectron. Eng.*, vol. 84, pp. 822-824, 2007.
- [195] V. R. Manfrinato, L. H. Zhang, D. Su, H. G. Duan, R. G. Hobbs, E. A. Stach, and K. K. Berggren, "Resolution Limits of Electron-Beam Lithography toward the Atomic Scale," *Nano Lett.*, vol. 13, pp. 1555-1558, 2013.
- [196] A. E. Grigorescu and C. W. Hagen, "Resists for sub-20-nm electron beam lithography with a focus on HSQ: state of the art," *Nanotechnology*, vol. 20, pp. 292001, 2009.
- [197] Y. Ekinici, M. Vockenhuber, M. Hojeij, L. Wang, and N. M. Mojarad, "Evaluation of EUV resist performance with interference lithography towards 11 nm half-pitch and beyond," *Proc. SPIE*, vol. 8679, pp. 867910, 2013.
- [198] M. E. Krysak, J. M. Blackwell, S. E. Putna, M. J. Leeson, T. R. Younkin, S. Harlson, K. Frasure, and F. Gstrein, "Investigation of novel inorganic resist materials for EUV lithography," *Proc. SPIE*, vol. 9408, pp. 904805, 2014.
- [199] J. K. Stowers, A. Telecky, M. Kocsis, B. L. Clark, D. A. Keszler, A. Grenville, C. N. Anderson, and P. P. Naulleau, "Directly patterned inorganic hardmask for EUV lithography," *Proc. SPIE*, vol. 7969, pp. 796915, 2011.
- [200] B. T. Flynn, D. Kim, B. L. Clark, A. Telecky, L. Arnadottir, J. Szanyi, D. A. Keszler, and G. S. Herman "In-situ characterization of aqueous-based hafnium oxide hydroxide sulfate thin films," *Surf. Interface Anal.*, vol. 46, pp. 210-215, 2014.
- [201] X. Thrun, K. H. Choi, M. Freitag, A. Grenville, M. Gutsch, C. Hohle, J. K. Stowers, and J. W. Bartha, "Evaluation of direct patternable inorganic spin-on hard mask materials using electron beam lithography," *Microelectron. Eng.*, vol. 98, pp. 226-229, 2012.

- [202] R. P. Oleksak, R. E. Ruther, F. Luo, K. C. Fairley, S. R. Decker, W. F. Stickle, D. W. Johnson, E. L. Garfunkel, G. S. Herman, and D. A. Keszler, "Chemical and structural investigation of high-resolution patterning with HafSOx," *ACS Appl. Mater. Interfaces*, vol. 6, pp. 2917-2921, 2014.
- [203] R. P. Oleksak and G. S. Herman, "Characterization of high-resolution HafSOx inorganic resists," *Proc. SPIE*, vol. 9048, pp. 90483H, 2014.
- [204] J. M. Amador, S. R. Decker, S. E. Lucchini, R. E. Ruther, and D. A. Keszler, "Patterning chemistry of HafSOx resist," *Proc. SPIE*, vol. 9051, pp. 90511A, 2014.
- [205] R. E. Ruther, B. M. Baker, J. H. Son, W. H. Casey, and M. Nyman, "Hafnium Sulfate Prenucleation Clusters and the Hf-18 Polyoxometalate Red Herring," *Inorg. Chem.*, vol. 53, pp. 4234-4242, 2014.
- [206] J. K. Stowers, A. J. Telecky, D. A. Keszler, and A. Grenville, "Patterned Inorganic Layers, Radiation Based Patterning Compositions and Corresponding Methods," U.S. Patent 8,415,000 B2, 2013.
- [207] J. C. Dupin, D. Gonbeau, P. Vinatier, and A. Levasseur, "Systematic XPS studies of metal oxides, hydroxides and peroxides," *Phys. Chem. Chem. Phys.*, vol. 2, pp. 1319-1324, 2000.
- [208] J. H. Park, Y. B. Yoo, K. H. Lee, W. S. Jang, J. Y. Oh, S. S. Chae, and H. K. Baik, "Low-Temperature, High-Performance Solution-Processed Thin-Film Transistors with Peroxo-Zirconium Oxide Dielectric," *ACS Appl. Mater. Interfaces*, vol. 5, pp. 410-417, 2013.
- [209] Z. Cui, "A new analytical model for simulating resist heating in electron beam lithography," *J. Phys. D Appl. Phys.*, vol. 25, pp. 919-923, 1992.
- [210] D. C. Chu, W. K. Wong, K. E. Goodson, and R. F. W. Pease, "Transient temperature measurements of resist heating using nanothermocouples," *J. Vac. Sci. Technol. B*, vol. 21, pp. 2985-2989, 2003.
- [211] T. R. Groves, "Theory of beam-induced substrate heating," *J. Vac. Sci. Technol. B*, vol. 14, pp. 3839-3844, 1996.

- [212] R. A. Wiedle, M. Warner, J. Tate, P. N. Plassmeyer, and C. J. Page, "Thermal conductivity of amorphous thin-film Al-P-O on silicon," *Thin Solid Films*, vol. 548, pp. 225-229, 2013.
- [213] M. A. Panzer, M. Shandalov, J. A. Rowlette, Y. Oshima, Y. W. Chen, P. C. McIntyre, and K. E. Goodson, "Thermal Properties of Ultrathin Hafnium Oxide Gate Dielectric Films," *IEEE Electr. Device L.*, vol. 30, pp. 1269-1271, 2009.
- [214] D. Menzel and R. Gomer, "Desorption from metal surfaces by low-energy electrons," *J. Chem. Phys.*, vol. 41, pp. 3311-3328, 1964.
- [215] P. Redhead, "Interaction of slow electrons with chemisorbed oxygen," *Can. J. Phys.*, vol. 42, pp. 886-905, 1964.
- [216] P. J. Feibelman and M. L. Knotek, "Reinterpretation of electron-stimulated desorption data from chemisorption systems," *Phys. Rev. B*, vol. 18, pp. 6531-6539, 1978.
- [217] M. L. Knotek and P. J. Feibelman, "Ion Desorption By Core-Hole Auger Decay," *Phys. Rev. Lett.*, vol. 40, pp. 964-967, 1978.
- [218] F. Ohuchi and P. H. Holloway, "General-model of sodium desorption and diffusion during electron-bombardment of glass," *J. Vac. Sci. Technol.*, vol. 20, pp. 863-867, 1982.
- [219] I. I. Rzeznicka, J. Lee, and J. T. Yates, "Electron-stimulated desorption study of oxygen adsorbed on Ag(110). Observation of inclined physisorbed species," *J. Phys. Chem. C*, vol. 111, pp. 3705-3709, 2007.
- [220] T. E. Madey and J. T. Yates, "Desorption by electron impact - Oxygen adsorbed on tungsten," *Surf. Sci.*, vol. 11, pp. 327-351, 1968.
- [221] R. M. Jaeger, K. Homann, H. Kühlenbeck, and H. J. Freund, "Lifetimes of electronically excited-states of molecules on oxide versus metal-surfaces," *Chem. Phys. Lett.*, vol. 203, pp. 41-45, 1993.
- [222] P. Wargo and W. G. Shepherd, "Electron-Bombardment-Induced Dissociation of Alkaline Earth Oxides," *Phys. Rev.*, vol. 106, pp. 694-703, 1957.

- [223] H. Schlichting and D. Menzel, "Techniques for attainment, control, and calibration of cryogenic temperatures at small single-crystal samples under ultrahigh-vacuum," *Rev. Sci. Instrum.*, vol. 64, pp. 2013-2022, 1993.
- [224] C. Lourenco, M. D. Michelini, J. Marcalo, J. K. Gibson, and M. C. Oliveira, "Gas-Phase Reaction Studies of Dipositive Hafnium and Hafnium Oxide Ions: Generation of the Peroxide HfO_2^{2+} ," *J. Phys. Chem. A*, vol. 116, pp. 12399-12405, 2012.
- [225] M. A. Henderson, M. M. Shen, Z. T. Wang, and I. Lyubinetsky, "Characterization of the Active Surface Species Responsible for UV-Induced Desorption of O_2 from the Rutile TiO_2 (110) Surface," *J. Phys. Chem. C*, vol. 117, pp. 5774-5784, 2013.
- [226] T. Kamiya, K. Nomura, and H. Hosono, "Present status of amorphous In-Ga-Zn-O thin-film transistors," *Sci. Technol. Adv. Mat.*, vol. 11, pp. 044305, 2010.
- [227] D. H. Lee, K. Nomura, T. Kamiya, and H. Hosono, "Metal-Semiconductor Field-Effect Transistor Made Using Amorphous In-Ga-Zn-O Channel and Bottom Pt Schottky Contact Structure at 200 °C," *ECS Solid State Lett.*, vol. 1, pp. Q8-Q10, 2012.
- [228] Z. Q. Wang, H. Y. Xu, X. H. Li, H. Yu, Y. C. Liu, and X. J. Zhu, "Synaptic Learning and Memory Functions Achieved Using Oxygen Ion Migration/Diffusion in an Amorphous InGaZnO Memristor," *Adv. Funct. Mater.*, vol. 22, pp. 2759-2765 2012.
- [229] S. C. Wu, H. T. Feng, M. J. Yu, I. T. Wang, and T. H. Hou, "Flexible Three-Bit-Per-Cell Resistive Switching Memory Using a-IGZO TFTs," *IEEE Electr. Device L.*, vol. 34, pp. 1265-1267, 2013.
- [230] Y. S. Fan, P. T. Liu, and C. H. Hsu, "Investigation on amorphous InGaZnO based resistive switching memory with low-power, high-speed, high reliability," *Thin Solid Films*, vol. 549, pp. 54-58, 2013.
- [231] H. Y. Jeong, J. Y. Lee, and S. Y. Choi, "Direct observation of microscopic change induced by oxygen vacancy drift in amorphous TiO_2 thin films," *Appl. Phys. Lett.*, vol. 97, pp. 042109, 2010.

- [232] J. S. Rajachidambaram, S. Murali, J. F. Conley, S. L. Golledge, and G. S. Herman, "Bipolar resistive switching in an amorphous zinc tin oxide memristive device," *J. Vac. Sci. Technol. B*, vol. 31, pp. 01A104, 2013.
- [233] Y. Shimura, K. Nomura, H. Yanagi, T. Kamiya, M. Hirano, and H. Hosono, "Specific contact resistances between amorphous oxide semiconductor In–Ga–Zn–O and metallic electrodes," *Thin Solid Films*, vol. 516, pp. 5899-5902, 2008.
- [234] D. H. Lee, K. Nomura, T. Kamiya, and H. Hosono, "Diffusion-Limited a-IGZO/Pt Schottky Junction Fabricated at 200 °C on a Flexible Substrate," *IEEE Electr. Device L.*, vol. 32, pp. 1695-1697, 2011.
- [235] H. Kim, S. Kim, K. K. Kim, S. N. Lee, and K. S. Ahn, "Electrical Characteristics of Pt Schottky Contacts Fabricated on Amorphous Gallium Indium Zinc Oxides," *Jpn. J. Appl. Phys.*, vol. 50, pp. 105702, 2011.
- [236] S. H. Rha, U. K. Kim, J. Jung, H. K. Kim, Y. S. Jung, E. S. Hwang, Y. J. Chung, M. Lee, J. H. Choi, and C. S. Hwang, "The Electrical Properties of Asymmetric Schottky Contact Thin-Film Transistors with Amorphous-In₂Ga₂ZnO₇," *IEEE T. Electron Dev.*, vol. 60, pp. 1128-1135, 2013.
- [237] H. Cho, E. A. Douglas, A. Scheurmann, B. P. Gila, V. Craciun, E. S. Lambers, S. J. Pearton, and F. Ren, "Al₂O₃/InGaZnO₄ Heterojunction Band Offsets by X-Ray Photoelectron Spectroscopy," *ECS Solid State Lett.*, vol. 14, pp. H431-H433, 2011.
- [238] S. Iwamatsu, K. Takechi, T. Yahagi, Y. Watanabe, H. Tanabe, and S. Kobayashi, "Depth-Profiling Study on Amorphous Indium–Gallium–Zinc Oxide Thin-Film Transistors by X-ray Photoelectron Spectroscopy," *Jpn. J. Appl. Phys.*, vol. 52, pp. 03BB03, 2013.
- [239] A. W. C. Lin, N. R. Armstrong, and T. Kuwana, "X-ray Photoelectron/Auger Electron Spectroscopic Studies of Tin and Indium Metal Foils and Oxides," *Anal. Chem.*, vol. 49, pp. 1228-1235, 1977.
- [240] M. Pessa, A. Vuoristo, M. Vulli, S. Aksela, J. Vayrynen, T. Rantala, and H. Aksela, "Solid-state effects in M_{4,5}N_{4,5} Auger spectra of elements from ⁴⁹In to ⁵²Te," *Phys. Rev. B*, vol. 20, pp. 3115-3123, 1979.
- [241] C. Korber, S. P. Harvey, T. O. Mason, and A. Klein, "Barrier heights at the SnO₂/Pt interface: In situ photoemission and electrical properties," *Surf. Sci.*, vol. 602, pp. 3246-3252, 2008.

- [242] F. Chen, R. Schafranek, W. B. Wu, and A. Klein, "Reduction-induced Fermi level pinning at the interfaces between $\text{Pb}(\text{Zr,Ti})\text{O}_3$ and Pt, Cu and Ag metal electrodes," *J. Phys. D Appl. Phys.*, vol. 44, pp. 255301, 2011.
- [243] Z. D. Lin, F. Xu, and J. H. Weaver, "Surface segregation at metal – III-V-compound-semiconductor interfaces," *Phys. Rev. B*, vol. 36, pp. 5777-5783, 1987.
- [244] P. Claverie, B. Carriere, R. Pinchaux, and G. Rossi, "Experimental determination of local-bonding configuration at the early stages of growth of the heterogeneous Pt/InP(110) interface by synchrotron-radiation spectroscopy," *Phys. Rev. B*, vol. 38, pp. 1659-1666, 1988.
- [245] C. H. Jung, H. I. Kang, and D. H. Yoon, "The electrical, optical, and structural properties of amorphous indium gallium zinc oxide films and channel thin-film transistors," *Solid State Electron.*, vol. 79, pp. 125-129, 2013.
- [246] J. H. Choi, S. M. Hwang, C. M. Lee, J. C. Kim, G. C. Park, J. Joo, and J. H. Lim, "Effect of Ga content and sintering time on electrical properties of InGaZnO thin film transistors fabricated by sol-gel process," *J. Cryst. Growth*, vol. 326, pp. 175-178, 2011.
- [247] J. H. Kang, E. N. Cho, C. E. Kim, M. J. Lee, S. J. Lee, J. M. Myoung, and I. Yun, "Mobility enhancement in amorphous InGaZnO thin-film transistors by Ar plasma treatment," *Appl. Phys. Lett.*, vol. 102, pp. 222103, 2013.
- [248] G. W. Simmons and B. C. Beard, "Characterization of Acid-Base Properties of the Hydrated Oxides on Iron and Titanium Metal Surfaces," *J. Phys. Chem-US*, vol. 91, pp. 1143-1148, 1987.
- [249] E. McCafferty and J. P. Wightman, "Determination of the Concentration of Surface Hydroxyl Groups on Metal Oxide Films by a Quantitative XPS Method," *Surf. Interface Anal.*, vol. 26, pp. 549-564, 1998.
- [250] A. R. Gonzalez-Elipé, J. P. Espinos, A. Fernandez, and G. Munuera, "XPS study of the surface carbonation/hydroxylation state of metal oxides," *Appl. Surf. Sci.*, vol. 45, pp. 103-108, 1990.
- [251] F. Voigts, F. Bebensee, S. Dahle, K. Volgmann, and W. Maus-Friedrichs, "The adsorption of CO_2 and CO on Ca and CaO films studied with MIES, UPS and XPS," *Surf. Sci.*, vol. 603, pp. 40-49, 2009.

- [252] R. Schafrank, S. Payan, M. Maglione, and A. Klein, "Barrier height at (Ba,Sr)TiO₃/Pt interfaces studied by photoemission," *Phys. Rev. B*, vol. 77, pp. 195310, 2008.
- [253] A. Klein, F. Sauberlich, B. Spath, T. Schulmeyer, and D. Kraft, "Non-stoichiometry and electronic properties of interfaces," *J. Mater. Sci.*, vol. 42, pp. 1890-1900, 2007.
- [254] K. Lee, K. Nomura, H. Yanagi, T. Kamiya, E. Ikenaga, T. Sugiyama, K. Kobayashi, and H. Hosono, "Band alignment of InGaZnO₄/Si interface by hard x-ray photoelectron spectroscopy," *J. Appl. Phys.*, vol. 112, pp. 033713, 2012.
- [255] W. Monch, "Metal-semiconductor contacts: electronic properties," *Surf. Sci.*, vol. 299/300, pp. 928-944, 1994.
- [256] Y. Nishihata, J. Mizuki, T. Akao, H. Tanaka, M. Uenishi, M. Kimura, T. Okamoto, and N. Hamada, "Self-regeneration of a Pd-perovskite catalyst for automotive emissions control," *Nature*, vol. 418, pp. 164-167, 2002.
- [257] M. R. Goldwasser, M. E. Rivas, M. L. Lugo, E. Pietri, J. Perez-Zurita, M. L. Cubeiro, A. Griboval-Constant, and G. Leclercq, "Combined methane reforming in presence of CO₂ and O₂ over LaFe_{1-x}CO_xO₃ mixed-oxide perovskites as catalysts precursors," *Catal. Today*, vol. 107-108, pp. 106-113, 2005.
- [258] H. J. Su, L. Q. Jing, K. Y. Shi, C. H. Yao, and H. G. Fu, "Synthesis of large surface area LaFeO₃ nanoparticles by SBA-16 template method as high active visible photocatalysts," *J. Nanopart. Res.*, vol. 12, pp. 967-974, 2010.
- [259] N. N. Toan, S. Saukko, and V. Lantto, "Gas sensing with semiconducting perovskite oxide LaFeO₃," *Physica B*, vol. 327, pp. 279-282, 2003.
- [260] X. F. Wang, H. W. Qin, L. H. Sun, and J. F. Hu, "CO₂ sensing properties and mechanism of nanocrystalline LaFeO₃ sensor," *Sensor. Actuat. B*, vol. 188, pp. 965-971, 2013.
- [261] S. P. Simner, J. R. Bonnett, N. L. Canfield, K. D. Meinhardt, J. P. Shelton, V. L. Sprenkle, and J. W. Stevenson, "Development of lanthanum ferrite SOFC cathodes," *J. Power Sources*, vol. 113, pp. 1-10, 2003.

- [262] S. V. Chavan, and R. N. Singh, "Preparation, properties, and reactivity of lanthanum strontium ferrite as an intermediate temperature SOFC cathode," *J. Mater. Sci.*, vol. 48, pp. 6597-6604, 2013.
- [263] N. Yamazoe, "Oxidation Catalysis of Perovskites --- Relationships to Bulk Structure and Composition (Valency, Defect, etc.)," *Catal. Today*, vol. 8, pp. 175-199, 1990.
- [264] J. L. G. Fierro, and L. G. Tejuca, "Non-stoichiometric Surface Behavior of LaMO_3 Oxides as Evidenced by XPS," *Appl. Surf. Sci.*, vol. 27, pp. 453-457, 1987.
- [265] M. A. Pena, and J. L. G. Fierro, "Chemical Structures And Performance Of Perovskite Oxides," *Chem. Rev.*, vol. 101, pp. 1981-2017, 2001.
- [266] C. W. Lee, R. K. Behera, S. Okamoto, R. Devanathan, E. D. Wachsman, S. R. Phillpot, and S. B. Sinnott, "Stabilization Mechanisms of LaFeO_3 (010) Surfaces Determined with First Principles Calculations," *J. Am. Ceram. Soc.*, vol. 94, pp. 1931-1939, 2011.
- [267] B. H. Li, M. B. Katz, Q. J. Zhang, L. Chen, G. W. Graham, and X. Q. Pan, "Surface-termination-dependent Pd bonding and aggregation of nanoparticles on LaFeO_3 (001)," *J. Chem. Phys.*, vol. 138, pp. 144705, 2013.
- [268] L. H. Sun, J. F. Hu, H. W. Qin, M. Zhao, and K. Fan, "Influences of Ca Doping and Oxygen Vacancy upon Adsorption of CO on the LaFeO_3 (010) Surface: A First-Principles Study," *J. Phys. Chem. C*, vol. 115, pp. 5593-5598, 2011.
- [269] E.N. Armstrong, K.L. Duncan, and E.D. Wachsman, "Effect of A and B-site cations on surface exchange coefficient for ABO_3 perovskite materials," *Phys. Chem. Chem. Phys.*, vol. 15, pp. 2298-2308, 2013.
- [270] L. Qiao, K. H. L. Zhang, M. E. Bowden, T. Varga, V. Shutthanandan, R. Colby, Y. Du, B. Kabius, P. V. Sushko, M. D. Biegalski, and S. A. Chambers, "The Impacts of Cation Stoichiometry and Substrate Surface Quality on Nucleation, Structure, Defect Formation, and Intermixing in Complex Oxide Heteroepitaxy- LaCrO_3 on SrTiO_3 (001)," *Adv. Funct. Mater.*, vol. 23, pp. 2953-2963, 2013.

- [271] S. Thevuthasan, C. H. F. Peden, M. H. Engelhard, D. R. Baer, G. S. Herman, W. Jiang, Y. Liang, and W. J. Weber, "The ion beam materials analysis laboratory at the environmental molecular sciences laboratory," *Nucl. Instr. Meth. A*, vol. 420, pp. 81-89, 1999.
- [272] M. Mayer, SIMNRA User's Guide, Report IPP 9/113, Max-Planck-Institut für Plasmaphysik, Garching, Germany, 1997.
- [273] S. I. Yi, Y. Liang, S. Thevuthasan, and S. A. Chambers, "Morphological and structural investigation of the early stages of epitaxial growth of α - Fe_2O_3 (0001) on α - Al_2O_3 (0001) by oxygen-plasma-assisted MBE," *Surf. Sci.*, vol. 443, pp. 212-220, 1999.
- [274] C. J. Powell, and A. Jablonski, NIST Electron Inelastic-Mean-Free-Path Database, version 1.2, SRD 71; National Institute of Standards and Technology: Gaithersburg, MD, 2010.
- [275] S. Tanuma, C. J. Powell, and D. R. Penn, "Calculations Of Electron Inelastic Mean Free Paths. V. Data For 14 Organic-Compounds Over The 50-2000 eV Range," *Surf. Interface Anal.*, vol. 21, pp. 165-176, 1994.
- [276] T. Arima, Y. Tokura, and J. B. Torrance, "Variation of optical gaps in perovskite-type 3d transition-metal oxides," *Phys. Rev. B*, vol. 48, pp. 17006-17009, 1993.
- [277] Y. Matuura, S. Matsushima, M. Sakamoto, and Y. Sadaoka, "NO₂-Sensitive LaFeO₃ Film prepared by Thermal Decomposition of the Heteronuclear Complex, {La[Fe(CN)₆·5H₂O]}_x," *J. Mater. Chem.*, vol. 3, pp. 767-769, 1993.
- [278] C. J. Powell, A. Jablonski, I. S. Tilinin, S. Tanuma, and D. R. Penn, "Surface sensitivity of Auger-electron spectroscopy and X-ray photoelectron spectroscopy," *J. Electron Spectrosc.*, vol. 98, pp. 1-15, 1999.
- [279] L. A. Gianuzzi, J. L. Drown, S. R. Brown, R. B. Irwin, and F. A. Stevie, "Applications of the FIB Lift-Out Technique for TEM Specimen Preparation," *Microsc. Res. Techniq.*, vol. 41, pp. 285-290, 1998.
- [280] V. Shutthanandan, S. Thevuthasan, Y. J. Kim, and C. H. F. Peden, "Channeling Studies of CeO₂ and Ce_{1-x}ZrxO₂ Films on Yttria-Stabilized

- ZrO₂(111)," *Mat. Res. Soc. Symp. Proc.*, vol. 654, pp. AA2.6.1-AA2.6.6, 2001.
- [281] T. Yamashita, and P. Hayes, "Analysis of XPS spectra of Fe²⁺ and Fe³⁺ ions in oxide materials," *Appl. Surf. Sci.*, vol. 254, pp. 2441-2449, 2008.
 - [282] J. F. Moulder, W. F. Stickle, P. E. Sobol, and K. D. Bomben, *Handbook of X-ray Photoelectron Spectroscopy*. Eden Prairie, MN, USA: Perkin-Elmer Corporation, 1992.
 - [283] J. M. D. Tascon, J. L. G. Fierro, and L. G. Tejuca, "Physicochemical Properties Of LaFeO₃ - Kinetics of Reduction and of Oxygen Adsorption," *J. Chem. Soc., Faraday Trans. I*, vol. 81, pp. 2399-2407, 1985.
 - [284] P. E. Marti and A. Baiker, "Influence of the A-site cation in AMnO_{3+x} and AFeO_{3+x} (A = La, Pr, Nd and Gd) perovskite-type oxides on the catalytic activity for methane combustion," *Catal. Lett.*, vol. 26, pp. 71-84, 1994.
 - [285] J. Suntivich, H. A. Gasteiger, N. Yabuuchi, H. Nakanishi, J. B. Goodenough, and Y. Shao-Horn, "Design principles for oxygen-reduction activity on perovskite oxide catalysts for fuel cells and metal-air batteries," *Nature Chem.*, vol. 3, pp. 546-550, 2011.
 - [286] P. A. W. van der Heide and J. W. Rabalais, "Photoelectron spectroscopic study of the temperature-dependent termination of the LaAlO₃(100) surface," *Chem. Phys. Lett.*, vol. 297, pp. 350-356, 1998.
 - [287] D. D. Sarma and C. N. R. Rao, "XPES Studies of Oxides of Second- and Third-Row Transition Metals Including Rare Earths," *J. Electron Spectrosc.*, vol. 20, pp. 25-45, 1980.
 - [288] P. L. J. Gunter, O. L. J. Gijzeman, and J. W. Niemantsverdriet, "Surface roughness effects in quantitative XPS: magic angle for determining overlayer thickness," *Appl. Surf. Sci.*, vol. 115, pp. 342-346, 1997.
 - [289] M. A. Henderson, C. L. Perkins, M. H. Engelhard, S. Thevuthasan, and C. H. F. Peden, "Redox properties of water on the oxidized and reduced surfaces of CeO₂(111)," *Surf. Sci.*, vol. 526, pp. 1-18, 2003.

- [290] E. J. Crumlin, E. Mutoro, W. T. Hong, M. D. Biegalski, H. M. Christen, Z. Liu, H. Bluhm, and Y. Shao-Horn, "In Situ Ambient Pressure X-ray Photoelectron Spectroscopy of Cobalt Perovskite Surfaces under Cathodic Polarization at High Temperatures," *J. Phys. Chem. C*, vol. 117, pp. 16087-16094, 2013.
- [291] P. A. W. van der Heide, "Systematic x-ray photoelectron spectroscopic study of $\text{La}_{1-x}\text{Sr}_x$ -based perovskite-type oxides," *Surf. Interface Anal.*, vol. 33, pp. 414-425, 2002.